PhD Thesis

University of Lille

Design of Metal Catalysts for Carbon Monoxide Hydrogenation with High Activity, Selectivity and Stability

PhD candidate: Mr. Bang GU

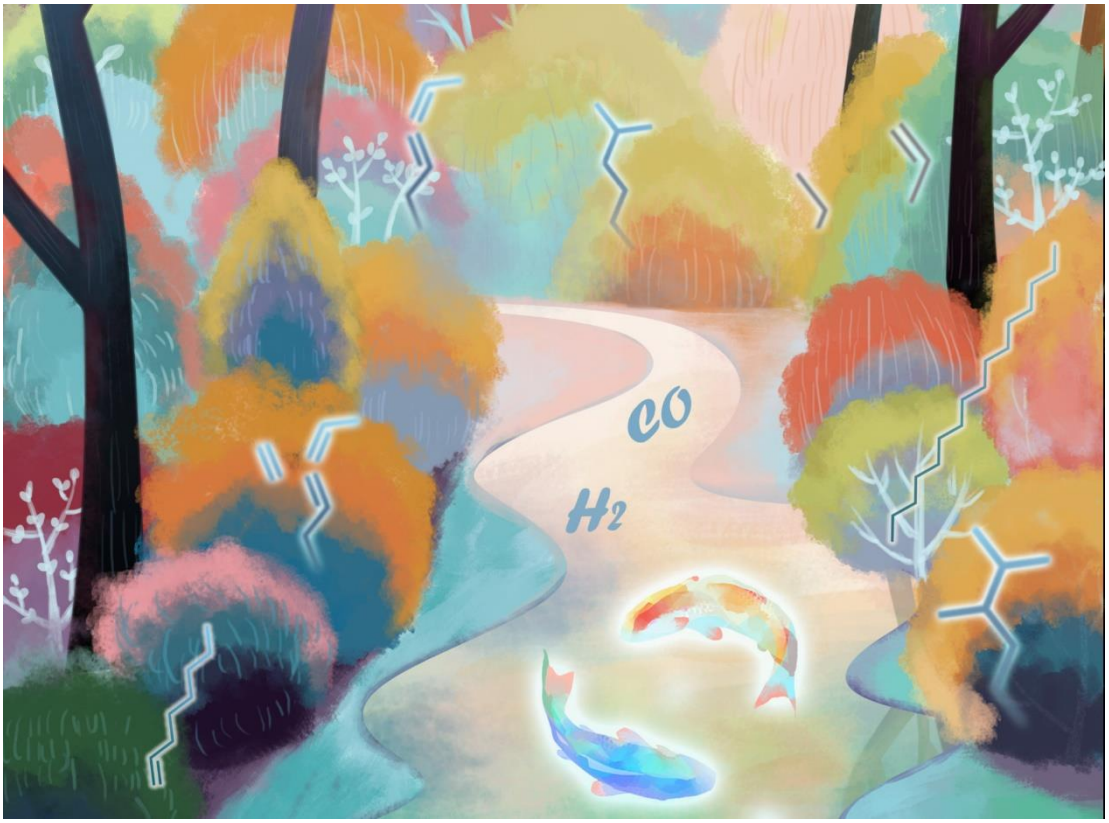

THESE DE DOCTORAT

PRESENTEE PAR

BANG GU

POUR L'OBTENTION DU TITRE DE

DOCTEUR DE L'UNIVERSITE DE LILLE

Ecole Doctorale: Sciences de la Matiére, du Rayonnement et de l'Environnement

Spécialité: Chimie organique, minerale, industrielle

Conception de catalyseurs métalliques pour l'hydrogénation du monoxyde de carbone avec une activité, sélectivité et stabilité élevées

Soutenue le 27 septembre 2019 devant le jury composé de:

Dr. Cuong PHAM-HUU	Directeur de recherche CNRS	Rapporteur
Prof. Joris W. THYBAUT	University of Gent, Belgium	Rapporteur
Dr. Vitaly V. ORDOMSKY	CNRS	Examinateur
Dr. Mirella VIRGINIE	ENSCL	Examinateur invité
Dr. Andrei Y. KHODAKOV	Directeur de recherche CNRS	Directeur de thèse

——Smile, never give up!

Contents

Résumé 1

Abstract 4

Chapter 1. Literature Review 7

1.1 General Introduction 7

1.2 Mechanism of FTS Reaction and Main Challenges 8

1.3 Olefin Synthesis from Syngas 12

1.3.1 Light olefins synthesis from syngas 12

1.3.2 Long chain α-olefins synthesis from syngas 15

1.3.3 Key factors affecting FTO selectivity and activity 18

1.4 Catalysts Deactivation in Syngas Conversion 23

1.4.1 Mechanism of catalyst deactivation 24

1.4.2 The strategies for improving catalyst stability 31

. 1.5 The Objectives and Research Methods of this Thesis 34

1.5.1 Promotion effect in Fe-based FTO catalysts. 35

1.5.2 From outside to inside the CNT tubes over Fe-based FTO catalysts. 35

1.5.3 Long chain α-olefins synthesis in the presence of carboxylic acids 36

1.5.4 Design highly stable cobalt and nickel catalysts in CO hydrogenation. 37

1.6 Outline of the Thesis. 37

1.7 Reference 39

Chapter 2. Catalysts and Experiments 47

2.1 Catalyst Preparation 47

2.1.1. Carbon nanotubes pretreatment. 47

2.1.2 Preparation of CNT supported iron-based catalysts. 47

2.1.3 Preparation of CNT confined iron-based catalysts. 48

2.1.4 Preparation of Al_2O_3 supported Co catalysts 49

2.1.5 Preparation of SiO_2 supported Cobalt and Nickel catalysts. 49

2.2 Evaluation of Catalytic Performance 50

2.2.1 Equipment for evaluation of Fe-based catalysts in the centimetric reactor. 50

2.2.2 Equipment for Water-Gas-Shift reaction 52

2.2.3 Avantium high throughput equipment for evaluation for long chain olefins synthesis. 52

2.2.4 Equipment with 3 parallel reactors for testing Co and Ni based catalysts. 54

2.3 Analysis method 55

2.4 Catalyst Characterization 56

2.4.1 X-ray diffraction 56

2.4.2 Surface area and porosity 57

2.4.3 Transmission electron microscopy 57

2.4.4 Temperature-programmed reduction 58

2.4.5 Pulse oxidation 59

2.4.6 CO chemisorption 59

2.4.7 Temperature-programmed hydrogenation 59

2.4.8 Infrared spectroscopy analysis (FT-IR) 59

2.4.9 Elemental analysis 60

2.4.10 XPS with sample pretreatment 60

2.4.11 In-situ magnetic characterization 61

2.4.12 Mössbauer spectroscopy 62

2.4.13 Ex-situ and in-situ X-ray absorption fine structure (XAFS) 62

2.5 Reference 64

Chapter 3. Effects of the Promotion with Bismuth and Lead on Direct Synthesis of Light Olefins from Syngas over Carbon Nanotube Supported Iron Catalysts 65

3.1. Introduction 66

3.2. Results and Discussion 69

3.2.1 Calcined catalysts 69

3.2.2 Carbidized iron catalysts 73

3.2.3 Catalytic results 79

3.2.4. Interaction of iron species with promoters and catalytic performance in FT synthesis

.....85

3.3. Conclusion.....90

3.4. Reference.....91

Chapter 4. Synergy of Nanoconfinement and Promotion in the Design of Efficient Supported Iron Catalysts for Direct Olefin Synthesis from Syngas.....95

4.1. Introduction.....96

4.2. Results and Discussion.....97

4.2.1 Catalyst characterization.....97

4.2.2 Catalytic performance.....113

4.3 Conclusion.....124

4.4 Reference.....125

Chapter 5. Size and Promoter Effects on Iron Nanoparticles Confined in Carbon Nanotubes and their Catalytic Performance in Light Olefin Synthesis from Syngas.....129

5.1 Introduction.....130

5.2 Results and Discussion.....132

5.2.1 Catalyst structure.....132

5.2.2 Catalytic results.....141

5.3. Conclusion.....151

5.4. Reference.....152

Chapter 6. Selectivity shift from paraffins to α-olefins in low temperature Fischer-Tropsch synthesis in the presence of carboxylic acids.....155

6.1. Introduction.....156

6.2 Results and Discussion.....158

6.3 Conclusion.....167

6.4 Reference.....168

Chapter 7. Self-regeneration of Cobalt and Nickel Catalysts Promoted with Bismuth and Non-deactivating Performance in Carbon Monoxide Hydrogenation.....171

7.1. Introduction.....172

7.2. Results and Discussion.....174

7.2.1. Catalyst characterization 174
7.2.2. Catalytic performance 178
7.2.3. Coke deposition 181
7.2.4. Sintering 188
7.3. Conclusion 190
7.4. Reference 191
Chapter 8. General Conclusion and Perspectives 195
8.1 General Conclusion 195
8.1.1 Syngas direct conversion to olefins over iron and cobalt catalysts 195
8.1.2 Synergy of nanoconfinement and promotion for iron catalysts in FTO 196
8.1.3 Design of high stable cobalt and nickel catalysts 197
8.2 Perspectives 198
8.2.1 Increase in the olefin selectivity over iron and cobalt catalysts 198
8.2.1 Design high stable metal catalysts in CO hydrogenation 199

Résumé

La synthèse de Fischer-Tropsch (FT) est l'un des moyens les plus pratiques de convertir les ressources carbonées alternatives, telles que le charbon, la biomasse, le gaz naturel et le gaz de schiste, en carburants et en produits chimiques à haute valeur ajoutée via le gaz de synthèse. Les hydrocarbures issus de la synthèse FT suivent une distribution large Anderson-Schulz-Flory (ASF). C'est donc un grand défi d'améliorer la sélectivité en hydrocarbures spécifiques. En plus de la sélectivité, la stabilité insuffisante des catalyseurs restreint une large implémentation de la synthèse FT dans l'industrie. Dans cette thèse, nous explorons les effets dus à la promotion avec des métaux de soudure tels que le bismuth et le plomb sur l'activité catalytique, la sélectivité et la stabilité des catalyseurs au fer, au cobalt et au nickel. Une autre stratégie repose sur la synergie du confinement des particules de fer dans des nanotubes de carbone couplée avec la promotion et la variation de la taille de particules de fer afin d'améliorer les performances catalytiques. Enfin, la co-alimentation du syngas en acides est proposée comme l'un des moyens pour améliorer la sélectivité des catalyseurs au cobalt en α-oléfines à longue chaîne.

Les effets dus à la promotion des catalyseurs au fer supporté par des nanotubes de carbone au bismuth et au plomb sur la synthèse directe d'oléfines légères à partir de gaz de synthèse ont été étudiés dans le chapitre 3. Par rapport aux catalyseurs au fer non promus, une vitesse de réaction de Fischer-Tropsch deux fois plus importante et une sélectivité considérablement plus élevée ont été observées. Une meilleure sélectivité observée était due à des ralentissements de l'hydrogénation secondaire des oléfines et de la croissance de la chaîne lors de la synthèse Fischer-Tropsch. Une migration remarquable des promoteurs lors de l'activation du catalyseur et une décoration des nanoparticules de carbure de fer par les promoteurs ont été mis en évidence.

Dans le chapitre 4, en utilisant un large éventail de techniques ex situ et in situ, nous avons découvert, plusieurs effets synergiques majeurs issus du nanoconfinement du fer

dans les nanotubes de carbone et de sa promotion au bismuth et au plomb sur la structure et les performances catalytiques. Le nanoconfinement du fer dans les nanotubes de carbone, associé à la promotion au Bi ou au Pb, permet d'obtenir un rendement en oléfines légères dix fois plus élevé. Le nanoconfinement conduit principalement à des meilleures dispersion et stabilité, tandis que l'activité intrinsèque du fer (TOF) reste inchangée. La promotion au Bi et au Pb entraîne une augmentation majeure du TOF dans les catalyseurs confinés et non confinés. Apres l'optimisation, la synthèse Fischer-Tropsch se produit sous pression atmosphérique avec une conversion élevée et une sélectivité accrue en oléfines légères sur les catalyseurs promus et confinés. De plus, le nanoconfinement ralentit le frittage du fer au cours de la réaction et améliore la stabilité des catalyseurs.

Dans le chapitre 5, nous avons examiné l'effet de la taille des particules de fer dans les catalyseurs confinés sur la conversion du gaz de synthèse en oléfines Nous avons démontré d'un part, que le TOF augmente lors que la taille des nanoparticules de fer confinés promues ou non-promues augmente de 2.5 à 12 nm. D'autre part, la sélectivité en olefines légères dépend fortement de la promotion. Dans les catalyseurs non-promus, la taille des particules de fer encapsulées dans les nanotubes de carbone ne produit aucun effet notable sur la sélectivité en oléfines légères, tandis que dans les catalyseurs promus au Bi et au Pb, la sélectivité en oléfines légères était supérieure sur les petites nanoparticules de fer et diminuait avec l'augmentation de la taille de nanoparticules.

Dans le chapitre 6, nous avons élaboré une nouvelle approche pour la synthèse d'oléfines alpha linéaires lors de la synthèse de FT à basse température sur les catalyseurs à base de Co. Nous avons constaté que la co-alimentation du syngas en acides carboxyliques induisait une modification de la sélectivité et son déplacement vers les oléfines alpha. La sélectivité en olefines alpha atteint 39 % en présence des acides.

En fin, nous avons proposé une nouvelle stratégie pour améliorer considérablement la stabilité des catalyseurs Co et Ni pour l'hydrogénation du CO via leur promotion au

bismuth. Les catalyseurs promus ont démontré une stabilité exceptionnelle lors de la réaction. Les expériences menées ont révélé l'auto-régénération continue du catalyseur au cours de la réaction via l'oxydation du carbone déposé par l'oxygène généré lors de la dissociation du CO à l'interface de nanoparticules métalliques et du promoteur de bismuth. La formation d'une couche de bismuth protégeait également les nanoparticules métalliques du frittage.

Mots clés: synthèse Fischer-Tropsch, promotion, effet de confinement, taille des particules, oléfines, désactivation des catalyseurs.

Abstract

Fischer-Tropsch (FT) synthesis is one of the most practicable routes to convert non-petroleum carbon resources, such as coal, biomass, natural gas and shale gas, via syngas into valuable fuels and chemicals. This reaction follows surface polymerization mechanism and the primary products follows the Ander-Schulz-Flory (ASF) distribution. It's a big challenge to improve the target products selectivity. Apart from the selectivity, catalyst deactivation also restricts the wide application in FT synthesis.

In this thesis, we are exploring catalyst promotion with soldering metals such as bismuth and lead on the catalytic activity, selectivity and stability of iron, cobalt and nickel catalysts. Another strategy is based on the confinement of iron particles in carbon nanotubes in synergy with the promotion and iron particle size effects in order to improve the catalytic performance. Finally, cofeeding with acids is considered is one of the routes to improve the selectivity of cobalt catalysts to long chain α-olefins.

The effect of the promotion with bismuth and lead on direct synthesis of light olefins from syngas over carbon nanotube supported iron catalysts was investigated in Chapter 3. Compared to the un-promoted iron catalysts, a twice higher Fischer-Tropsch reaction rate and higher selectivity to light olefins were obtained. This promotion effect is more significant under atmospheric pressure with 2-4 times higher activity while the selectivity of light olefins reaches as high as ~60 %. The promoters simultaneously slow down secondary olefin hydrogenation and Fischer-Tropsch chain growth and thus then increase the light olefins selectivity. Remarkable migration of promoters during the catalyst activation and decoration of the iron carbide nanoparticles were uncovered by characterization.

Moreover, in Chapter 4 we uncovered using a wide range of *ex-situ* and *in-situ* techniques several major synergetic effects arising from the iron nanoconfinement and promotion with bismuth and lead on the structure and catalytic performance of iron catalysts supported by carbon nanotubes in high temperature FT synthesis resulting in

light olefins. Iron nanoconfinement inside carbon nanotubes combined with the promotion with Bi or Pb result in a 10-fold higher yield of light olefins. Nanoconfinement in carbon nanotubes mostly leads to better iron dispersion and stability, while intrinsic activity is only slightly affected. Promotion with Bi and Pb results in a major increase in the site intrinsic activity (TOF) in both confined and non-confined catalysts. Over the optimized promoted and confined catalysts, Fischer-Tropsch synthesis occurs under atmospheric pressure with high conversion and enhanced selectivity to light olefins. Nanoconfinement of iron particles slows down iron sintering during the reaction and thus improves the catalyst stability.

Apart from the confinement effect, we also study the particle size effect in the confined system for syngas conversion to light olefins over both promoted and unpromoted iron catalysts in Chapter 5. The TOF increases with increasing in the iron nanoparticles sizes from 2.5 to 12 nm over the carbon nanotubes containing encapsulated monometallic or Bi- or Pb-promoted iron nanoparticles. The iron particles size of unpromoted catalysts encapsulated in carbon nanotubes does not show any noticeable effect on the light olefin selectivity, while in the Bi- and Pb-promoted catalysts, the light olefin selectivity was higher over smaller encapsulated iron nanoparticles and decreased with the increase in the nanoparticle size.

In Chapter 6, we introduced a new approach for the synthesis of linear α-olefins during low temperature FT synthesis over the Co based catalysts. We found that the co-feeding carboxylic acids leads to a shift of selectivity from paraffins to α-olefins which has been assigned to stabilization of olefins by intermediate formation of esters. The α-olefins selectivity is as high as 39 % in the presence of acids.

In the end, we propose a new strategy, which substantially improves the stability of Co and Ni catalysts for CO hydrogenation via their promotion with bismuth. The promoted catalysts demonstrated exceptionally stable performance. The conducted experiments uncovered continuous catalyst self-regeneration during the reaction via oxidation of deposed carbon by oxygen scavenged after CO dissociation at the interface of metal nanoparticles and bismuth promoter. Formation of the bismuth-protecting

layer over metal nanoparticles protects them against sintering.

Key words: Fischer-Tropsch synthesis, promotion, confinement effect, particle size, olefins, catalysts deactivation.

Chapter 1. Literature Review

1.1 General Introduction

With the rapid development of the economy, the global energy demand especially that of developing countries, has risen sharply. Energy shortages, particularly the continuous depletion of oil resources and fierce competition in global energy supply and demand, have become increasingly severe. This has become a constraint for the sustainable and peaceful development of human society [1, 2].

According to the <World Energy Outlook 2018> [3], the World Energy Agency predicts that fossil fuels dominated by oil, coal, and natural gas (including unconventional natural gas such as shale gas) will continue to be the main source of human development for the foreseeable future. However, in view of the coming petroleum depletion, the development of new methods for the efficient conversion and utilization of coal and gas (including coalbed methane and shale gas) are of great significance for alleviating the scarcity of petroleum resources.

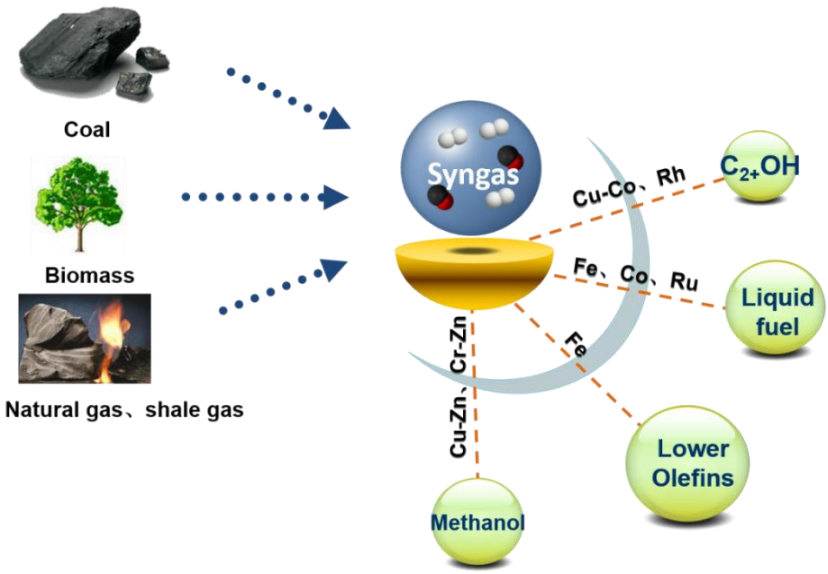

Figure 1.1. *Utilization of non-oil-based carbon resources via syngas conversion to liquid fuels and chemicals*

Manufacturing olefins and other chemicals via catalytic conversion of syngas (H_2 + CO) is one of the most feasible ways to convert non-oil-based carbon resources such as coal, natural gas, shale gas, and biomass (Figure 1.1). This process also known as Fischer-Tropsch synthesis (FTS). Syngas conversion can produce both hydrocarbons and organic oxygenates. The hydrocarbons may be liquid fuels such as gasoline (C_5-C_{11}), diesel (C_{10}-C_{20}), jet fuel (C_8-C_{16}), or other important chemical materials such as light olefins (C_2-C_4 olefins) and long chain olefins. The oxygenates include methanol, ethanol, ethylene glycol and other important chemicals or fuel additives. With the advent of the "post-petroleum era", syngas chemistry will inevitably attract wider attention from both academia and industry [4-6].

1.2 Mechanism of FTS Reaction and Main Challenges

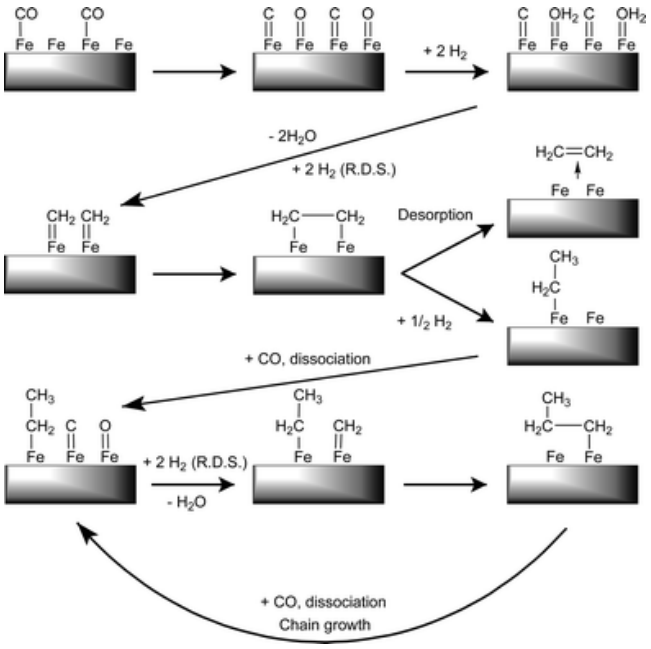

Figure 1.2. *Surface carbide mechanism. RDS：The rate determining steps [7].*

Fischer-Tropsch synthesis is a very complex reaction. Its products include alkanes, olefins, oxygenates, etc. Therefore, control of the selectivity to the target products is particularly important. With a high selectivity for specific products, it is undoubtedly critical to choose a suitable catalyst in addition to the optimized reaction conditions. On the other hand, the study of the mechanism of product formation helps and guides the

catalyst and process design. Therefore, the research on the mechanism of the Fischer-Tropsch reaction is very important. Several classical reaction mechanisms have been proposed int the literature. They include: surface carbide mechanism [8], oxygen-containing intermediate polycondensation mechanism [9], CO insertion mechanism [10].

Surface Carbide Mechanism: It was the earliest proposed and widely accepted mechanism which is shown as a simplified scheme in Figure 1.2 [11]. Hans Fischer and Franz Tropsch suggested that the mechanism involves alkyls, alkylenes and alkenyl species. Figure 1.2 uses an iron catalyst as an example, CO is dissociated and adsorbs on the surface of the catalyst to form carbide active species, and forms CH_2 active species with the adsorbed hydrogen, which further polymerize into alkanes and alkenes [12]. This mechanism can explain the production of alkanes, but it cannot explain the production of oxygenates and branched hydrocarbons.

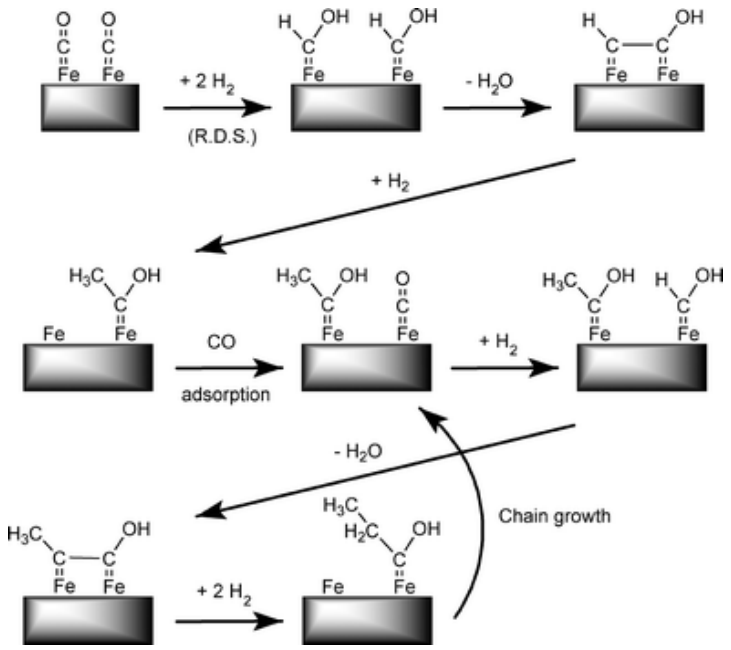

Figure 1.3. *Surface enol mechanism. RDS：The rate determining steps [7].*

Oxygen-containing Intermediate Polycondensation Mechanism: In order to explain the formation of oxygenates, researchers have proposed the polycondensation mechanism of oxygenated intermediates, also known as the enol mechanism (Figure 1.3). This model assumes that CO does not dissociate on the surface of the catalyst but

forms hydrogenated oxygen-containing intermediate hydroxy olefin (HCOH) species with the adsorbed hydrogen. Further condensation reactions take place. During carbon chain growth, hydroxyl-olefins are split into aldehydes or dehydroxylated to olefins and then hydrogenated to produce alkanes or alcohols [13-15]. Emmett et al. confirmed this assumption by isotope ^{14}C tracking [14, 16-19]. However, oxygenated intermediate hydroxyl-olefins have not been directly proven and have been questioned.

CO Insertion Mechanism: This mechanism was first proposed by Pichler and Schulz in 1958 [10], corrected by Henrici-Olive [20] and Masters [21]. Figure 1.4 shows an example of this mechanism occurring on an iron-based catalyst. Hydrogen is adsorbed on the surface of catalyst, CO is inserted into the Fe-H bond to form formyl, and then hydrogenated to a bridged methylene intermediate, which can be further hydrogenated to generate methyl groups and carbene, and then through repeated insertion and CO hydrogenation can generate a variety of hydrocarbon compounds. This mechanism can well explain the formation of linear hydrocarbons and oxygenates, but it cannot explain the formation of branched products.

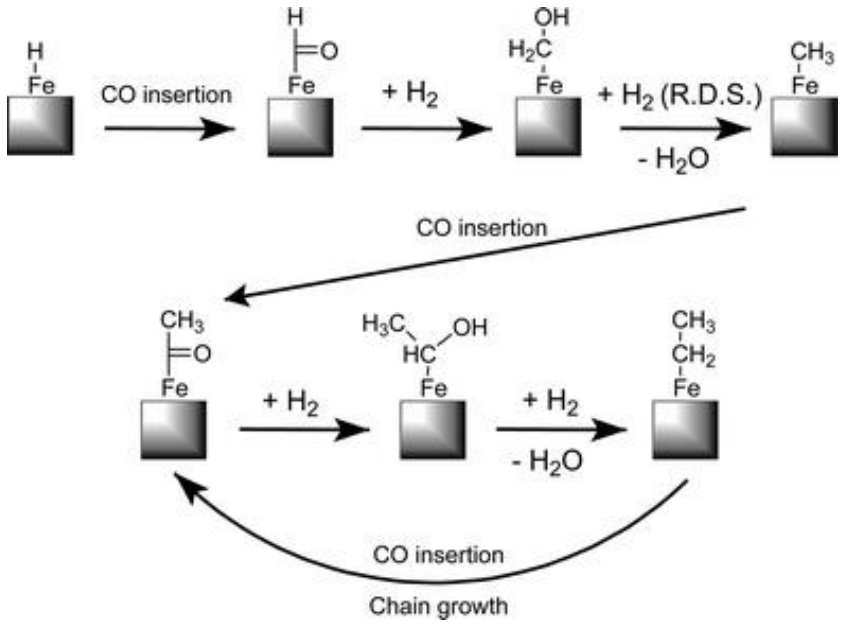

Figure 1.4. *CO insertion mechanism. RDS：The rate determining steps[7].*

Despite the fact all the mentioned mechanisms explain some of the reaction results, contradictory data exist for all of them [22]. No matter what kind of mechanism, the Fischer-Tropsch synthesis can be considered as a surface polymerization reaction, the product stream consists of a range of products which follows the Anderson-Schulz-Flory(ASF) kinetics model [7]. In this model the probability of chain growth factor is defined between 0 and 1. The relationship between molar fraction M_n and chain growth factor is $M_n = (1-\alpha)\ \alpha^{n-1}$. The selectivity to specific products is restricted by ASF distribution. The maximum selectivity for C_5-C_{11} is ~45 %, for C_{12}-C_{18} is ~26 % and for C_2-C_4 range is ~58 % (Figure 1.5) [11]. How to break the ASF product distribution and to increase a specific range of hydrocarbon is one of the hot topics and challenges in FT synthesis [23-25].

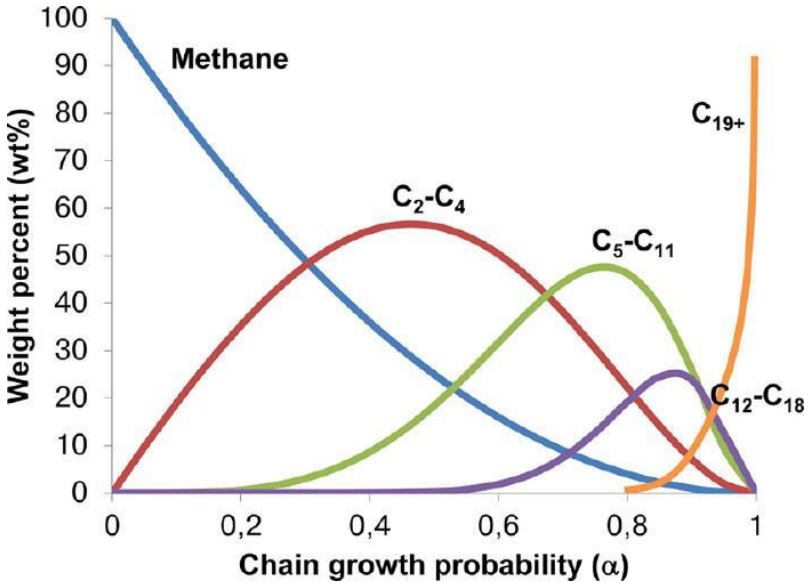

Figure 1.5. *Hydrocarbon selectivity as function of the chain growth probability factor (α) [11].*

Another challenge is how to decrease the catalyst deactivation and then improve the stability. The deactivation of FT synthesis catalysts is postulated to be due to a number of different deactivation phenomena, such as sintering of active phase, carbon formation on the catalysts, active phase change and poisoning. These problem restrict wide application of FT synthesis in the industry. So, design of high active and stable FTS catalysts demands a lot of efforts.

1.3 Olefin Synthesis from Syngas

1.3.1 Light olefins synthesis from syngas

Figure 1.6 shows a schematic diagram of feasible routes for the synthesis of light olefins from syngas as raw materials. These routes can be broadly divided into two categories: direct and indirect process. Fischer-Tropsch synthesis is a short route to the synthesis of light olefins, but the selectivity to light olefins is not high. The indirect process concludes two steps: synthesis methanol, dimethyl ether or other intermediate products by using coal or biomass and then production of light olefins via C-C coupling or dehydration and cracking processes. This indirect processes are more selective than the direct route. However, the investment in equipment is large, and the economic cost can be much higher.

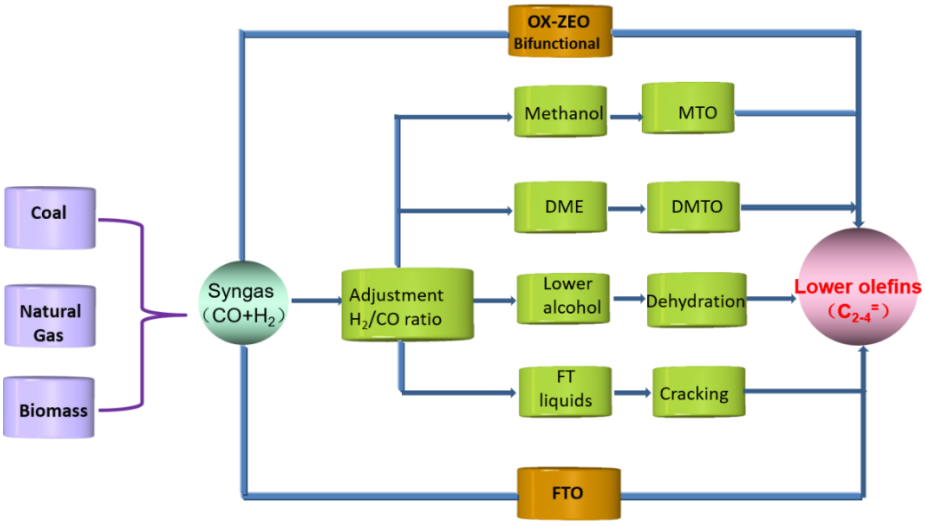

Figure 1.6. *Process for the transformation of CO-rich synthesis gas into light olefins [11, 26].*

Fischer-Tropsch to Olefins (FTO) is a key process for the direct single-step transformation of various alternative carbon resources such as coal, natural gas, renewable biomass and waste into light olefins via syngas [27-29]. Iron-based catalysts are the catalysts of choice for the FTO process because of their high selectivity towards light olefins, lower cost and high water-gas-shift activity, which can adjust the H_2/CO ratio in syngas produced from the biomass- or coal-derived feedstocks. Iron has also

stronger resistance to the contaminants in syngas (sulfur, nitrogen compounds) compared with cobalt and ruthenium based catalysts [24]. Some promising results have been achieved for iron catalysts. de Jong and co-workers [28, 30, 31]observed enhanced selectivity to light olefins (about 60 %) over a modified Fe/α-Al_2O_3 catalyst containing small amounts of sulfur and sodium. The best results in that report were obtained at very low CO conversion. The inert low surface area α-Al_2O_3 support showed week interaction with iron species. It was suggested that sodium could reduce methane selectivity by increasing the chain growth probability while sulfur have reduced the hydrogen coverage of the catalyst and its hydrogenation activity. The proximity between iron and promoters (Na, S) was a key parameter, which determined hydrocarbon distribution.

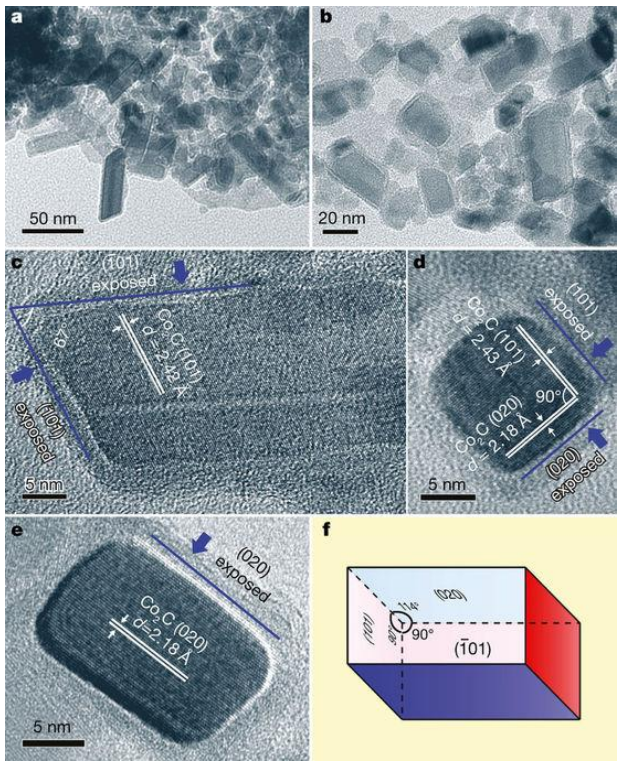

Figure 1.7. *TEM images of the CoMn catalysts after reaching steady state. a, b, Low-resolution TEM images. c-e, High-resolution images of Co_2C nanoprisms with exposed facets of (101), (101) and (020). d, distance (length) of the lattice fringes. f, The Co_2C nanoprism has a parallelepiped shape, with four rectangular faces and two rhomboid faces [32].*

It is widely accepted that metallic Co preferentially produces heavy hydrocarbons with high selectivity for the C_{5+} hydrocarbons [33, 34]. The formation of Co_2C is considered to be one of the main reasons for deactivation of the Co-based FT reaction because cobalt carbide has lower activity in the CO hydrogenation [26, 35, 36]. However, Zhong et al [32] reported that, under mild reaction conditions (250 °C, 0.1-0.5 MPa), Co_2C nanoprisms catalyze syngas conversion with high selectivity for the production of light olefins (~60 %, total olefins ~80 %) with very little methane (about 5.0 %), and high ratio of olefin/paraffin (~30) among the C_2-C_4 products. The product distribution deviated markedly from the classical ASF distribution and showed the highest selectivity for propylene. The catalyst also showed good stability under long-term operation; no obvious deactivation was detected after 600 h. Based on structural characterization and DFT calculations, a strong facet effect for the Co_2C nanoparticles during syngas conversion was suggested. Specifically, the (101) and (020) facets of Co_2C promote the production of olefins and inhibit the formation of methane (Figure 1.7).

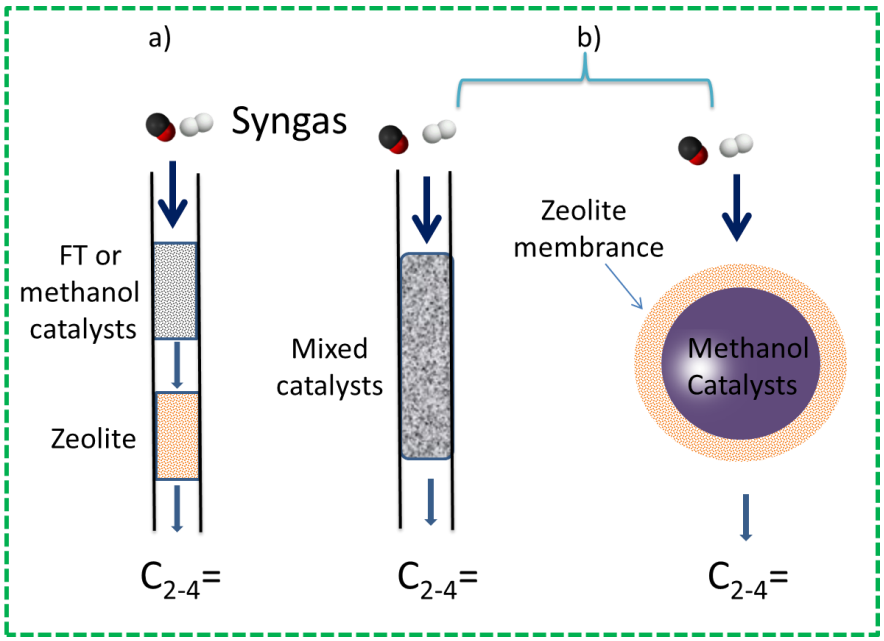

Figure 1.8. *Representative bifunctional syngas to olefins catalytic systems. (a) Dual-bed reactor configuration (b) hybrid system with physical mixed catalysts and core-shell structured catalysts.*

Bifunctional catalysts are another choice for syngas direct conversion to light olefins (Figure 1.8). Recently, two groups in China reported the new OX-ZEO process, which is based on the combination of methanol synthesis and MTO on a single bifunctional catalyst constituted either by the Zn-Cr [37]or by Zr-Zn [38] systems and SAPO-34. It is important to emphasize that the selectivity of the OX-ZEO process can be potentially higher (light olefins ~ 80 %) than that of the conventional FT synthesis. In the conventional FT synthesis, the maximum selectivity to the C_2-C_4 hydrocarbons (including both olefins and paraffins) is around 58 % with the chain growth probability (α) of 0.46. The challenges of this new technology are relevant to attaining higher olefin yields and improving catalyst stability at higher CO conversion levels.

1.3.2 Long chain α-olefins synthesis from syngas

In addition to light olefins, higher linear α-olefins (C_{5+} olefins) are also very valuable products and intermediates, which are used in a large number of commercial products like polymers, surfactants and additives [39-41]. For example, the C_5-C_8 olefins are used as co-monomers in polyethylene products, C_{10}-C_{14} are used for the synthesis of surfactants like LABS (linear alkyl benzene sulfonate) for aqueous detergent formulations; C_{16}-C_{18} counterparts find their primary application as the hydrophobes in oil-soluble surfactants and as lubricating fluids; C_{20}-C_{30} are used for the synthesis of polymers. At the present, almost all processes for production of linear α-olefins are based on oligomerization of ethylene or propylene [42] by Ziegler process using triethyl aluminum for the synthesis of linear olefins with a broad Schulz-Flory distribution. These processes require expensive complexes as catalysts.

Fischer-Tropsch (FT) synthesis is a surface polymerization of the CH_x monomers formed by hydrogenation of CO over metallic catalysts leading to the formation of a broad range of hydrocarbons according to Anderson-Schulz-Flory (ASF) distribution [43]. Termination of hydrocarbon chains on the surface of metal catalyst might involve β-hydrogen abstraction leading to α-olefins or

hydrogenation of surface hydrocarbon fragments to form linear paraffins. The primary α-olefins, however, participate in fast secondary hydrogenation to paraffins. This effect is more pronounced with the increase in the chain length due to a longer residence time of heavier α-olefins over metal surface [40].

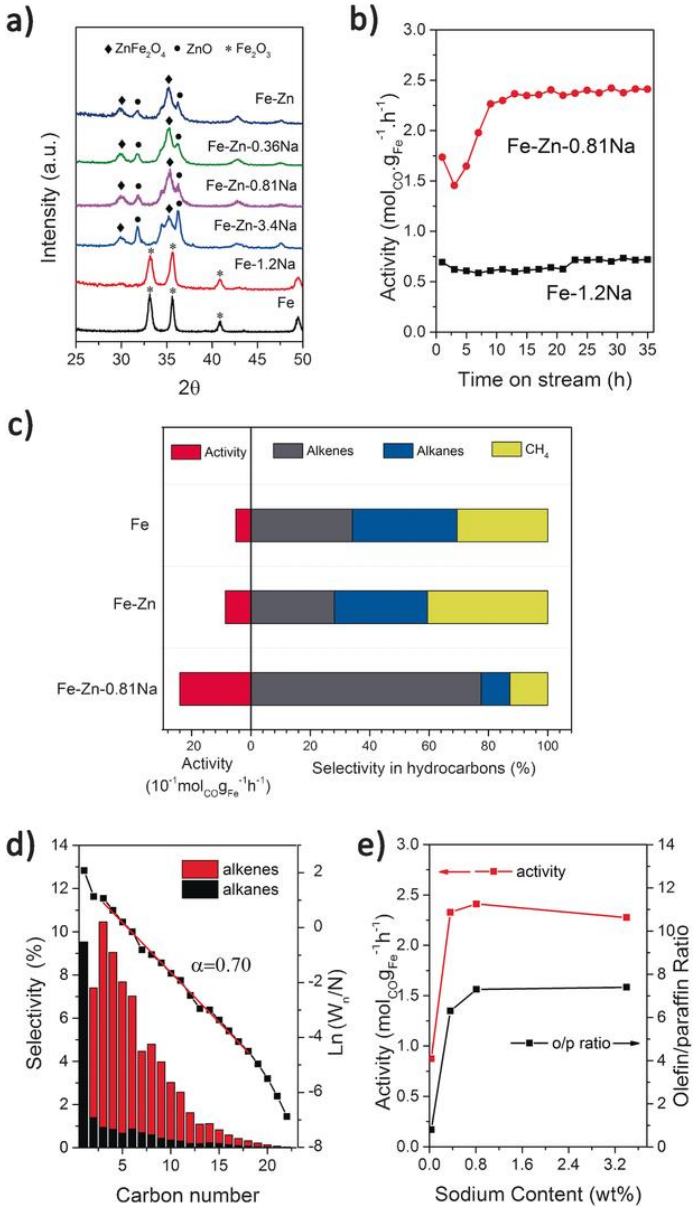

Figure 1. 9. *a) XRD patterns for the calcined catalysts. b) The comparison of activity vs. time between Fe-Zn-0.81 Na and Fe-1.2 Na catalysts. c)The activity and product distribution on Fe-Zn-0.81 Na, Fe-Zn, and Fe catalysts. d) The detailed hydrocarbon product distribution obtained over Fe-Zn-0.81 Na. e) Catalytic activity and o/p molar ratio as a function of Na content [44].*

Synthesis of long chain α-olefins by FT synthesis is a very desirable and sustainable process. Soled [40] and co-works reported the Fe-Zn catalysts promoted with K and Cu selectivity produce α-olefins at typically FT synthesis condition (H_2/CO = 2/1, P = 1 MPa, T = 270 ºC). The C_5-C_{15} α-olefins yields reach approximately 25 % of the hydrocarbon fraction. Catalytic behavior is strongly influenced by synergistic promoter effect (Cu, K) and by the controlled in situ conversion of iron oxide precursors to carbides. The Zn- and Na-modulated Fe catalysts also demonstrated high selectivity toward alkenes (above 50 %, Figure 1.9) in the C_{5+} hydrocarbon range due to change of electronic structure and suppression of hydrogenation activity of Fe [44] .

Low temperature FT synthesis over Ru and Co based catalysts leads mainly to the synthesis of paraffins. Recently Co@Co_2C promoted with Mn catalysts have been reported to convert syngas with high selectivity to higher alcohols and olefins accompanied by low amount of methane and hydrocarbons as the main side product (Figure 1.10). However, a major decline in the reaction rate was observed with introducing Mn promoters [45].

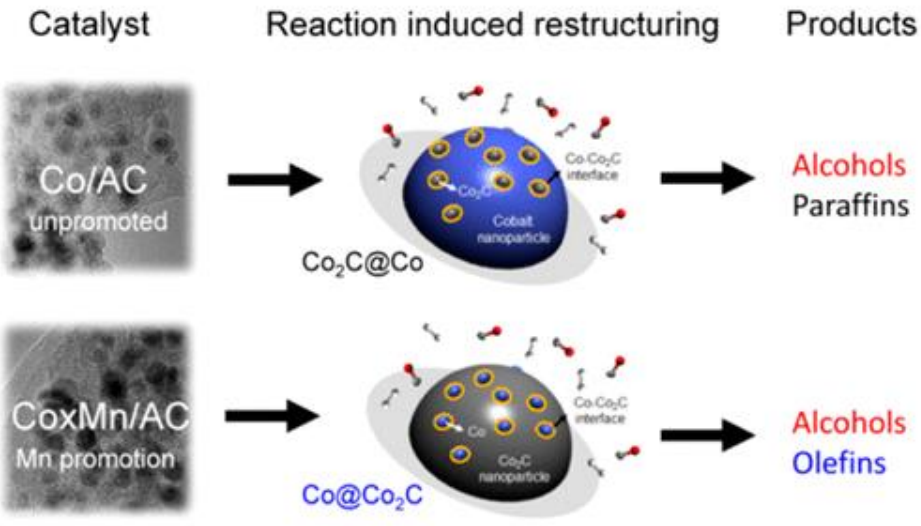

Figure 1.10. *Schematic illustration of alcohol and olefin formation mechanism on the surface of Co@Co_2C catalyst [45].*

Another strategy for low temperature FT synthesis of olefins available from the literature is based on application of supercritical conditions in FT synthesis.

The content of α-olefins in supercritical conditions during FTS has been found to be higher in comparison with the conventional FT synthesis [46-48]. Enhanced diffusion and desorption of α-olefins in supercritical conditions leads to their less significant secondary hydrogenation to paraffins. However, this route requires high excess of solvents and high pressure in the reactor, which is hard to implement in the industry.

1.3.3 Key factors affecting FTO selectivity and activity

The FTO route becomes more feasible with every improvement in the activity, selectivity, and stability of the catalytic system. Iron can be presented as the metal of choice for the FTO reaction as it is inexpensive, it is highly selective toward olefins, and it is possible to achieve methane selectivity below the prediction of the ASF product distribution. The design of effective FTO catalysts for the selective production of light olefins involves several factors: promotion; support; nanoparticle size effect, active phase microenvironment, process and reactor.

Promotion: It has been shown by many researchers that addition of promoters can improve light olefins selectivity of iron-based catalysts [49]. Among various promoters, potassium [47, 50], sodium [50, 51], copper [52], manganese [53] and zinc [54] are often used. These promoters are considered to work as “electronic modifiers”, which tune CO and H_2 chemisorption behaviors on catalyst surfaces [24, 55]. The selectivity to light olefins could be improved significantly by using these promoters. For example, Qiao and co-workers [56] reported the conversion of syngas to light olefins over the K modified Fe/rGO catalyst and the light olefins selectivity could reach 68 % with a 1.0 wt. % K. The volcanic evolution of the activity is attributed to the interplay among the positive effect of K on the formation of Hägg carbide, the active phase for FTO, and the negative roles of K in increasing the size of Hägg carbide at high content and blocking the active phase by K-induced carbon deposition. The monotonic increase in the selectivity to light olefins is ascribed to the improved chain-growth ability and surface CO/H_2 ratio in the presence of K, which favorably suppresses the unwanted

CH_4 production and secondary hydrogenation of light olefins. Khodakov and co-workers observed a remarkable increase in the FT reaction rate and light olefin selectivity over the silica and carbon nanotubes supported iron catalysts promoted with soldering elements such as Bi and Pb [57, 58]. So, the adequate choice of promoters to increase the selectivity to light olefins and minimize methane production is a good way to design highly efficient FTO catalysts (Figure 1.11). The selection of a support that enables the formation of the active phase and its intimate contact with the chemical promoters is favorable for higher selectivity to light olefins.

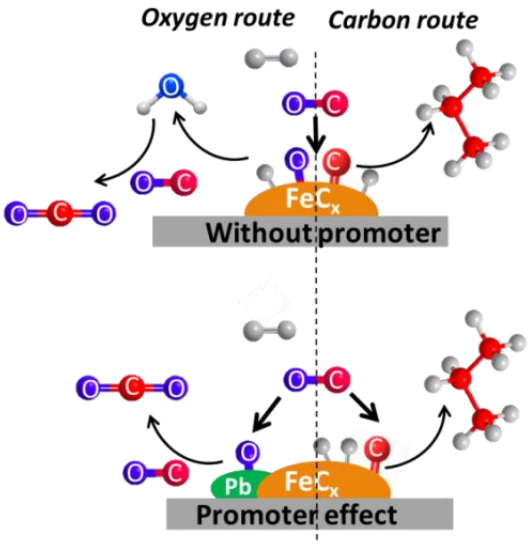

Figure 1.11. *Effect of promotion with soldering atoms on FT synthesis [57].*

Support: Supports are typically used to disperse reactive metals, which also influence the selectivity and activity of FTO process. SiO_2, Al_2O_3, TiO_2, Zeolite and other oxide materials with high surface area are usually chosen as supports of FT catalysts. Besides oxide materials, carbon materials such as activated carbon (AC), carbon nanofibers (CNF), carbon nanotubes (CNT), carbon sphere (CS) and ordered mesoporous carbon have been used as supports for FTO synthesis. Different to commonly used oxide supports, carbon does not form inert mixed compounds between iron and supports (e.g. iron silicate or aluminate) which are difficult to reduce and to carbidize during the catalyst activation and reaction [59]. Cheng et al. [60] examined support effects in high temperature Fischer-Tropsch synthesis on iron catalyst. Higher

Fischer-Tropsch reaction rates were observed on carbon supported iron catalysts compared to silica supported counterparts (Figure 1.12). The catalytic performance principally depends on iron phase composition rather than on iron dispersion. Iron catalysts supported on carbon nanotubes and activated carbon showed highest activity in Fischer-Tropsch synthesis, which could be attributed to the formation of composites of iron carbide and residual magnetite.

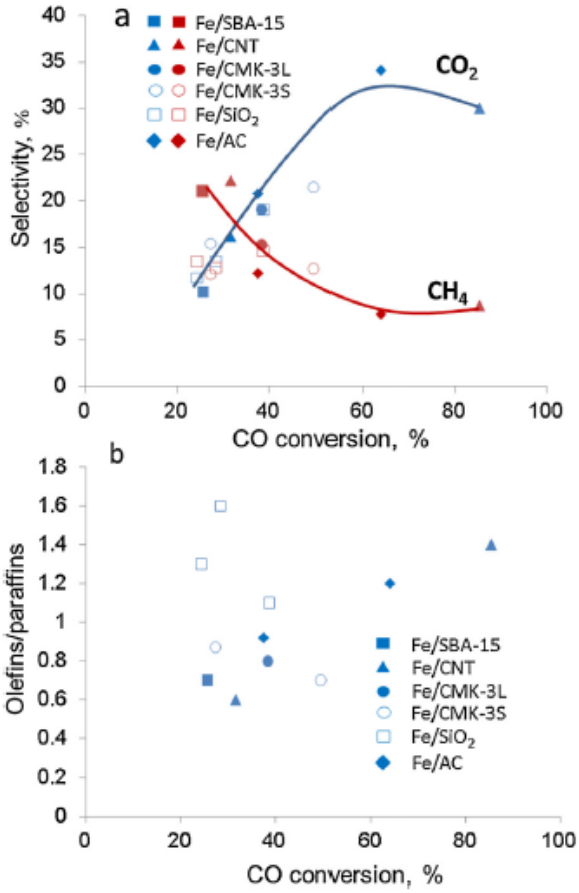

Figure 1.12. *Selectivity to methane and CO_2 (a) and C_2-C_4 olefin to paraffin ratio (b) as functions of CO conversion over iron catalysts (P = 2 MPa, H_2/CO = 2/1, GHSV =16 L $h^{-1}g^{-1}$cat, T = 300 °C) [60].*

Nanoparticle size: The Fischer−Tropsch synthesis to olefins is recognized as a structure sensitive reaction. This means that the intrinsic catalytic performance is strongly related to the particle size of the metal or active phase [61]. The effect of metal particle size has been extensively studied for cobalt [62, 63] and ruthenium [63]. However, in the case of iron, the number of research studies concerning the effect of

particle size is limited since iron catalysts used in the Fischer−Tropsch synthesis are often unsupported or bulk.

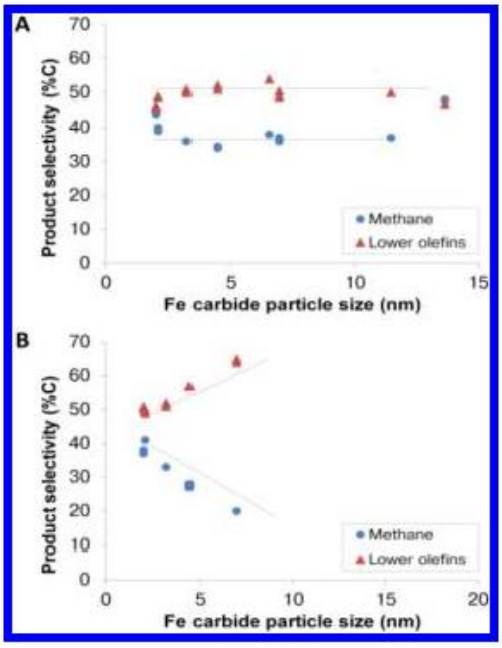

Figure 1.13. *Product selectivity as a function of particle size. Selectivity toward methane and light olefins of Fe/CNF catalysts: (A) unpromoted and (B) promoted. Product selectivity: C_2−C_4 olefins (▲) and methane (●) (reaction conditions: 1 bar, 350 °C, H_2/CO = 1, TOS, 15 h) [64].*

With respect to FTO on iron-based catalysts, de Jong and co-works [64] checked the iron carbide particle size of promoted and unpromoted carbon nanofiber supported catalysts. The surface-specific activity (apparent TOF) based on the initial activity of unpromoted catalysts at 1 bar increased 6−8-fold when the average iron carbide size decreased from 7 to 2 nm, while methane and light olefins selectivities were not affected. The same decrease in particle size for the catalysts promoted by Na plus S resulted at 20 bar in a 2-fold increase of the apparent TOF based on initial activity which was mainly caused by a higher yield of methane for the smallest particles (Figure 1.13). Methane formation seems to take place at highly active low coordination sites residing at corners and edges, which are more abundant on small iron carbide particles. Light olefins are produced at promoted (stepped) terrace sites. These results demonstrate that the iron carbide particle size plays a crucial role in the design of active and selective

FTO catalysts. Note that Lablokov et al. [65] reported that the selectivity of methane and light olefins decreased as Fe particle size increased on Fe/MCF-17 catalysts, which is different from de Jong's results for the unpromoted iron catalysts.

Active phase microenvironment: The position or the microenvironment of active phase in the catalyst has been found to exert significant influences on the activity and selectivity in FT synthesis [66, 67]. Qiao et al. [68] synthesized highly dispersed iron oxide nanoparticles embedded in carbon spheres (Fe@C) by a hydrothermal cohydrolysis-carbonization process afforded a catalyst with a high fraction of iron carbides after reduction and high olefins/paraffins ratio. Iron confinement in CNT has been studied in low temperature Fischer-Tropsch synthesis, the iron inside the CNT tubes has higher reducibility and facile formation of the more active iron carbide phase compared with iron outside the CNT channels (Figure 1.14). The resulting catalysts showed enhanced activity in syngas conversion towards the C_{5+} hydrocarbons and light olefins [69, 70].

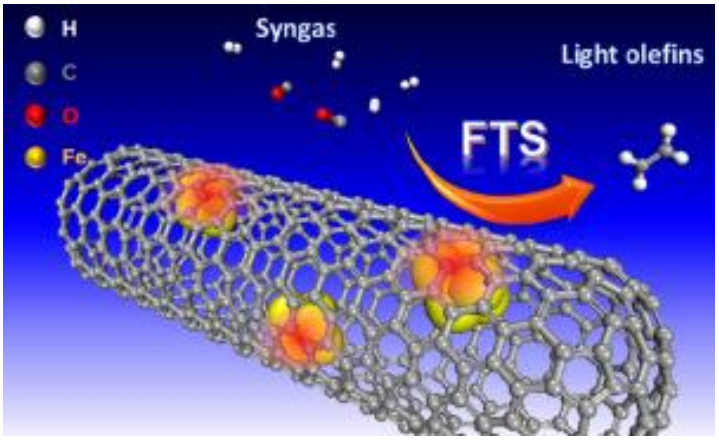

Figure 1.14. *Syngas conversion to light olefins on CNT confined iron catalysts [70]*.

Process and reactor: The selection of optimum process conditions and reactor is important to get the best productivity without compromising product selectivity and to maximize the catalyst life. Since Sasol developed the Fischer-Tropsch synthesis technology in the 1950s, it has successively used in a variety of reactor processes. The type and operating conditions of the reactor have an important influence on the catalytic reaction. The types of reactors are mainly fixed-bed, slurry-bed and fluidized- bed.

Different reactors have different characteristics. The fixed-bed reactor is easy to operate but has a temperature gradient inside it, so it is difficult to control the temperature, which leads to easy sintering of the catalyst. The fluidized-bed reactor is suitable for strong exothermic reactions and can accurately control the internal temperature. The contact time between the reaction gas and catalyst is short. The produced olefins are immediately taken out, which reduces their secondary reactions. The selectivity to light olefins is high, but the catalyst should be mechanically stable. The slurry bed reaction temperature is low and it is not suitable for the production of light olefins. In addition, the separation of catalyst and product is difficult. Operating conditions such as reaction pressure, flow rate, and temperature have a great influence on the activity and selectivity of the catalyst. It pointed out that only with an appropriate combination of the catalyst， process and reactor could it obtain the maximum efficiency for its industrialization [26].

Among them, the advanced fluidized bed reactor technology was put into industrial application in 1989. The capital cost per unit product is only 40 % of the traditional circulating fluidized bed reactor, and the operating cost is also greatly reduced. In addition, the catalyst consumption is reduced by 60 % and the maintenance cost is reduced by 85 %. The high-temperature process mainly produces gasoline (C_5-C_{11}) and light olefins (C_2-$C_4^=$), and can obtain products such as polymerization grade ethylene and propylene [71]. The Beijing University of Chemical Technology used cofeeding the supercritical solvent with syngas to the Fischer-Tropsch synthesis plant to improve the selectivity of light olefins and prolong the life of the catalyst. The conversion rate is as high as 98 %, the hydrocarbon selectivity in the gas-phase product is above 91 %, the methane content is low, and the yield of light olefins can reach 55 % [72].

1.4 Catalysts Deactivation in Syngas Conversion

The Fe-based and Co-based catalysts were considered as the most promising catalysts in Fischer-Tropsch synthesis because their high activity and low cost. The Fe-based catalyst in the high-temperature Fischer-Tropsch process (HTFT, 573-623 K)

generates mainly C_{1-15} hydrocarbons in a fluidized bed, which is mainly used for the production of olefins and gasoline. Low-temperature Fischer-Tropsch process (LTFT, 473-513 K) usually produces long-chain high-carbon waxes using Fe-based or Co-based catalysts [73]. In addition to having a high catalyst activity and selectivity, catalyst deactivation is an important topic for industrial catalyst development and is often less studied in the academic environment.

1.4.1 Mechanism of catalyst deactivation

Currently deactivation of iron or cobalt catalysts is postulated to be due to a number of different deactivation phenomena [74-77]: (i) sintering of small metal crystallites into larger ones (ii) carbon deposition(iii) phase change of the active metal to an inactive phase, (iv) surface reconstruction, (v) metal-support interaction and (vi) poisoning by sulphur or nitrogen containing compounds in the synthesis gas feed.

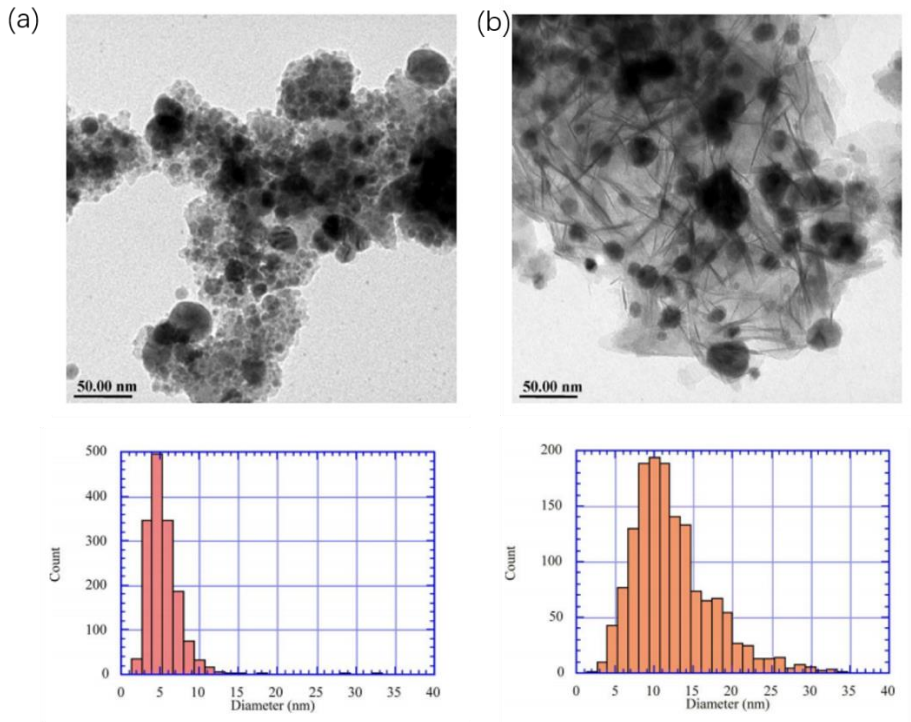

Figure 1.15. *TEM and cobalt particle size distribution of the fresh reduced and spent Co-Re/SiO_2 catalysts[78].*

Sintering: Its one of the main reasons of the iron and cobalt based catalyst deactivation in FT reaction. Mansker et al.[79] reported sintering in their study of a

precipitated FTS catalyst. The researchers found that the change in carbide phase composition from Fe_7C_3 to *x*-Fe_5C_2 was accompanied by a progressive growth in crystallite size after 330 h on stream with a dramatical decrease in CO conversion. The group of Davis et al. [80, 81] has mentioned sintering of cobalt in spent Co/Al_2O_3 catalysts, and showed with extended X-ray absorption fine structure (EXAFS) that the coordination number for the first Co-Co shell of the metallic phase increased from 2.7 to 7.6 during FTS using a catalyst with cobalt crystallites of 5-6 nm. Kiss et al. [78] observed for a Co-Re/SiO_2 catalyst water induced sintering of cobalt crystallites from 5 to 11 nm, as measured with TEM, after FTS at 220 ^oC, 35 bar total pressure and 10 bar steam (Figure 1.15).

From the increase in the area of average cobalt crystallite size with time on stream it was calculated, assuming a direct correlation between cobalt metal surface area and cobalt catalyst activity, that sintering can contribute to about 30 % of the observed loss in activity [82].

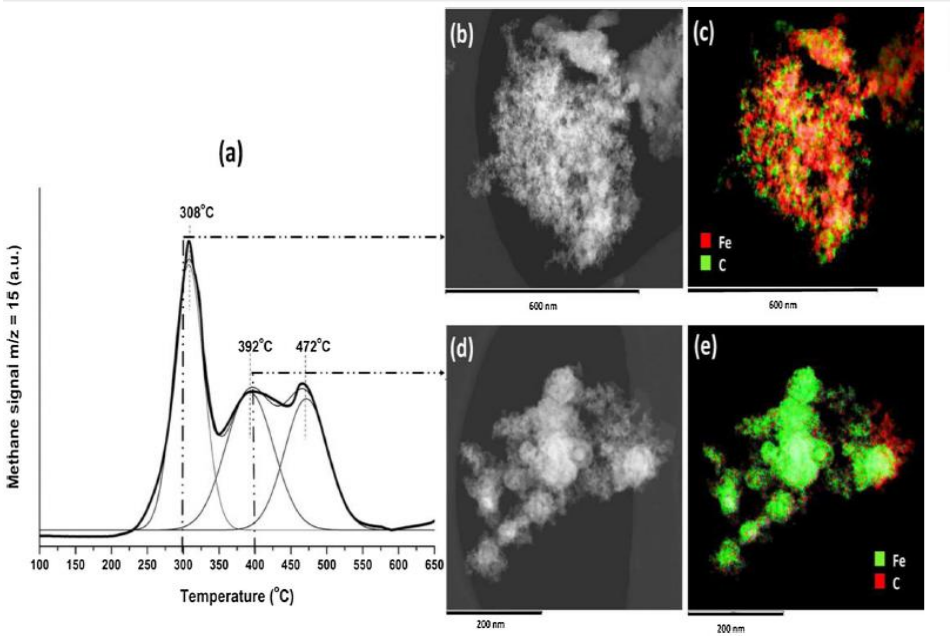

Figure 1.16. *TPH-MS/STEM-EDX images [83]: (a) TPH-MS of the spent catalyst after wax-extraction, (b) high-angle annular dark-field imaging (HAADF) of spent catalyst wax-extracted after TPH at 300 °C, (c) iron and carbon map, (d) HAADF of spent catalyst wax-extracted after TPH at 400 °C, (e) iron and carbon map.*

Carbon deposition: Carbon is present on iron or cobalt FTS catalysts due to the dissociation of CO, which is considered as an elementary step in the reaction. This carbon is an intermediate species which can be converted via hydrogenation and coupling to FTS products. The carbon may also be transformed to more stable species over time which may affect the FTS activity. Heavy hydrocarbons produced by the Fischer-Tropsch reaction also may accumulate with the formation of carbon which will cover the surface-active sites. Carbon deposition is one of the main reasons for the deactivation of iron and cobalt-based FTS catalysts [74, 77].

Rønning et al [83] found the presence of aliphatic hydrocarbons from wax products and oxygenate compounds by in situ DRIFTS. The presence of different carbon species on the surface after wax product extraction is evident from TPH-MS measurements. GC-MS analysis shows that the strongly adsorbed carbon species remaining on the catalyst surface from wax products are mainly α-olefins and branched carboxylic species. The interaction of oxygenate compounds, especially carboxylate species with iron oxide, may form stable complexes limiting further iron catalyst carburization. STEM-EDX analysis shows that carbon is preferentially located on iron particles (Figure 1.16). Bukur et al. [84-86] observed deposition of carbon during the activation treatment as well as during FT synthesis over iron catalysts. Under FTS conditions, the *x*-Fe_5C_2 phase was gradually converted into inactive carbon deposits. The authors commented that the catalysts containing some amount of binder deactivated much slower. This is ascribed mainly to the reduced extent of masking of active sites by carbonaceous deposits. The authors confirm that some sintering also contributes to the overall deactivation of the catalyst

Chen et al. [87] provided evidence that the amorphous carbon does not influence the FT reaction as it can be easily hydrogenated under reaction conditions. Graphitic carbon is rapidly formed and cannot be removed. The graphic carbon amount is increasing as the time going (Table 1.1). This unreactive form of carbon is located on terrace sites and mainly decreases the CO conversion by limiting CH_4 formation. Sasol studied catalyst deactivation by periodically removing samples from a pilot slurry

bubble column reactor operated for 6 months. Wax was removed by inert solvent extraction before the catalyst samples were characterized by temperature programmed hydrogenation and oxidation, chemisorption, TEM and LEIS. Polymeric carbon was found both on the alumina support and on cobalt. This carbon is resistant to hydrogen treatment at temperatures above the FT synthesis temperature. The amount of polymeric carbon correlated well with observed long term deactivation [88].

Table 1.1. *In situ formed graphitic carbon content on spent cobalt catalysts upon different experimental procedures[87].*

Temperature(°C)	P_{CO} (mbar)	P_{H_2} (mbar)	TOS(h)	C_{graph}/Co_{surf}[a]
220	200	400	45	0.09
220	200	200	45	0.35
260	200	400	45	0.43
260	200	200	5	0.26
260	200	200	15	0.48
260	200	200	45	0.91

[a] C_{graph}/Co_{surf} determined by integration of the CH_4 signal above 260 °C during TPH

Phase change: The conversion of the active phase (metal, carbide, etc.) to an inert phase (oxide, different carbide phase) has been reported to be a reason for the deactivation for the iron and cobalt catalysts [74, 75]. Davis et al. [89] investigated the phase transformation for the K-promoted and unpromoted iron catalysts during Fischer-Tropsch synthesis. The catalysts activated in CO for 24 h show the presence of 93 % iron carbide and 7 % magnetite in unpromoted catalysts and 81 % iron carbide and 19 % magnetite for the K-promoted catalysts. The initial CO conversion was as high as 85 %, however, the conversion decreased to approximately 30 % after 280 h test. For the unpromoted catalysts, the iron carbide gradually decreased over time to the magnetite phase. However, for the K-promoted one, only the iron carbide phase (χ-Fe_5C_2) gradually decrease, while the other ($Fe_{2.2}C$) phase steadily increased.

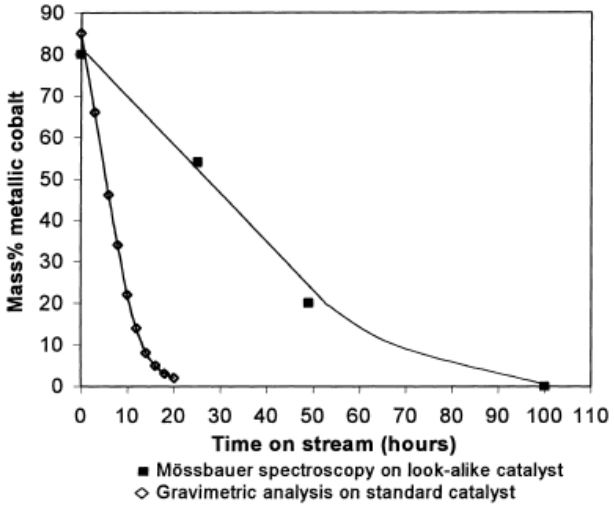

Figure 1.17. *Direct observation of the oxidation behavior of freshly reduced catalysts at the conditions: 150 °C; atmosphere pressure; (Ar or N_2) +H_2O environment; P_{H2O} = 0.25 bar [90].*

For the cobalt catalysts, oxidation of the active cobalt metal phase to the inactive cobalt oxide phase during Fischer-Tropsch synthesis have been extensively studied in the literature [90, 91]. Berge et al. [90] studied the oxidation of supported cobalt based slurry bed Fischer-Tropsch catalysts by water which is one of the Fischer-Tropsch reaction products. Model experiments using Mössbauer emission spectroscopy and thermogravimetry as well as realistic Fischer-Tropsch synthesis runs were performed. It was demonstrated that Mössbauer emission spectroscopy could successfully be applied to the investigation of Fischer-Tropsch catalysts with high cobalt content. Strong indications were found that oxidation of reduced cobalt catalysts occurred under realistic Fischer-Tropsch conditions. Mössbauer emission spectroscopy and thermogravimetry results showed that the oxidation depended on the P_{H_2}/P_{H_2O} ratio. The formation of both reducible and less reducible cobalt oxide species was observed, and the relative ratio between these species depended on the severity of the oxidation conditions (Figure 1.17).

Surface reconstruction: Iron and cobalt surfaces reconstruct during FTS and this reconstruction could alter the catalyst behavior. Changes in the surface configuration during FTS may lead to alternation of the nature of active sites and hence to activity

variations. The reconstruction may also render the surface more sensitive to events which may deactivate the catalyst. These changes may be induced from adsorbed species, e.g. CO, O, N, S or other molecules including carbon containing intermediates and products. Thus, an indirect contribution of surface reconstruction to activity loss should not be neglected [74, 75].

Table 1.2. *Fit Parameters of the First Co-Co Shell of IEN4 and IWA1 after in situ Reduction (Red) and after 1 h in situ Catalysis (FT) [62] (*ΔK *3.3-12* $Å^{-1}$, ΔR *1.8-2.6 Å)*[a]

Catalyst	N	R(Å)	$\Delta\sigma_2(Å^2)$	ΔE_o(ev)	K3 Variance		Size(nm)[a]
					Im.	Abs.	
IEN4 Red	10.1	2.48	9.9 E^{-4}	-0.78	0.0042	0.0150	2.7(1.4-5)
IEN4 FT	9.5	2.48	1.3 E^{-3}	0.92	0.0048	0.0120	
IWA1 Red	9.5	2.48	7.7 E^{-4}	-1.00	0.0025	0.0051	1.7(1.2-3)
IWA1 FT	8.8	2.48	8.8 E^{-4}	-1.01	0.0077	0.0125	

[a] The cobalt particle size and size range have been derived from N and $N \pm \Delta N$, respectively.

Raupp et al. [92] found that surface reconstruction due to iron carbide formation was still occurring even at long reaction time over Fe/SiO_2 catalysts in FT reaction. The bulk-phase iron acts as a getter for surface carbon, thereby controlling surface composition and, hence, the active site density of the catalyst. de Jong et al. [62] investigated the influence of cobalt particle size on FTS. In accordance with the above described studies they reported experimental indications of cobalt surface reconstruction. EXAFS data taken from spent carbon nanofiber supported cobalt catalysts, with crystallites in the range of 2.6-27 nm, revealed a decrease in the first shell Co-Co coordination number of about 6-7 % after exposure to synthesis gas (Table 1.2). This change in the coordination number indicates a reconstruction of the cobalt crystallites during FT synthesis. It is worth to mention that the authors did not detect any other phenomena that may lead to catalyst deactivation, i.e. sintering, re-oxidation or carbidization.

Metal-support interaction: Porous oxides are usually chosen as supports in iron and cobalt based FT catalysts and deactivation of the FT catalysts is observed on all commonly used supports. The selection of support materials relies mainly on their ability to be easily manipulated and provide phases with high surface area, unique metal-support interactions and mechanical strength at a competitive price. However, the relatively strong metal-support interaction leads to the formation of hardly reducible iron or cobalt species and thus then decrease the amount of active site. The formation of mixed metal-support compounds is known to occur already during the preparation of the catalyst. Calcination and reduction are the steps with high potential for mixed oxide formation. The metal loading is also a critical parameter in metal-support compound formation [75]. Various authors [93, 94] have also claimed that high water partial pressure increases the formation of aluminate in cobalt-based catalysts either during FTS or at model conditions in mixtures of H_2/H_2O. Often the observed deactivation is ascribed to the formation of aluminate or silicate. It is proposed that the irreducible metal-support species are formed from/at the expense of active metallic metals.

Poisoning: Poisoning of cobalt and iron catalysts by sulfur or nitrogen containing compounds is a difficult problem in a number of catalytic processes, but particularly in Fischer-Tropsch synthesis using coal-derived feed gases. Indeed, the presence of a few ppm H_2S or NH_3 in the feed gas can limit catalysts life to a few hours or days. Thus, it is necessary to purify syngas from sulfur and nitrogen compounds to the lowest practical levels possible. It is also desirable to be able to model the deactivation process at low H_2S levels in order to predict catalyst life. Moreover, the effects of sulfur poisons on the selectivity behavior of Fischer-Tropsch catalysts need to be determined for purposes of predicting product distributions as a function of time.

Amongst these mentioned deactivation mechanisms, carbon deposition and sintering have been identified as the major contributors to the overall deactivation of the catalyst. Studying the catalyst deactivation mechanism can help us to design efficient and stable Fischer-Tropsch catalysts [95].

1.4.2 The strategies for improving catalyst stability

Taking into consideration that sintering and carbon deposition are the most important deactivation phenomena, the newly developed catalysts should be resistant to these two deactivation mechanisms. Many studies have been performed to improve the long-time stability of metal-supported catalysts towards sintering by control of metal-support interactions (SMSI) [96, 97], or tuning the dispersion and size of the active metal, or developing new efficient promoters, or encapsulating metal particles with a carbon support.

Dalai et al. [98] investigated the effect of acid pre-treatment on physico-chemical properties and stability of CNTs supported iron Fischer-Tropsch catalysts. They found that acid treatment of CNT increased the metal-support interactions which reducing higher dispersion and thus then increased the stability during the FT reaction. Soled et al [99] illustrated several successful examples of supported cobalt based FT catalysts by different synthesis strategies for modifying interaction between the supports and cobalt precursor, promoting reduction, stabilizing catalysts to high-temperature treatments and minimizing deleterious metal-support interactions.

Hu et al. [100] reported nitrogen-doped carbon nanotubes (NCNTs) supported iron catalysts for syngas conversion to light olefins. The constructed Fe/NCNTs catalyst showed high dispersion of iron particles by anchoring effect by nitrogen in CNT without pre-modification (Figure 1.18). The Fe/NCNTs catalyst presents excellent catalytic performance in FTS with high selectivity for light olefins of up to 46.7 % as well as high activity and stability. Lee et al. [101] also found that the particle size distributions affected the stability of cobalt based FT catalysts. They prepared cobalt oxide nanoparticles in the range of 3-16 nm from colloidal solution of Co_3O_4 in different temperature (150-250 ºC) and stabilized by capping agent. These size-defined cobalt catalysts showed considerably higher FTS activity and better TOF (s^{-1}) than conventional catalysts and with the increase in the cobalt particle size, their deactivation rates also decreased.

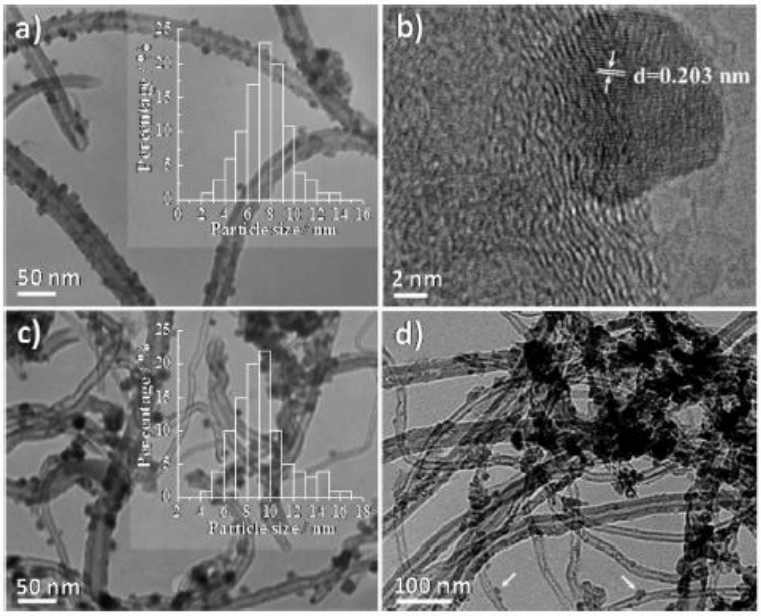

Figure 1.18. *TEM and HRTEM images of activated catalysts with an Fe loading of 10 wt. %: (a, b) Fe/NCNTs; (c) Fe/t-CNTs; (d) Fe/u-CNTs [100].*

Park et al. [102] developed phosphorous-modified γ- Al_2O_3 (P- Al_2O_3) to be applied for a preparation of cobalt-supported Co/P-Al_2O_3 catalysts. The γ-Al_2O_3 surface was partially transformed to aluminum phosphates after phosphorous modification, and the newly formed aluminum phosphate phases simultaneously altered the surface hydrophilicity and cobalt dispersion. The partial formation of the tridymite aluminum phosphate ($AlPO_4$) phases on the P-Al_2O_3 support eventually enhanced the dispersion of the supported cobalt crystallites and suppressed aggregation of cobalt nanoparticles by forming the strongly interacted cobalt crystallites on the P-Al_2O_3 surfaces. A higher stability of the Co/P-Al_2O_3 catalyst at an optimal phosphorous content in the range of 0.5-1.0 mol % was attributed to homogeneously distributed cobalt crystallites and less significant deposition of heavy hydrocarbons by forming macro-emulsion droplets with the help of trace amount of alcohols formed during FTS reaction (Figure 1.19). This was confirmed by in-situ analysis of adsorbed intermediates with surface hydrophilicity and some surface characterizations such as crystallite size, reducibility, and electronic state of the supported cobalt nanoparticles. Saeys et al. [103] found that boron promoted Co/γ-Al_2O_3 catalyst showed six-fold lower deactivation rate without affecting the initial

activity or selectivity. They ascribe the boron promotion to reducing the deposition of resilient carbon species.

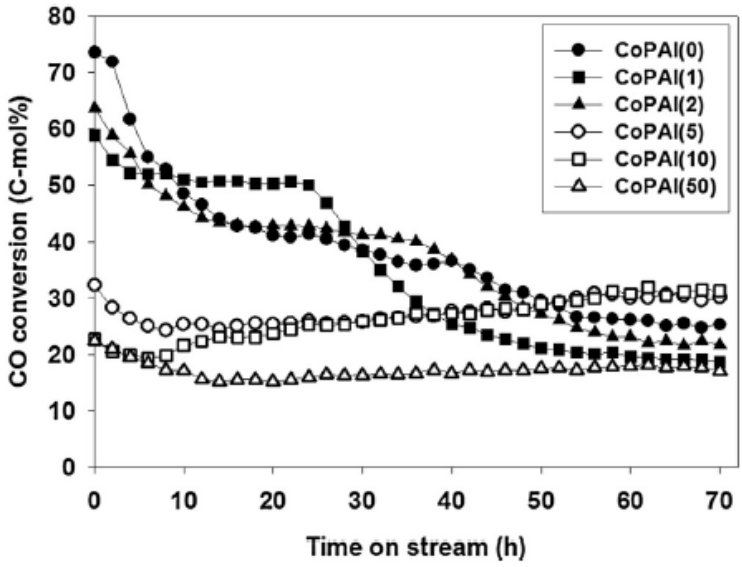

Figure 1.19. *Catalytic activity and stability with time on stream (h) on the CoPAl catalysts [102].*

Confinement effect have been widely used to improve the stability of iron and cobalt catalysts by decreasing sintering and carbon deposition during the FT reaction [68, 104, 105]. Ahmad et al. [106] developed a method to control the position of the catalytic sites on either inner or outer surface of carbon nanotubes, Deposition of iron inside CNT tubes decreased the average size of the iron oxide from 14 nm to 7 nm and increased the reducibility. The confined iron catalyst showed 23 % higher initial activity, more importantly, deposition of catalytic sites on interior surface of CNT tubes results in a more stable catalysts, while its counterpart experienced 46.4 % deactivation within a period of 720 h due to catalytic sites sintering. Dalai et al. [107] also found the similar results in carbon nanotubes confined cobalt catalyst in FT reaction.

Another strategy to improve the life time of the catalysts is regeneration of the spent catalysts. Regeneration of cobalt or iron cased FT synthesis catalysts is largely described in the patent literature. The options involve treatment of the catalyst with air (oxygen), hydrogen and/or CO and variations thereof in addition to procedures for removing produced wax. Therefore, regeneration addresses reversing the main

deactivation processes of carbon deposition, metal oxidation and sintering by combustion, reduction and re-dispersion, respectively. Figure 1.20 shows that following oxidative regeneration the spent catalyst recovered its activity completely to that of the fresh catalyst [75].

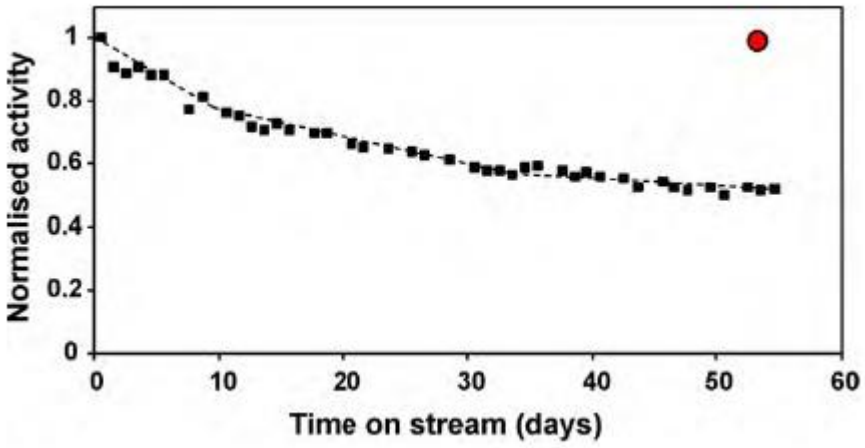

Figure 1.20. *Normalized activity for a Co/Pt/Al_2O_3 catalyst during realistic Fischer-Tropsch synthesis in a demonstration scale slurry reactor and spent sample subject to ex situ oxidative regeneration (closed circle) [75].*

. 1.5 The Objectives and Research Methods of this Thesis

Though FT synthesis is a rather mature reaction, this technology still presents several major challenges. Among these challenges, insufficient selectivity to specific hydrocarbon fractions and in particular to olefins and catalyst stability seem to be most important. An attempt has been made in this thesis to find solution for these two challenges by designing new efficient catalyst on basis of iron and cobalt and new processes.

In this thesis, we are exploring catalyst promotion with soldering metals such as bismuth and lead on the catalytic activity, selectivity and stability of iron, cobalt and nickel catalysts. Another possible strategy is based on the confinement of iron particles in carbon nanotubes in synergy with the promotion effect in order to improve the catalytic performance of iron catalysts. Finally, cofeeding with acids is considered is one of the routes to improve the selectivity of cobalt catalysts to long chain α-olefins.

The specific objectives of this work are detailed below:

1.5.1 Promotion effect in Fe-based FTO catalysts.

Design of Fe based catalysts with high activity and selectivity is challenging. The present work focuses on the promotion of carbon nanotube supported iron catalysts with Bi and Pb for direct light olefin synthesis. This part has two specific objectives: first, to develop extremely active, selective and stable iron catalysts for direct olefin synthesis on the basis of CNT; second, to provide deep insights into the localization and structure of active sites and mechanisms of interaction of the Bi and Pb promoters with iron carbide and CNT.

1.5.2 From outside to inside the CNT tubes over Fe-based FTO catalysts.

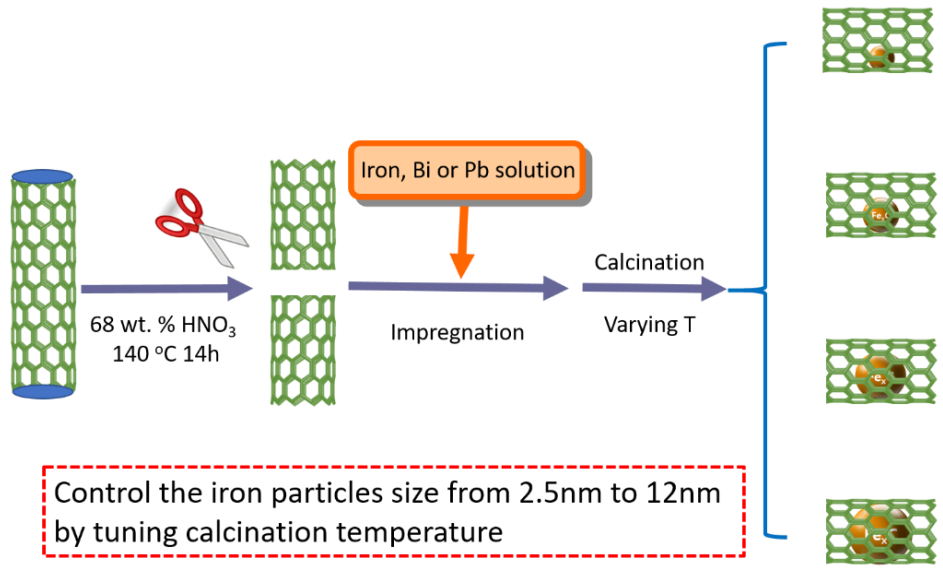

Figure 1.22. *Design strategy for the synthesis of nanoconfined iron catalysts with different particle size.*

In the early reports of our group, Bi and Pb promoters have shown strong effects on the activity and selectivity over iron catalysts. In addition to the promotion, nanoconfinement of active phase into porous matrix has been also an efficient way to improve the activity and selectivity of the Fe-based FT catalysts. Metal nanoparticle

nanoconfinement within carbon nanotubes (CNT) has been particularly remarkable. The present work focuses on the synergetic effects, which arise from the combination of the nanoconfinement of iron nanoparticles in CNT and their promotion with Bi and Pb on the structure, catalytic performance and stability of iron catalysts in high temperature FT synthesis.

Then, the particle size effect inside the CNT tubes has been studied. Even though cobalt particle size effect has been widely studied by different groups, the iron particle size is rarely examined and controversy for different research. As far as we know, there was no literature focus on the iron particle size effect in the confined system. CNT encapsulated iron catalysts with different particle size has been synthesized (Figure 1.22) and tested in FTO reaction. We aim to have a deeper understanding about the particle size effect in the nanoconfined system.

1.5.3 Long chain α-olefins synthesis in the presence of carboxylic acids

Long chain α-olefins are valuable products and widely derived from Ziegler process using expensive catalysts. The synthesis of α-olefins via FT synthesis is a very desirable and sustainable process. Our approach for the synthesis of linear α-olefins addresses application of carboxylic acids for stabilization of olefins formed during low temperature FT process over Co based catalysts. The effect of co-feeding with labelled acetic acid has been earlier studied by Davis [108] et al. but only over Fe catalyst in batch reactor at 270 ºC during FT synthesis. The authors observed formation of ethane by hydrogenation of acetic acid and increase in the olefin to paraffin ratio with additional formation of different oxygenates such as glycol and ether. To the best of our knowledge, there is no research about effect of addition of carboxylic acids on the reaction selectivity during low temperature FT synthesis over Co based catalysts in fixed bed reactor. The goal of this thesis is to demonstrate that cofeeding with carboxylic acids can strongly affect the selectivity of FTS reaction.

1.5.4 Design highly stable cobalt and nickel catalysts in CO hydrogenation.

Catalysts deactivation remains one of the main challenges of the carbon monoxide hydrogenation. Catalysts deactivation in syngas conversion could be caused by carbon deposition, metals sintering, oxidation and poisoning [109]. Many researches have been focused on the mechanisms of the Co and Ni deactivation, however, few studies provided efficient strategies to improve the stability. In this thesis, we aim to design high stable cobalt and nickel catalysts in syngas conversion. New efficient Bi-promoted SiO_2 supported cobalt and catalysts for CO hydrogenation were developed. Both cobalt and nickel catalysts show higher stability compared with the unpromoted counterparts.

1.6 Outline of the Thesis.

This thesis consists of eight chapters as follows:

Chapter 1 introduces the mechanism of FT synthesis and main challenge relative to the selectivity and stability. Syngas direct conversion to olefins is still a hot topic in the research. The chapter addresses in particular, mechanism of FTS and its main challenges, choice of catalysts and processes of olefin synthesis from syngas and catalyst deactivation phenomena.

Chapter 2 presents the methodology of catalysts preparation, catalytic evaluation and characterization.

Chapter 3 focuses on design highly efficient Bi and Pb promoted CNT supported iron catalyst for FTO reaction. This study aims to enhance both the activity and light olefins selectivity. We also try to optimize the catalysts in order to perform this reaction under atmospheric pressure.

Chapter 4 is development of Chapter 3. Combination of the nanoconfinement of iron nanoparticles in CNT and their promotion with Bi and Pb on the structure results in a major increasement in the activity and olefin yields compared with unconfined counterparts. A thorough characterization of these catalysts was attempted via a large

combination of techniques: XRD, XPS, *in-situ* XANES, TEM-EDX, H_2-TPR, CO-TPR, *in-situ* magnetization measurements, ICP, BET.

Chapter 5 is based the results of Chapter 4. We study the iron particles size effect in the nanoconfinement system both the unpromoted and promoted catalysts. The nanoconfined iron catalysts with the particle size varying from 2.5 nm to 12 nm have been synthesized by tuning the calcination temperature. The iron particle size effects towards the intrinsic activity and light olefins selectivity are discussed in this chapter.

Chapter 6 provides a new method for producing the long chain α-olefins by introducing carboxylic acids in lower temperature Co based FT system. The function of carboxylic acids and mechanism in improving α-olefins selectivity has been discussed.

In chapter 7, we target to improve the catalysts stability of cobalt and nickel catalysts in CO hydrogenation. A simple and efficient way proposed via their promotion with Bi.

Chapter 8 provides general conclusion and draws perspectives of this work.

1.7 Reference

[1] N. Lior, Sustainable energy development: the present (2011) situation and possible paths to the future, Energy, 43 (2012) 174-191.

[2] S. Yang, L. Xiao, S. Yang, A. Kraslawski, Y. Man, Y. Qian, Sustainability Assessment of the Coal/Biomass to Fischer-Tropsch Fuel Processes, ACS Sustainable Chemistry & Engineering, 2 (2013) 80-87.

[3] https://www.iea.org/weo2018/.

[4] Q. Yan, Y. Lu, C. Wan, J. Han, J. Rodriguez, J.-j. Yin, F. Yu, Synthesis of aromatic-rich gasoline-range hydrocarbons from biomass-derived syngas over a Pd-promoted Fe/HZSM-5 catalyst, Energy & Fuels, 28 (2014) 2027-2034.

[5] J. Yang, W. Ma, D. Chen, A. Holmen, B.H. Davis, Fischer-Tropsch synthesis: A review of the effect of CO conversion on methane selectivity, Applied Catalysis A: General, 470 (2014) 250-260.

[6] Q. Zhang, K. Cheng, J. Kang, W. Deng, Y. Wang, Fischer-Tropsch catalysts for the production of hydrocarbon fuels with high selectivity, ChemSusChem, 7 (2014) 1251-1264.

[7] E. de Smit, B.M. Weckhuysen, The renaissance of iron-based Fischer-Tropsch synthesis: on the multifaceted catalyst deactivation behaviour, Chemical Society Reviews, 37 (2008) 2758-2781.

[8] R.A. Dictor, A.T. Bell, Fischer-Tropsch synthesis over reduced and unreduced iron oxide catalysts, Journal of Catalysis, 97 (1986) 121-136.

[9] P. Biloen, J. Helle, W.M. Sachtler, Incorporation of surface carbon into hydrocarbons during Fischer-Tropsch synthesis: mechanistic implications, Journal of Catalysis, 58 (1979) 95-107.

[10] v.H. Pichler, H. Schulz, Neuere Erkenntnisse auf dem Gebiet der Synthese von Kohlenwasserstoffen aus CO und H2, Chemie Ingenieur Technik, 42 (1970) 1162-1174.

[11] H.M. Torres Galvis, K.P. de Jong, Catalysts for production of lower olefins from synthesis gas: a review, ACS catalysis, 3 (2013) 2130-2149.

[12] B. Wojciechowski, The kinetics of the Fischer-Tropsch synthesis, Catalysis Reviews Science and Engineering, 30 (1988) 629-702.

[13] G.A. Huff Jr, C.N. Satterfield, Intrinsic kinetics of the Fischer-Tropsch synthesis on a reduced fused-magnetite catalyst, Industrial & Engineering Chemistry Process Design and Development, 23 (1984) 696-705.

[14] J. Kummer, P. Emmett, Fischer-Tropsch synthesis mechanism studies. The addition of radioactive alcohols to the synthesis gas, Journal of the American Chemical Society, 75 (1953) 5177-5183.

[15] M. Vannice, The catalytic synthesis of hydrocarbons from carbon monoxide and hydrogen, Catalysis Reviews—Science and Engineering, 14 (1976) 153-191.

[16] W.K. Hall, R. Kokes, P. Emmett, Mechanism studies of the Fischer-Tropsch synthesis. The addition of radioactive methanol, carbon dioxide and gaseous formaldehyde, Journal of the American Chemical Society, 79 (1957) 2983-2989.

[17] W.K. Hall, R. Kokes, P. Emmett, Mechanism studies of the Fischer-Tropsch synthesis: the incorporation of radioactive ethylene, propionaldehyde and propanol, Journal of the American Chemical Society, 82 (1960) 1027-1037.

[18] J. Kummer, H. Podgurski, W. Spencer, P. Emmett, Mechanism Studies of the Fischer—Tropsch Synthesis. The Addition of Radioactive Alcohol, Journal of the American Chemical Society, 73 (1951) 564-569.

[19] G. Blyholder, P. Emmett, Fischer-Tropsch synthesis mechanism studies. The addition of radioactive ketene to the synthesis gas, The Journal of Physical Chemistry, 63 (1959) 962-965.

[20] G. Henrici-Olivé, S. Olive, The Fischer-Tropsch synthesis: molecular weight distribution of primary products and reaction mechanism, Angewandte Chemie International Edition in English, 15 (1976) 136-141.

[21] C. Masters, The Fischer-Tropsch Reaction, in: Advances in Organometallic Chemistry, Elsevier, 1979, pp. 61-103.

[22] C.K. Rofer-DePoorter, A comprehensive mechanism for the Fischer-Tropsch synthesis, Chemical Reviews, 81 (1981) 447-474.

[23] K. Cheng, J. Kang, D.L. King, V. Subramanian, C. Zhou, Q. Zhang, Y. Wang, Chapter Three - Advances in Catalysis for Syngas Conversion to Hydrocarbons, in: C. Song (Ed.) Advances in Catalysis, Academic Press, 2017, pp. 125-208.

[24] B. Gu, S. He, W. Zhou, J. Kang, K. Cheng, Q. Zhang, Y. Wang, Polyaniline-supported iron catalyst for selective synthesis of lower olefins from syngas, Journal of Energy Chemistry, 26 (2017) 608-615.

[25] Q. Zhang, W. Deng, Y. Wang, Recent advances in understanding the key catalyst factors for Fischer-Tropsch synthesis, Journal of Energy Chemistry, 22 (2013) 27-38.

[26] D. Yunjie, Co_2C nanoprisms for syngas conversion to lower olefins with high selectivity, Chinese Journal of Catalysis, 38 (2016) 1-4.

[27] M. Casavola, J. Xie, J.D. Meeldijk, N.A. Krans, A. Goryachev, J.P. Hofmann, A.I. Dugulan, K.P. de Jong, Promoted Iron Nanocrystals Obtained via Ligand Exchange as Active and Selective Catalysts for Synthesis Gas Conversion, ACS Catalysis, 7 (2017) 5121-5128.

[28] H.M.T. Galvis, J.H. Bitter, C.B. Khare, M. Ruitenbeek, A.I. Dugulan, K.P. de Jong, Supported iron nanoparticles as catalysts for sustainable production of lower olefins, Science, 335 (2012) 835-838.

[29] T.W. van Deelen, H. Su, N.A.J.M. Sommerdijk, K.P. de Jong, Assembly and activation of supported cobalt nanocrystal catalysts for the Fischer-Tropsch synthesis, Chemical communications, (2018).

[30] H.M.T. Galvis, A.C. Koeken, J.H. Bitter, T. Davidian, M. Ruitenbeek, A.I. Dugulan, K.P. de Jong, Effects of sodium and sulfur on catalytic performance of supported iron catalysts for the Fischer-Tropsch synthesis of lower olefins, Journal of catalysis, 303 (2013) 22-30.

[31] H.M.T. Galvis, A.C. Koeken, J.H. Bitter, T. Davidian, M. Ruitenbeek, A.I. Dugulan, K.P. de Jong, Effect of precursor on the catalytic performance of supported iron catalysts for the Fischer-

Tropsch synthesis of lower olefins, Catalysis today, 215 (2013) 95-102.
[32] L. Zhong, F. Yu, Y. An, Y. Zhao, Y. Sun, Z. Li, T. Lin, Y. Lin, X. Qi, Y. Dai, Cobalt carbide nanoprisms for direct production of lower olefins from syngas, Nature, 538 (2016) 84-87.
[33] F. Diehl, A.Y. Khodakov, Promotion of cobalt Fischer-Tropsch catalysts with noble metals: a review, Oil & Gas Science and Technology-Revue de l'IFP, 64 (2009) 11-24.
[34] A.Y. Khodakov, W. Chu, P. Fongarland, Advances in the development of novel cobalt Fischer-Tropsch catalysts for synthesis of long-chain hydrocarbons and clean fuels, Chemical Reviews, 107 (2007) 1692-1744.
[35] M. Claeys, M. Dry, E. Van Steen, E. Du Plessis, P. Van Berge, A. Saib, D. Moodley, In situ magnetometer study on the formation and stability of cobalt carbide in Fischer-Tropsch synthesis, Journal of Catalysis, 318 (2014) 193-202.
[36] J.C. Mohandas, M.K. Gnanamani, G. Jacobs, W. Ma, Y. Ji, S. Khalid, B.H. Davis, Fischer-Tropsch synthesis: characterization and reaction testing of cobalt carbide, ACS Catalysis, 1 (2011) 1581-1588.
[37] F. Jiao, J. Li, X. Pan, J. Xiao, H. Li, H. Ma, M. Wei, Y. Pan, Z. Zhou, M. Li, Selective conversion of syngas to light olefins, Science, 351 (2016) 1065-1068.
[38] K. Cheng, B. Gu, X. Liu, J. Kang, Q. Zhang, Y. Wang, Direct and Highly Selective Conversion of Synthesis Gas into Lower Olefins: Design of a Bifunctional Catalyst Combining Methanol Synthesis and Carbon-Carbon Coupling, Angewandte Chemie, 128 (2016) 4803-4806.
[39] L. Guo, J. Sun, X. Ji, J. Wei, Z. Wen, R. Yao, H. Xu, Q. Ge, Directly converting carbon dioxide to linear α-olefins on bio-promoted catalysts, Communications Chemistry, 1 (2018) 11.
[40] S.L. Soled, E. Iglesia, S. Miseo, B.A. DeRites, R.A. Fiato, Selective synthesis of α-olefins on Fe-Zn Fischer-Tropsch catalysts, Topics in Catalysis, 2 (1995) 193-205.
[41] J. Zheng, J. Cai, F. Jiang, Y. Xu, X. Liu, Investigation of the highly tunable selectivity to linear [small alpha]-olefins in Fischer-Tropsch synthesis over silica-supported Co and CoMn catalysts by carburization-reduction pretreatment, Catalysis Science & Technology, 7 (2017) 4736-4755.
[42] J. Skupinska, Oligomerization of. alpha.-olefins to higher oligomers, Chemical reviews, 91 (1991) 613-648.
[43] M.E. Dry, The Fischer-Tropsch process: 1950-2000, Catalysis Today, 71 (2002) 227-241.
[44] P. Zhai, C. Xu, R. Gao, X. Liu, M. Li, W. Li, X. Fu, C. Jia, J. Xie, M. Zhao, X. Wang, Y.-W. Li, Q. Zhang, X.-D. Wen, D. Ma, Highly Tunable Selectivity for Syngas-Derived Alkenes over Zinc and Sodium-Modulated Fe_5C_2 Catalyst, Angewandte Chemie International Edition, 55 (2016) 9902-9907.
[45] Z. Zhao, W. Lu, R. Yang, H. Zhu, W. Dong, F. Sun, Z. Jiang, Y. Lyu, T. Liu, H. Du, Y. Ding, Insight into the Formation of $Co@Co_2C$ Catalysts for Direct Synthesis of Higher Alcohols and Olefins from Syngas, ACS Catalysis, 8 (2018) 228-241.
[46] L. Fan, K. Fujimoto, Fischer-Tropsch synthesis in supercritical fluid: characteristics and application, Applied Catalysis A: General, 186 (1999) 343-354.
[47] H. Wan, B. Wu, C. Zhang, H. Xiang, Y. Li, Promotional effects of Cu and K on precipitated

iron-based catalysts for Fischer-Tropsch synthesis, Journal of Molecular Catalysis A: Chemical, 283 (2008) 33-42.

[48] W. Linghu, X. Liu, X. Li, K. Fujimoto, Selective synthesis of higher linear α-olefins over cobalt Fischer-Tropsch catalyst, Catalysis letters, 108 (2006) 11-13.

[49] W.M.H. Sachtler, D.F. Shriver, W.B. Hollenberg, A.F. Lang, Promoter action in Fischer-Tropsch catalysis, Journal of Catalysis, 92 (1985) 429-431.

[50] W. Ngantsoue-Hoc, Y. Zhang, R.J. O'Brien, M. Luo, B.H. Davis, Fischer-Tropsch synthesis: activity and selectivity for Group I alkali promoted iron-based catalysts, Applied Catalysis A: General, 236 (2002) 77-89.

[51] K. Cheng, V.V. Ordomsky, B. Legras, M. Virginie, S. Paul, Y. Wang, A.Y. Khodakov, Sodium-promoted iron catalysts prepared on different supports for high temperature Fischer-Tropsch synthesis, Applied Catalysis A: General, 502 (2015) 204-214.

[52] P. Chernavskii, V.O. Kazak, G. Pankina, Y.D. Perfiliev, T. Li, M. Virginie, A. Khodakov, Influence of Copper and Potassium on the Structure and Carbidisation of Supported Iron Catalysts for Fischer-Tropsch Synthesis, Catalysis Science & Technology, (2017).

[53] A. Nakhaei Pour, S.M.K. Shahri, H.R. Bozorgzadeh, Y. Zamani, A. Tavasoli, M.A. Marvast, Effect of Mg, La and Ca promoters on the structure and catalytic behavior of iron-based catalysts in Fischer-Tropsch synthesis, Applied Catalysis A: General, 348 (2008) 201-208.

[54] P. Zhai, C. Xu, R. Gao, X. Liu, M. Li, W. Li, X. Fu, C. Jia, J. Xie, M. Zhao, Highly Tunable Selectivity for Syngas-Derived Alkenes over Zinc and Sodium-Modulated Fe_5C_2 Catalyst, Angewandte Chemie International Edition, 55 (2016) 9902-9907.

[55] X. Chen, D. Deng, X. Pan, Y. Hu, X. Bao, N-doped graphene as an electron donor of iron catalysts for CO hydrogenation to light olefins, Chemical communications, 51 (2015) 217-220.

[56] Y. Cheng, J. Lin, K. Xu, H. Wang, X. Yao, Y. Pei, S. Yan, M. Qiao, B. Zong, Fischer-Tropsch synthesis to lower olefins over potassium-promoted reduced graphene oxide supported iron catalysts, ACS catalysis, 6 (2015) 389-399.

[57] V.V. Ordomsky, Y. Luo, B. Gu, A. Carvalho, P.A. Chernavskii, K. Cheng, A.Y. Khodakov, Soldering of Iron Catalysts for Direct Synthesis of Light Olefins from Syngas under Mild Reaction Conditions, ACS Catalysis, 7 (2017) 6445-6452.

[58] B. Gu, V.V. Ordomsky, M. Bahri, O. Ersen, P.A. Chernavskii, D. Filimonov, A.Y. Khodakov, Effects of the Promotion with Bismuth and Lead on Direct Synthesis of Light Olefins from Syngas over Carbon Nanotube Supported Iron Catalysts, Applied Catalysis B: Environmental, 234 (2018) 153-166.

[59] X. Pan, Z. Fan, W. Chen, Y. Ding, H. Luo, X. Bao, Enhanced ethanol production inside carbon-nanotube reactors containing catalytic particles, Nature materials, 6 (2007) 507.

[60] K. Cheng, V. Ordomsky, M. Virginie, B. Legras, P. Chernavskii, V. Kazak, C. Cordier, S. Paul, Y. Wang, A. Khodakov, Support effects in high temperature Fischer-Tropsch synthesis on iron catalysts, Applied Catalysis A: General, 488 (2014) 66-77.

[61] Y. Yuan, S. Huang, H. Wang, Y. Wang, J. Wang, J. Lv, Z. Li, X. Ma, Monodisperse Nano-Fe_3O_4

on α-Al2O3 Catalysts for Fischer-Tropsch Synthesis to Lower Olefins: Promoter and Size Effects, ChemCatChem, 9 (2017) 3144-3152.

[62] G.L. Bezemer, J.H. Bitter, H.P. Kuipers, H. Oosterbeek, J.E. Holewijn, X. Xu, F. Kapteijn, A.J. van Dillen, K.P. de Jong, Cobalt particle size effects in the Fischer-Tropsch reaction studied with carbon nanofiber supported catalysts, Journal of the American Chemical Society, 128 (2006) 3956-3964.

[63] J. Den Breejen, P. Radstake, G. Bezemer, J. Bitter, V. Frøseth, A. Holmen, K.d. Jong, On the origin of the cobalt particle size effects in Fischer-Tropsch catalysis, Journal of the American Chemical Society, 131 (2009) 7197-7203.

[64] H.M. Torres Galvis, J.H. Bitter, T. Davidian, M. Ruitenbeek, A.I. Dugulan, K.P. de Jong, Iron particle size effects for direct production of lower olefins from synthesis gas, Journal of the American Chemical Society, 134 (2012) 16207-16215.

[65] V. Iablokov, Y. Xiang, A. Meffre, P.-F. Fazzini, B. Chaudret, N. Kruse, Size-dependent activity and selectivity of Fe/MCF-17 in the catalytic hydrogenation of carbon monoxide using Fe (0) nanoparticles as precursors, ACS Catalysis, 6 (2016) 2496-2500.

[66] F. Fischer, H. Tropsch, Über die direkte Synthese von Erdöl-Kohlenwasserstoffen bei gewöhnlichem Druck.(Erste Mitteilung), Berichte der deutschen chemischen Gesellschaft (A and B Series), 59 (1926) 830-831.

[67] C. Wang, X. Pan, X. Bao, Direct production of light olefins from syngas over a carbon nanotube confined iron catalyst, Chinese Science Bulletin, 55 (2010) 1117-1119.

[68] G. Yu, B. Sun, Y. Pei, S. Xie, S. Yan, M. Qiao, K. Fan, X. Zhang, B. Zong, Fe_xO_y@ C spheres as an excellent catalyst for Fischer-Tropsch synthesis, Journal of the American Chemical Society, 132 (2009) 935-937.

[69] W. Chen, Z. Fan, X. Pan, X. Bao, Effect of confinement in carbon nanotubes on the activity of Fischer− Tropsch iron catalyst, Journal of the American Chemical Society, 130 (2008) 9414-9419.

[70] X. Chen, D. Deng, X. Pan, X. Bao, Iron catalyst encapsulated in carbon nanotubes for CO hydrogenation to light olefins, Chinese Journal of Catalysis, 36 (2015) 1631-1637.

[71] M.E. Dry, The Fischer-Tropsch process-commercial aspects, Catalysis today, 6 (1990) 183-206.

[72] B.U.o.C. Technology, Method for preparing low-carbon olefin by two-stage method using synthesis gas as raw material, China Patent, 101265149 (2008).

[73] B.H. Davis, Fischer-Tropsch Synthesis: Comparison of Performances of Iron and Cobalt Catalysts, Industrial & Engineering Chemistry Research, 46 (2007) 8938-8945.

[74] E. de Smit, B.M. Weckhuysen, The renaissance of iron-based Fischer-Tropsch synthesis: on the multifaceted catalyst deactivation behaviour, Chemical Society Reviews, 37 (2008) 2758-2781.

[75] A.M. Saib, D.J. Moodley, I.M. Ciobîcă, M.M. Hauman, B.H. Sigwebela, C.J. Weststrate, J.W. Niemantsverdriet, J. van de Loosdrecht, Fundamental understanding of deactivation and regeneration of cobalt Fischer-Tropsch synthesis catalysts, Catalysis Today, 154 (2010) 271-282.

[76] D. Schanke, A.M. Hilmen, E. Bergene, K. Kinnari, E. Rytter, E. Ådnanes, A. Holmen, Study of the deactivation mechanism of Al_2O_3-supported cobalt Fischer-Tropsch catalysts, Catalysis

Letters, 34 (1995) 269-284.
[77] N.E. Tsakoumis, M. Rønning, Ø. Borg, E. Rytter, A. Holmen, Deactivation of cobalt based Fischer-Tropsch catalysts: A review, Catalysis Today, 154 (2010) 162-182.
[78] G. Kiss, C.E. Kliewer, G.J. DeMartin, C.C. Culross, J.E. Baumgartner, Hydrothermal deactivation of silica-supported cobalt catalysts in Fischer-Tropsch synthesis, Journal of Catalysis, 217 (2003) 127-140.
[79] L.D. Mansker, Y. Jin, D.B. Bukur, A.K. Datye, Characterization of slurry phase iron catalysts for Fischer-Tropsch synthesis, Applied Catalysis A: General, 186 (1999) 277-296.
[80] G. Jacobs, P.M. Patterson, Y. Zhang, T. Das, J. Li, B.H. Davis, Fischer-Tropsch synthesis: deactivation of noble metal-promoted Co/ Al_2O_3 catalysts, Applied Catalysis A: General, 233 (2002) 215-226.
[81] G. Jacobs, Y. Zhang, T. Das, J. Li, P. Patterson, B. Davis, Deactivation of a Ru promoted Co/ Al_2O_3 catalyst for FT synthesis, in: Studies in Surface Science and Catalysis, Elsevier, 2001, pp. 415-422.
[82] M. Overett, B. Breedt, E. Du Plessis, W. Erasmus, J. Van De Loosdrecht, Sintering as a deactivation mechanism for an alumina supported cobalt Fischer-Tropsch synthesis catalyst, Prepr. Pap.炯Am. Chem. Soc., Div. Pet. Chem, 53 (2008) 126.
[83] D. Peña, A. Cognigni, T. Neumayer, W. van Beek, D.S. Jones, M. Quijada, M. Rønning, Identification of carbon species on iron-based catalysts during Fischer-Tropsch synthesis, Applied Catalysis A: General, 554 (2018) 10-23.
[84] D.B. Bukur, M. Koranne, X. Lang, K. Rao, G.P. Huffman, Pretreatment effect studies with a precipitated iron Fischer-Tropsch catalyst, Applied Catalysis A: General, 126 (1995) 85-113.
[85] D.B. Bukur, K. Okabe, M.P. Rosynek, C. Li, D. Wang, K. Rao, G. Huffman, Activation studies with a precipitated iron catalyst for fischer-tropsch synthesis: I. characterization studies, Journal of Catalysis, 155 (1995) 353-365.
[86] D.B. Bukur, L. Nowicki, R.K. Manne, X. Lang, Activation Studies with a Precipitated Iron Catalyst for Fischer-Tropsch Synthesis: II. Reaction Studies, Journal of Catalysis, 155 (1995) 366-375.
[87] W. Chen, T.F. Kimpel, Y. Song, F.-K. Chiang, B. Zijlstra, R. Pestman, P. Wang, E.J. Hensen, Influence of Carbon Deposits on the Cobalt-Catalyzed Fischer-Tropsch Reaction: Evidence of a Two-Site Reaction Model, ACS Catalysis, 8 (2018) 1580-1590.
[88] R.L. Espinoza, A.P. Steynberg, B. Jager, A.C. Vosloo, Low temperature Fischer-Tropsch synthesis from a Sasol perspective, Applied Catalysis A: General, 186 (1999) 13-26.
[89] V.R.R. Pendyala, U.M. Graham, G. Jacobs, H.H. Hamdeh, B.H. Davis, Fischer-Tropsch Synthesis: Morphology, Phase Transformation, and Carbon-Layer Growth of Iron-Based Catalysts, ChemCatChem, 6 (2014) 1952-1960.
[90] P.J. van Berge, J. van de Loosdrecht, S. Barradas, A.M. van der Kraan, Oxidation of cobalt based Fischer-Tropsch catalysts as a deactivation mechanism, Catalysis Today, 58 (2000) 321-334.
[91] C. Lancelot, V.V. Ordomsky, O. Stéphan, M. Sadeqzadeh, H.l. Karaca, M. Lacroix, D. Curulla-

Ferré, F. Luck, P. Fongarland, A. Griboval-Constant, Direct Evidence of Surface Oxidation of Cobalt Nanoparticles in Alumina-Supported Catalysts for Fischer-Tropsch Synthesis, ACS Catalysis, 4 (2014) 4510-4515.

[92] G.B. Raupp, W.N. Delgass, Mössbauer investigation of supported Fe catalysts: III. In situ kinetics and spectroscopy during Fischer-Tropsch synthesis, Journal of Catalysis, 58 (1979) 361-369.

[93] J. Li, X. Zhan, Y. Zhang, G. Jacobs, T. Das, B.H. Davis, Fischer-Tropsch synthesis: effect of water on the deactivation of Pt promoted Co/Al2O3 catalysts, Applied Catalysis A: General, 228 (2002) 203-212.

[94] D. Schanke, A. Hilmen, E. Bergene, K. Kinnari, E. Rytter, E. Ådnanes, A. Holmen, Study of the deactivation mechanism of Al_2O_3-supported cobalt Fischer-Tropsch catalysts, Catalysis Letters, 34 (1995) 269-284.

[95] C.H. Bartholomew, R.M. Bowman, Sulfur poisoning of cobalt and iron fischer-tropsch catalysts, Applied Catalysis, 15 (1985) 59-67.

[96] M. Cagnoli, A. Alvarez, N. Gallegos, J. Bengoa, C.D. de Souza, M. Schmal, S. Marchetti, Mössbauer and XPS spectroscopies studies of SMSI effect on Fe/Nb2O5 catalysts for the Fischer-Tropsch synthesis, Applied Catalysis A: General, 326 (2007) 113-119.

[97] J.A. Farmer, C.T. Campbell, Ceria maintains smaller metal catalyst particles by strong metal-support bonding, Science, 329 (2010) 933-936.

[98] R.M.M. Abbaslou, A. Tavasoli, A.K. Dalai, Effect of pre-treatment on physico-chemical properties and stability of carbon nanotubes supported iron Fischer-Tropsch catalysts, Applied Catalysis A: General, 355 (2009) 33-41.

[99] S.L. Soled, E. Iglesia, R.A. Fiato, J.E. Baumgartner, H. Vroman, S. Miseo, Control of metal dispersion and structure by changes in the solid-state chemistry of supported cobalt Fischer-Tropsch catalysts, Topics in catalysis, 26 (2003) 101-109.

[100] J. Lu, L. Yang, B. Xu, Q. Wu, D. Zhang, S. Yuan, Y. Zhai, X. Wang, Y. Fan, Z. Hu, Promotion Effects of Nitrogen Doping into Carbon Nanotubes on Supported Iron Fischer-Tropsch Catalysts for Lower Olefins, ACS Catalysis, 4 (2014) 613-621.

[101] J.-Y. Park, Y.-J. Lee, P.R. Karandikar, K.-W. Jun, K.-S. Ha, H.-G. Park, Fischer-Tropsch catalysts deposited with size-controlled Co3O4 nanocrystals: Effect of Co particle size on catalytic activity and stability, Applied Catalysis A: General, 411-412 (2012) 15-23.

[102] S.-J. Park, J.M. Cho, C.-I. Ahn, Y.-J. Lee, K.-W. Jun, B.G. Cho, J.W. Bae, Roles of phosphorous-modified Al_2O_3 for an enhanced stability of Co/Al_2O_3 for CO hydrogenation to hydrocarbons, Journal of Molecular Catalysis A: Chemical, 426 (2017) 177-189.

[103] K.F. Tan, J. Chang, A. Borgna, M. Saeys, Effect of boron promotion on the stability of cobalt Fischer-Tropsch catalysts, Journal of catalysis, 280 (2011) 50-59.

[104] W. Wang, M. Ding, L. Ma, X. Yang, J. Li, N. Tsubaki, G. Yang, T. Wang, X. Li, Fe_2O_3 nanoparticles encapsulated in TiO_2 nanotubes for Fischer-Tropsch synthesis: The confinement effect of nanotubes on the catalytic performance, Fuel, 164 (2016) 347-351.

[105] Z. Yang, X. Pan, J. Wang, X. Bao, FeN particles confined inside CNT for light olefin synthesis from syngas: Effects of Mn and K additives, Catalysis Today, 186 (2012) 121-127.
[106] R.M.M. Abbaslou, A. Tavassoli, J. Soltan, A.K. Dalai, Iron catalysts supported on carbon nanotubes for Fischer-Tropsch synthesis: Effect of catalytic site position, Applied Catalysis A: General, 367 (2009) 47-52.
[107] A. Tavasoli, M. Trépanier, A.K. Dalai, N. Abatzoglou, Effects of Confinement in Carbon Nanotubes on the Activity, Selectivity, and Lifetime of Fischer-Tropsch Co/Carbon Nanotube Catalysts, Journal of Chemical & Engineering Data, 55 (2010) 2757-2763.
[108] A. Sarkar, R.A. Keogh, S. Bao, B.H. Davis, Fischer-Tropsch Synthesis: Reaction Pathways for 14 C-Labeled Acetic Acid, Catalysis Letters, 120 (2008) 25-33.
[109] N.E. Tsakoumis, M. Rønning, Ø. Borg, E. Rytter, A. Holmen, Deactivation of cobalt based Fischer-Tropsch catalysts: a review, Catalysis Today, 154 (2010) 162-182.

Chapter 2. Catalysts and Experiments

2.1 Catalyst Preparation

2.1.1. Carbon nanotubes pretreatment

The multi-walled carbon nanotubes (CNT, Iolitec nanomaterial, 95 %, outer diameter of 20-40 nm) were treated with nitric acid to remove contaminations with metals and to make CNT hydrophilic. The hydrophilicity of CNT obtained after the treatment in nitric acid makes it easier for impregnation with aqueous solutions. The oxygen-containing groups also help to anchor the cations in the surface of CNT and then to reduce sintering during the calcination. Typically, 3.0 g of CNT were pretreated in concentrated HNO_3 (68 %, 210 mL) during 14 h under reflux conditions at 140 °C. After, the samples were filtered, washed with distilled water until pH = 7 and dried at 100 °C overnight.

As for the study of CNT confinement effect, different type of CNT was used (Iolitec nanomaterial, 95 %, inter diameter 5-12 nm, outer diameter 10-30 nm). The treatments of CNT were according to previous literature [1, 2]. CNT were treated with condensed nitric acid in high temperature (140 ^oC 14 h) to open the tubes channel and remove contaminations with metals and to make CNT hydrophilic. The obtained CNTs with opened tubes is denoted as CNT-open. For comparison, the CNT with closed tubes is obtained by treatment with nitric acid under mild condition (34 wt. % HNO_3 for 6 h at 110 ^oC). The acquired sample with closed tubes is labeled as CNT-close.

2.1.2 Preparation of CNT supported iron-based catalysts

The iron catalysts were prepared by incipient wetness impregnation of the CNT support with aqueous solutions of iron nitrate ($Fe(NO_3)_3.9H_2O$, Sigma-Aldrich). Lead nitrate ($Pb(NO_3)_2$, Sigma-Aldrich) and bismuth nitrate ($Bi(NO_3)_3.5H_2O$, Sigma-Aldrich) were used for preparation of the Bi- and Pb-promoted iron catalysts by co-impregnation.

The Fe loading was fixed at 10 wt. %. The molar ratios of Fe/Pb and Fe/Bi are 100/2. The Bi/CNT (10 wt. %) and Pb/CNT (10 wt. %) catalysts were prepared by impregnation of CNT with bismuth and lead nitrates. After the impregnation, the samples were dried in an oven at 80 °C for 12 h followed by thermal treatment at 400 °C for 4 h under a flow of nitrogen (50 mL/min). The calcined catalysts are labeled as FeM /CNT, where M represents the promoters (Bi or Pb).

For comparison, several Bi- and Pb-promoted iron catalysts were prepared by mechanical mixing. The Fe/CNT and Bi/CNT or Pb/CNT samples were mechanically mixed in an agate mortar for 10 min to attain the same molar ratio. The obtained physical mixtures were denoted as Fe/CNT + *M*/CNT, where *M* represents the promoters (Bi or Pb).

2.1.3 Preparation of CNT confined iron-based catalysts

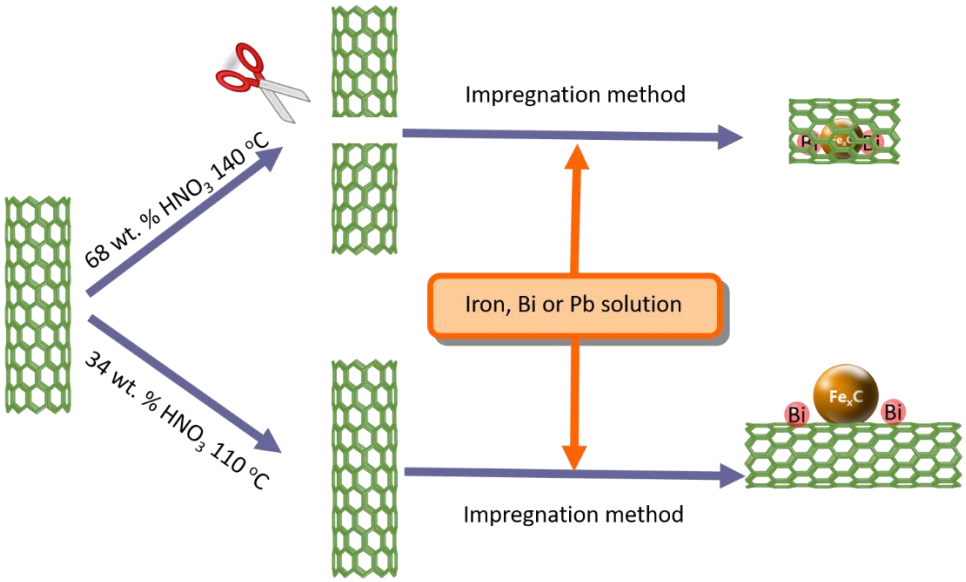

Figure 2.1. *Synthesis procedure of CNT confined and unconfined iron-based catalysts.*

Different with CNT supported iron catalysts, the aqueous solution was drawn into the CNT channels by capillary forces aided by ultrasonic treatment and stirring to obtained confined catalysts. The Fe loading was fixed at 10 wt. %. The molar ratios of Fe/Pb and Fe/Bi are 100/2. After the impregnation, the samples were dried in an oven at 80 °C for 12 h followed by thermal treatment at 400 °C for 4 h under a flow of

nitrogen (50 mL/min). The procedure is illustrated in Figure 2.1. The calcined catalysts are labeled as Fe*M*/CNT-in or Fe*M*/CNT-out, where "*M*" represents the promoters (Bi or Pb), "in" represents iron inside the CNT tubes and "out" represents iron outside the CNT tubes.

As for the study of the particle size effect inside the CNT tubes, the synthesis procedure is similar with Fe*M*/CNT-in. The only difference is the calcination temperature which is varying from 573 K to 873 K. The obtained catalysts are denoted as Fe*M*/CNT-in-*T*, where "*M* " represents the promoters (Bi or Pb), "in" represents iron inside the CNT tubes and "*T* " represents the calcination temperature.

2.1.4 Preparation of Al_2O_3 supported Co catalysts

Alumina-supported cobalt catalyst containing 25 wt. % Co and 0.1 wt. % Pt were prepared via two-step aqueous incipient wetness co-impregnation of Puralox SCCA-5/170 γ-alumina (S_{BET} = 165 m^2/g, pore diameter of 8.3 nm and pore volume of 0. 477 cm^3/g, Sasol) with solutions of cobalt (II) nitrate ($Co(NO_3)_2$ $6H_2O$) and tetraammineplatinum (II) nitrate ($Pt(NH_3)_4(NO_3)_2$). After impregnation, the catalyst was dried in air flow at 373 K and then calcined at 773 K for 5 h with the temperature ramp of 1 K/min.

2.1.5 Preparation of SiO_2 supported Cobalt and Nickel catalysts

Commercial amorphous silica (CARIACT Q-10, Fuji Silysia) was used as catalytic support. The Co*x*Bi/SiO_2 and Ni*x*Bi/SiO_2 catalysts were prepared by incipient wetness impregnation of the support with aqueous solutions of hydrous bismuth nitrate $Bi(NO_3)_3{\cdot}5H_2O$ and nitrates of cobalt ($Co(NO_3)_2{\cdot}6H_2O$) or nickel ($Ni(NO_3)_2{\cdot}6H_2O$), where *x* represents the weight percent of promoter (Bi). The metal loadings of Co and Ni were kept at 15 wt.%. The Bi/SiO_2 (15 wt.%) catalyst was prepared by impregnation of SiO_2 with bismuth nitrate. After the impregnation, the catalysts were dried overnight in an oven at 100 °C. Then they were calcined in air at 400 °C for 4 h with 1 °C/min temperature ramping.

To prepare the carbonized catalysts, the calcined Co/SiO_2 and $Co0.2Bi/SiO_2$ were impregnated with fructose in order to obtain 10 wt.% of fructose in the samples. After the impregnation, the catalysts were dried overnight in an oven at 100 °C. Then they were calcined in nitrogen at 350 °C for 4 h with 1 °C/min temperature ramping. The obtained catalysts were denoted as Co/SiO_2-C and $Co0.2Bi/SiO_2$-C, respectively.

2.2 Evaluation of Catalytic Performance

2.2.1 Equipment for evaluation of Fe-based catalysts in the centimetric reactor

The syngas conversion was performed in a fixed-bed reactor (8 mm inner diameter, Figure 2.2). Typically, the calcined catalyst (0.20 g, 100-150 μm) was loaded in the stainless-steel reactor and then activated in the CO gas flow (50 ml/min, atmospheric pressure) at 350 °C with a heating rate of 2 °C/min for 10 h before the reaction. The activation procedure was chosen on the basis of our previous publication [3]. After the reactor was cooled down to 180 °C, a syngas with a H_2/CO ratio of 1/1 and a pressure of 10 bar was introduced into the reactor. Nitrogen with a fixed flow rate of 1 ml/min in the syngas was used as an internal standard for the calculation of CO conversion. The temperature was raised with the ramping rate of 1°C/min to the desired reaction temperature (350 °C). The catalytic test was conducted at 10 bar and 350 °C with syngas (H_2/CO = 1). GHSV has been varied in the range 3.4-20.4 L h^{-1} g^{-1}. The absence of mass transport resistances was checked by Weisz-Prater Criterion (N_{W-P}) for internal diffusion [4-6].

$$N_{W-P} = \frac{R{r_p}^2}{D_{eff}C_s} \leq 0.3$$

where R = observed reaction rate (mol_{CO} g^{-1} s^{-1}), r_p= catalyst particle radius (m), D_{eff} = effective diffusivity (cm^2 s^{-1}), Cs = gas concentration of CO at the external surface of the catalyst (mol cm^{-3}). We considered a total gas flow rate of 57 ml min^{-1} with ~ 60 % CO conversion and a catalyst particle size of 0.10 - 0.15 mm. The pressure

was 10 bar and the reaction rate was calculated from the measured FTY of $6.1*10^{-4}$ $mol_{CO}\ g_{Fe}^{-1}s^{-1}$. Cs and D_{eff} are calculated according to the literature [7] with the values of $4.9*10^{-5}$ and 0.0229 $cm^2\ s^{-1}$, respectively. The $N_{w\text{-}p}$ value is calculated to be 2×10^{-3}, which is much lower than 0.3.

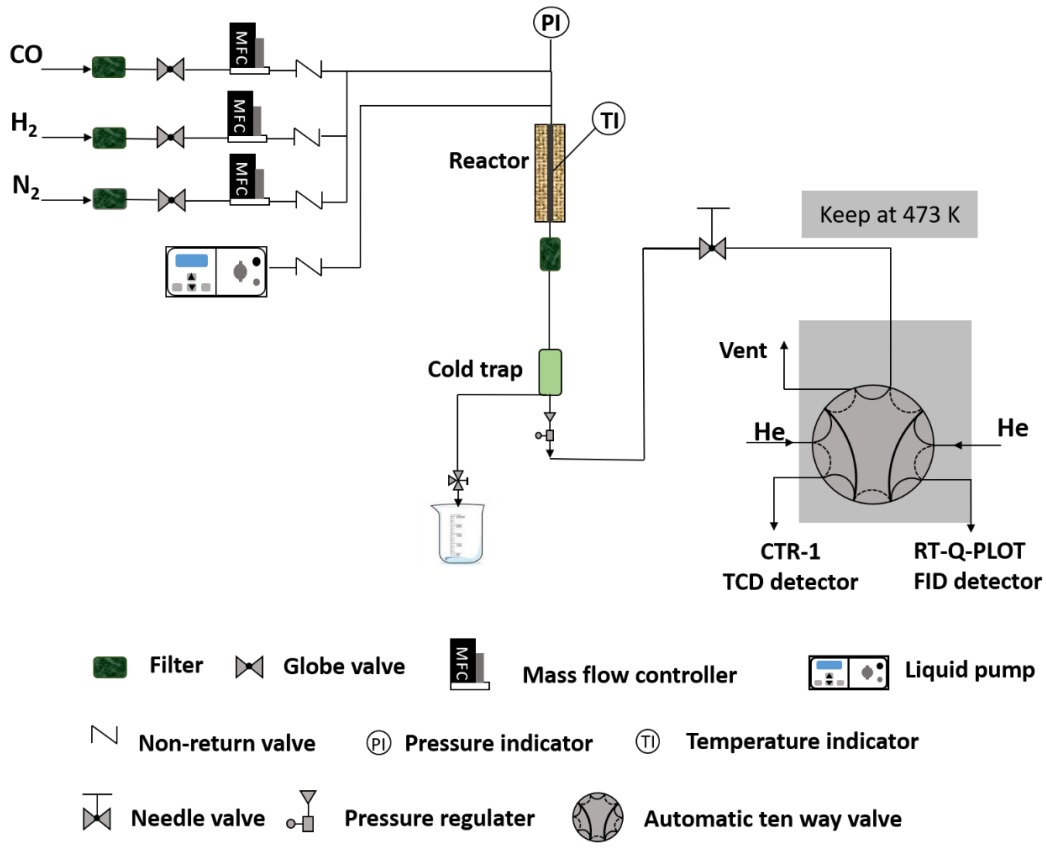

Figure 2.2. *Schematic diagram of device for Fischer-Tropsch synthesis and Water-Gas-Shift reaction over iron-based catalysts.*

The reaction products were analyzed using a gas chromatograph (Bruker GC-450), which was equipped with a thermal conductivity (TCD) and a flame ionization (FID) detectors. Analysis of N_2, CO, CO_2, and CH_4 was performed using a packed CTR-1 column and a TCD detector. The C_1-C_5 hydrocarbons were separated in a capillary Rt-Q PLOT column and analyzed by a FID detector. The liquid products (oil and water phases) were collected in a trap kept at 20 °C and analyzed off-line by gas chromatography. The selectivities were calculated on a molar carbon basis. Iron time yields (FTY) were expressed as moles of CO converted per gram of total iron per second. The product selectivities were reported as percentage of CO converted into a

given product, respectively, and expressed on carbon basis. The CO_2 free hydrocarbon selectivities were calculated taking into account only hydrocarbon production in FT synthesis. The carbon balance was better than 90 %. The chain growth probabilities, α, were calculated for the C_5-C_{12} hydrocarbon range from the slope of the curve ln (S_n/n) versus n, where n is the carbon number of the hydrocarbon and S_n is the selectivity to the corresponding hydrocarbon.

2.2.2 Equipment for Water-Gas-Shift reaction

For the Water-Gas Shift reaction, 0.2 g of the as-prepared catalyst was placed in the same reactor with the Fe-based catalysts and then reduced at 400 °C for 1 h under hydrogen flow (50 ml/min). The temperature after the reduction was decreased to 180 °C. Prior to the reaction, the catalyst was first heated in N_2 atmosphere from 180 °C to 350 °C, then water steam was added to the mixture and then CO was introduced to the reactor. The products were analyzed using the same gas chromatograph as for FT reaction.

2.2.3 Avantium high throughput equipment for evaluation for long chain olefins synthesis

Carbon monoxide hydrogenation was carried out on the REALCAT platform in a Flowrence® high-throughput unit (Avantium, Figure 2.3) equipped with 16 parallel milli-fixed-bed reactors (d = 2 mm) [8] operating at a pressure of 20 bar, H_2/CO = 2 molar ratio, T = 220 ºC and GHSV from 13-54 Lh^{-1} g_{cat}^{-1}. The molar ratio of acid to CO 0.25 and 0.12 has been used during the test.

The catalyst loading was 100 mg per reactor. Prior to the catalytic test all the samples were activated in a flow of hydrogen at atmospheric pressure during 10 h at 400 °C. During the activation step, the temperature ramp was 3 °C/min. After the reduction, the catalysts were cooled down to 180 °C and a flow of premixed syngas was gradually introduced to the catalysts. When pressure attained pressure of the reaction, the temperature was slowly increased to the temperature of the reaction. The reaction has

been conducted for 60 h at different GHSV of syngas. The reaction has been conducted in 3 steps: catalytic test without addition of acid for 12 h, test in the presence of acid flow 30 h and the last step without addition of acid. Gaseous reaction products were analyzed by on-line gas chromatography. Analysis of permanent gases was performed using a Molecular Sieve column and a thermal conductivity detector. C_1-C_4 hydrocarbons were separated in a PPQ column and analyzed by a thermoconductivity detector. C_5-C_{12} hydrocarbons were analyzed using CP-Sil5 column and a flame-ionization detector. High-molecular-weight products were collected at atmospheric pressure in vials heated at 80 °C and analyzed by SIMDIS technique. The carbon monoxide contained 5 % of helium, which was used as an internal standard for calculating carbon monoxide conversion. The catalytic test with labelled acid has been performed by taking samples of gas phase and subsequent analysis in Shimadzu GCMS-QP2010 SE. The product selectivity (S) was reported as the percentage of CO converted into a given product and expressed on carbon basis.

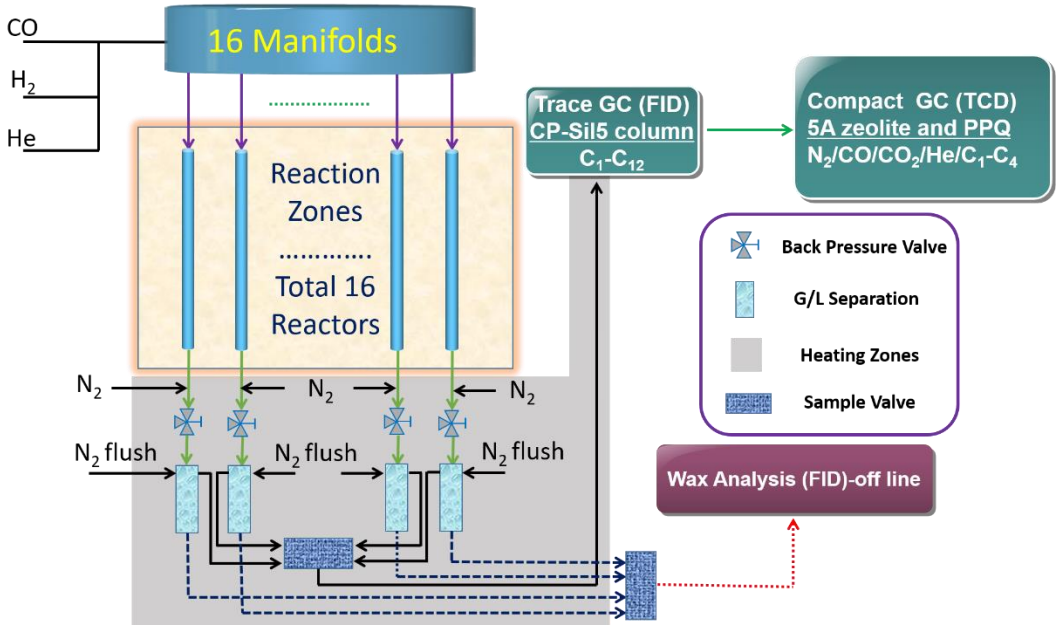

Figure 2.3. *Avantium's parallel fixed bed 16-reactors systems.*

The hydrogenation of octene or octylacetate has been tested separately by addition of 5 mmol/h of octene or octylacetate to 20 mg of reduced catalyst at 220 °C under 20

bar at hydrogen flow 6 ml/min and CO flow 2 ml/min.

2.2.4 Equipment with 3 parallel reactors for testing Co and Ni based catalysts

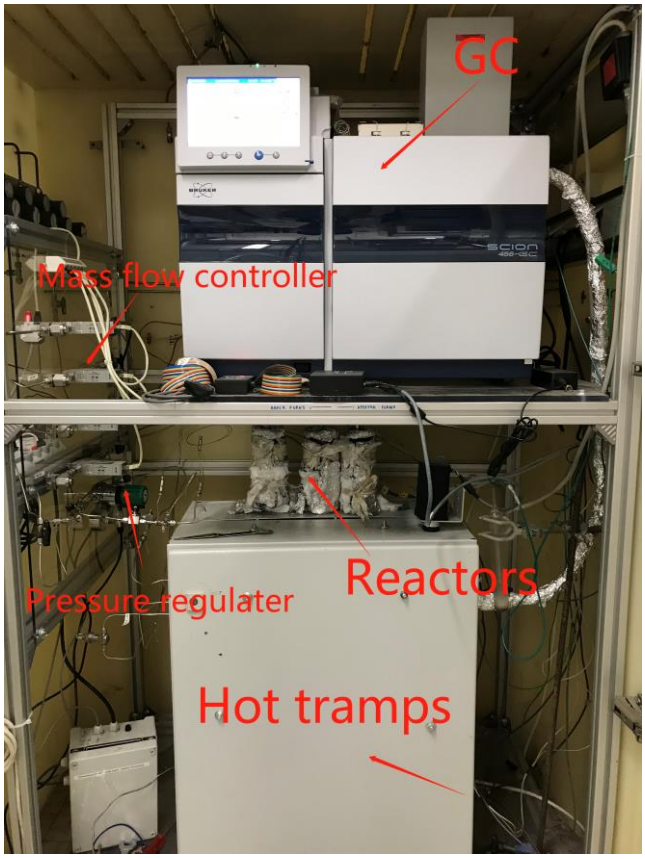

Figure 2.4. *Picture of device for CO hydrogenation over cobalt-based and nickel-based catalysts.*

The syngas conversion was performed in a high-throughput unit (Figure 2.4) equipped with 3 parallel milli-fixed-bed reactors (d = 2 mm). Typically, the calcined catalyst (0.10 g, 100-150 μm) was loaded in the stainless-steel reactor and then activated in the H_2 gas flow (50 ml/min, atmospheric pressure) at 400 °C with a ramping rate of 2 °C/min for 10 h before the reaction. After the reduction, the catalysts were cooled down to 180 °C and a flow of premixed syngas was gradually introduced to the catalysts. When the pressure attained the reaction pressure, the temperature was slowly increased to the temperature of the reaction. The reaction products were analyzed using a gas chromatograph (Bruker GC-456), which was equipped with a thermal

conductivity (TCD) and a flame ionization (FID) detectors. Analysis of N_2, CO, CO_2, and CH_4 was performed using a packed ShinCarbon ST 100/120 column and a TCD detector. The C_1-C_8 hydrocarbons were separated in a capillary Rt-Q PLOT column and analyzed by a FID detector. The liquid products (oil and water phases) were collected in a trap kept at 80 °C and analyzed off-line by gas chromatography. The selectivities were calculated on a molar carbon basis. The product selectivities were reported as percentage of CO converted into a given product, respectively, and expressed on carbon basis. The CO_2 free hydrocarbon selectivities were calculated taking into account only hydrocarbon production in FT synthesis over Co and Ni catalysts. The carbon balance was better than 90 %.

2.3 Analysis Method

The feed gas conversion and products selectivity are based on gas chromatograph (GC). The *A* appearing in the following calculation method indicates the peak area in the GC, *f* indicates the calibration factor, *n* means moles of products (in terms of carbon atom moles), and *x* and *y* indicate the number of carbon atoms and the number of hydrogen atoms in any one hydrocarbon and *S* shows products selectivity.

The CO conversion rate is calculated using N_2 (or He) as an internal standard:

$$CO_{(Conv.)\%} = \left(1 - \frac{A_{initial\ N2}/A_{reaction\ N2}}{A_{initial\ CO}/A_{reaction\ CO}}\right) * 100\% \quad (2\text{-}1)$$

The feed gas of the internal standard gas (N_2 or He) is controlled by mass flow controller (MFC). The inlet molars of CO and N_2 (n_{CO} and n_{N2}) can be calculated from the gas state equation (Equation 2-2). So, the generation rate of CH_4 and CO_2 can be calculated by Equation 2-3 and Equation 2-4, respectively, and the selectivity can be also calculated by Equation 2-5 and Equation 2-6, respectively.

$$P*V = nRT \quad (2\text{-}2)$$

$$n_{CH_4} = \frac{A_{CH_4}/f_{CH_4}}{A_{Ar}/f_{Ar}} * n_{Ar} \quad (2\text{-}3)$$

$$n_{CO_2} = \frac{A_{CO_2}/f_{CO_2}}{A_{Ar}/f_{Ar}} * n_{Ar} \quad (2\text{-}4)$$

$$S_{CH_4} = \frac{n_{CH_4}}{n_{CO*CO_{(Conv.)\%}} - n_{CO_2}} * 100\% \quad (2\text{-}5)$$

$$S_{CO_2} = \frac{n_{CO_2}}{n_{CO*CO_{(Conv.)\%}}} * 100\% \quad (2\text{-}6)$$

Due to the correlation between the two detectors, the product selectivity calculation is calculated by using CH_4 as the second internal standard in the product, that is, the relative amount of each product to CH_4 is first calculated, and the product selectivity is calculated. FID is a carbon counting device [9], which can be understood as a carbon atom corresponding to a unit peak area. The relative amounts and selectivity of each component of the carbon-containing compound in the products can be calculated by Equation 2-7 and 2-8, respectively.

$$n_{C_j} = \frac{A_{C_j}/f_{C_j}}{A_{CH_4}/f_{CH_4}} * n_{CH_4} \quad (2\text{-}7)$$

$$S_{C_j} = \frac{n_{C_j}}{n_{CO*CO_{(Conv.)\%}} - n_{CO_2}} * 100\% \quad (2\text{-}8)$$

The carbon balance is calculated by the total amount of carbon actually detected (the sum of all carbon-containing compounds detected by the FID plus the CO_2 detected on the TCD) divided by the total amount of carbon consumed in the reaction.

$$C_{balance} = \frac{n_{CO_2} + \sum_{j=1}^{max} n_{C_j}}{n_{CO*CO_{(Conv.)\%}}} * 100\% \quad (2\text{-}9)$$

For the Water-Gas-Shift reaction, the CO conversion and CO2 product selectivity are also calculated by Equation 2-1 and Equation 2-6.

2.4 Catalyst Characterization

2.4.1 X-ray diffraction

The X-ray diffraction patterns (XRD) were recorded on a PANalytical Empyrean X-ray diffractometer in Bragg-Brentano configuration with the 0.02° step size and 1 s step time. The Cu Kα radiation (40 kV and 30 mA) was used as the X-ray source. The crystalline phases were identified by comparing the diffraction patterns with those of the standard powder XRD files (JCPDS). Crystal average size was calculated using the

Scherrer equation.

2.4.2 Surface area and porosity

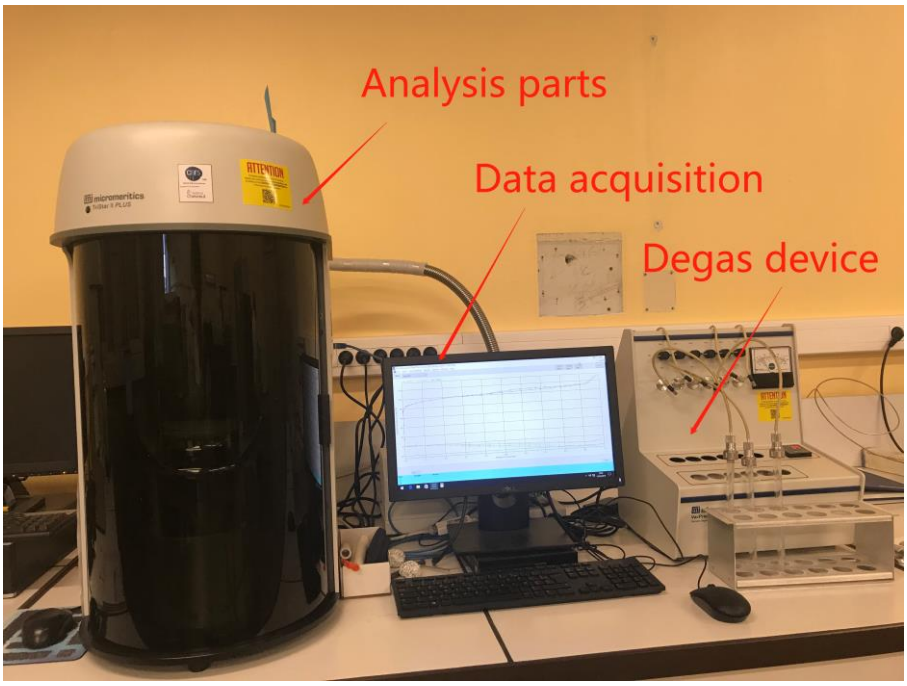

Figure 2.5. *Picture of Micromeritics Tristar Model 3020 Surface Area and Porosimetry analyzer.*

Low temperature (77 K) N_2 adsorption and desorption experiments were performed on a Micromeritics Tristar Model 3020 Surface Area and Porosimetry analyzer (Figure 2.5). 0.1 g of the samples was degassed under vacuum for 250 °C for 2 h, then N_2 was used as the adsorbate, and the adsorption isotherm of the sample was measured at 77 K. The specific surface area of the sample was calculated by the BET method between 0.05 and 0.3 relative pressure.

2.4.3 Transmission electron microscopy

The TEM (Transmission Electron Microscopy) analyses were carried out on a Jeol 2100F (field emission gun) microscope operating at 200 kV equipped with a probe corrector for the spherical aberrations. The point-to-point resolution reached was on the order of 2 Å under the parallel TEM mode and 1 Å under the STEM (Scanning TEM) mode. High angle annular dark field (HAADF)-scanning transmission electron

microscopy (STEM) imaging, and energy dispersive X-ray spectroscopy (EDX) of the calcined analysis were performed on a double corrected CFEG Jeol-ARM200 transmission electron microscope, operated at 200 kV and by using scanning speed 20 µs/px for imaging and 0.05 µs/px for EDX for a with a 0.1 nm probe size and a current of 120 pA.

The TEM analysis of the samples was also performed using a Tecnai instrument, equipped with a LaB6 crystal operated at 200 kV. Prior to the analysis, the samples were dispersed in ethanol for 5 min, and a drop of solution was deposited onto a carbon membrane located on a 300-mesh copper grid. More than 250 particles were counted to estimate the average Fe particle size and standard deviation from TEM images.

2.4.4 Temperature-programmed reduction

The H_2 temperature-programmed reduction (H_2-TPR) and CO-temperature programmed reduction (CO-TPR) experiments were carried out by the AutoChem II 2920 apparatus (Micromeritics Figure 2.6) using 0.05 g of the sample in a flow of H_2/Ar (5 vol. % H_2) or CO/Ar (5 vol. % CO) stream (30 ml/min). The temperature was increased from room temperature to 900 °C at a rate of 10 °C/min.

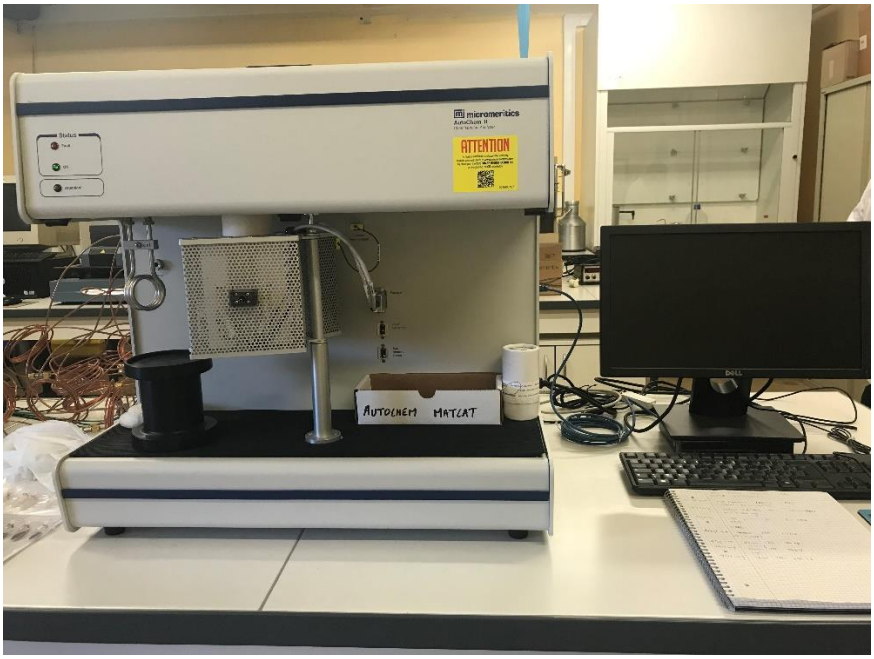

Figure 2.6. *Picture of Micromeritics AutoChem II 2920 apparatus.*

2.4.5 Pulse oxidation

The reduction degree of Co catalysts (EOR) was measured by O_2 pulse oxidation method. Typically, the calcined sample was placed in the same apparatus as used for the TPR experiments. After reduction with pure H_2 at 400 °C for 6 h, the gas was switched to pure helium. Calibrated pulses of O_2-He (3 vol.% O_2) were then added into the continuous He flow until no further consumption of O_2 was detected by the thermal conductivity detector located downstream of the reactor. The extent of reduction was calculated assuming stoichiometric re-oxidation of Co to Co_3O_4.

2.4.6 CO chemisorption

CO chemisorption measurements were carried out using the same instrument as used for TPR experiments. Before each measurement, the sample was reduced for 6 h in flowing H_2 at 400 ºC. After the reduction, the sample was cooled down to room temperature. Calibrated pulses of CO-He (10 vol.% CO) were then added into continuous He flow until no further consumption of CO was detected. Calculations were made using the total amount of adsorbed CO corrected with reduction degree measured and a stoichiometry of one CO per cobalt surface atom.

2.4.7 Temperature-programmed hydrogenation

The temperature-programmed hydrogenation (TPH-MS) was also performed using AutoChem II 2920. Typically, 50 mg of the sample was heated from room temperature to 800 ºC in a flow of H_2/Ar (5 vol. % H_2) stream (50 ml/min), while the signal of methane (m/e = 15) was detected by MS.

2.4.8 Infrared spectroscopy analysis (FT-IR)

Infrared spectra have been observed using Nicolet IS50 FT-IR with 4 cm^{-1} optical resolution (Figure 2.7). Prior to the analysis, the catalysts were pressed with KBr in the discs. Ion exchange or other reactions with KBr have not been observed.

Figure 2.7. *Picture of Fourier transform infrared (FT-IR) setup with homemade vacuum system.*

2.4.9 Elemental analysis

Quantitative elemental analyses were performed by inductively coupled plasma-optic emission spectroscopy 720-ES ICP-OES (Agilent) with axially viewing and simultaneous CCD detection. The quantitative determination of metal content in the catalysts was made based on the analysis of certificated standard solution. The ICP ExpertTM software (version 2.0.4) provided metal concentration in the samples allowing estimating the weight percentage of components. The minimum detection limitation is 0.1 ppm and the accuracy is better than 5 %.

2.4.10 XPS with sample pretreatment

The in-situ XPS spectra were recorded using a VG ESCALAB 220 XL spectrometer using the Al Kα source (1486.6 eV). The powder samples were pressed into 6 mm diameter pellets. In each experiment, the XPS spectra of the fresh catalyst were first measured and then the pelleted catalyst was placed into the in-situ reaction cell heated under a flow of CO (50 mL/min, 1 bar) from room temperature to 350 °C at a heating

rate of 10 °C/min and kept for 3h. The treated sample was then transferred under vacuum without exposure to air to the analytical chamber to record the XPS spectra of the catalyst. After that, the catalyst was retreated with H_2/CO mixture (50 mL/min, 1 bar) at 350°C for 3 h in the reaction cell, and transferred under vacuum to the analytical chamber to record the XPS spectra of the reacted catalyst. The binding energies were corrected with respect to C1s of 284.6 eV and the binding energies were estimated within ± 0.2 eV.

2.4.11 In-situ magnetic characterization

Table 2.1. *Magnetic properties of iron compounds [10].*

Compound	Properties (room temperature)	Curie or Neel temperatures
α-Fe_2O_3 (hematite)	Antiferromagnetic with very week ferromagnetisms	682 °C
λ-Fe_2O_3 (maghemite)	Ferrimagnetic	470-695 °C (unstable from 250 °C)
Fe_3O_4 (magnetite)	Ferrimagnetic	585 °C
FeO (wustite)	Paramagnetic (antiferromagnetic below Neel temperature)	-73 °C
Metallic Fe	Ferromagnetic	770 °C
χ-Fe_5C_2 (Hägg carbide)	Ferromagnetic	205-256 °C
Hexagonal ε-Fe_2C	Ferromagnetic	380 °C
Pseudo-hexagonal ε' $Fe_{2.2}C$	Ferromagnetic	450 °C
Orthorhombic θ-Fe_3C (cementite)	Ferromagnetic	208 °C

The magnetic properties of the catalysts were investigated *in situ* using a Foner vibrating-sample magnetometer [11, 12] with the 10 mg catalyst loading. The magnetometer was calibrated using 1 mg of pure metallic Fe before each experiment. First, the sample was heated to 200 °C with a 6.6 °C/min ramping under 15 ml/min feed of pure CO and kept for 10 min and then sequentially heated to 350 °C with a 4.7 °C/min ramping and kept for 120 min. After the activation, the sample was cooled to the room temperature in the flow of CO. During the whole treatment, the saturation

magnetization curve was recorded by the magnetometer. The pretreatment with syngas was performed using the same procedure. The magnetic properties, Curie and Neel temperature of iron compounds are summarized in Table 2.1.

2.4.12 Mössbauer spectroscopy

The ^{57}Fe Mössbauer spectra were recorded in a transmission mode on a constant acceleration Mossbauer spectrometer (MS1104, Rostov-na-Donu, Rossia) with a ^{57}Co/Rh source, equipped with a liquid nitrogen cryostat. The fitting procedure was performed with custom software. All isomer shifts (IS) were referenced to ^{57}Fe in α-Fe at 300 K.

2.4.13 Ex-situ and in-situ X-ray absorption fine structure (XAFS)

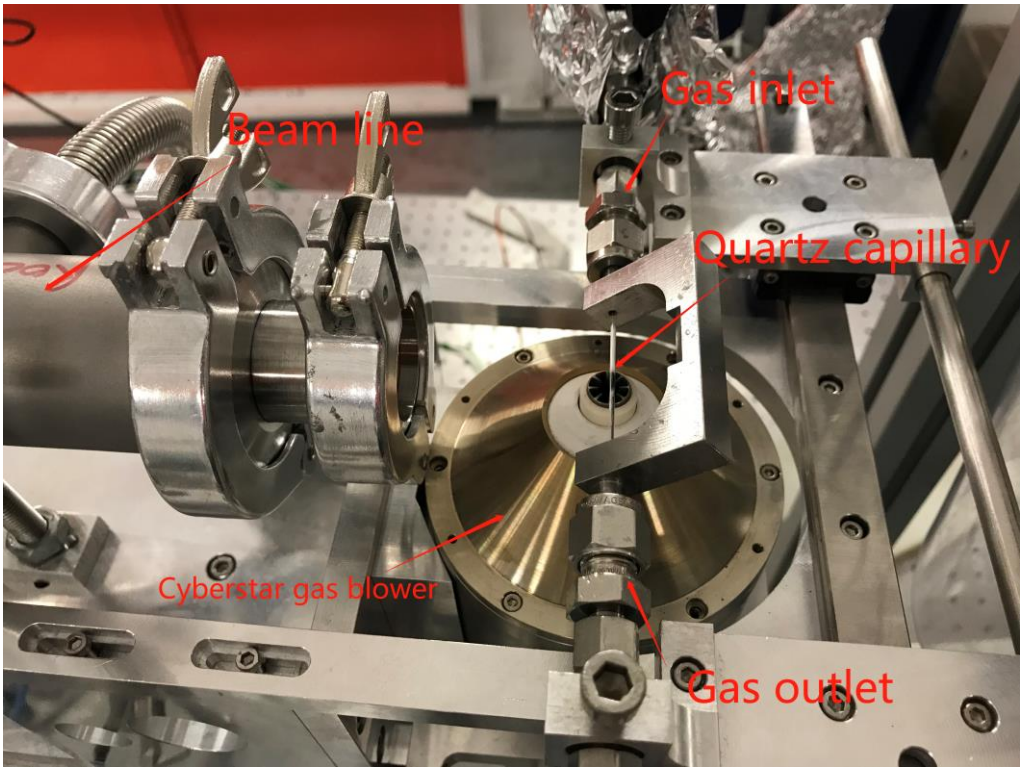

Figure 2.8. *Capillary reactor used for in-situ and ex-situ XANES.*

Ex-situ and in-situ Fe K-edge and Bi L3-edge X-ray absorption fine structure (XAFS) spectra under atmosphere pressure were measured at Beamline XDS (Figure 2.6), Laboratório Nacional de Luz Síncrotron (LNLS), Campinas, Brazil, with electron beam

energy of 5-30 KeV. For the in-situ XAFS, 2-3 mg of catalyst are loaded in the quartz capillary (OD = 1mm, wall thickness 0.1mm) and pressed from both sides with quartz wool. The activation was performed under CO flow (5 ml/min) at 350 ºC with the ramp of 5 ºC/min for 90 min and then cooling to 100 ºC. After activation, syngas with H_2/CO ratio 1/1 (10ml/min) was introduced to the system and increased temperature to 350 ºC with the ramp of 10 ºC/min for 90 min and then cooling to room temperature. The data were collected in fluorescence mode with a Lytle detector and Si (111), Si (311) monochromator. The data were analyzed with Athena software.

2.5 Reference

[1] W. Chen, Z. Fan, X. Pan, X. Bao, Effect of confinement in carbon nanotubes on the activity of Fischer-Tropsch iron catalyst, Journal of the American Chemical Society, 130 (2008) 9414-9419.

[2] X. Pan, Z. Fan, W. Chen, Y. Ding, H. Luo, X. Bao, Enhanced ethanol production inside carbon-nanotube reactors containing catalytic particles, Nature materials, 6 (2007) 507-511.

[3] K. Cheng, M. Virginie, V.V. Ordomsky, C. Cordier, P.A. Chernavskii, M.I. Ivantsov, S. Paul, Y. Wang, A.Y. Khodakov, Pore size effects in high-temperature Fischer-Tropsch synthesis over supported iron catalysts, Journal of catalysis, 328 (2015) 139-150.

[4] D.E. Mears, Tests for Transport Limitations in Experimental Catalytic Reactors, Industrial & Engineering Chemistry Process Design and Development, 10 (1971) 541-547.

[5] P. Weisz, C. Prater, Interpretation of measurements in experimental catalysis, Advances in Catalysis, 6 (1954), 143-196.

[6] A. Primo, J. He, B. Jurca, B. Cojocaru, C. Bucur, V.I. Parvulescu, H. Garcia, CO_2 methanation catalyzed by oriented MoS_2 nanoplatelets supported on few layers graphene, Applied Catalysis B: Environmental, 245 (2019) 351-359.

[7] Y.-N. Wang, Y.-Y. Xu, H.-W. Xiang, Y.-W. Li, B.-J. Zhang, Modeling of Catalyst Pellets for Fischer-Tropsch Synthesis, Industrial & Engineering Chemistry Research, 40 (2001) 4324-4335.

[8] http://www.avantium.com/flowrence/.

[9] T. Holm, Aspects of the mechanism of the flame ionization detector, Journal of Chromatography A, 842 (1999) 221-227.

[10] K. Cheng, V. Ordomsky, M. Virginie, B. Legras, P. Chernavskii, V. Kazak, C. Cordier, S. Paul, Y. Wang, A. Khodakov, Support effects in high temperature Fischer-Tropsch synthesis on iron catalysts, Applied Catalysis A: General, 488 (2014) 66-77.

[11] P. Chernavskii, J.-A. Dalmon, N. Perov, A. Khodakov, Magnetic characterization of Fischer-Tropsch catalysts, Oil & Gas Science and Technology-Revue de l'IFP, 64 (2009) 25-48.

[12] P.A. Chernavskii, A.Y. Khodakov, G.V. Pankina, J.-S. Girardon, E. Quinet, In situ characterization of the genesis of cobalt metal particles in silica-supported Fischer-Tropsch catalysts using Foner magnetic method, Applied Catalysis A: General, 306 (2006) 108-119.

Chapter 3. Effects of the Promotion with Bismuth and Lead on Direct Synthesis of Light Olefins from Syngas over Carbon Nanotube Supported Iron Catalysts

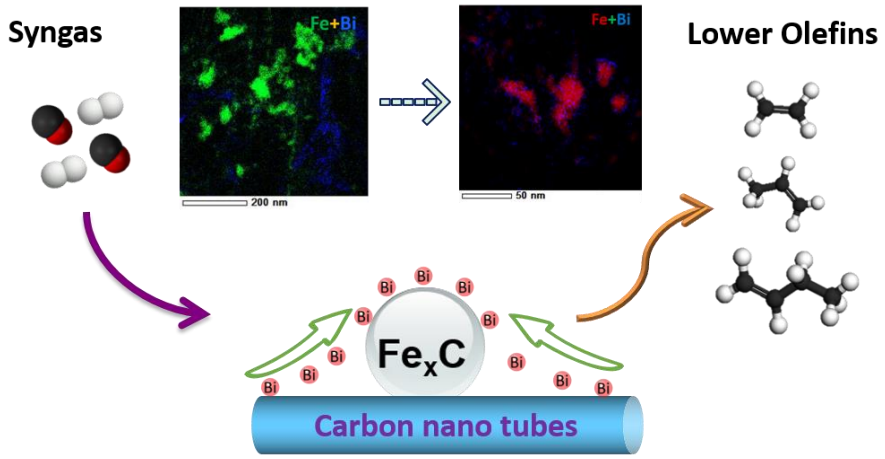

Abstract: Light olefins are important platform molecules in chemical industry. Fischer-Tropsch synthesis provides an alternative technology for direct synthesis of light olefins from syngas, which can be generated from renewable feedstocks such as organic waste, used plastics and biomass. The Bi- and Pb-promoted iron catalysts supported by carbon nanotubes have been prepared for direct conversion of syngas to light olefins. Compared to the un-promoted iron catalysts, a twice higher Fischer-Tropsch reaction rate and higher selectivity to light olefins were obtained. A combination of characterization techniques reveals remarkable migration the promoting elements, which occurs during the catalyst activation. After the activation, the iron carbide nanoparticles are decorated with the promoting elements. The lower melting points and high mobility of these two metal promoters during the catalyst activation are crucial for the intimate contact between Fe and promoters. The promoting effects of bismuth and lead result in a better reducibility and easier carbidization of iron nanoparticles. The higher yield of light olefins over the carbon nanotube supported catalysts in the presence of promoters is due to slowing down secondary hydrogenation of olefins and a decrease in the chain growth probability.

This chapter is based on the following publication:

Bang Gu, Vitaly V. Ordomsky, Mounib Bahri, Ovidiu Ersen, Petr A. Chernavskii and Andrei Y. Khodakov*, *Applied Catalysis B: Environmental* 234 (**2018**) 153-166.

3.1. Introduction

Development of novel routes for the efficient utilization of non-petroleum resources including organic waste, used plastics and biomass to produce chemicals and ultraclean liquid fuels has attracted much attention because of environmental concerns and the depletion of fossil resources. Light olefins (C_2-$C_4^=$) are key building blocks in the chemical industry. They are important intermediates for production of a wide range of packing materials, synthetic textiles and solvents [1, 2].

In conventional technologies, light olefins are produced from steam cracking of naphtha, ethane cracking, methanol to olefins (MTO) and dimethyl ether to olefins (DMTO) processes. In the naphtha steam cracking, olefins are by-products and the selectivity to specific olefins is low. Ethylene is also produced by cracking of ethane present in the shale gas. Despite many important advantages, this process however requires very high temperature and yields only ethylene. The MTO and DMTO processes have been developed and commercialized in several countries with important coal resources [3-5]. MTO and DMTO show high selectivity towards light olefins, while the technologies are multistage and require synthesis of intermediate products such as methanol and dimethyl ether. Catalyst deactivation has been a serious challenge of these processes.

Recently, two groups in China reported the new OX-ZEO process, which is based on the combination of methanol synthesis and MTO on a single bifunctional catalyst constituted either by the Zn-Cr [6] or by Zr-Zn [3] systems and SAPO-34. It is important to emphasize that different to FT synthesis, the selectivity of the OX-ZEO process can be potentially higher than that of the conventional FT synthesis. In the conventional FT synthesis, the maximum selectivity to the C_2-C_4 hydrocarbons (including both olefins and paraffins) is around 58 % with the chain growth probability (α) of 0.46. The challenges of this new technology are relevant to attaining higher olefin yields and improving catalyst stability at higher CO conversion levels [7].

Fischer-Tropsch to Olefins (FTO) is a key process for the direct single-step

transformation of various alternative carbon resources such as coal, natural gas, renewable biomass and waste into light olefins via syngas [8-10]. Iron-based catalysts are the catalysts of choice for the FTO process because of their high selectivity towards light olefins, lower cost and high water-gas-shift activity, which can adjust the H_2/CO ratio in syngas produced from the biomass- or coal-derived feedstocks [11, 12]. Iron has also stronger resistance to the contaminants in syngas (sulfur, nitrogen compounds) compared with cobalt and ruthenium-based catalysts.

The iron-based catalysts for FT synthesis can be divided into two major groups: bulk catalysts and supported catalysts. Although the unsupported fused or precipitated iron catalysts modified by promoters can achieve high selectivity to light olefins, their poor mechanical stability especially in the presence of carbidization/decarbidization results in breaking up of the iron particles, formation of fines and thus, can be prohibitive for the practical applications [13].

Porous supports with high surface area are favorable for better dispersion of iron active phase and therefore for enhanced catalytic performance. Catalytic supports can be also efficient in increasing the mechanical stability of iron-based catalysts. Several supports (oxide, zeolites, carbon materials) have been used for iron FT catalysts.

The properties of the FT catalysts can be modified by adding electronic or structural promoters to improve the selectivity to light olefins or to enhance catalytic activity[14, 15]. Among various promoters, potassium [16, 17], sodium [18-20], copper [21], manganese [22] and zinc [20] are often used. These promoters are considered to work as electronic donors, which tune the CO and H_2 chemisorption and dissociation on the catalyst surfaces. Consequently, the reaction selectivity to light olefins could be significantly improved. Several authors also consider Ln and Zn as structural promoters. Lohitharn [23, 24] et al investigated the silica supported iron catalysts promoted with Mn and identified the role of Mn as a structural promoter. Higher reaction rates observed for the Mn-promoted Fe catalysts were attributed to higher number of active surface intermediates, while their intrinsic activity was not affected. Ma [20] et al considered Zn as structural promoter in their catalysts.

de Jong and co-workers [13] observed enhanced selectivity to light olefins (about 60 %) over a modified Fe/α-Al_2O_3 catalyst containing small amounts of sulfur and sodium. The best results in that report were obtained at very low CO conversion. The inert α-Al_2O_3 support showed week interaction with iron species. It was suggested that sodium could reduce methane selectivity by increasing the chain growth probability while sulfur have reduced the hydrogen coverage of the catalyst and its hydrogenation activity. The proximity between iron and promoters (Na, S) was a key parameter, which determined hydrocarbon distribution [25, 26]. Recently we observed [27] a remarkable increase in the FT reaction rate and light olefins selectivity over the silica supported iron catalysts promoted with soldering elements such as Bi and Pb.

It is known that the catalyst structure can significantly evolve during many catalytic reactions. The active phase can be modified and promoters can migrate to or from the active sites [28, 29]. Li. et al [30] found that Mn could migrate to the surface of the iron and result in encapsulation of unreduced FeO in MnO . The migration of the alkali promoters from iron catalysts may cause deterioration of the support acidity and then increase carbon deposition. The migration of promoters may also have an effect for the product selectivity. In the alkali promoted iron catalysts, alkali ions can migrate from iron species to the support. As a result, the reaction shifts towards lighter and more paraffinic hydrocarbons, which are usually observed over the unpromoted catalysts [31].

Carbon nanotubes (CNT) as catalytic supports for iron Fischer-Tropsch catalysts have several important advantages. Different to commonly used oxide supports, carbon does not form inert mixed compounds between iron and supports (e.g. iron silicate or aluminate) which are difficult to reduce and to carbidize during the catalyst activation and reaction. Iron catalysts supported on carbon nanotubes and activated carbon show highest activity in FT synthesis, which could be attributed to the formation of composites of iron carbide and residual magnetite [18] and to possible electronic transfer between carbon and iron species [32].

Similar to metal oxide-supported catalysts, Fe catalysts supported on carbon materials are sensitive to promoters, especially alkali metals. Xu et al. [33]reported that

on the CNT-supported Fe-Mn nanoparticles, the selectivity to light olefins was 31.5 % with the methane selectivity of 6.1 %. However, the CO conversion decreased from 60.2 % to 43.9 % after adding the Mn elements. Lu et al. [34] found that iron catalysts decorated with K and supported on N-CNT showed higher light olefin selectivity (54.6 %), compared to the Fe/N-CNT catalyst. The iron catalysts supported by CNT and promoted with Mo also showed an increase in the selectivity to light olefins from 30% to 40%, while the reaction rate was not much affected [35]. Finally, more accurate information about localization of iron and promoters can be obtained on the catalysts supported by CNT, because of better contrast in TEM and other imaging techniques.

The present chapter focuses on the promotion of carbon nanotube supported iron catalysts with Bi and Pb for direct light olefin synthesis. This chapter has two specific objectives: first, to develop extremely active and selective iron catalysts for direct olefin synthesis on the basis of CNT; second, to provide deep insights into the localization and structure of active sites and mechanisms of interaction of the Bi and Pb promoters with iron carbide and CNT. At different stages of catalyst preparation, activation and catalytic reaction, the catalysts were characterized by combination of techniques; the catalytic performance was evaluated in a fixed bed reactor at a wide range of operating conditions.

3.2. Results and Discussion

3.2.1 Calcined catalysts

Table 1 shows textural properties and elemental composition of the CNT support and iron catalysts supported by CNT calcined in nitrogen. The pristine CNT has the BET surface area of 143.3 m^2/g and pore volume of 0.55 cm^3/g. The impregnation of CNT with iron and promoters decreases both the surface area and pore volume. The effect can be due to two phenomena. First, introduction of iron may result in the effect of "dilution" of carbon nanotubes with iron. Second, the impregnation can lead to blocking of CNT inner channels with iron species and promoters (Table 3.1).

The elemental analysis data are displayed in Table 3.1. All the catalysts showed similar iron content (around 10 wt. %) which is close to inventory, while the content of Bi and Pb were 0.82 wt. % and 0.86 wt. %, respectively.

Table 3.1. *Physical properties of supports and supported Fe catalysts.*

Sample	S_{BET}[a] (m^2/g)	V_{tot}[b] (cm^3/g)	D_{meso}[c] (nm)	D_{Fe}[d] (nm)	Total H_2 Consumption[e] (mmol/g)	Reduction degree[e] (%)	Fe content[f] (wt%)	Bi or Pb content[f] (wt%)
CNT	143.3	0.55	15.4				-	-
Fe/CNT	131.2	0.45	13.9	6.3	1.28	33.3	11.4	-
FeBi/CNT	126.5	0.47	12.3	5.9	2.04	41.4	10.9	0.82
FePb/CNT	120.4	0.48	13.1	6.5	1.66	39.2	11.2	0.86

[a] BET surface area.

[b] Single point desorption total pore volume of pores, P/P_0=0.975.

[c] The pore diameter in the mesoporous region evaluated by the BJH method.

[d] Average particle size of iron oxide by TEM.

[e] The total H_2 consumption and iron reducibility degree from TPR analysis.

[f] The Fe, Bi and Pb content from ICP-OES.

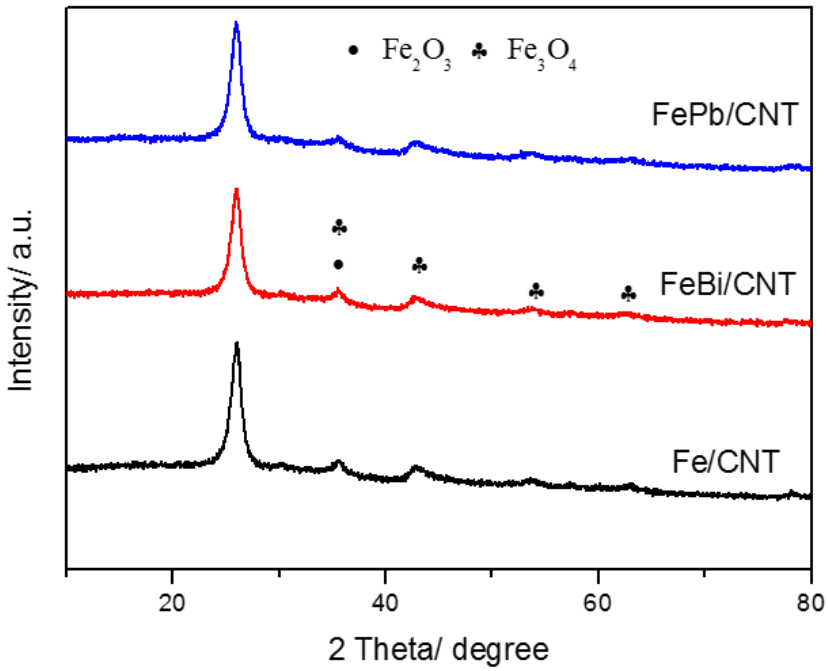

Figure 3.1. *XRD patterns of the Fe/CNT, FeBi/CNT and FePb/CNT catalysts calcined in nitrogen*

Figure 3.1 displays XRD profiles of the catalysts calcined in nitrogen. The peaks at 26.3° and 43.8° are attributed to the (002) and (101) reflections of the CNT supports. The diffraction lines at 2θ of 35.6° are assignable to the hematite phase (Fe_2O_3, JCPDS 13-0534), while the diffraction lines at 2θ of 35.8°,43.5° and 53.9° can be ascribed to the magnetite phase (Fe_3O_4, JCPDS 75-0449). The results are similar to previous reports, which showed that decomposition of iron nitrate in nitrogen results in the formation of mostly the magnetite phase [18, 36]. The XRD profiles also suggest that adding Bi or Pb does not modify the iron oxide phase composition in the calcined catalysts.

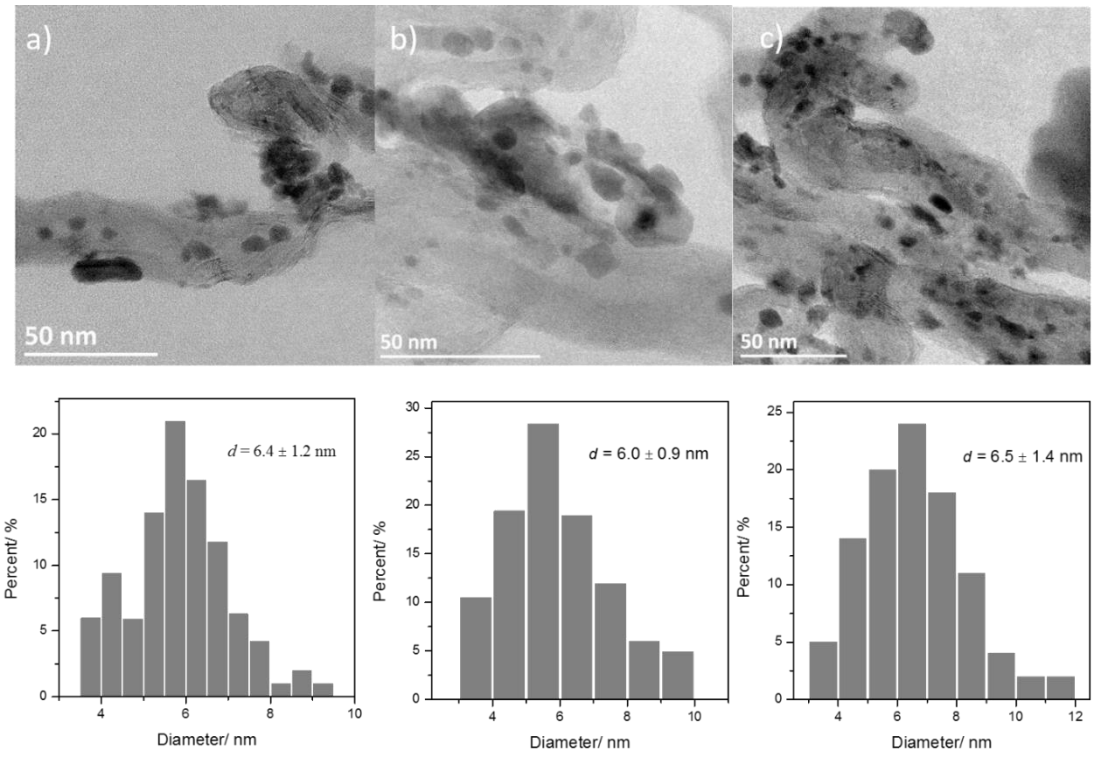

Figure 3.2. *TEM micrographs and particle size distributions for fresh Fe catalysts: (a) Fe/CNT, (b) FeBi/CNT and (c) FePb/CNT.*

Figure 3.2 displays TEM images of the calcined unpromoted and promoted iron catalysts. Carbon nanotubes and iron oxide nanoparticles are clearly observed. Quantitative analysis using particle size histograms also give the average iron oxide nanoparticle diameters of 5-6 nm, which is consistent with the XRD data. Interestingly, the sizes of iron oxide crystallites are not affected by the promotion. This suggests that

the promotion of iron catalysts with Bi and Pb does not affect to any noticeable extent iron dispersion.

Reducibility is another essential parameter of iron catalyst. Figure 3.3 shows the H_2-TPR profiles of the un-promoted Fe/CNT catalyst and Bi- and Pb-promoted counterparts. Three main groups of hydrogen consumption peaks were observed for all the catalysts. The reduction of iron oxides is a stepwise process, which occurs as follows: $Fe_2O_3 \rightarrow Fe_3O_4 \rightarrow FeO \rightarrow Fe$ [37-39]. The TPR peaks were however very broad. This can be due to broad iron particle size distribution, metal-support interactions, promotion effects or temperature ramping rate. Generally, the first TPR peak at 250-420 ^oC is assignable to the reduction of Fe_2O_3 to Fe_3O_4, the second peak can be ascribed to the reduction of Fe_3O_4 to FeO and the third peak (600-700 ^oC) can be attributed to the reduction of FeO to Fe^0. The broad peak above 720 ^oC can be caused by gasification of the CNT support [34, 36].

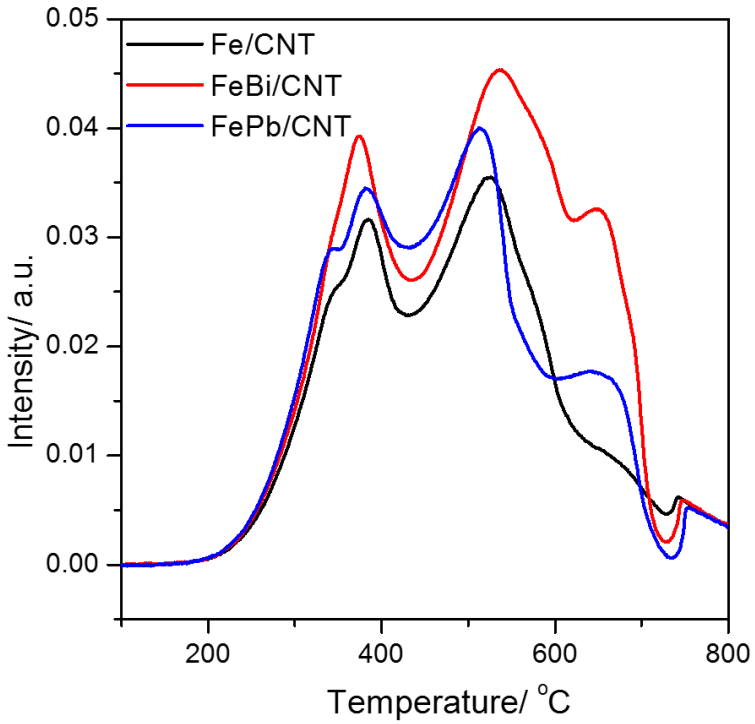

Figure 3.3. *H_2-TPR profiles of Fe/CNT, FeBi/CNT and FePb/CNT.*

Note that the molar concentrations of Bi and Pb were 50 times lower than iron. Even if the Bi and Pb promoters can be reduced under these conditions, no visible TPR peaks are expected during the reduction of promoters. Figure 3.3 also shows that the presence of Bi and Pb promoters shifts the reduction peaks from 250-420 °C to lower temperature. Similar results were obtained with iron catalysts supported on carbon nanotubes

promoted with Mn [33]. Interestingly, higher intensity of the TPR peaks, which are assigned to the FeO reduction to metallic Fe was observed on the Bi and Pb promoted catalysts. This suggests that the presence of these elements facilitates formation of iron metallic phases. The total hydrogen consumption during TPR experiments is an important parameter, which provides information about the reducibility of supported iron species. TPR results therefore suggest the following sequence of studied iron catalysts relative to total hydrogen consumption and iron reducibility: Fe/CNT < FeBi/CNT < FePb/CNT (Table 3.1).

3.2.2 Carbidized iron catalysts

Iron carbides, which are generated in the presence of carbon monoxide or syngas are usually considered as active phase for FT synthesis. The catalysts were exposed to the flow of CO at 350 °C for iron carbidization. Figure 3.4a shows the XRD profiles of the catalysts after the treatment under CO at 350 °C for 10 h. A broad diffraction peak is observed at ca. 44° irrespective of the catalyst composition. This broad peak can be assigned to iron carbides, indicating that iron oxides are converted into iron carbides during the CO pretreatment.

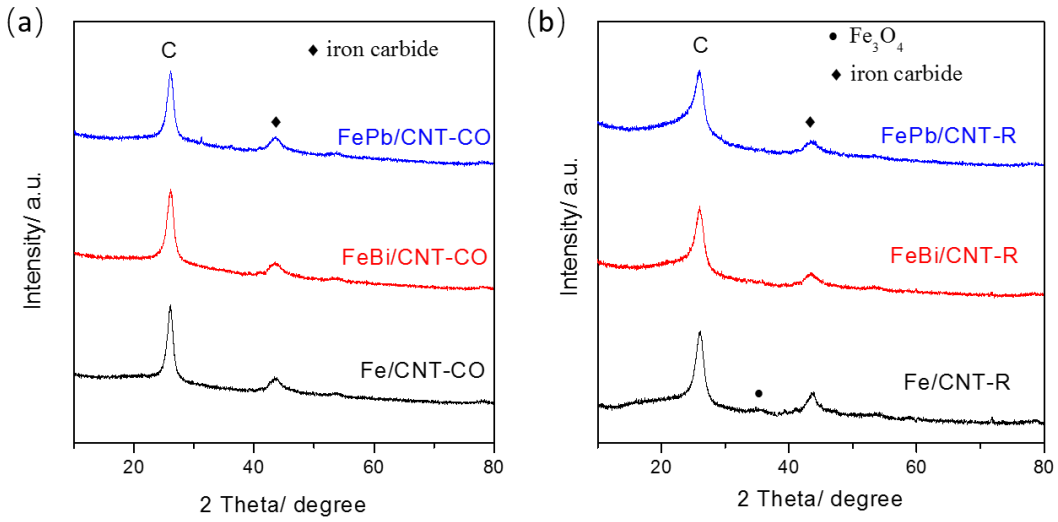

Figure 3.4. *XRD profiles the catalysts: (a) after treatment at 350 °C for 10h under CO gas flow, (b) the used catalysts.*

Several iron carbides such as Fe_3C, χ-Fe_5C_2, ε-$Fe_{2.2}C$ can be present in the carbidized iron catalysts. The identification of individual iron carbide phases can be only performed for larger iron carbide crystals, which exhibit relatively distinct and well

resolved XRD peaks. A comparison of the XRD peaks of the activated catalysts with those observed for the iron carbide reference compounds indicates the presence of either χ-Fe_5C_2 or ε-Fe_2C in the activated catalysts. Note that XRD characterization nearly excludes the presence of θ-Fe_3C or Fe_7C_3. Due to a significant broadening and overlapping of the carbide XRD peaks, the unambiguous identification of specific χ-Fe_5C_2 or ε-Fe_2C carbide phases seems rather challenging from XRD patterns. A weak peak at ca. 52.5° of magnetite is also detected which may be caused either by incomplete carbidization of iron oxides or by the surface oxidation during the sample transfer and XRD acquisition.

Table 3.2. *Mössbauer spectrum data of the fresh and used catalysts*.

Sample	Mössbauer parameters[a]				Phase	Area (%)
	δ(mm/ s)	ΔEQ	H (T)	Γ		
Fe/CNT	0.49	0.39	54.1	0.28	Fe^{3+}, Fe_2O_3 well crystalline	20
	0.45	0.04	52.1	0.43	Fe^{3+}, probably γ-Fe_2O_3	23
	0.42	-0.09	49.4	0.44	Fe^{3+}, Fe_2O_3 poor crystalline (I)	13
	0.51	-0.14	44.7	1.62	Fe^{3+}, Fe_2O_3 poor crystalline (II)	27
	0.42	0.91	-	0.86	Fe^{3+}, superparamagnetic	18
Fe/CNT-used	0.49	0.00	52.7	0.47	Fe^{3+}, Fe_2O_3	16
	0.83	0.00	45.7	1.34	Fe^{3+}, Fe_3O_4 and/or γ-Fe_2O_3	12
	0.42	-0.05	50.6	0.43	Fe^{2+}, Fe_3O_4	16
	0.39	0.07	25.2	0.46	Fe^{3+}, Fe_5C_2 (I)	16
	0.35	-0.05	20.8	0.60	Fe^{3+}, Fe_5C_2 (II)	17
	0.29	0.02	12.1	0.60	Fe^{3+}, Fe_5C_2 (III)	12
	0.24	0.20	3.6	0.36	Fe^{3+}, superparamagnetic	11
FePb/CNT	0.48	0	<5-55>	-	Fe^{3+}, superparamagnetic Fe_2O_3	100
FePb/CNT-used	0.43	0.00	24.9	0.70	χ-Fe_5C_2 (I)	32
	0.36	0.01	20.4	0.56	χ-Fe_5C_2 (II)	23
	0.32	-0.04	13.0	0.70	χ-Fe_5C_2 (III)	19
	0.34	0.15	4.1	0.55	Fe^{3+}, superparamagnetic	26

The iron phases in the fresh and used catalysts were analyzed by the Mössbauer spectrometry (Figure 3.5). The fresh catalysts mainly contain Fe_2O_3 phase, the used FePb/CNT catalyst generates much more χ-Fe_5C_2 than the used Fe/CNT catalyst with relative areas of 74 % and 45 %, respectively (Table 3.2).

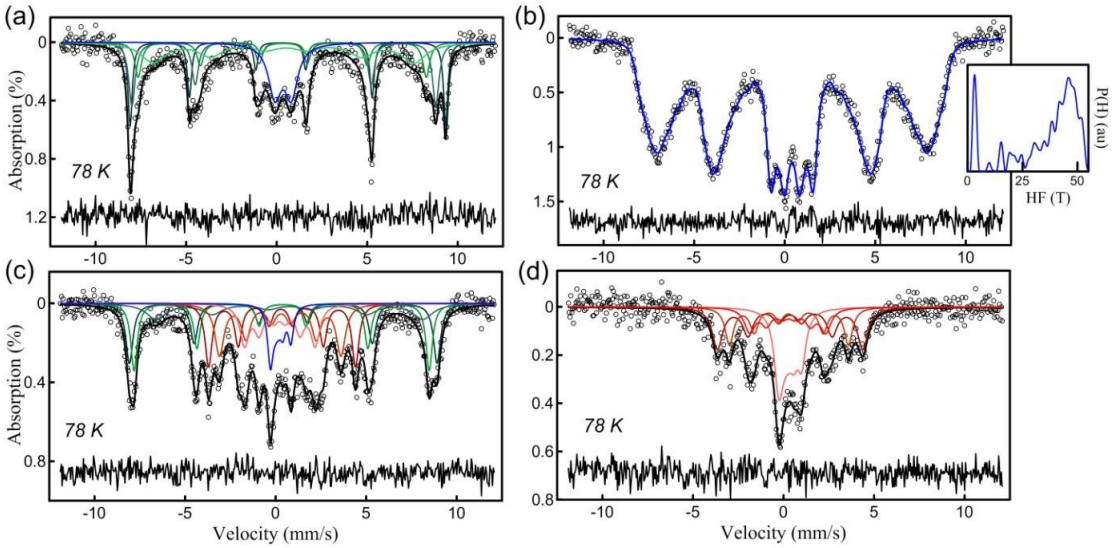

Figure 3.5. *Mössbauer spectra of the fresh and used catalysts, measured at 78 K: (a) Fe/CNT, (b) FePb/CNT, (c) Fe/CNT-used, (d) FePb/CNT-used*

The in situ magnetic measurements were performed at different temperatures under the flow of carbon monoxide and syngas. They have provided more specific and quantitative information about type and concentration of iron carbides in activated CNT supported iron catalysts. Prior to the in-situ magnetic measurements, the catalysts were carbidized in a flow of carbon monoxide at 350°C. Figure 3.6 shows variation of catalyst magnetization with temperature during cooling of the samples after the carbidization in CO or syngas. The shapes of thermomagnetic curves obtained after carbidization in CO and syngas are very similar. Low magnetization at higher temperatures could be due to the disordering of magnetic domains after attaining the Curie temperature for the ferromagnetic phases present in the activated catalysts. Several iron ferromagnetic compounds may exist: iron carbides, metallic iron and magnetite (Fe_3O_4). The Curie temperature for these compounds is given in our previous report [18]. Indeed, the Curie temperature of χ-Fe_5C_2 is close to 250 ºC, while the Curie temperatures of magnetite and metallic iron are 580 and 770 ºC, respectively [18, 40]. Note that a decrease in magnetization to zero at temperatures higher than 300 °C rules out the presence of any noticeable concentrations of metallic iron, magnetite or hexagonal ε-Fe_2C carbide (T_{Curie} = 380 °C). All these compounds have relatively high Curie temperature. The presence of θ-Fe_3C in the activated catalysts has been already

excluded by the XRD data.

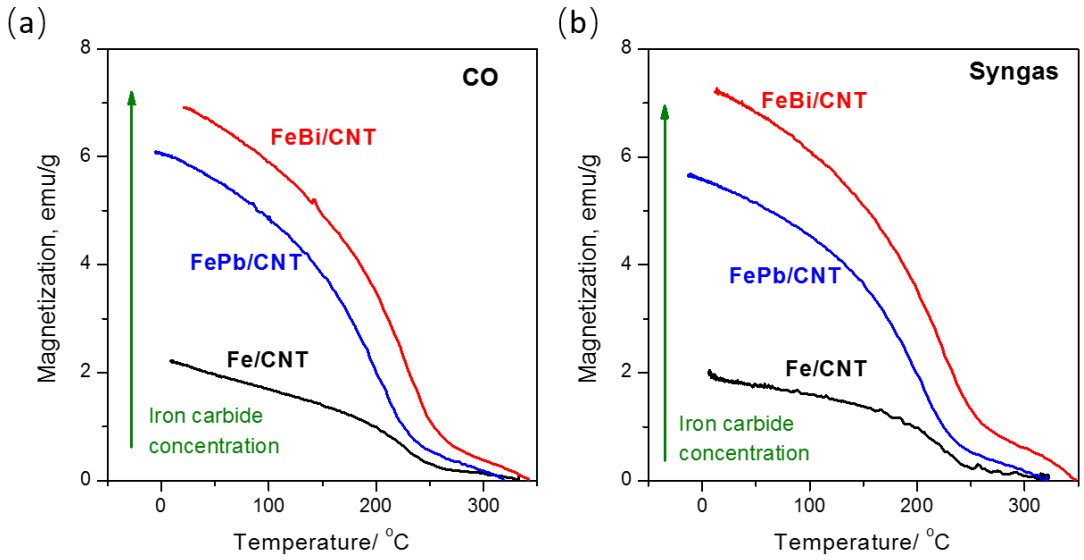

Figure 3.6. *Catalyst magnetization measured: (a) during cooling down after CO treatment at 350 °C, (b) during cooling down after syngas treatment at 350 °C.*

The Curie temperature was evaluated from the first derivative of the magnetization variation with temperature. The unpromoted Fe/CNT and Bi- and Pb promoted catalysts exhibit the presence of Hägg χ-Fe_5C_2 iron carbide, which has the Curie temperature around 250 °C. Besides of χ-Fe_5C_2, a small concentration of ferromagnetic phase with the Curie temperature at 280 °C was detected. This phase cannot be attributed to any known iron bulk phase. Indeed, all known iron phases do not have Curie temperature in this range [18]. This phase was tentatively attributed to non-stoichiometric iron carbide species.

It is important to emphasize that in the CNT supported catalysts activated in CO and exposed to syngas, the thermomagnetic curves shown in Figure 3.6 are indicative of iron carbides as the only ferromagnetic phases. Thus, the saturation magnetization can be directly related to the iron carbide concentration. Therefore, the extent of carbidization can be estimated from the total magnetization at a given temperature. The magnetization results are indicative of higher magnetization of the Bi- and Pb-promoted catalysts compared to the unpromoted Fe/CNT. These catalysts have the same iron content. Higher magnetization observed in the promoted catalysts is therefore indicative of higher extent of iron carbidization. After activation in CO, higher amount

of the Hägg iron carbide was observed in the promoted catalysts compared to the unpromoted one. This observation is also consistent what iron carbide hydrogenation data which were also indicative of higher extent of iron carbidization in the promoted catalysts. This observation is also consistent with Mössbauer data, which were also indicative of higher extent of iron carbidization in the promoted catalysts.

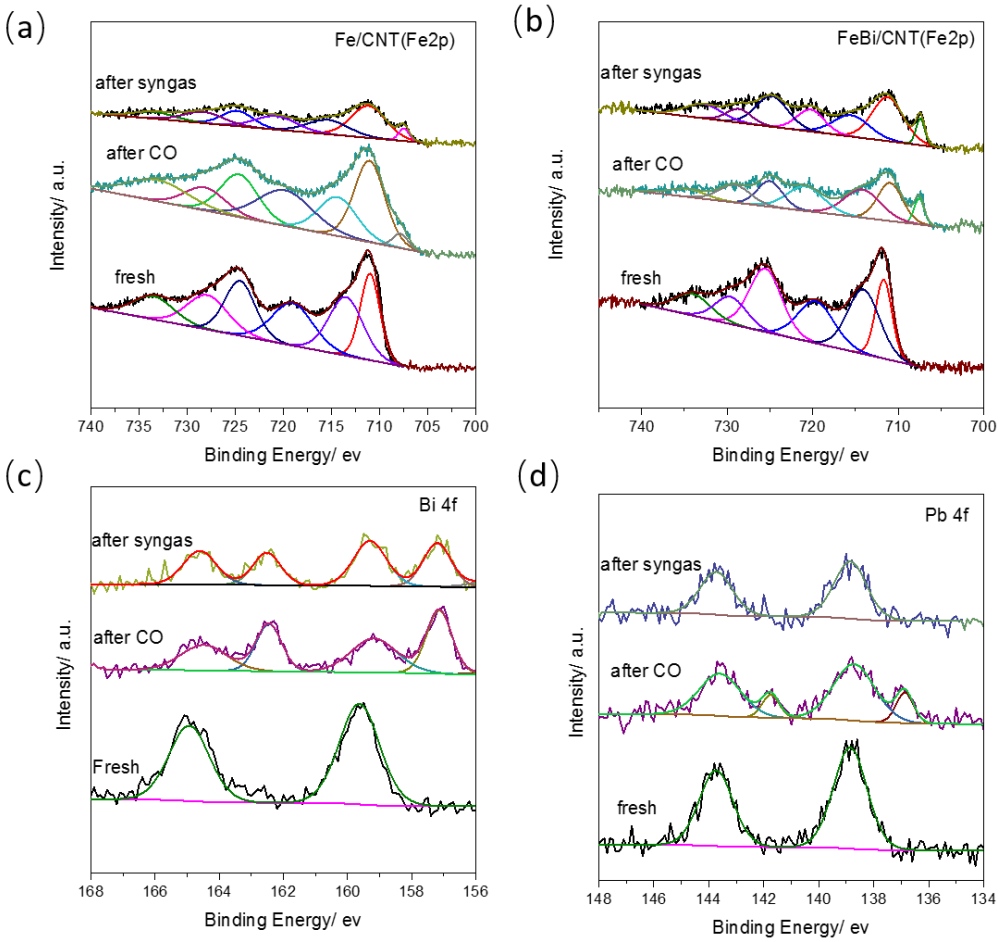

Figure 3.7. *a) Fe 2p XPS spectra of the Fe/CNT catalyst after calcination, exposure to carbon monoxide and syngas, b) Fe 2p XPS spectra of the FeBi/CNT catalyst after calcination, exposure to carbon monoxide and syngas, c) Bi 4f XPS spectra of the FeBi/CNT catalyst after calcination, exposure to carbon monoxide and syngas, d) Pb 4f XPS spectra of the FePb/CNT catalyst after calcination, exposure to carbon monoxide and syngas.*

The subsurface structure of iron catalysts was investigated by XPS (Figure 3.7). The catalyst was transferred from the pre-treatment chamber to the XPS analysis chamber

of the spectrometer without exposure to air. The Fe 2p XPS spectra (Figure 3.7a and b) display peaks at 710.9 and 724.1 eV in a 2:1 peak area ratio, which are assigned to the Fe $2p_{3/2}$ and Fe $2p_{1/2}$ signals, respectively. The spectra are typical for the Fe^{3+} species in Fe_2O_3 [41] (Figure 3.7a). After treatment with CO at 350 ^oC for 120 min, the XPS peaks attributed to Fe^{3+} significantly decrease in intensity. A broad peak with the binding energy of 707.3 eV assignable to iron carbide (Fe_5C_2) was detected [41, 42]. This suggests coexistence of the iron oxide and iron carbide in the activated catalysts. When the activated Fe/CNT sample was exposed to a mixture of CO/H_2 = 1 (v/v) at 350 ^oC for 120 min, the intensity of XPS peak at 707.3 eV increases. A higher amount of iron carbide seems to have been formed during the catalyst exposure in syngas. Interestingly, the intensity of iron carbide XPS peaks at 707 eV was much higher in the Bi-promoted catalyst. This is also consistent with higher extent of iron carbidization in the promoted catalysts compared to the unpromoted counterpart.

The Bi 4f XPS data were indicative of the presence of Bi in the oxidized state after calcination (Figure 3.7c). The peaks with binding energies of 158.6 and 165 eV [43] were observed. Catalyst activation in carbon monoxide leads to partial Bi reduction to metallic state with a characteristic XPS peak at 156.9 eV [44]. This suggests that catalyst treatment with carbon monoxide results in the removal of oxygen atoms from the promoter. Importantly, bismuth also remains in the metallic state after the subsequent exposure to syngas.

Slightly different phenomena were observed by XPS for the lead promoted catalysts. The Pb 4f XPS spectra were indicative of the presence of Pb in the oxidized state after calcination (Figure 3.7d). Similar to the Bi-promoted catalyst, activation in CO results in partial Pb reduction. Note however that different to FeBi/CNT, exposure of FePb/CNT to syngas results in lead oxidation. Lead can easily change oxidation state during FT reaction. After syngas treatment, Bi is present in both metallic and oxide states, however the Pb remains oxide state. The oxidation state of lead seems much more sensitive to the reaction environment [27]. This is also consistent with the electrochemical potentials of bismuth and lead (+ 0.317 V and - 0.126 V respectively).

Variation of the oxidation states of the Bi and Pb promoters is essential for the enhanced catalytic performance. The promoters, which are located at the interface of iron carbide particles, facilitate CO dissociation by scavenging O atoms. The reasons of lead oxidation during FT reaction are discussed in section 3.2.4.

3.2.3 Catalytic results

Table 3.3. Catalytic performances of supported Fe catalysts for FT synthesis. [a]

Catalyst	Reaction condition		FTY,10^{-4} $molg_{Fe}^{-1}s^{-1}$	CO conv. (%)	CO_2 selec. (%)	Hydrocarbon selectivity (%)				C_2-$C_4^=$/ C_2-C_4^o	α
	P bar	GHSV $Lg^{-1}h^{-1}$				CH_4	C_2-$C_4^=$	C_2-C_4^o	C_{5+}		
Fe/SiO_2	10	3.4	0.2	10.1	29	26.4	29.6	25.4	18.8	1.17	0.47
Fe/CNT	10	3.4	1.0	57.3	40	29.1	32.4	17.3	21.9	1.87	0.55
	1	3.4	0.09	4.5	23	31.0	49	7.4	12.6	6.6	0.48
FeBi/CNT	10	3.4	1.6	78.3	47	26.1	35.2	25.6	14.1	1.38	0.43
	10	13.6	4.2	50.7	46	26.5	36.1	15.6	21.8	2.31	0.42
	1	3.4	0.2	10.0	33	28.1	60.9	6.1	3.9	10.0	0.34
FePb/CNT	10	3.4	2.0	96	50	22.4	28.4	20.8	28.4	1.37	0.50
	10	13.6	4.8	56.8	48	27.7	35.8	18.7	17.7	1.91	0.47
	1	3.4	0.4	18.6	35	25.6	57.7	7.4	9.3	7.80	0.36
Fe/CNT+Bi/CNT	10	3.4	1.4	67.6	43	26.5	34.5	26.9	12.1	1.28	0.46
Fe/CNT+Pb/CNT	10	3.4	1.6	77.6	44	23.6	32.6	18.3	25.5	1.78	0.48
Bi/CNT or Pb/CNT	10	3.4	0	0	0	0	0	0	0	0	-

[a] Reaction conditions: W = 0.2 g, H_2/CO = 1, T = 350 °C, P = 10 bar or 1 bar, time on stream = 20 h.

The catalytic data for the CNT supported Fe catalysts promoted with Bi and Pb are shown in Table 3.3. Table 3.3 also displays the catalytic data obtained under the same conditions for the Fe/SiO_2 catalyst. The data for Fe/SiO_2 is given for comparison. Methane, C_2-C_4 light olefins, C_{5+} hydrocarbons, carbon dioxide and water were the products of syngas conversion over the iron catalysts. Iron supported on CNT showed

around 5 times higher CO conversion compared with the SiO_2 supported iron catalyst under the same conditions. These results are consistent with previous reports about the catalytic performance of iron catalysts in FT synthesis. Indeed, iron catalysts supported on carbon materials have been shown to be usually more active than those loaded on SiO_2, because of higher carbidization of iron [11, 18] and possible electron dative effect from carbon [45] on iron species, which facilitates dissociation of carbon monoxide.

Importantly, promotion with Bi and Pb also produces a very strong effect on the catalytic activity of iron catalysts supported on carbon nanotubes. At GHSV = 3.4 L/g_{cat} h, the CO conversion increased from 57.3 % observed over the Fe/CNT catalyst to 78.3 % and 96 % over the Bi and Pb-promoted counterparts, respectively (Table 3.3).

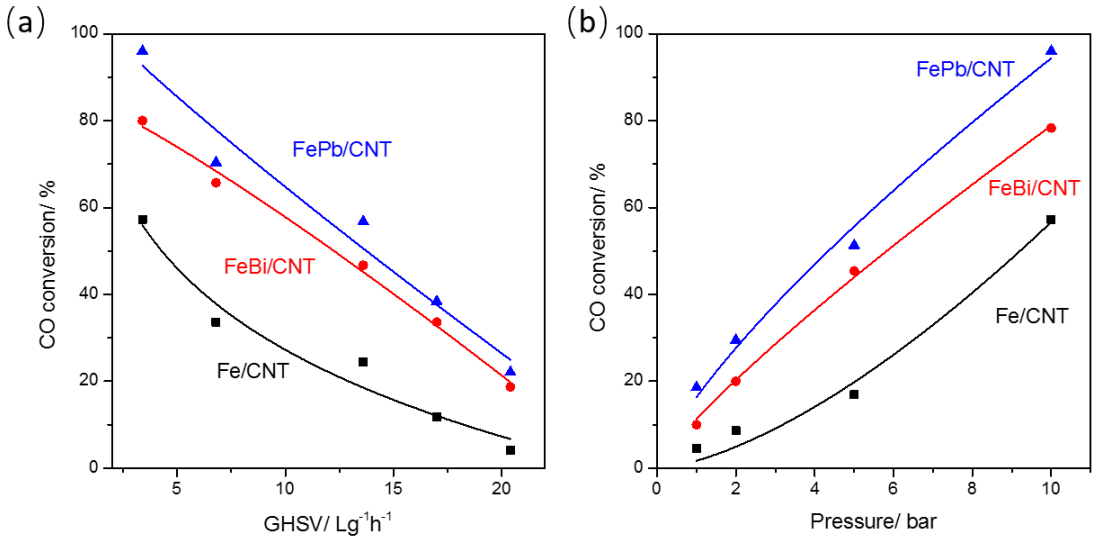

Figure 3.8. *Carbon monoxide conversion over CNT supported iron catalysts under different reaction condition: (a) under different GHSV, (b) under different pressure. Reaction conditions: W = 0.2 g, H_2/CO = 1, P = 1-10 bar, T = 350 °C, GHSV = 3.4-20.4 L h^{-1} g^{-1}.*

Figure 3.8 shows the effects of pressure and GHSV on the CO conversion. At the same pressure, the CO conversion increases as the GHSV is decreasing. The result is rather expected and is due to the variation of the residence time. At iso-GHSV, the FT reaction rates on unpromoted and promoted catalysts increase with the pressure. Interestingly, the Bi or Pb promoted catalysts show higher CO conversion under both the same pressure and GHSV compared with the unpromoted iron catalyst. Interestingly,

the promotion effect remains very significant even at low pressure (1 bar). While the carbon monoxide conversion over the unpromoted Fe/CNT was very low (4.5 %) at GHSV = 3.4 L/gcat h at atmospheric pressure, the catalysts promoted with Bi and Pb showed noticeable CO conversions of 10-20 % under the same conditions.

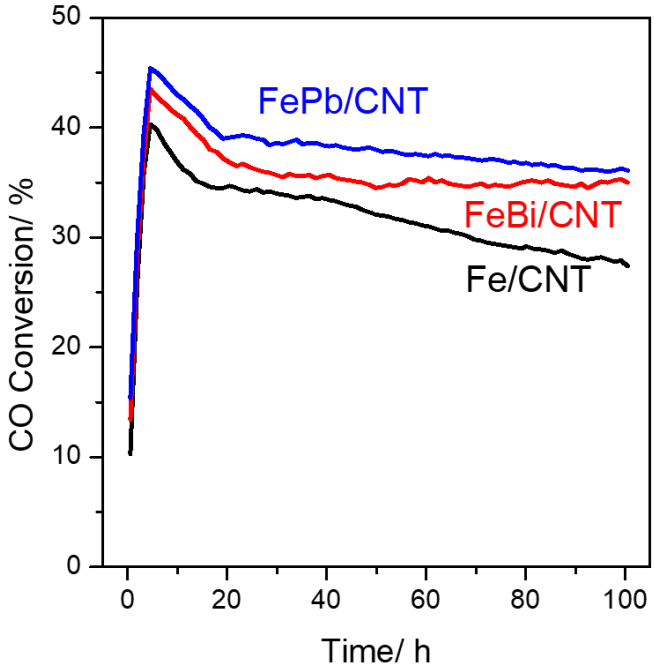

Figure 3.9. *Carbon monoxide conversion as a function of tie of stream for the pristine Fe/CNT and Bi and Pb promoted catalysts (H_2/CO = 1, P = 10 bar, T = 350 °C, GHSV for Fe/CNT 6.8 L $g^{-1}h^{-1}$, FeBi/CNT and FePb/CNT 17 L $g^{-1}h^{-1}$)*

Promotion with Pb and Bi produces also a noticeable effect on the catalyst stability. Figure 3.9 shows carbon monoxide conversion as a function of time on stream. Similar CO conversion were obtained variation of GHSV. The promoted catalysts exhibit better stability compared to the pristine Fe/CNT.

Interestingly, over promoted catalysts the decrease in the pressure to 1 bar leads to increase in the selectivity to the C_2-C_4 olefins by about 20 % reaching ~ 60 % at the conversion levels of 10-20 % under the same conditions. The olefin yield from syngas observed under these conditions is one of the best reported so far in the literature (Table 3.3). At the same time, lower reaction pressure also leads to lower C_{5+} hydrocarbon selectivity (Figure 3.10). Note that the Bi- and Pb-promoted catalysts show much lower

selectivity to light paraffins and C_{5+} hydrocarbons in comparison with the reference Fe/CNT unpromoted catalyst (Figure 3.10, Table 3.3).

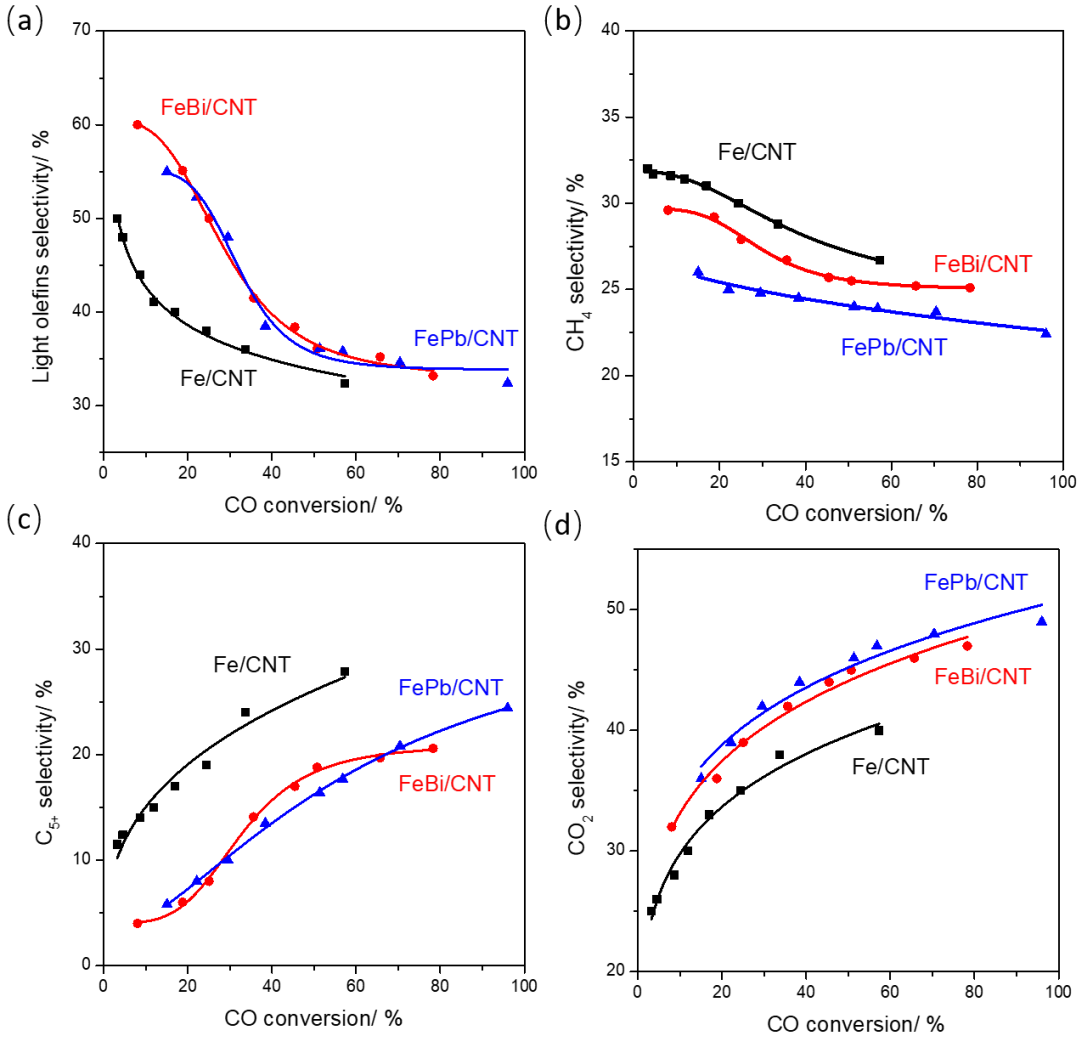

Figure 3.10. *Product selectivity versus CO conversion over CNT supported iron catalysts. Reaction conditions: W = 0.2 g, H_2/CO = 1, P = 10 bar, T = 350 °C, GHSV = 3.4-20.4 L $h^{-1}g^{-1}$.*

The observed selectivity phenomena also coincide with the gradual decrease in the chain growth probability (α) with the pressure decrease. The Anderson-Schulz-Flory distribution predicts maximum selectivity to the C_2-C_4 hydrocarbons of about 57 % at α value of 0.46. The pressure decrease from 10 to one bar leads to lower α, which is favorable for the selectivity to light hydrocarbons. Indeed, it has been shown [46-50] that higher total pressure and low H_2/CO ratio is favorable for synthesis of long chain

paraffinic hydrocarbon at the expense of light olefins. On the other hand, the Bi- and Pb- promoters seem to slow down secondary olefin hydrogenation and impose some restrictions on the FT chain growth probability. Indeed, the olefin to paraffin ratio in the products is much higher over the Bi- and Pb-promoted catalysts compared to the Fe/CNT and in particular at lower reaction pressure. Thus, use of the Bi- and Pb-promoters makes it possible to produce light olefins over iron catalysts with higher yield and selectivity under mild reaction conditions and in particular, at lower reaction pressures.

The products selectivities for the Bi and Pb promoted iron catalyst and Fe/CNT measured as a function of carbon monoxide conversion are summarized in Figure 3.10 The selectivity to light olefins typically decreases with increasing CO conversion for the three examined catalysts (Table 3.3, Figure 3.10). More importantly, the promoted iron catalysts showed higher selectivity of light olefins in the similar CO conversion compared with the Fe/CNT catalysts. The presence of promoters stabilizes selectivity to light olefins at 10 bar at high conversion. The selectivity is close to 35 % with suppression of the secondary transformation of olefins. This effect of the Bi and Pb promoters on the FT reaction selectivity is somewhat similar but more complex compared to that observed in the presence of alkali promoters [15, 19]. Indeed, the presence of alkali ions in iron catalysts leads to higher olefin to paraffin ratio in the FT reaction products. Note that the increase in the olefin to paraffin ratio over the catalysts promoted with alkali ions usually coincides with lower methane selectivity, higher selectivity to the long-chain hydrocarbons and an increase in the chain growth probability. Indeed, the Bi or Pb promoted catalysts exhibit lower selectivity to methane compared with Fe/CNT catalyst, this effect is also found in Na- [2, 25] and Mn- [22] promoted iron catalysts for light olefin synthesis. Different to the alkali promotion, however, the Bi and Pb-promoted catalysts exhibit lower selectivity to long chain hydrocarbons.

WGS is an important side reaction, which occurs during FT synthesis on iron catalysts. It yields water and CO_2, affects the H_2/CO ratio in the reactor and selectivity

to different reaction products. Figure 3.10d shows the CO_2 selectivity at different CO conversions. The selectivity of CO_2 over the promoted catalysts is higher than over the unprompted catalysts, which may be caused by the higher rate of WGS reaction. Carbon dioxide selectivity is also getting higher at higher carbon monoxide conversion. Water gas shift reaction ($CO + H_2O = CO_2 + H_2$) represents one of the possible reaction pathways for the CO_2 production in FT synthesis. Usually, the WGS reaction is expected to be more significant at higher CO conversion when water production is getting more important. Note however, that over the Bi and Pb-promoted iron catalysts, high carbon dioxide selectivity is observed even at very low CO conversion levels. This suggests that over promoted catalysts, carbon dioxide can be among the primary reaction products and is produced during the initial reaction steps [27].

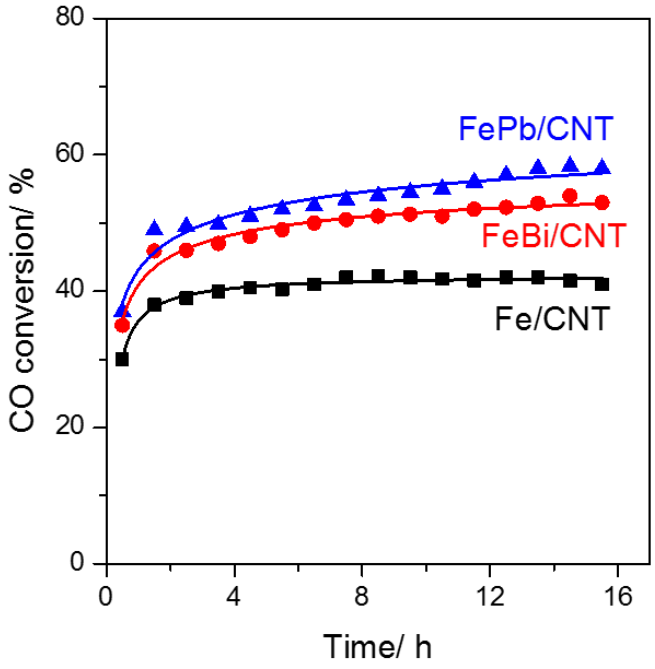

Figure 3.11. *CO conversion in Water-Gas Shift reaction over un-promoted and promoted iron catalysts. Reaction conditions: p = 1 bar, CO = 5 ml/min, N_2 = 30 ml/min, H_2O = 0.5 ml/h.*

The performance of iron catalysts in the WGS reaction was also evaluated in a fixed bed reactor. The effect of Bi and Pb promoters on CO conversion for WGS reaction with time-on-stream is shown in Figure 3.11. In the first 10 minutes, the CO conversion of Fe/CNT is 30 %, while the Bi and Pb promoted catalysts show higher CO conversion,

which are 35 % and 37 %, respectively. After 15 h time on stream, the CO conversion for Fe/CNT, FeBi/CNT and FePb/CNT are 40 %, 52 % and 59 %, respectively (Figure 3.11). This suggests that Bi and Pb improve the activity of iron catalysts in the WGS reaction. This effect was also found in alkali promoted iron catalysts [51].

3.2.4. Interaction of iron species with promoters and catalytic performance in FT synthesis

FT synthesis is a structure-sensitive reaction over metal and carbide catalysts. The catalytic activity and selectivity strongly depend on the catalyst structure and in particular on the metal or carbide particle size, especially in the nano-size range. For iron catalysts, previous reports [52] suggest the influence of particle size on the catalytic performance when the particle size is below 6 nm and negligible when the particle size is above 6 nm. XRD (Figure 3.1) and TEM (Figure 3.2) show that the particle sizes for the Fe/CNT and Bi or Pb promoted Fe/CNT catalysts were almost identical and in the range of 5.9~6.5 nm.

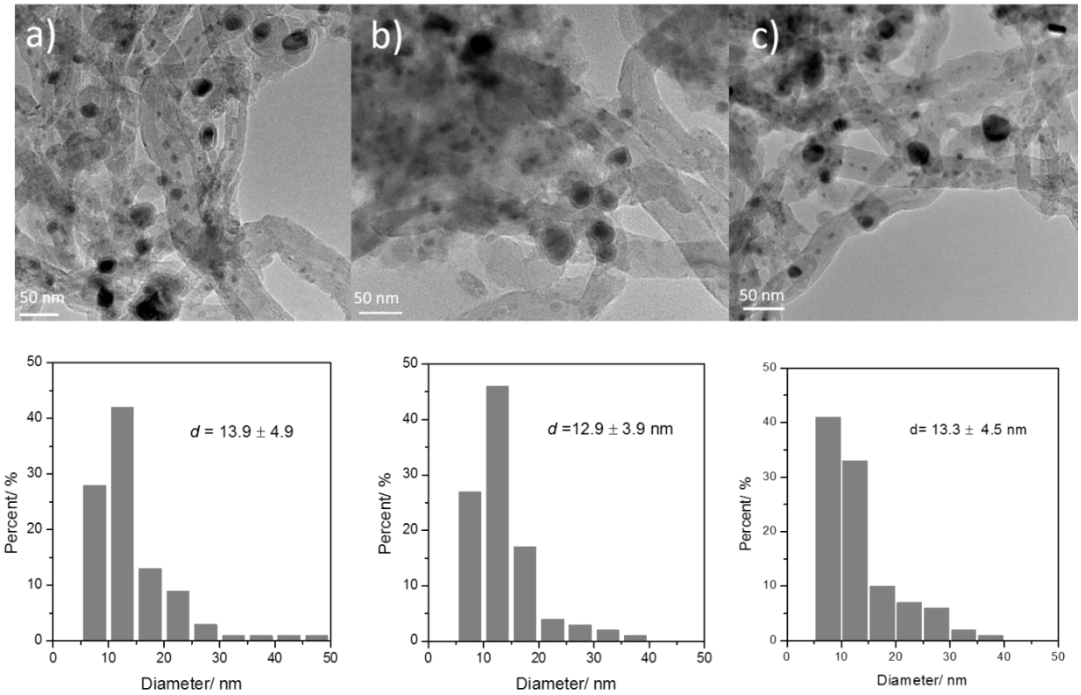

Figure 3.12. *TEM micrographs and particle size distributions for spent supported Fe catalysts after reaction: (a) Fe/CNT, (b) FeBi/CNT, (c) FePb/CNT.*

Figure 3.12 displays the TEM images and histograms of iron nanoparticles in the

catalysts after the FT reaction tests. The catalytic reaction results in some sintering of iron nanoparticles; Remarkably, while the size of iron carbide nanoparticle increases from 5-6 to 12-14 nm during the reaction, the nanoparticle diameter remains the same for the unpromoted and promoted iron catalysts. This suggests that the promoters do not affect to any significant extent the rate of iron sintering in these catalysts. Thus, variation of iron particle size with promotion is not the crucial factor for their much different catalytic performances.

The second important parameter can be iron reducibility/carbidization. Indeed, the TPR profile (Figure 3.3) indicate some enhancement in iron reducibility especially for FeO→Fe reduction step in the promoted catalysts. The in-situ magnetization measurements also suggest better iron carbidization in the promoted catalysts compared to the unpromoted counterpart. The magnetization data are also quantitatively consistent with the XPS (Figure 3.7) which showed some increase in the amount of iron carbide in the iron catalysts after the promotion.

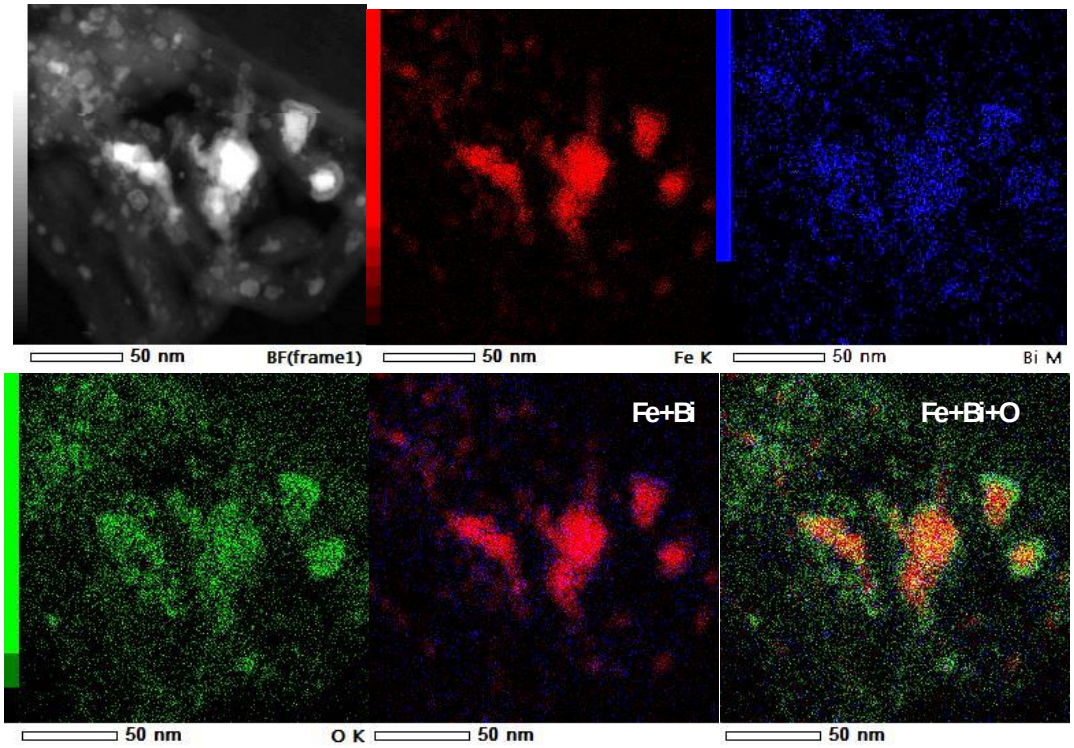

Figure 3.13. *STEM-HAADF image and EDX mapping of the activated FeBi/CNT catalyst (CO treatment for 10h at 350 °C)*

The STEM-HAADF (High Angle Annular Dark Field) images and EDX (Energy Dispersive X-ray Spectroscopy) mapping data have provided the in-depth information about the interaction between iron and Bi and Pb promoters. The observed strong effects on the catalytic performance of Fe catalysts might be therefore due to the intimate contact between Fe and promoter, which can be obtained because of their higher mobility. The Bi and Pb promoters have low melting temperature (Bi 271 ºC and Pb 327 ºC) and the migration could therefore occur at the reaction temperature (350 ºC). Figure 3.13 shows STEM-HAADF image and EDX mapping of the FeBi/CNT catalyst prepared by co-impregnation and activated in CO. Interestingly, in the activated catalyst, the Bi promoter is located in close proximity to iron.

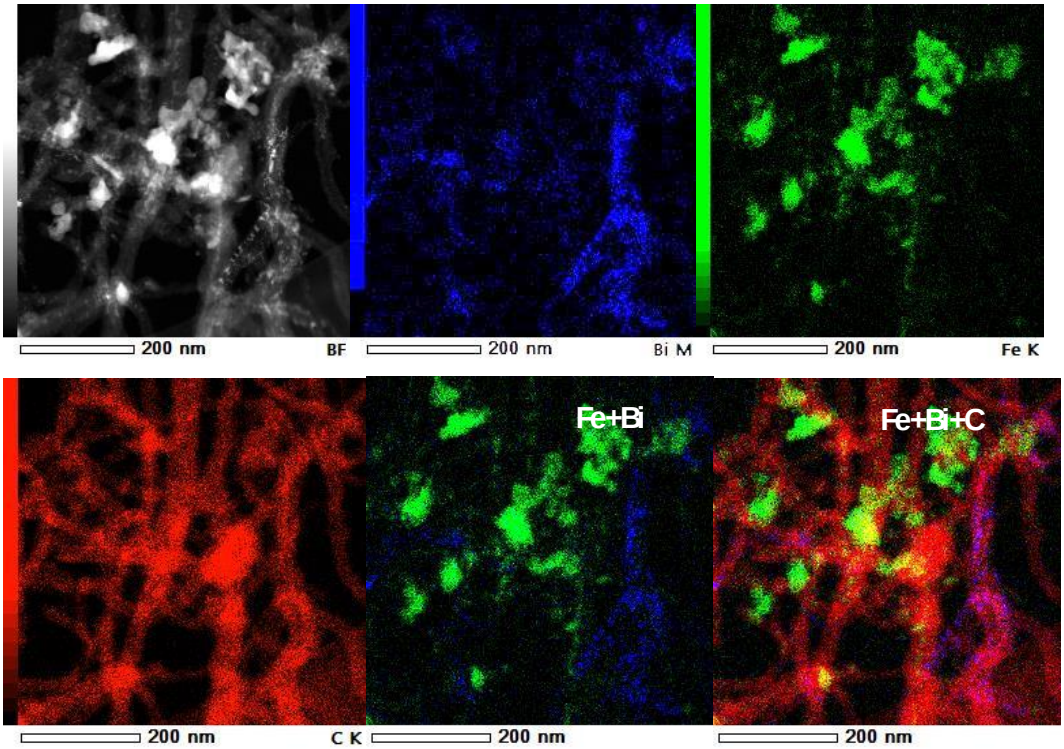

Figure 3.14. *STEM-HAADF image and EDX mapping of the mixed Fe/CNT+Bi/CNT catalyst calcined in nitrogen*

In order to provide further insights into the migration phenomena of the promoter, we prepared FeBi and FePb hybrid catalysts by mechanical mixing of Fe/CNT with Bi/CNT for 10 min in an agate mortar. The hybrid catalysts have the same Fe/Bi or Fe/Pb molar ratios as in the counterparts prepared by impregnation. Figure 3.14 shows

STEM-HAADF image and EDX mapping of the freshly mixed and calcined Fe/CNT +Bi/CNT catalysts. In the freshly calcined catalysts, the zones with higher Fe and Bi contents are clearly separately over the CNT support. Interestingly, Bi oxide species preferentially occupy the internal channels of CNT, while iron species are located both on the CNT outer surface and inside the CNT. Iron and bismuth distributions radically change after catalyst activation in carbon monoxide (Figure 3.15). The images of the activated samples clearly show that most of the Bi particles are present in the surface of the iron and form a shell of promoter over the iron carbide core. Similar localization of the promoters at the interface of iron carbide nanoparticles was also observed in the spent catalysts after the reaction (Figure 3.16). The particles inside the CNT tubes sinter to a lesser degree. This is consistent with previous works [45, 53, 54].

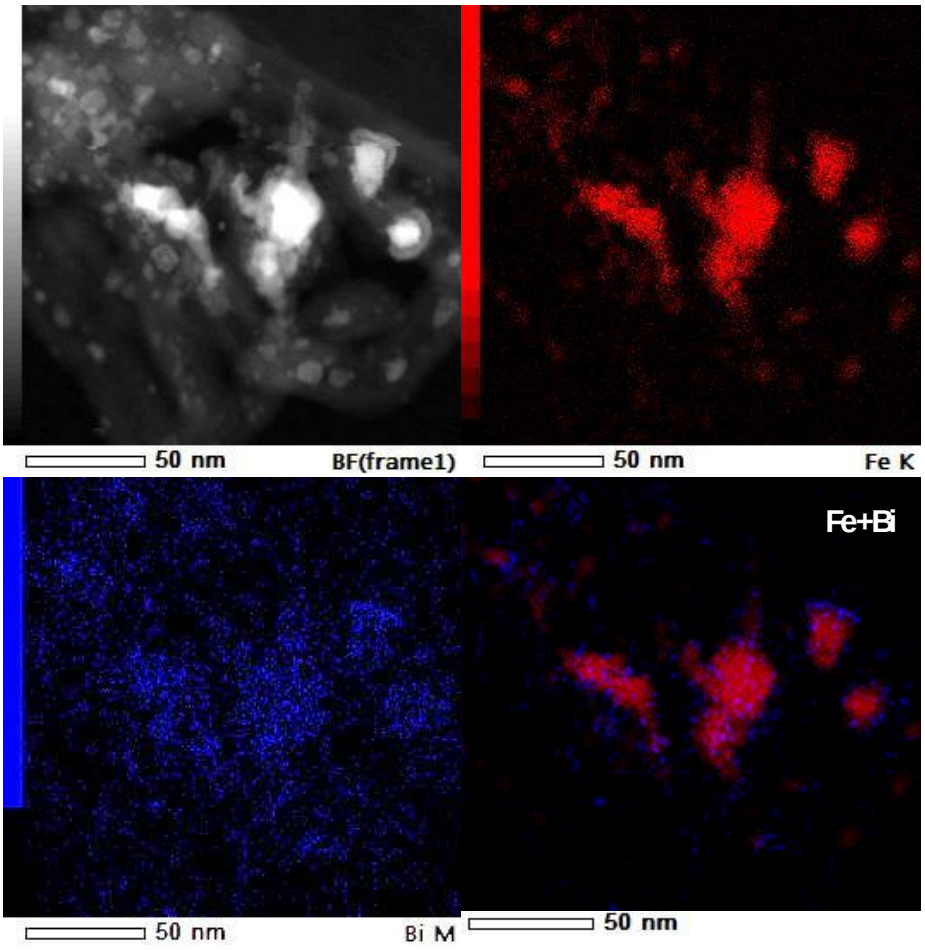

Figure 3.15. *STEM-HAADF image and EDX mapping of the activated mixed Fe/CNT+Bi/CNT catalyst after carbidization in CO*

The characterization data are consistent with the catalytic results. The mixed

catalysts also show high activity compared with the Fe/CNT catalysts (Table 3.3). Thus, we can conclude that Bi and Pb migrate to the surface of the iron during the reaction. This migration shows positive effect to the activity and selectivity.

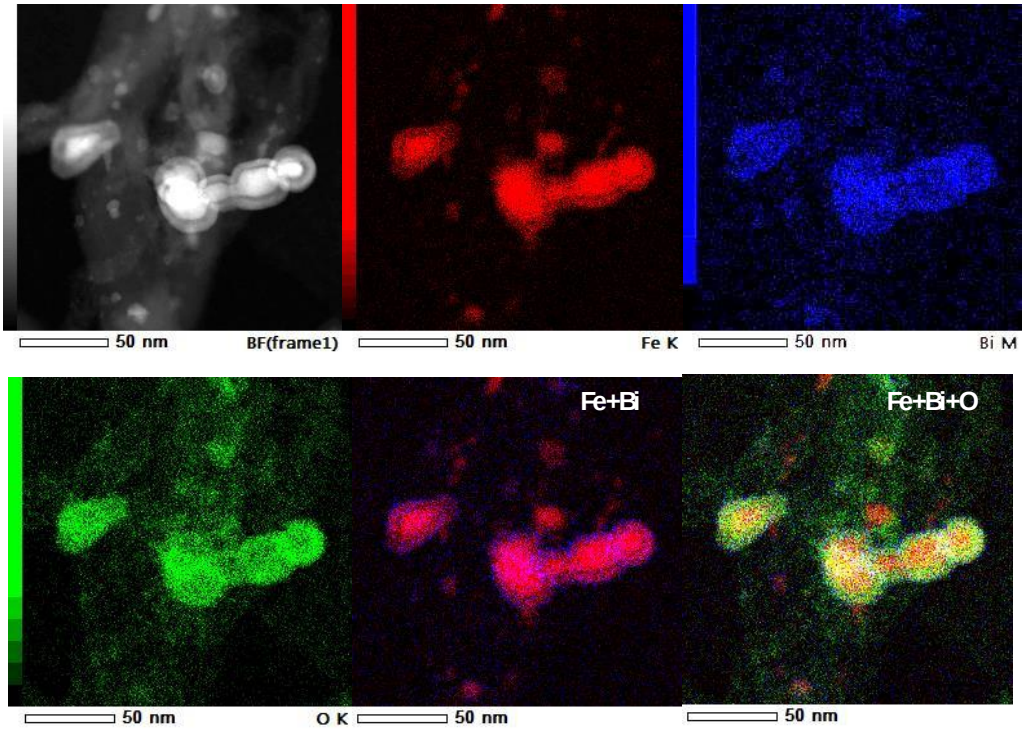

Figure 3.16. *STEM-HAADF image and EDX mapping of the spent mixed Fe/CNT+Bi/CNT catalyst (after the catalytic test)*

To summarize, the following phenomena due to the promotion can positively affect the reaction rate and selectivity over the iron catalysts supported by CNT. First, a close contact between iron and promoters seems to enhance iron carbidization in the promoted catalysts. This suggestion is consistent with the Mössbauer, in-situ magnetization and XPS data.

Second, the catalytic performance can be enhanced by facilitating CO dissociation on iron carbide via oxygen removal from iron carbide by scavenging with the promoters. Similar effects were previously observed over the silica supported iron catalysts. The promoting elements located at the interface to iron carbide nanoparticles showed very easy changes of the oxidation state from metal to the oxide one in the presence of syngas. These changes attributed to the migration of oxygen atoms during carbon monoxide dissociation can lead to the partial oxidation of promoters. The oxidized promoters can

be then reduced by carbon monoxide with release of carbon dioxide molecules. The suggestion about facilitating of carbon oxide dissociation in the presence of promoters with scavenging of oxygen atoms is consistent with higher WGS reaction rates observed over the promoted catalysts. High CO_2 selectivity observed over the Bi and Pb-promoted catalysts after extrapolation to zero conversion indicates that CO_2 could be a primary reaction product over these catalysts.

The third effect occurring on the promotion is relevant to simultaneous slowing down secondary hydrogenation of olefins, reducing chain growth probability and C_{5+} hydrocarbon selectivity. The promoted catalysts display lower chain growth probability and higher olefin to paraffin ratio compared to the Fe/CNT reference catalysts in particular at lower reaction pressure. This leads to less significant decrease in light olefin selectivity with higher conversion at higher reaction pressure and higher olefin selectivity observed at low reaction pressure in comparison with the unpromoted CNT supported iron catalyst.

3.3. Conclusion

New efficient Bi and Pb-promoted CNT supported iron catalysts for the syngas direct conversion to light olefins under mild reaction conditions were developed for light olefin synthesis from syngas. The promoted iron catalysts present higher FT reaction rate and higher selectivity to the C_2-C_4 olefins (55 %-65 %) under atmospheric pressure compared to the unpromoted counterpart. The promotion effect of Bi and Pb on iron carbide has been reinforced by their migration during the catalyst activation, which leads to their preferential localization at the interface with iron carbide nanoparticles.

The promotion effect of Bi and Pb on the catalytic performance of CNT supported iron catalysts can be tentatively attributed to three phenomena: enhancement of iron carbidization and reducibility, facilitation of carbon monoxide dissociation via scavenging of oxygen atoms by the promoters, slowing down secondary olefin hydrogenation and carbon chain growth.

3.4. Reference

[1] H.M.T. Galvis, J.H. Bitter, C.B. Khare, M. Ruitenbeek, A.I. Dugulan, K.P. de Jong, Supported iron nanoparticles as catalysts for sustainable production of lower olefins, Science, 335 (2012) 835-838.

[2] H.M.T. Galvis, A.C. Koeken, J.H. Bitter, T. Davidian, M. Ruitenbeek, A.I. Dugulan, K.P. de Jong, Effect of precursor on the catalytic performance of supported iron catalysts for the Fischer-Tropsch synthesis of lower olefins, Catalysis today, 215 (2013) 95-102.

[3] K. Cheng, B. Gu, X. Liu, J. Kang, Q. Zhang, Y. Wang, Direct and Highly Selective Conversion of Synthesis Gas into Lower Olefins: Design of a Bifunctional Catalyst Combining Methanol Synthesis and Carbon-Carbon Coupling, Angewandte Chemie, 128 (2016) 4803-4806.

[4] P. Tian, Y. Wei, M. Ye, Z. Liu, Methanol to Olefins (MTO): From Fundamentals to Commercialization, ACS Catalysis, 5 (2015) 1922-1938.

[5] S. Xu, A. Zheng, Y. Wei, J. Chen, J. Li, Y. Chu, M. Zhang, Q. Wang, Y. Zhou, J. Wang, F. Deng, Z. Liu, Direct Observation of Cyclic Carbenium Ions and Their Role in the Catalytic Cycle of the Methanol-to-Olefin Reaction over Chabazite Zeolites, Angewandte Chemie International Edition, 52 (2013) 11564-11568.

[6] F. Jiao, J. Li, X. Pan, J. Xiao, H. Li, H. Ma, M. Wei, Y. Pan, Z. Zhou, M. Li, Selective conversion of syngas to light olefins, Science, 351 (2016) 1065-1068.

[7] K.P. de Jong, Surprised by selectivity, Science, 351 (2016) 1030-1031.

[8] X. Chen, D. Deng, X. Pan, Y. Hu, X. Bao, N-doped graphene as an electron donor of iron catalysts for CO hydrogenation to light olefins, Chemical communications, 51 (2015) 217-220.

[9] M. Casavola, J. Hermannsdörfer, N. de Jonge, A.I. Dugulan, K.P. de Jong, Fabrication of Fischer-Tropsch Catalysts by Deposition of Iron Nanocrystals on Carbon Nanotubes, Advanced Functional Materials, 25 (2015) 5309-5319.

[10] M. Casavola, J. Xie, J.D. Meeldijk, N.A. Krans, A. Goryachev, J.P. Hofmann, A.I. Dugulan, K.P. de Jong, Promoted Iron Nanocrystals Obtained via Ligand Exchange as Active and Selective Catalysts for Synthesis Gas Conversion, ACS Catalysis, 7 (2017) 5121-5128.

[11] B. Gu, S. He, W. Zhou, J. Kang, K. Cheng, Q. Zhang, Y. Wang, Polyaniline-supported iron catalyst for selective synthesis of lower olefins from syngas, Journal of Energy Chemistry, 26 (2017) 608-615.

[12] E. de Smit, B.M. Weckhuysen, The renaissance of iron-based Fischer-Tropsch synthesis: on the multifaceted catalyst deactivation behaviour, Chemical Society Reviews, 37 (2008) 2758-2781.

[13] H.M. Torres Galvis, K.P. de Jong, Catalysts for production of lower olefins from synthesis gas: a review, ACS catalysis, 3 (2013) 2130-2149.

[14] H.M.T. Galvis, A.C. Koeken, J.H. Bitter, T. Davidian, M. Ruitenbeek, A.I. Dugulan, K.P. de Jong, Effects of sodium and sulfur on catalytic performance of supported iron catalysts for the Fischer-Tropsch synthesis of lower olefins, Journal of catalysis, 303 (2013) 22-30.

[15] X. Duan, D. Wang, G. Qian, J.C. Walmsley, A. Holmen, D. Chen, X. Zhou, Fabrication of K-promoted iron/carbon nanotubes composite catalysts for the Fischer-Tropsch synthesis of lower olefins, Journal of Energy Chemistry, 25 (2016) 311-317.

[16] F. Jiang, M. Zhang, B. Liu, Y. Xu, X. Liu, Insights into the influence of support and potassium or sulfur promoter on iron-based Fischer-Tropsch synthesis: understanding the control of catalytic activity, selectivity to lower olefins, and catalyst deactivation, Catalysis Science & Technology, 7 (2017) 1245-1265.

[17] Y. Yuan, S. Huang, H. Wang, Y. Wang, J. Wang, J. Lv, Z. Li, X. Ma, Monodisperse Nano-Fe3O4 on α-Al2O3 Catalysts for Fischer-Tropsch Synthesis to Lower Olefins: Promoter and Size Effects, ChemCatChem, 9 (2017) 3144-3152.

[18] K. Cheng, V.V. Ordomsky, B. Legras, M. Virginie, S. Paul, Y. Wang, A.Y. Khodakov, Sodium-promoted iron catalysts prepared on different supports for high temperature Fischer-Tropsch synthesis, Applied Catalysis A: General, 502 (2015) 204-214.

[19] Z. Li, L. Zhong, F. Yu, Y. An, Y. Dai, Y. Yang, T. Lin, S. Li, H. Wang, P. Gao, Y. Sun, M. He, Effects of Sodium on the Catalytic Performance of CoMn Catalysts for Fischer-Tropsch to Olefin Reactions, ACS Catalysis, 7 (2017) 3622-3631.

[20] P. Zhai, C. Xu, R. Gao, X. Liu, M. Li, W. Li, X. Fu, C. Jia, J. Xie, M. Zhao, Highly Tunable Selectivity for Syngas-Derived Alkenes over Zinc and Sodium-Modulated Fe5C2 Catalyst, Angewandte Chemie International Edition, 55 (2016) 9902-9907.

[21] H. Wan, B. Wu, C. Zhang, H. Xiang, Y. Li, Promotional effects of Cu and K on precipitated iron-based catalysts for Fischer-Tropsch synthesis, Journal of Molecular Catalysis A: Chemical, 283 (2008) 33-42.

[22] Y. Liu, J.-F. Chen, J. Bao, Y. Zhang, Manganese-Modified Fe_3O_4 Microsphere Catalyst with Effective Active Phase of Forming Light Olefins from Syngas, ACS Catalysis, 5 (2015) 3905-3909.

[23] N. Lohitharn, J.G. Goodwin Jr, Effect of K promotion of Fe and FeMn Fischer-Tropsch synthesis catalysts: Analysis at the site level using SSITKA, Journal of Catalysis, 260 (2008) 7-16.

[24] N. Lohitharn, J.G. Goodwin Jr, An investigation using SSITKA of chain growth on Fe and FeMnK Fischer-Tropsch synthesis catalysts, Catalysis Communications, 10 (2009) 758-762.

[25] P. Munnik, P.E. de Jongh, K.P. de Jong, Recent developments in the synthesis of supported catalysts, Chemical reviews, 115 (2015) 6687-6718.

[26] A.C. Koeken, T. Galvis, M. Hirsa, T. Davidian, M. Ruitenbeek, K.P. De Jong, Suppression of Carbon Deposition in the Iron-Catalyzed Production of Lower Olefins from Synthesis Gas, Angewandte Chemie International Edition, 51 (2012) 7190-7193.

[27] V.V. Ordomsky, Y. Luo, B. Gu, A. Carvalho, P.A. Chernavskii, K. Cheng, A.Y. Khodakov, Soldering of Iron Catalysts for Direct Synthesis of Light Olefins from Syngas under Mild Reaction Conditions, ACS Catalysis, 7 (2017) 6445-6452.

[28] G. Connell, J.A. Dumesic, Migration of potassium on iron and alumina surfaces as studied by Auger electron spectroscopy, Journal of Catalysis, 92 (1985) 17-24.

[29] A.N. Pour, Y. Zamani, A. Tavasoli, S.M. Kamali Shahri, S.A. Taheri, Study on products distribution of iron and iron-zeolite catalysts in Fischer-Tropsch synthesis, Fuel, 87 (2008) 2004-2012.

[30] T. Li, Y. Yang, C. Zhang, X. An, H. Wan, Z. Tao, H. Xiang, Y. Li, F. Yi, B. Xu, Effect of manganese on an iron-based Fischer-Tropsch synthesis catalyst prepared from ferrous sulfate, Fuel, 86 (2007) 921-928.

[31] A. Nakhaei Pour, S.M.K. Shahri, Y. Zamani, M. Irani, S. Tehrani, Deactivation studies of bifunctional Fe-HZSM5 catalyst in Fischer-Tropsch process, Journal of Natural Gas Chemistry, 17 (2008) 242-248.

[32] X. Pan, Z. Fan, W. Chen, Y. Ding, H. Luo, X. Bao, Enhanced ethanol production inside carbon-nanotube reactors containing catalytic particles, Nature materials, 6 (2007) 507-511.

[33] J.-D. Xu, K.-T. Zhu, X.-F. Weng, W.-Z. Weng, C.-J. Huang, H.-L. Wan, Carbon nanotube-supported Fe-Mn nanoparticles: A model catalyst for direct conversion of syngas to lower olefins, Catalysis today, 215 (2013) 86-94.

[34] J. Lu, L. Yang, B. Xu, Q. Wu, D. Zhang, S. Yuan, Y. Zhai, X. Wang, Y. Fan, Z. Hu, Promotion Effects of Nitrogen Doping into Carbon Nanotubes on Supported Iron Fischer-Tropsch Catalysts for Lower Olefins, ACS Catalysis, 4 (2014) 613-621.

[35] R.M. Malek Abbaslou, J. Soltan, A.K. Dalai, Iron catalyst supported on carbon nanotubes for Fischer-Tropsch synthesis: Effects of Mo promotion, Fuel, 90 (2011) 1139-1144.

[36] R.M.M. Abbaslou, A. Tavassoli, J. Soltan, A.K. Dalai, Iron catalysts supported on carbon nanotubes for Fischer-Tropsch synthesis: Effect of catalytic site position, Applied Catalysis A: General, 367 (2009) 47-52.

[37] K. Mai, T. Elder, L.H. Groom, J.J. Spivey, Fe-based Fischer Tropsch synthesis of biomass-derived syngas: effect of synthesis method, Catalysis Communications, 65 (2015) 76-80.

[38] V. Subramanian, V.V. Ordomsky, B. Legras, K. Cheng, C. Cordier, P.A. Chernavskii, A.Y. Khodakov, Design of iron catalysts supported on carbon-silica composites with enhanced catalytic performance in high-temperature Fischer-Tropsch synthesis, Catalysis Science & Technology, (2016).

[39] G. Yu, B. Sun, Y. Pei, S. Xie, S. Yan, M. Qiao, K. Fan, X. Zhang, B. Zong, Fe_xO_y@ C spheres as an excellent catalyst for Fischer-Tropsch synthesis, Journal of the American Chemical Society, 132 (2009) 935-937.

[40] C.P. Hunt, B.M. Moskowitz, S.K. Banerjee, Magnetic properties of rocks and minerals, Rock physics & phase relations: a handbook of physical constants, 3 (1995) 189-204.

[41] M.D. Shroff, D.S. Kalakkad, K.E. Coulter, S.D. Kohler, M.S. Harrington, N.B. Jackson, A.G. Sault, A.K. Datye, Activation of Precipitated Iron Fischer-Tropsch Synthesis Catalysts, Journal of Catalysis, 156 (1995) 185-207.

[42] C. Yang, H. Zhao, Y. Hou, D. Ma, Fe5C2 Nanoparticles: A Facile Bromide-Induced Synthesis and as an Active Phase for Fischer-Tropsch Synthesis, Journal of the American Chemical Society,

134 (2012) 15814-15821.

[43] C. Wang, C. Shao, Y. Liu, L. Zhang, Photocatalytic properties BiOCl and Bi_2O_3 nanofibers prepared by electrospinning, Scripta Materialia, 59 (2008) 332-335.

[44] C. Chang, L. Zhu, Y. Fu, X. Chu, Highly active Bi/BiOI composite synthesized by one-step reaction and its capacity to degrade bisphenol A under simulated solar light irradiation, Chemical engineering journal, 233 (2013) 305-314.

[45] J. Xiao, X. Pan, S. Guo, P. Ren, X. Bao, Toward fundamentals of confined catalysis in carbon nanotubes, Journal of the American Chemical Society, 137 (2014) 477-482.

[46] G.P. Van Der Laan, A. Beenackers, Kinetics and selectivity of the Fischer-Tropsch synthesis: a literature review, Catalysis Reviews, 41 (1999) 255-318.

[47] R.A. Dictor, A.T. Bell, Fischer-Tropsch synthesis over reduced and unreduced iron oxide catalysts, Journal of Catalysis, 97 (1986) 121-136.

[48] B.H. Davis, Fischer-Tropsch synthesis: relationship between iron catalyst composition and process variables, Catalysis Today, 84 (2003) 83-98.

[49] M.E. Dry, The Fischer-Tropsch process-commercial aspects, Catalysis today, 6 (1990) 183-206.

[50] M.E. Dry, Practical and theoretical aspects of the catalytic Fischer-Tropsch process, Applied Catalysis A: General, 138 (1996) 319-344.

[51] W. Ngantsoue-Hoc, Y. Zhang, R.J. O'Brien, M. Luo, B.H. Davis, Fischer-Tropsch synthesis: activity and selectivity for Group I alkali promoted iron-based catalysts, Applied Catalysis A: General, 236 (2002) 77-89.

[52] J.-Y. Park, Y.-J. Lee, P.K. Khanna, K.-W. Jun, J.W. Bae, Y.H. Kim, Alumina-supported iron oxide nanoparticles as Fischer-Tropsch catalysts: Effect of particle size of iron oxide, Journal of Molecular Catalysis A: Chemical, 323 (2010) 84-90.

[53] W. Chen, Z. Fan, X. Pan, X. Bao, Effect of confinement in carbon nanotubes on the activity of Fischer− Tropsch iron catalyst, Journal of the American Chemical Society, 130 (2008) 9414-9419.

[54] Z. Yang, X. Pan, J. Wang, X. Bao, FeN particles confined inside CNT for light olefin synthesis from syngas: Effects of Mn and K additives, Catalysis today, 186 (2012) 121-127.

Chapter 4. Synergy of Nanoconfinement and Promotion in the Design of Efficient Supported Iron Catalysts for Direct Olefin Synthesis from Syngas

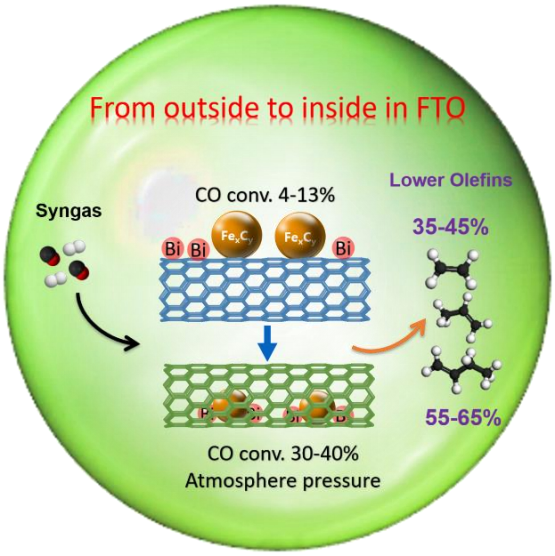

Abstract: Light olefins are important building blocks in chemical industry. High temperature Fischer-Tropsch synthesis provides a remarkable opportunity for direct synthesis of light olefins from syngas derived from a wide range of alternative feedstocks (biomass, organic or plastic wastes, natural gas, shale gas or coal). The present work focuses on the combined synergetic effects of the iron nanoconfinement and promotion with bismuth and lead on the structure and catalytic performance of iron catalysts supported by carbon nanotubes in high temperature Fischer-Tropsch synthesis. Iron nanoconfinement inside carbon nanotubes combined with the promotion with Bi or Pb result a 10 times higher yield of light olefins. The iron time yield reaches as high as $23.4*10^{-4}$ $mol_{CO}g_{Fe}^{-1}s^{-1}$ for the FePb/CNT-in catalysts, which is one of the best results for the iron-based Fischer-Tropsch synthesis catalysts in the literature. Nanoconfinement in carbon nanotubes mostly leads to better iron dispersion and stability, while intrinsic activity is only slightly affected. Promotion with Bi and Pd results in a major increase in the site intrinsic activity in both confined and non-confined catalysts. Moreover, over the optimised promoted and confined catalysts, Fischer-Tropsch synthesis occurs even under atmospheric pressure with high conversion and enhanced selectivity to light olefins.

This chapter is based on the following publication:

Bang Gu, Shun He, Deizi V. Peron, Debora R. Strossi Pedrolo, Simona Moldovan, Mauro C. Ribeiro, Bruno Lobato, Petr A. Chernavskii, Vitaly V. Ordomsky* and Andrei Y. Khodakov*, *Journal of Catalysis*, 376 (**2019**) 1-16.

4.1. Introduction

Optimization of the catalytic performance of iron catalysts in FT synthesis can be addressed by catalyst promotion [1]. Most commonly, the promoters of iron FT catalysts are divided into two classes. The structural promoters affect formation and stability of the catalysts and its active phase, while electronic promoters modify the local electronic structure of active metals mostly by adding or withdrawing electron density. The electronic promoters also directly affect adsorption/desorption and elementary reaction steps. Alkali ions are most common promoters of iron FT catalysts. They have a noticeable effect on both the activity and selectivity of iron catalysts [2]. Other promoters and/or supports (e.g. CuO, Al_2O_3 and SiO_2) mainly facilitate iron reduction, stabilize a high metal surface area or improve the catalyst mechanical properties. Combined promotion of iron catalysts with sodium and sulphur was shown [3, 4] to improve the selectivity to light olefins. Higher olefin selectivity was observed over those catalysts at low conversions and coincided the decrease in the overall catalytic activity. Recently our group has found [5, 6] extremely strong promoting effects of soldering metals such as Bi and Pb on the catalytic performance of supported iron catalysts. The promoting effects of Bi and Pb on iron catalysts have been reinforced by their migration during the catalyst activation and their preferential localization at the surface of iron carbide nanoparticles leading to the core-shell structures.

In addition to the promotion, nanoconfinement of active phase into porous matrix has been also an efficient way to improve the activity and selectivity of the Fe [7-10], Co [11], Ni [12], Ru [13] and Rh [14] catalysts for CO hydrogenation. The nanoconfinement may potentially bring different benefits for the catalytic performance of iron catalysts such as better reducibility and carbidization, higher metal dispersion, electronic effects, better stability and shape selectivity effect on the intermediates and reaction products.

The nanoconfinement of iron nanoparticles can be achieved in mesoporous oxides, mesoporous zeolites and porous carbon materials. Metal nanoparticle nanoconfinement

within carbon nanotubes (CNT) [15] has been particularly remarkable. Bao [16-20] et al found that iron species located inside the CNT tubes had better reducibility and facilitated formation of active iron carbide phase compared to iron located outside the CNT channels. The resulting catalysts showed enhanced activity in low temperature FT synthesis and favoured formation of the C_{5+} hydrocarbons. The same group investigated [18, 20] the catalytic performance of the CNT confined Fe and FeN catalysts in direct olefin synthesis from syngas. The obtained hydrocarbon distributions were, however, similar over the confined and non-confined catalysts with the selectivity to light olefins of around 30-40 %.

Our present work focuses on the synergetic effects, which arise from the combination of the nanoconfinement of iron nanoparticles in CNT and their promotion with Bi and Pb on the structure, catalytic performance and stability of iron catalysts in high temperature FT synthesis. Combination of nanoconfinement and promotion effects results in the extremely high catalytic activity of iron catalysts even at atmospheric pressure with enhanced selectivity to light olefins. The catalysts have been characterized by a large combination of techniques: XRD, XPS, *in-situ* XANES, TEM-EDX, H_2-TPR, CO-TPR, *in-situ* magnetization measurements, ICP, BET. The characterization data are discussed alongside with the catalytic results in high temperature FT synthesis obtained in a fixed bed reactor under a wide range of operating conditions.

4.2. Results and Discussion

4.2.1 Catalyst characterization

4.2.1.1 Structure and morphology

The ICP elemental analysis data are displayed in Table 4.1. Both catalysts with non-confined and confined iron nanoparticles have similar iron content (around 10 wt. %), while the Bi and Pb contents were close to 0.8 wt. % in the promoted catalysts. The ICP results are therefore similar to the catalyst inventory composition. Table 4.1 also shows textural properties of the CNTs support and iron catalysts containing iron nanoparticles

located either outside or inside the CNTs tubes. As expected, the CNTs with closed tubes exhibit lower surface area compared with CNTs with open tubes. The impregnation of CNTs with iron and promoters decreases both the surface area and pore volume (Table 4.1). Interestingly, iron impregnation produces only a very small impact on the pore volume of CNT with closed tubes (from 0.54 cm^3/g to 0.52 cm^3/g). However, when the iron located inside the CNTs tubes, the pore volume decreases very significantly (from 0.83 cm^3/g to 0.50 cm^3/g). This is consistent with the iron nanoparticle localization inside the CNT tubes and partial blocking of the pore volume by iron species introduced via impregnation.

Table 4.1. *Physical properties of supports and supported Fe catalysts.*

Sample	S_{BET}[a] (m^2/g)	V_{tot}[b] (cm^3/g)	D_{meso}[c] (nm)	D_{metal}[d] (nm)	D_{metal}[e] (nm)	Total H_2 consumption[f] (mmol/g)	Fe content[g] (wt%)	Bi or Pb content[g] (wt%)
CNT-close	153.3	0.54	15.4	-	-	-	-	-
Fe/CNT-out	141.4	0.52	14.7	10.2	9.3	1.5	10.2	-
FeBi/CNT-out	134.7	0.52	15.3	9.6	8.9	1.7	10.4	0.84
FePb/CNT-out	128.3	0.52	16.3	10.3	9.5	1.6	10.6	0.82
CNT-open	230.3	0.83	14.4	-	-	-	-	-
Fe/CNT-in	192.9	0.52	10.8	5.3	4.9	1.6	10.3	-
FeBi/CNT-in	183.3	0.52	11.3	5.6	5.1	2.1	10.5	0.83
FePb/CNT-in	187.8	0.50	10.2	5.8	5.3	1.9	10.9	0.85

[a] BET surface area.
[b] Single point desorption total pore volume of pores, P/P_0=0.975.
[c] The pore diameter in the mesoporous region evaluated by the BJH method.
[d] Average particle size of iron oxide by XRD.
[e] Average particle size of iron oxide by TEM.
[f] The total H_2 consumption from TPR analysis.
[g] The Fe, Bi and Pb content from ICP-OES.

Figure 4.1a displays XRD profiles of the supported iron catalysts. The diffraction lines at 26.3° and 43.8° are attributed to the (002) and (101) reflections of the CNT supports. The peaks at 2θ of 35.6° are assignable to the hematite phase (Fe_2O_3, JCPDS

13-0534), while the peaks at 2θ of 35.8°,43.5° and 53.9° can be attributed to the magnetite phase (Fe_3O_4, JCPDS 75-0449). It is clear that the width of iron oxide XRD peaks for the catalysts containing iron nanoparticles outside the CNT tubes is smaller than for their counterparts with confined iron nanoparticles. This is indicative of the larger size of iron oxide nanoparticles located outside the CNT. These results are consistent with previous reports [16, 21]. Indeed, iron nanoconfinement inside CNT reduces the size of iron oxide nanoparticles possibly because of steric contains for iron nanoparticle growth. The XRD results also suggest that the Bi or Pb promotion does not noticeably affect the iron oxide phase composition and dispersion in the catalysts containing iron oxide nanoparticles outside or confined within CNT.

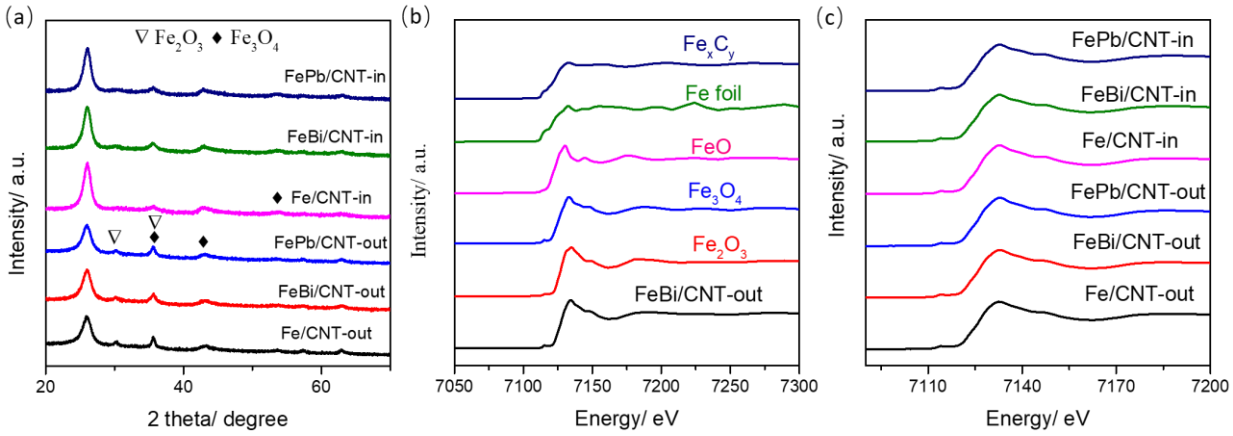

Figure 4.1. *Structural characterization of the catalysts. (a) XRD profiles of the confined and un-confined iron-based catalysts, (b) and (c) Normalized XAS of Fe L-edge of reference and iron-based catalysts.*

X-ray absorption near edge structure (XANES) of the calcined non-confined and CNT confined iron-based catalysts at iron K-absorption edge has provided information about iron coordination and iron oxidation state [22] (Figure 4.1c). Bulk FeO, Fe_2O_3, Fe_3O_4 and Fe foil have been used as references (Figure 4.1b). All iron oxides (except for FeO) show a pre-edge feature at 7.113 keV. This pre-edge feature is assigned to the *1s* → *3d* electron transition [23]. The six examined CNT supported iron-based catalysts show almost identical shape of the K-edge (Figure 4.1c**)**. The shape of the K-edge indicates coexistence of Fe_2O_3 and Fe_3O_4 in the catalysts pretreated in nitrogen. The fractions of Fe_2O_3 and Fe_3O_4 calculated from a XANES interpolation procedure

(ATHENA software) using the spectra of reference iron oxides are shown in Table 4.2. A slightly higher concentration of Fe_3O_4 was observed when iron nanoparticles are encapsulated inside carbon nanotubes in FeBi/CNT-in.

Table 4.2. *Iron and bismuth phase evolution of the fresh catalysts, activated catalysts and used catalysts by in-situ XANES (CO activation at 350 °C for 90 min, reaction in syngas at 350 °C for 90 min)*

Catalysts	Fresh (%)		CO activation (%)			Reaction in syngas (%)		
Fe XANES								
	Fe_2O_3	Fe_3O_4	Fe_2O_3	Fe_3O_4	Fe_xC_y	Fe_2O_3	Fe_3O_4	Fe_xC_y
Fe/CNT-out	48.4	51.6	10.3	22.3	67.4	5.2	19.7	75.1
FeBi/CNT-out	45.1	54.9	0	14.4	85.6	0	8.7	91.3
FeBi/CNT-in	38.6	61.4	0	0	100	0.1	0.2	99.7
Bi XANES								
	Bi_2O_3		Bi_2O_3		Bi	Bi_2O_3		Bi
FeBi/CNT-out	100		0		100	0.9		99.1
FeBi/CNT-in	100		0		100	1.1		98.9

Figure 4.2 shows the TEM micrographs of the fresh non-confined and confined iron CNT supported catalysts. The TEM images for iron Fe/AC catalyst supported on active carbon are also given for comparison (Figure 4.3a). The Fe/AC catalyst presents iron oxide particles with the average size of 12 nm. The TEM images confirm successful introduction of iron nanoparticles inside the CNTs tubes. Indeed, about 80 % of iron particles are located within the inner pores of the CNTs. This can be attributed to the tubular morphology of CNTs, which can induce capillary forces for iron nitrate during the impregnation process [24]. The iron oxide particles located outside CNT tubes in Fe/CNT-out, FeBi/CNT-out, FePb/CNT-out exhibit a broad particle size distribution of 4-14 nm with the average size of 9 nm (Table 4.1, Figure 4.2). On the contrary, the size distributions of iron oxide nanoparticles located inside the CNTs tubes in the Fe/CNT-

in, FeBi/CNT-in and FePb/CNT-in catalysts are very narrow with the average particles size of ~ 5 nm (Figure 4.2). Importantly, iron nanoconfinement inside CNT reduces iron oxide particle size. Smaller iron particle size inside CNT can be caused by their spatial nanoconfinement in CNTs and this phenomenon has been previously observed over the Fe [25] and Co [26] metals. Moreover, the size of iron oxide particle is close to the inner diameter of CNT (5-14 nm). The growth of iron oxide nanoparticles during decomposition of iron nitrate seems to be limited by the inner CNT walls. Furthermore, the Bi and Pb promoters do not affect the iron oxide morphology. The iron oxide particle size distribution is similar in iron monometallic and promoted catalysts. These results are in agreement with the XRD results.

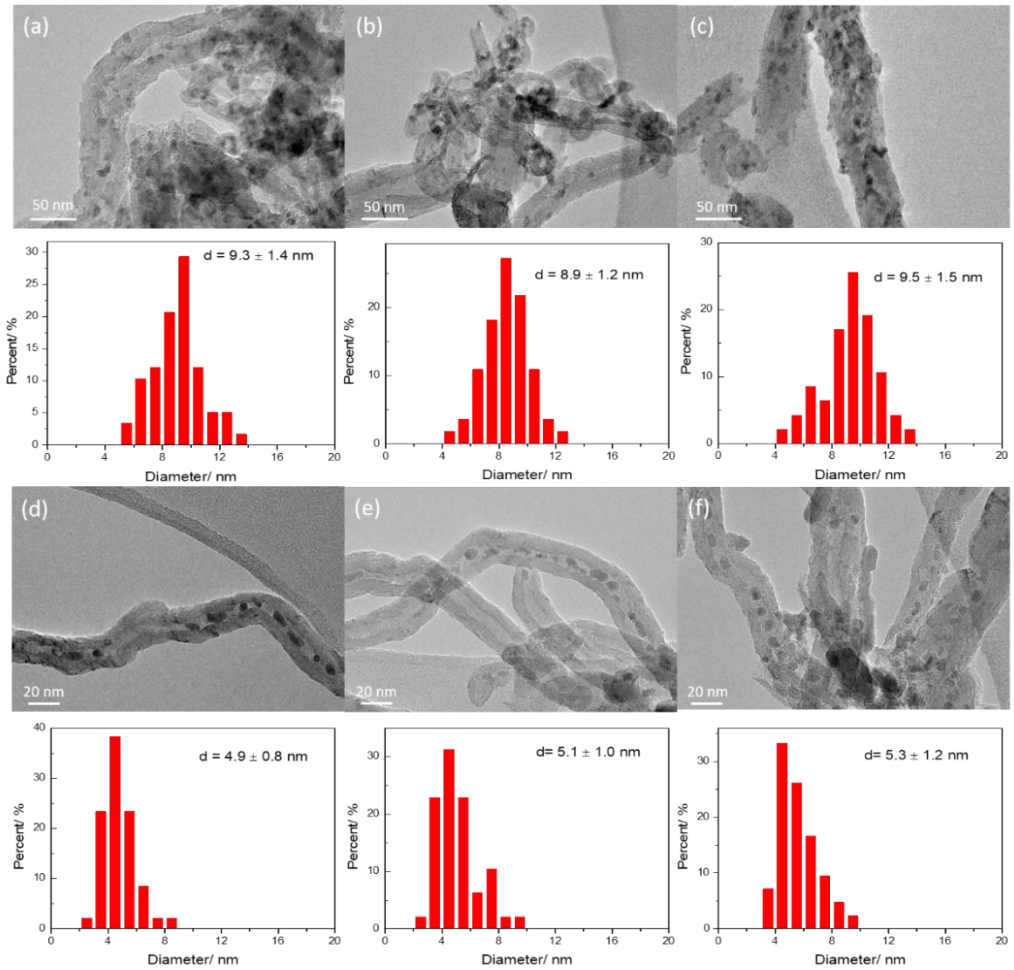

Figure 4.2. *TEM micrographs and particle size distribution for fresh confined and un-confined Fe catalysts after reaction: (a) Fe/CNT-out, (b) FeBi/CNT-out, (c) FePb/CNT-out, (d) Fe/CNT-in, (e) FeBi/CNT-in, (e) FePb/CNT-in.*

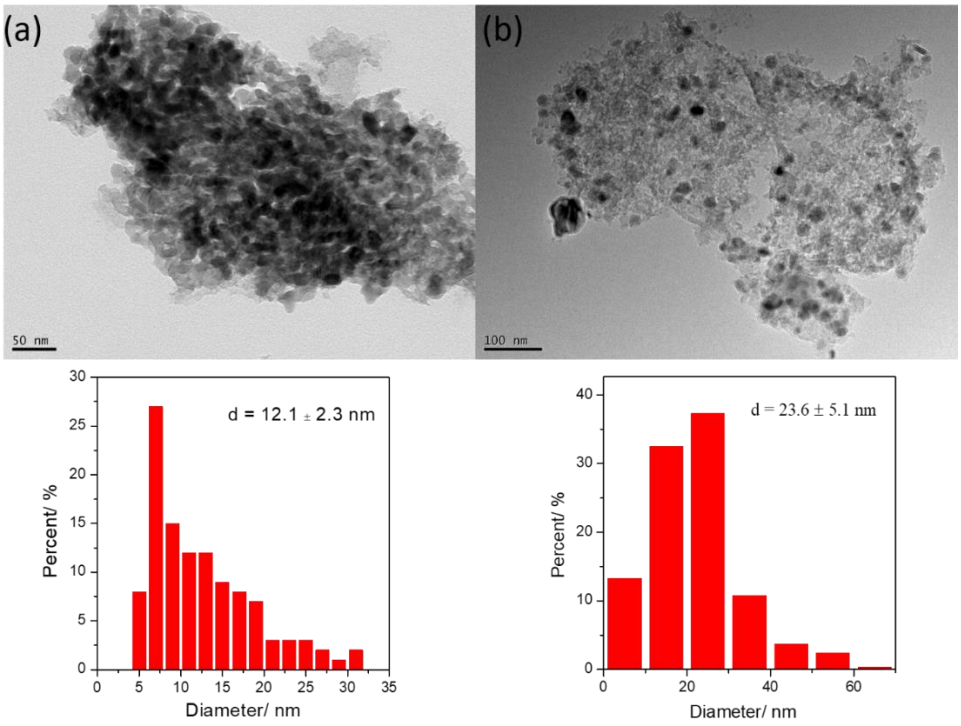

Figure 4.3. *TEM micrographs and particle distribution for active carbon supported iron catalysts after: (a) fresh, (b) after reaction.*

4.2.1.2 Iron reducibility and carbidization

Good iron reducibility and carbidization are essential for obtaining high activity of iron catalysts in FT synthesis. First, we examined reducibility and carbidization of iron oxide species in the confined and non-confined catalysts by H_2-TPR and CO-TPR (Figure 4.4)**.** All H_2-TPR profiles (Figure 4.4a**)** display three main well-separated reduction peaks, which are attributed to the multi-step iron reduction from Fe_2O_3 hematite to metallic iron [5]. In agreement with the literature [10, 27, 28], the first peak at 250-420 ºC can be ascribed to the reduction of Fe_2O_3 to Fe_3O_4, the second peak can be assigned to the reduction of Fe_3O_4 to FeO, whereas the third peak at 600-700 ºC can be attributed to the reduction of FeO to metallic Fe. Figure 4a shows that each reduction step occurs at lower temperatures in confined Fe/CNT-in in comparison with non-confined Fe/CNT-out. This suggests that nanoconfinement facilitates iron reduction. Interestingly, the promotion with Bi and Pb does not affect the positions of TPR peaks in the non-confined catalysts. The only difference is some increase in the total H_2

consumption (Table 4.1) over the promoted non-confined catalysts relative to Fe/CNT-out. In the confined Fe/CNT-in catalysts however, the promotion with Bi and Pb results in the 30 °C shift of the reduction peaks to lower temperatures. Some increase in the H_2 consumption was also observed in FeBi/CNT-in and FePb/CNT-in (Table 4.1).

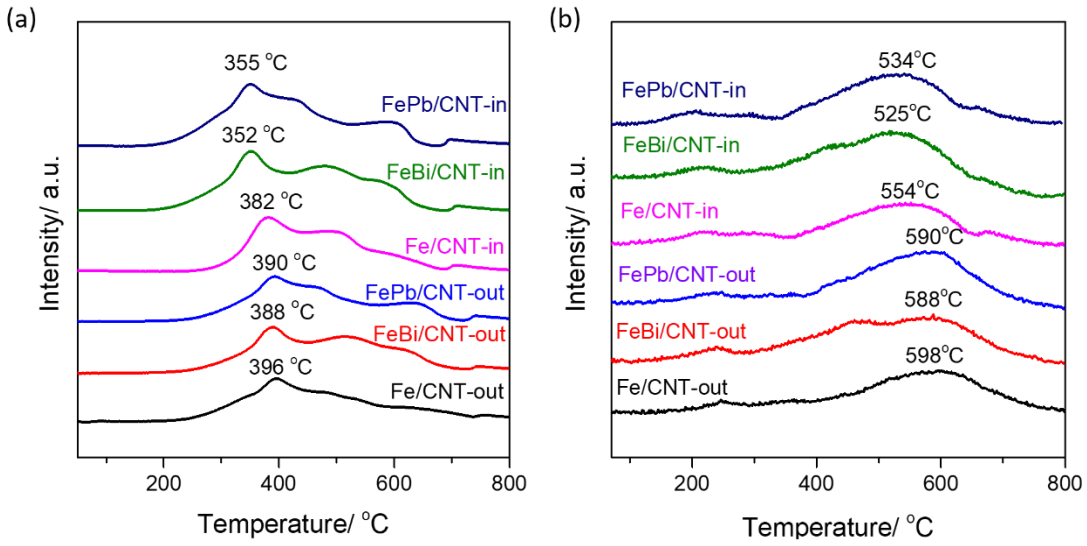

Figure 4.4. *TPR profiles of the confined and un-confined iron-based catalysts. (a) H_2-TPR, (b) CO-TPR.*

The CO-TPR profiles are shown in Figure 4.4b**.** All the catalysts exhibit two broad peaks. Previously it was shown [29-32] that carbidization of hematite proceeds via intermediate formation of magnetite according to the schema: $Fe_2O_3 \rightarrow Fe_3O_4 \rightarrow Fe_xC$. Similar to the H_2-TPR profiles, the CO-TPR peaks of the confined Fe/CNT-in catalysts shift to lower temperatures relative to the non-confined Fe/CNT-out counterparts. The effect of the promotion with Bi and Pb on the CO-TPR profiles can be only seen for the confined iron catalysts. The peaks in CO-TPR for the FeBi/CNT-in and FePb/CNT-in shift to lower temperatures compared to the unpromoted Fe/CNT-in. Thus, the confined iron nanoparticles exhibit higher reducibility and carbidization than the non-confined counterparts. In addition, the Bi and Pb promoters in the catalysts containing iron nanoparticles inside the CNT tubes decrease activation energy. Reduction/carbidization processes occur at significantly lower temperatures and the extent of iron reduction and of carbidization is improved.

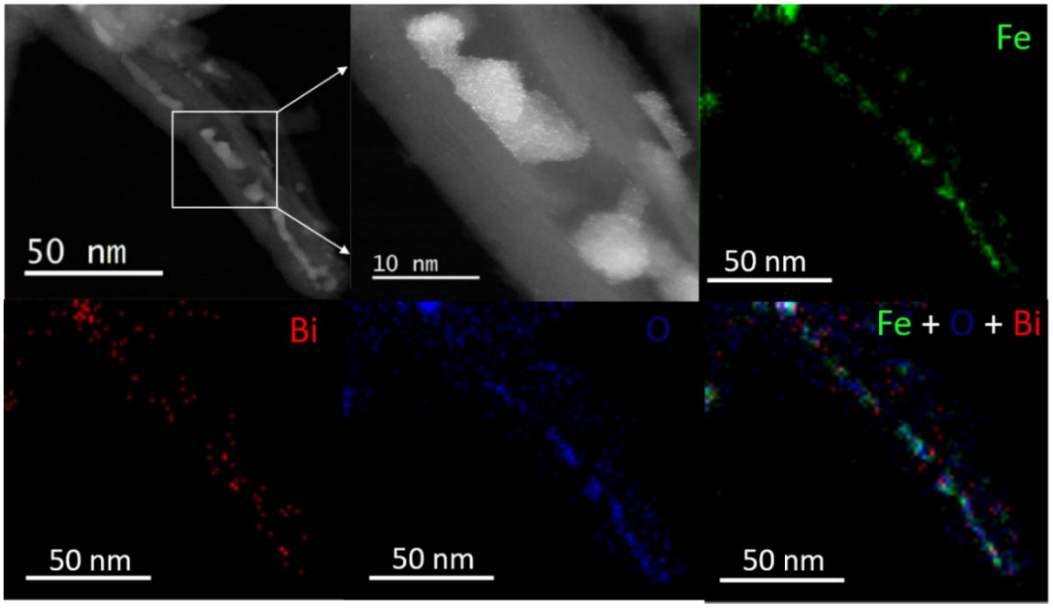

Figure 4.5. *STEM-HAADF and STEM-EDS images for the FeBi/CNT-in fresh catalyst.*

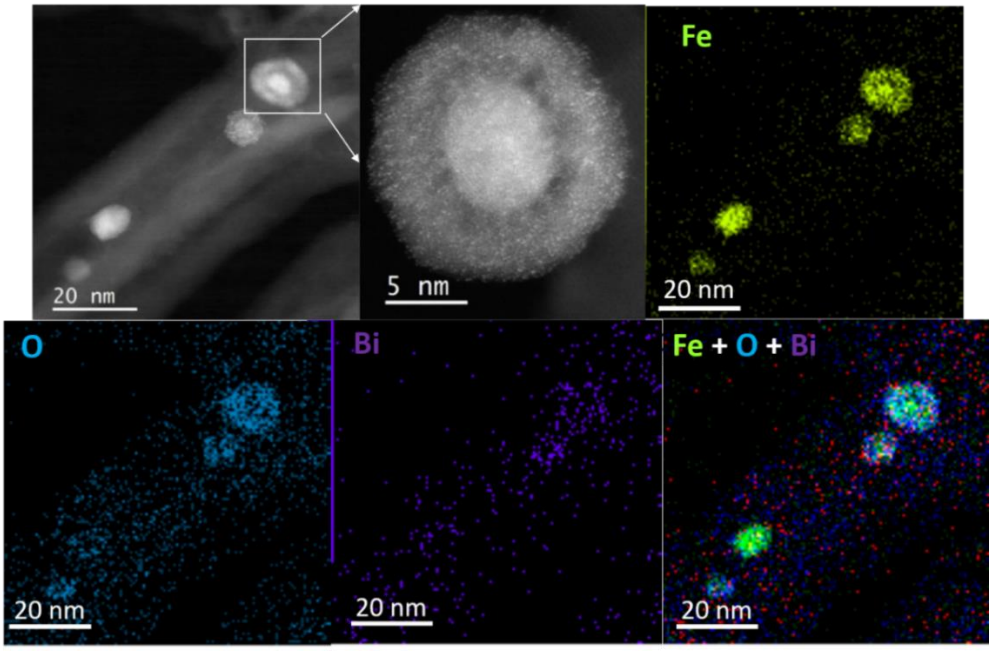

Figure 4.6. *STEM-HAADF and STEM-EDS images for the activated FeBi/CNT-in catalyst (CO treatment for 10 h at 350 °C).*

The evolution of Fe catalysts during activation or FT reaction and the identity of the active phase remain controversial. STEM-HAADF and STEM-EDS analyses have been performed to elucidate the localization of iron and promoters and the morphology evolution during activation and reaction (Figures 4.5-4.7).

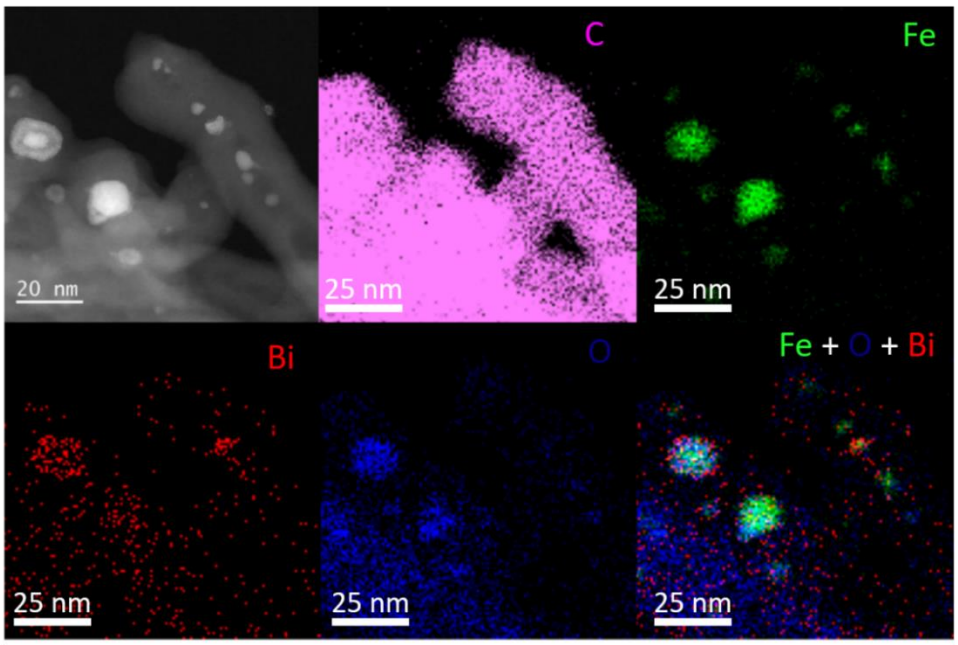

Figure 4.7. *STEM-HAADF and STEM-EDS images for the spent FeBi/CNT-in catalyst (after the catalytic test).*

In the STEM-HAADF images, the image intensity scals with the Z-atomic number of the constitutive elements, such that the Bi species correspond to brighter spots because of high atom weight compared with iron. Figure 4.5 shows the fresh FeBi/CNT-in catalysts, the iron and Bi are located inside the CNT tubes and Bi particles are uniformly mixed with Fe nanoparticles. The iron particles present pod-like morphology with the average particle size of ~ 5 nm. Interestingly, the core-shell structure was formed with the average particle size of ~ 8 nm during activation in CO, most of the Bi particles are present in the shell structure (Figure 4.6). The iron and bismuth distributions and morphology changes after activation in CO. When Bi species are located outside the CNT tubes, the Bi migrates forming bismuth species on the shell of iron carbide nanoparticles, while some Bi particles remain isolated (Figure 4.8). Similar promoter localization and iron morphology was also observed in the used FeBi/CNT-in catalysts (Figure 4.7). Some iron particles also migrate to outer surface of the CNT and undergo significant sintering yielding iron particles of ~15 nm dimeter. In addition, there are still many iron particles situated inside the CNT channels. The size of the iron nanoparticles located inside CNT remain unchanged after the activation in CO.

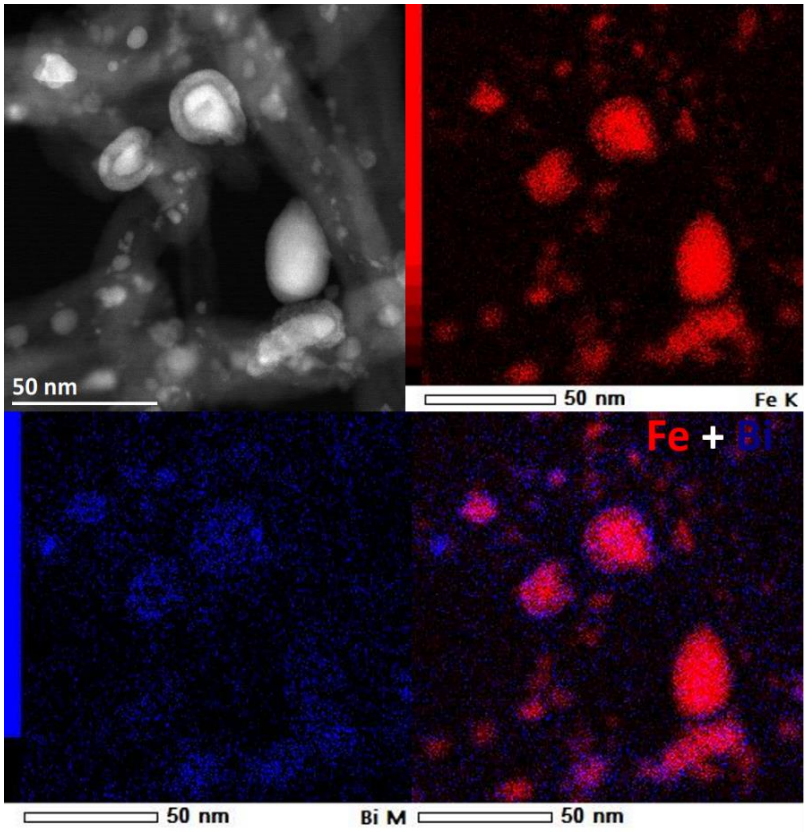

Figure 4.8. *STEM-HAADF and STEM-EDS images for the activated FeBi/CNT-out catalyst (CO treatment for 10 h at 350 °C).*

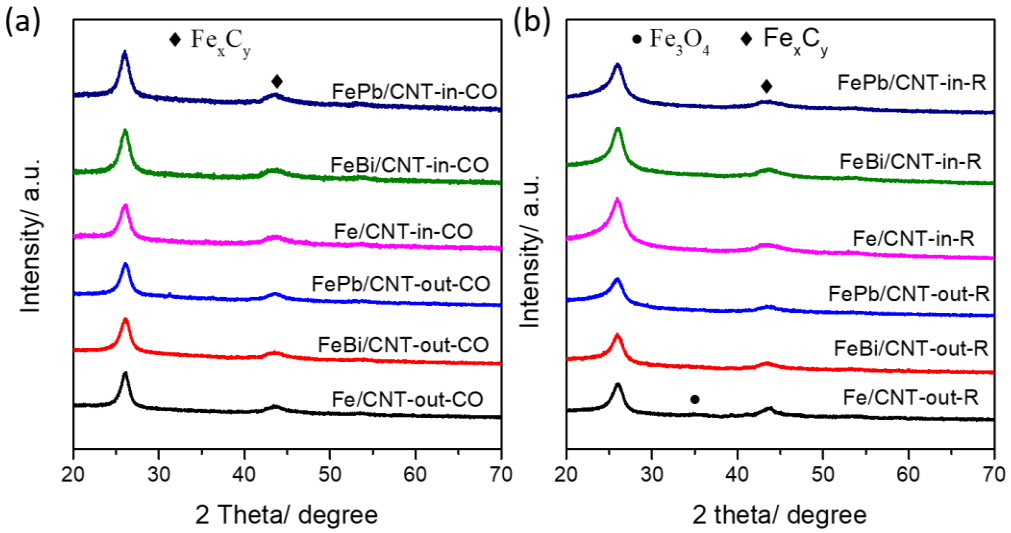

Figure 4.9. *XRD profiles of the carbonized. (a) catalysts after treatment at 350 °C for 10h, (b) catalysts after reaction.*

Several Fe phases, including α-Fe, Fe_3O_4, Fe_3C, $Fe_{2.2}C$, Fe_5C_2 and Fe_7C_3 have been reported [32] in freshly activated or used iron-based FT catalysts. Iron carbides are

commonly considered to be active phase [33, 34] in FT synthesis. The XRD profiles of the catalysts activated under CO at 350 °C and after reaction are displayed in Figure 4.9. Both the activated and used catalysts show a broad peak at ca. 44°, which can be assigned to iron carbides (χ-Fe_5C_2, ε-$Fe_{2.2}C$). Due to significant broadening and overlapping of the iron carbide XRD peaks, the unambiguous identification of the specific χ-Fe_5C_2 or ε-$Fe_{2.2}C$ carbide phases seems rather challenging from XRD patterns.

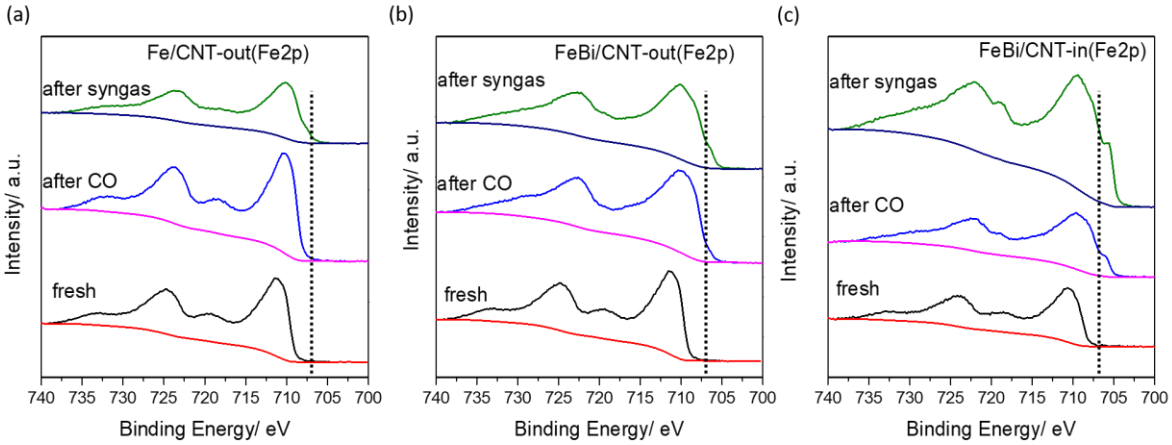

Figure 4.10. *Fe 2p XPS of the catalysts after calcination, exposure to carbon monoxide and syngas. (a) Fe/CNT-out, (b) FeBi/CNT-out, (c) FeBi/CNT-in.*

The subsurface structure of CNT supported iron-based catalysts was characterized by XPS (Figure 4.10). The Fe 2p peaks of fresh Fe/CNT-out, FeBi/CNT-out and FeBi/CNT-in appear at ~711.2 eV ($Fe2p_{3/2}$) and ~724.6 eV ($Fe\ 2p_{1/2}$) with a shakeup satellite peak at ~719.2 eV. After catalyst treatment with CO at 350 °C for 90 min, the intensity of XPS peak for Fe^{3+} decreases. A broad shoulder with the binding energy of 707.3 eV assignable to iron carbide [35] was detected. After exposure to syngas (H_2/CO = 1/1) for 90 min, higher amount of iron carbide has been formed due to further carbonization. Interestingly, the intensity of iron carbide peak at binding energy at ~707.3 eV is higher in the Bi promoted and CNT confined FeBi/CNT-in catalyst activated in CO and syngas compared to the FeBi/CNT-out and Fe/CNT-out counterparts (Figure 4.10). These results are consistent with higher extent of iron carbidization in the confined and promoted catalysts. During XPS experiments, iron carbidization was performed in the reactor chamber of synchrotron XPS spectrometer.

Because of shorter carbidization time and chamber geometry, the extent of iron carbidization could be smaller compared to the experiments conducted in the catalytic reactor.

4.2.1.3. In-situ investigation of iron carbidization

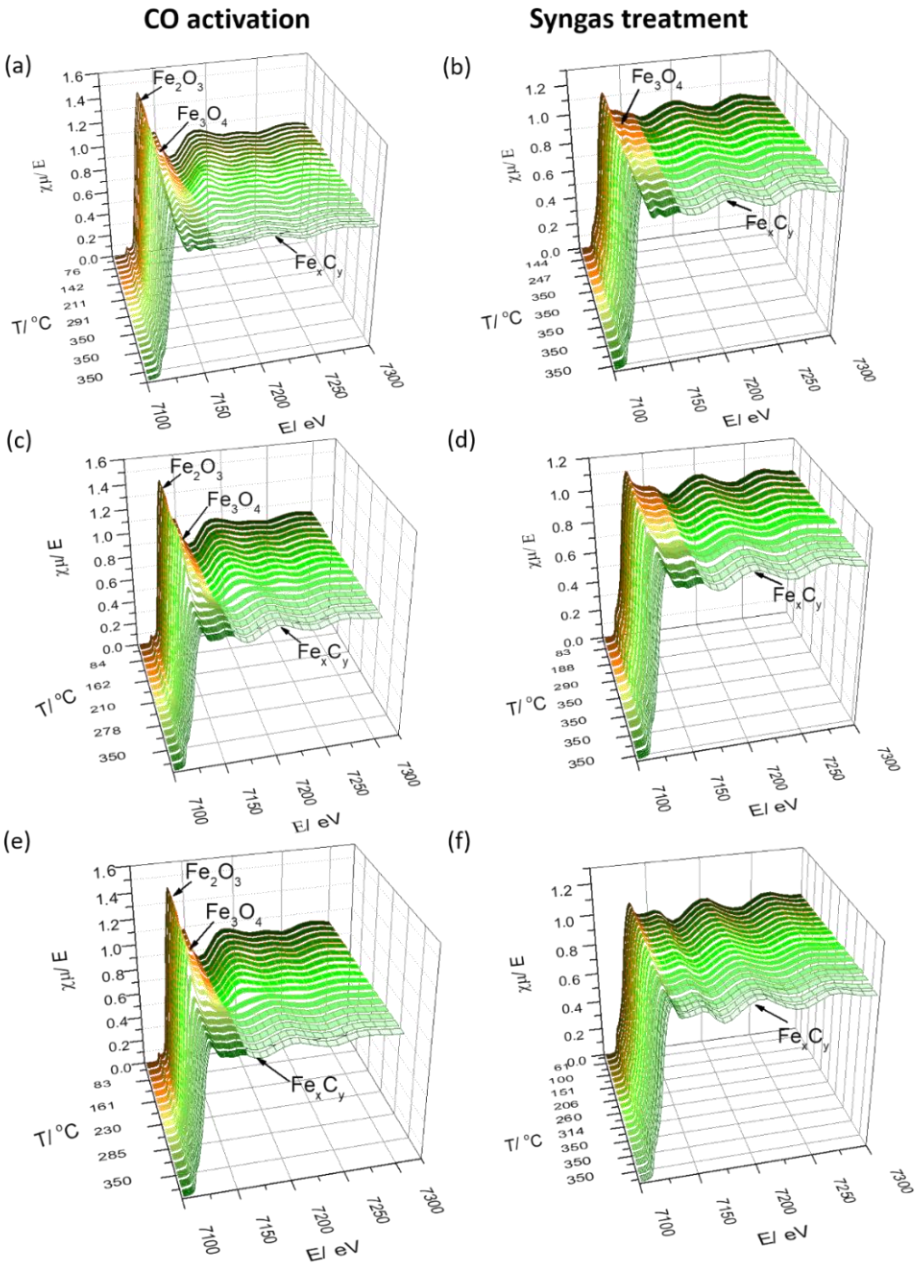

Figure 4.11. *Fe K-edge XANES spectra of the temperature-programmed carbonization and reaction of the un-confined and confined iron-based catalysts. Temperature ranged from 30 to 350 °C. (a) and (b) Fe/CNT-out, (c) and (d) FeBi/CNT-out, (e) and (f) FeBi/CNT-in.*

Further information about the type and concentration of iron carbides in non-confined and confined catalysts was obtained using *in-situ* XANES and *in-situ* magnetic measurements. The XANES experiments were performed with an *in-situ* spectroscopic cell under realistic activation and reaction conditions. Figure 4.11 displays evolution of the Fe K-edge XANES spectra as the temperature increases from 30 to 350 ºC under CO or syngas. The fractions of iron oxides and iron carbides present *in-situ* during the catalyst activation were evaluated using the XANES decomposition with the spectra of reference compounds (Figure 4.12). Iron-based catalysts undergo phase change of Fe_2O_3 to Fe_3O_4 and then to Fe_xC_y during the carbidization [29-32]. For the non-confined Fe/CNT-out catalyst (Figure 4.11a), the reduction of Fe_2O_3 to Fe_3O_4 is quite easy (> 120 ºC), however, the conversion of Fe_3O_4 to Fe_xC_y is a much slower process even under 350 ºC. After subsequent exposure to syngas at 350 ºC, the iron phase composition does not change a lot compared to that obtained in the presence of CO. The catalysts still contain a mixture of Fe_3O_4 and Fe_xC_y (Figure 4.11b). Figures 4.11c and d show the iron phase transformation in FeBi/CNT-out catalyst during exposure to CO. The carbidization of Fe_3O_4 to Fe_xC_y is facilitated in the presence of Bi. The carbidization proceeds much better over FeBi/CNT-out relative to Fe/CNT-out. After the contact of FeBi/CNT-out with syngas for 1 h at 350 ºC, the XANES spectra do not evolve anymore. This suggests that no additional iron carbide phase forms in syngas during the FT reaction. Interestingly, when iron nanoparticles are located inside the CNT channels, this Bi promotion effect is much stronger. The iron carbdidization occurs at temperature 44 ºC lower over confined FeBi/CNT-in compared with the non-confined FeBi/CNT-out catalyst (Figure 4.11e). The iron phase composition after carbidization at 350 °C is shown in Table 4.2. An enhancement of carbidization in the presence of the Bi promoter and after nanoconfinement is clearly observed. Note however that no further carbidization occurs, when the confined FeBi/CNT-in catalyst contacts with syngas after carbidization in CO.

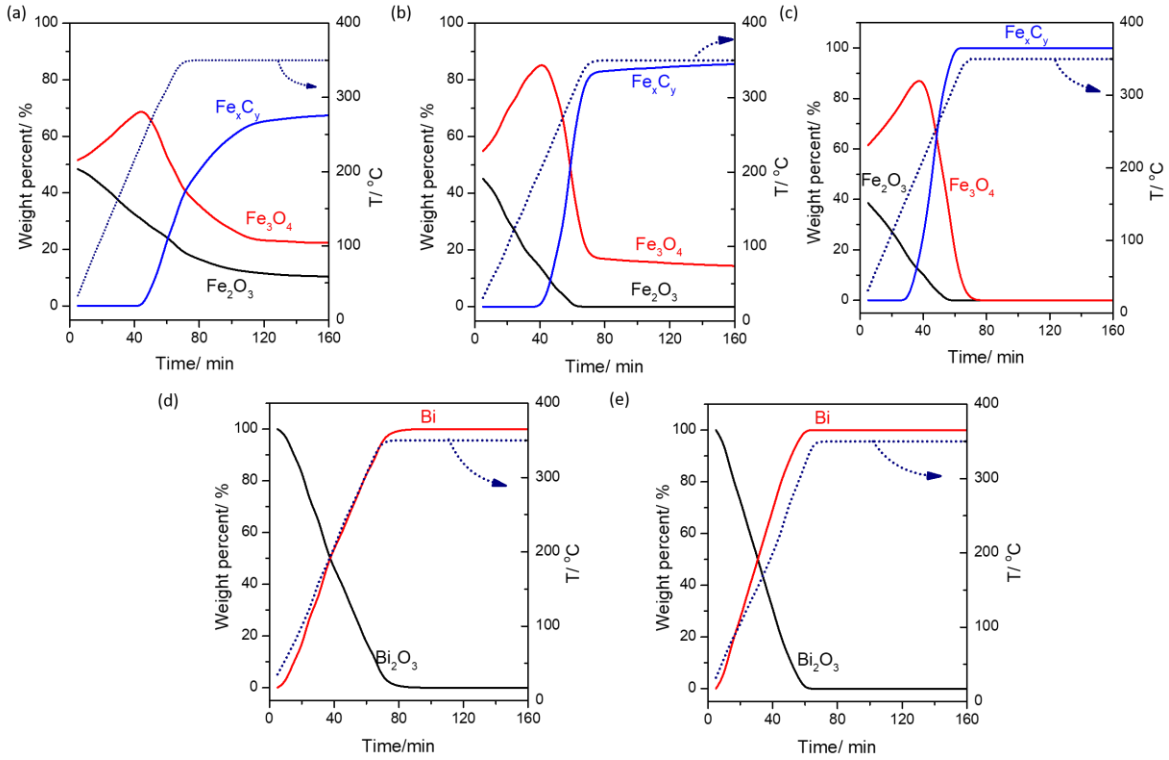

Figure 4.12. *Linear combination fitting of XANES for iron and bismuth phase evolution during activation in CO: (a) Fe/CNT-out, (b) and (d) FeBi/CNT-out, (c) and (e) FeBi/CNT-in.*

Less information is usually available about the promoters compared to the active iron phases. This is often due to lower promoter concentration in the catalysts that precludes the effectiveness of standard characterization techniques, such as XRD and TEM. Here, *in-situ* XANES spectra at the L_3-edge of Bi are also applied to follow the evolution of Bi phases during CO activation and reaction (Figure 4.13). The fractions of bismuth oxide and metallic bismuth were calculated from decomposition of XANES using spectra of reference Bi_2O_3 and metallic bismuth (Figure 4.12). XANES is indicative of the presence of the Bi_2O_3 phase in the fresh catalysts. The Bi_2O_3 oxide is gradually reduced to metallic Bi during CO treatment from 50 °C to 350 °C. Interestingly, the confined FeBi/CNT-in catalyst show easier reducibility of Bi oxides during activation in CO relative to non-confined FeBi/CNT-out. The metallic Bi phase forms at ~ 50 °C lower temperature in FeBi/CNT-in compared with non-confined FeBi/CNT-out. After 90 min activation in CO, syngas (H_2/CO = 1/1) was introduced the catalysts. Importantly, Bi remains in the metallic form during the reaction in the presence of

syngas at the temperatures from 180 °C to 350 °C.

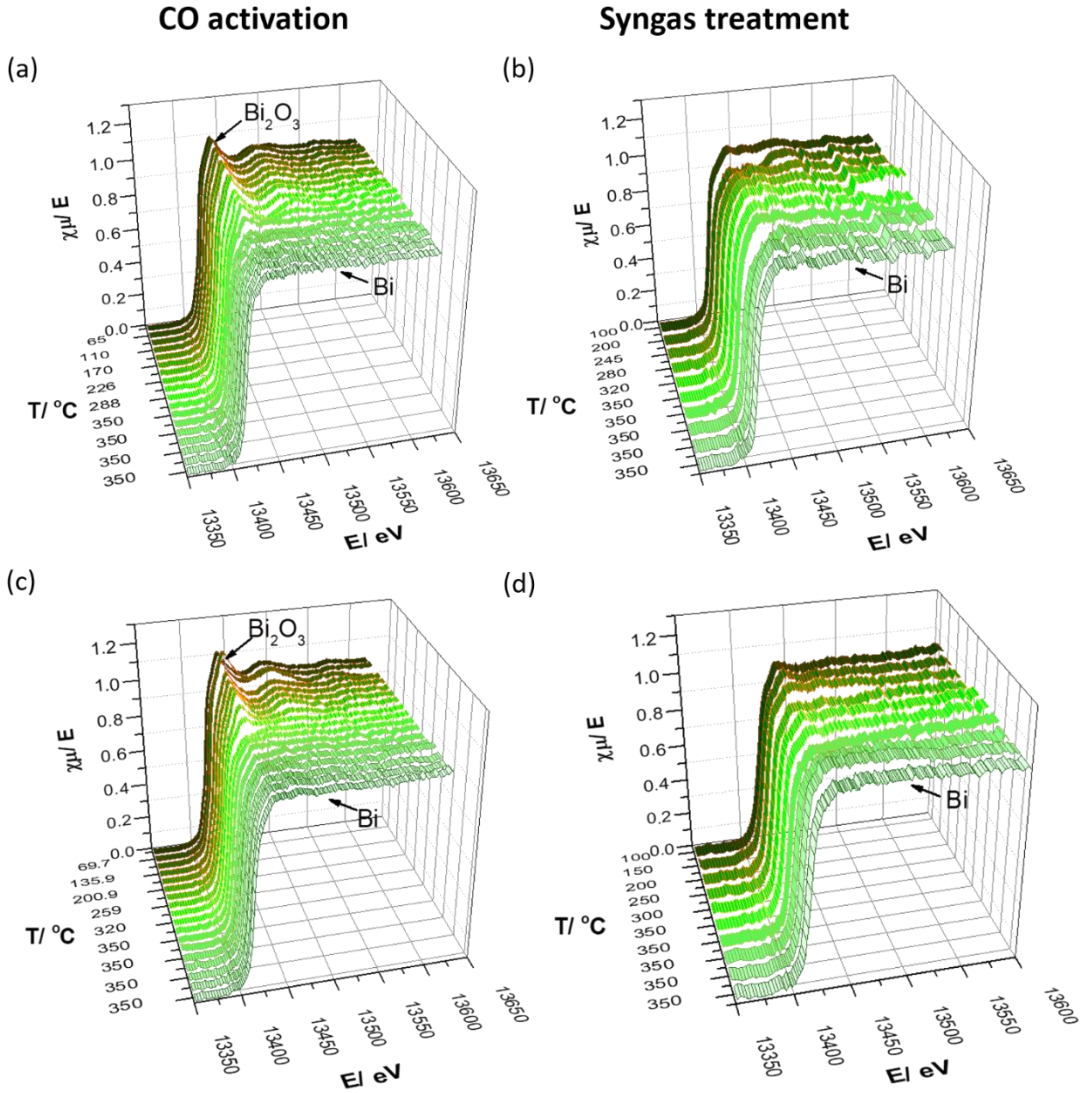

Figure 4.13. *Bi L_3-edge XANES spectra of the temperature-programmed carbonization and reaction of the un-confined and confined iron-based catalysts. (a) and (b) FeBi/CNT-out, (c) and (d) FeBi/CNT-in.*

Thus, the *in-situ* XANES results reveal that in both the non-confined and confined iron-based catalysts in the presence of CO Fe_2O_3 is first reduced to Fe_3O_4 and then carbidized to Fe_xC_y. This process is enhanced in the confined catalysts and in the presence of promoters (Bi and Pb). However, for all three studied catalysts, no noticeable iron phase composition changes occurs during subsequent contact with syngas. This indicates that iron reduction and carbidization mainly occur during the activation with CO. The Bi promoter is also reduced during the CO activation and

remains mostly metallic in syngas atmosphere. Note that because of accuracy limits of XANES, we cannot rule out the presence of small fraction of bismuth oxide (10 %). Bi reducibility is enhanced in the confined FeBi/CNT-in catalyst.

Furthermore, the *in-situ* magnetic measurements provided further information about the genesis of iron phases and iron carbides in the confined and non-confined iron catalysts. These measurements were performed at different temperatures under the flow of CO and syngas. Several ferri- or ferromagnetic phases (iron carbides, metallic iron and magnetite) may be present in the treated catalysts. These phases can be identified from their Curie temperatures, which can be evaluated from the dependence of magnetization on the temperatures (thermomagnetic curves). The Curie temperature of χ-Fe_5C_2 is close to 250 °C, while the Curie temperature of magnetite (Fe_3O_4) and metallic Fe are 580 °C and 770 °C, respectively [5, 36].

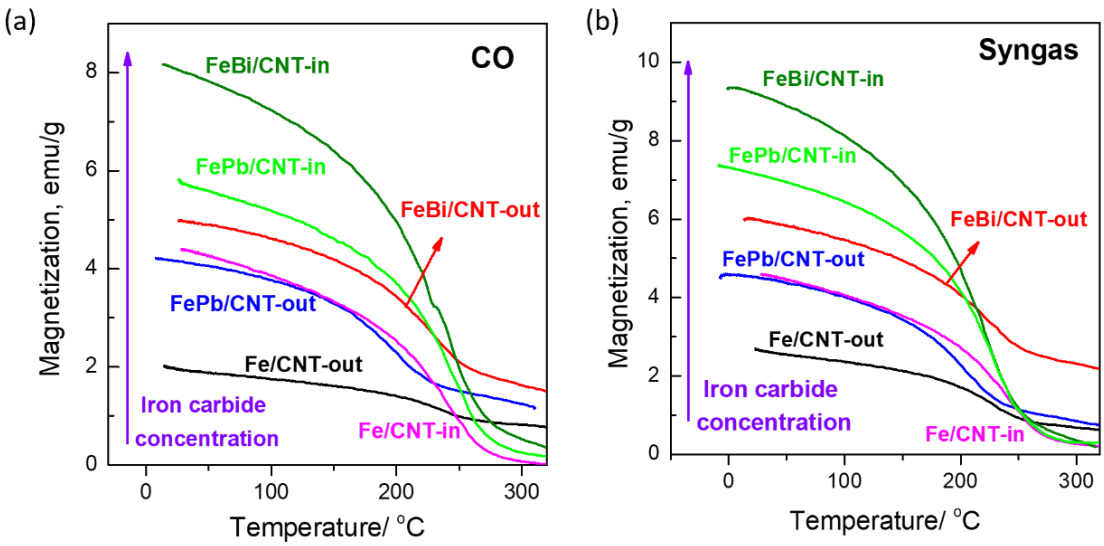

Figure 4.14. *Catalyst magnetization measured: (a) during cooling down after CO treatment at 350 °C, (b) during cooling down after syngas treatment at 350 °C.*

Figure 4.14 shows variation of catalyst magnetization with temperature during cooling the non-confined or confined, unpromoted or promoted iron catalysts after the carbidization in CO or syngas. All the catalysts show similar shape with the Curie temperature of around 250 °C. This suggests that χ-Fe_5C_2 is the predominant iron phase

in the carbidized catalysts. Both nanoconfinement and promotion affect the extent of iron carbidization. After the *in-situ* CO activation, the non-confined and non-promoted Fe/CNT-out catalyst shows lowest iron carbide concentration, the Bi and Pb promotions increase the iron carbide concentration even in the non-confined catalysts (Figure 4.14a). Iron nanoconfinement inside CNT increases extent of iron carbidization. Moreover, the confined Fe/CNT-in shows iron carbide concentration comparable with the Bi and Pb promoted but non-confined FeBi/CNT-out and FePb/CNT-out catalysts. The extent of iron carbidization can be further increased after introducing Bi and Pb into the Fe/CNT-in confined catalyst. The iron carbide concentration seems to be slightly higher after activation in syngas compared to the activation in CO (Figure 4.14b).

4.2.2 Catalytic performance

4.2.2.1. Effect of nanoconfinement and promotion of syngas conversion

Table 4.3. *Catalytic performance of un-encapsulated and encapsulated iron catalysts in FTO (10 bar, 350 °C, H2/CO = 1/1, GHSV = 17 L/g.h, TOS = 10h)*

Catalysts	FTY 10^{-4} $mol_{CO}g_{Fe}^{-1}s^{-1}$	TOF (s^{-1})	CO conv. (%)	CO_2 select. (%)	Hydrocarbon selectivity (%)				C_2-$C_4^=$/ C_2-C_4^o
					CH_4	C_2-$C_4^=$	C_2-C_4^0	C_{5+}	
Fe/AC	0.8	0.282	8.0	28.8	35.6	28.2	22.9	13.3	1.23
Fe/CNT-out	1.6	0.436	14.4	30.4	34.2	32.4	18.4	15.0	1.76
FeBi/CNT-out	3.3	0.862	28.9	38.8	32.3	37.5	16.0	14.2	2.34
FePb/CNT-out	3.9	1.080	34.3	41.1	30.8	35.3	17.4	14.5	2.03
Fe/CNT-in	2.8	0.403	24.8	39.9	28.5	36.9	13.8	20.8	2.67
FeBi/CNT-in	6.9	1.033	60.2	45.2	25.5	45.0	12.0	17.5	3.75
FePb/CNT-in	8.2	1.276	71.0	47.4	25	40.7	14.6	19.7	2.79
FePb/CNT-in*	23.4	-	45.0	39.4	26.1	41.0	15.9	17.0	2.58
FePbK/CNT-in	8.8	-	76.2	48.1	18.2	52.6	8.6	21.0	6.12

*P = 20 bar, T = 350 °C, GHSV = 84 L/g.h

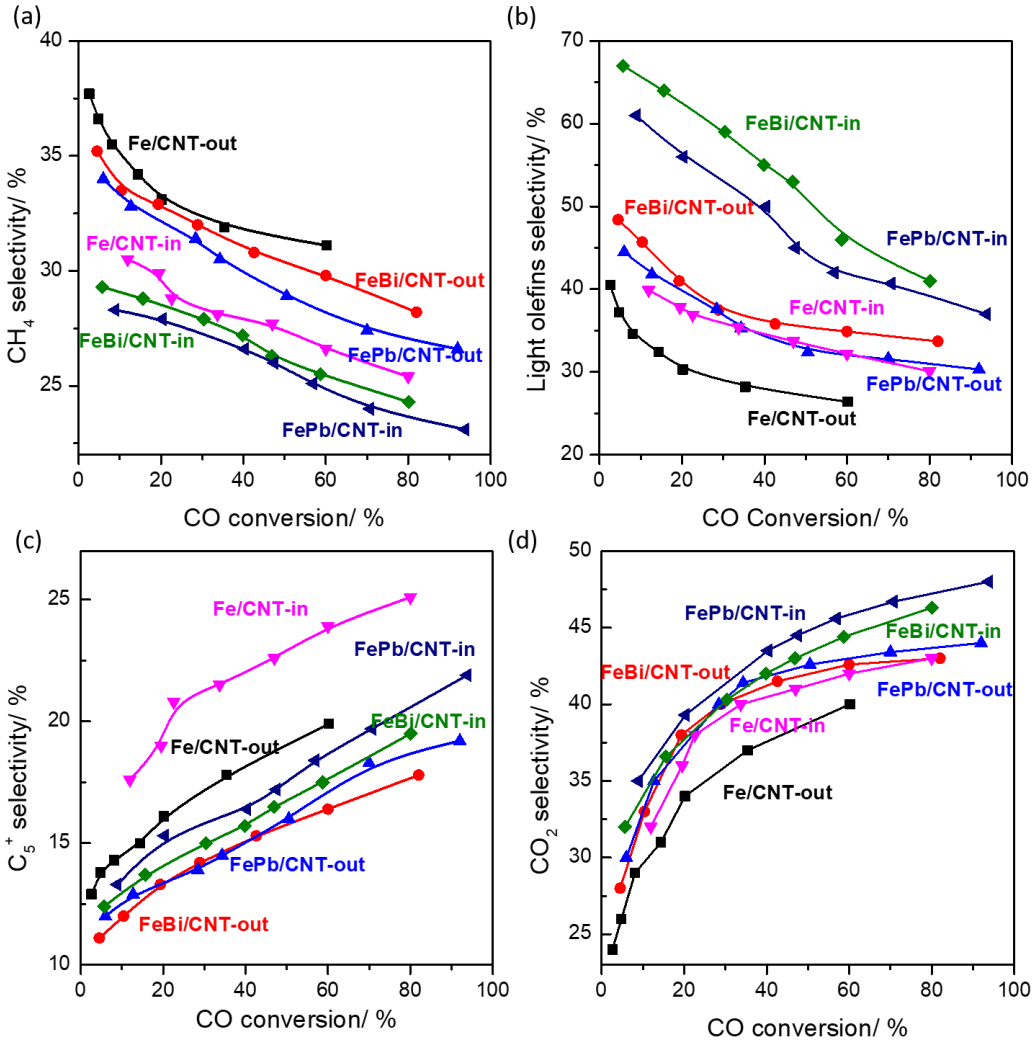

Figure 4.15. *Product selectivity versus CO conversion over CNT confined and non-confined iron catalysts. Reaction conditions: W = 0.1 g, H_2/CO = 1, P = 10 bar, T = 350 °C, GHSV = 10.2-30.6 L $h^{-1}g^{-1}$.*

The catalytic data in high temperature FT synthesis for the confined and non-confined iron-based catalysts under high pressure (10 bar) are shown in Tables 4.3 and Figure 4.15, 4.16. When the iron particles are located outside the CNT tubes in Fe/CNT-out, the CO conversion observed at the reaction pressure of 10 bar (Table 4.3) is low (14.4 %) with the FTY of $1.6*10^{-4}$ $mol_{CO}g_{Fe}^{-1}s^{-1}$ and high selectivity to methane (34.2 %). After introducing Bi and Pb promoter, the CO conversion over FeBi/CNT-out and FePb/CNT-out increases to 28.9 % and 34.3 %, respectively. The selectivity to methane decreases, however, the selectivity of light olefins slightly increases and reaches 36 %. Interestingly, when the iron particles are located inside the CNT tubes in

Fe/CNT-in, the CO conversion and FTY increase from 14.4 to 24.8 % and from 1.6 to 2.8 $mol_{CO}g_{Fe}^{-1}$ respectively. These results are consistent with previous works of the Bao' group [16-20] et al showing higher activity of catalysts containing iron nanoparticles inside CNT. Calculation assuming complete carbidization is indicative however, of similar TOF values, when iron nanoparticles are located inside or outside CNT (Table 4.3). This suggests that the enhancement of catalytic activity in the confined catalysts is principally due to higher iron dispersion.

Table 4.4. *Catalytic performance comparison in different high temperature Fischer-Tropsch catalytic system*

Catalysts	FTY 10^{-4} $mol_{CO}g_{Fe}^{-1}s^{-1}$	CO Con. / %	Reaction condition	Ref.
FePb/CNT-in	23.4	45	P=20 bar, T=350 °C, H_2/CO=1/1, GHSV= 84 $Lg^{-1}h^{-1}$	This work
FeMgK1/rGO	17.1	59-62	P=20 bar, T=340 °C, H_2/CO=1/1, GHSV= 168 $Lg^{-1}h^{-1}$	[37]
Fe/CNF(Na,S)	13.0	6	P=20 bar, T=340 °C, H_2/CO=1/1, GHSV= 84 $Lg^{-1}h^{-1}$	[4]
Fe_3O_4@Fe_5C_2	7.2	28	P=20 bar, T=300 °C, H_2/CO=1/1, GHSV= 18 $Lg^{-1}h^{-1}$	[38]
FeK1/rGO	6.5	58-64	P=20 bar, T=340 °C, H_2/CO=1/1, GHSV= 72 $Lg^{-1}h^{-1}$	[39]
0.6K38-Fe@C	4.9	59	P=20 bar, T=340 °C, H_2/CO=1/1, GHSV= 1 $Lg^{-1}h^{-1}$	[40]
Fe/CNF (Na, S)	2.0	12	P=20 bar, T=340 °C, H_2/CO=1/1, GHSV=3000 h^{-1}	[41]
Fe/α-Al_2O_3(Na, S)	0.9	77	P=20 bar, T=340 °C, H_2/CO=1/1GHSV= 1500 h^{-1}	[3]

The promotion of the confined Fe/CNT-in catalyst with Bi and Pb results in further important increase in the reaction rate. The CO conversion increases from 24.8 to 60-70 % over the Bi and Pb-promoted Fe/CNT-in samples and FTY increases 2.5-3.0 times from 2.8 to 6.9 and 8.2 $mol_{CO}g_{Fe}^{-1}$ s^{-1}. The iron time yield reaches 23.4*10^{-4} $mol_{CO}g_{Fe}^{-1}s^{-1}$ for the FePb/CNT-in catalysts at the total syngas pressure of 20 bar and GHSV 84 L/g.h which is one of the best results for the iron-based FT synthesis catalysts available

so far in the literature. The TOF values are also higher in the promoted catalysts (Table 4.4). This suggests electronic effects of the promotion with Bi and Pb on the intrinsic activity of iron carbide surface sites. Moreover, the presence of promoters inside the tubes changes the product selectivity compared with non-confined catalysts. The selectivity to methane decreases from 34 % to 25 %, while the light olefins selectivity increases from ~33 % to ~45 %. When a small amount of potassium was added to make the FePbK/CNT-in catalyst, the catalytic performance in FT synthesis was further improved (Table 4.3, Figure 4.16). The light olefin selectivity reaches 52.6 % at the carbon monoxide conversion of 76.2 %. The promotion with potassium seems to increase further the light olefins yield over the promoted and confined iron catalysts.

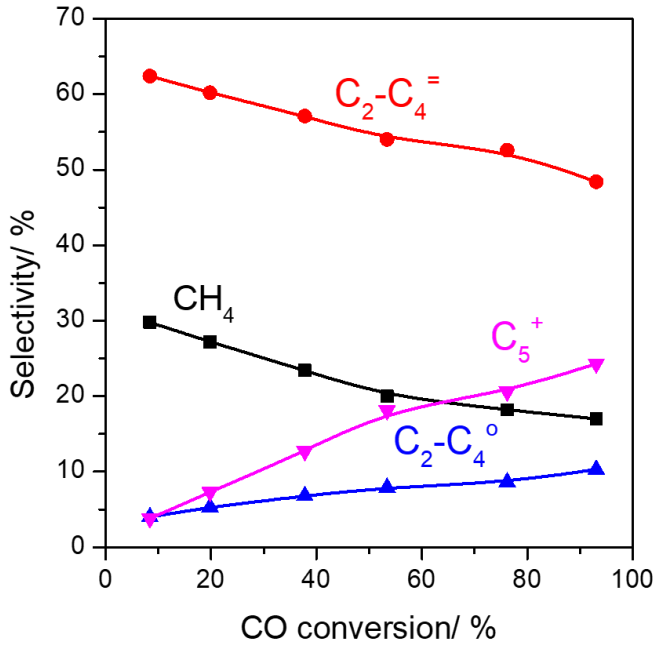

Figure 4.16. *Products selectivity vers CO conversion over FePbK/CNT-in catalyst. Reaction condition: P = 10 bar, H_2/CO = 1/1, T = 350 °C, GHSV = 13.8 - 68 L/g.h.*

The effect of GHSV and pressure on the CO conversion over the confined and non-confined iron catalysts are shown in Figure 4.17. As expected, the CO conversion increases with the decrease in GHSV at the same pressure (10 bar). The CO conversion also shows similar trend with increasing the pressure at the same GHSV. Indeed, higher total pressure in the range of 1-20 bar usually results in higher FT reaction rate over iron catalysts. Note however, that the confined iron catalysts show higher CO

conversion than the non-confined catalysts under the same reaction conditions. Interestingly, the confined and non-promoted Fe/CNT-in catalyst shows similar activity with the non-confined and promoted FeBi/CNT-out and FePb/CNT-out catalysts. Bao [42] et al discovered CO and H_2 enrichment inside the SWCNT tubes based on Monte Carlo simulation. They found that both CO and H_2 were enriched in the pressure range of 1-9 MPa inside the single wall CNT channels. The increased concentration of CO and H_2 could lead to higher reaction rate, while the altered H_2/CO ratio inside CNTS could also modify the product selectivity. Our results suggest that the observed higher activity over the confined catalysts can be primarily explained by higher dispersion of iron at the same iron total content when iron is located inside CNT. The TOF seems to be not much affected by iron confinement. Note that iron dispersion is not affected by the promotion with Bi and Pb but TOF noticeably increases. The strong promotion effect of Bi and Pb might be due to the intimate contact between Fe and promoters [5] inside the CNT. The metallic Bi and Pb have low melting temperature (Bi ~271 ºC and Pb ~327 ºC) and the promoter migration could therefore occur at the reaction temperature (350 ºC). Interestingly, the increase in TOF after the promotion is more significant, when iron nanoparticles are located inside CNT. The promoters inside the tubes may have closer contact with Fe due to nanoconfinement effect and thus strong promoting effect on the catalytic performance.

The product distributions observed over the confined and non-confined iron-based catalysts measured as a function of CO conversion are summarized in Figure 4.15. The selectivity to methane and light olefins decreases with increasing CO conversion for the examined catalysts (Table 4.3, Figure 4.15), More importantly, the confined iron catalysts showed higher selectivity to light olefins compared with the non-confined Fe/CNT-out catalysts at the similar CO conversion levels. The Bi and Pb promoters lead to higher selectivity to light olefins. The selectivities to CO_2 and C_{5+} hydrocarbons increase with the CO conversion (Figure 4.15). Higher CO_2 selectivity at higher CO conversion is usually observed over iron FT catalysts and can be relevant to the higher rate of water gas shift reaction due to intensive water production at high CO conversion

[43, 44]. Higher CO_2 selectivity was observed over the Bi- and Pb-promoted catalysts compared to the unpromoted catalyst (Figure 4.15). This can be due to the higher rate of carbon monoxide dissociation. In agreement with previous work, the rate of carbon dioxide dissociation over the promoted catalysts can be enhanced by oxygen scavenging in the presence of the Bi or Pb promoters localized at the interfaces of iron carbide nanoparticles. For a given catalyst, the selectivity to the C_{5+} hydrocarbons increase with the conversion. At iso-conversion, the selectivity to the C_{5+} hydrocarbons were higher over the unpromoted Fe/CNT-out and Fe/CNT-in catalysts.

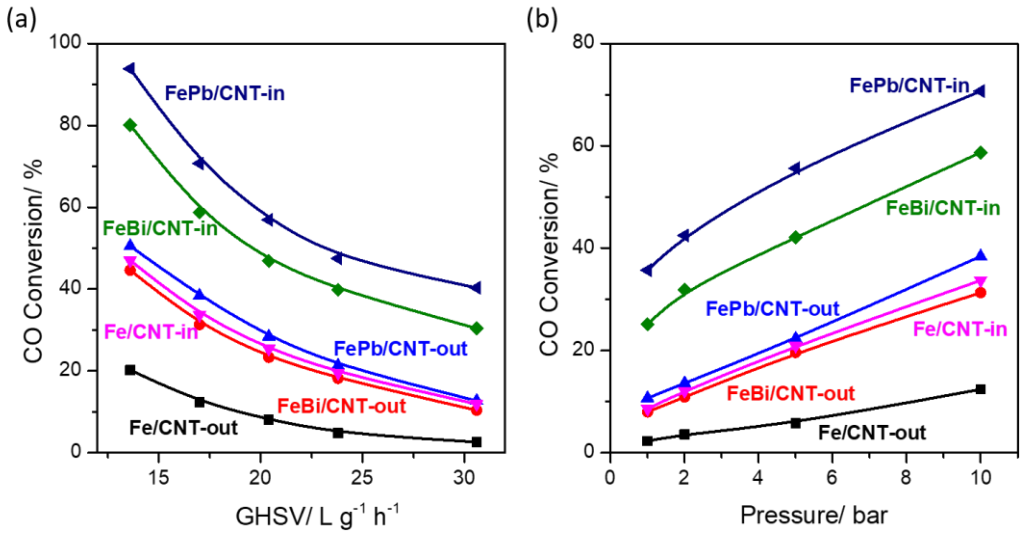

Figure 4.17. *Carbon monoxide conversion over CNT confined and un-confined iron-based catalysts under different reaction condition: (a) under different GHSV, (b) under different pressure. Reaction conditions: W = 0.2g, H_2/CO = 1, P = 1-10 bar, T=350 °C, GHSV= 13.6-30.6 L/g.h*

A simplified schema of FT reaction consistent with the selectivity variation to different reaction products as a function of carbon monoxide conversion is displayed in Figure 4.18. The schema suggests that CO and hydrogen adsorption on the metal catalysts is followed by formation of the C_1 monomer. Indeed, at very low conversion, the concentration of adsorbed C_1 monomer is very low to enable noticeable polymerization rate. Oligomerization of the C_1 monomers results in formation of the C_2-C_4 fragments on the catalyst surface. The desorption of these fragments results in light olefins. Hydrogenation of the C_2-C_4 species leads to light paraffins. Light olefins

can readsorb on the catalyst surface. This readsorption can result either in secondary olefin hydrogenation to light paraffins or to further chain growth favoring formation of long-chain hydrocarbons. This schema explains the observed decrease in the selectivity to light olefins and increase in the selectivity to the C_{5+} hydrocarbons with the CO conversion. Note however, that the Bi and Pb promoters decrease the C_{5+} selectivity and the product distribution shifts to lighter hydrocarbons. This is different compared with alkali promoters [45]. The alkali promoted iron catalysts usually show lower methane selectivity and enhanced selectivity to the C_{5+} hydrocarbons.

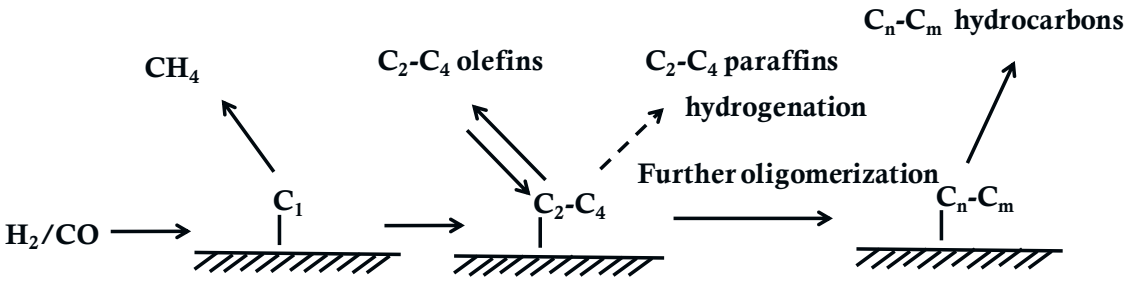

Figure 4.18. *Simplified schema of FT reaction*

4.2.2.2. Light olefin synthesis from syngas at atmospheric pressure

Table 4.5. *Catalytic performance of un-encapsulated and encapsulated iron catalysts in FTO (1 bar, 350 °C, H_2/CO = 1/1, GHSV = 3.4 L/g.h, TOS = 10 h)*

Catalysts	FTY 10^{-5} $mol_{CO}g_{Fe}^{-1}s^{-1}$	CO conv. (%)	CO_2 select. (%)	Hydrocarbon selectivity (%)				C_2-$C_4^=$/ C_2-C_4^o
				CH_4	C_2-$C_4^=$	C_2-C_4^0	C_5^+	
Fe/AC	0.5	2.5	18.7	40.3	34.4	18.7	6.6	1.84
Fe/CNT-out	0.8	4.3	20.2	37.3	35.2	18.9	11.6	1.86
FeBi/CNT-out	1.6	8.5	25.8	31.5	47.6	12.7	8.2	3.75
FePb/CNT-out	2.4	12.9	30.5	30.9	44.9	15.2	9.0	2.95
Fe/CNT-in	1.5	8.0	29.2	31.9	40.4	11.7	16.0	3.45
FeBi/CNT-in	4.7	25.6	37.3	27.0	62.4	6.5	4.6	9.60
FePb/CNT-in	6.6	35.9	39.9	26.1	58.9	7.4	7.6	7.96
FePbK/CNT-in	7.5	40.7	42.4	19.2	62.0	6.1	12.7	10.2

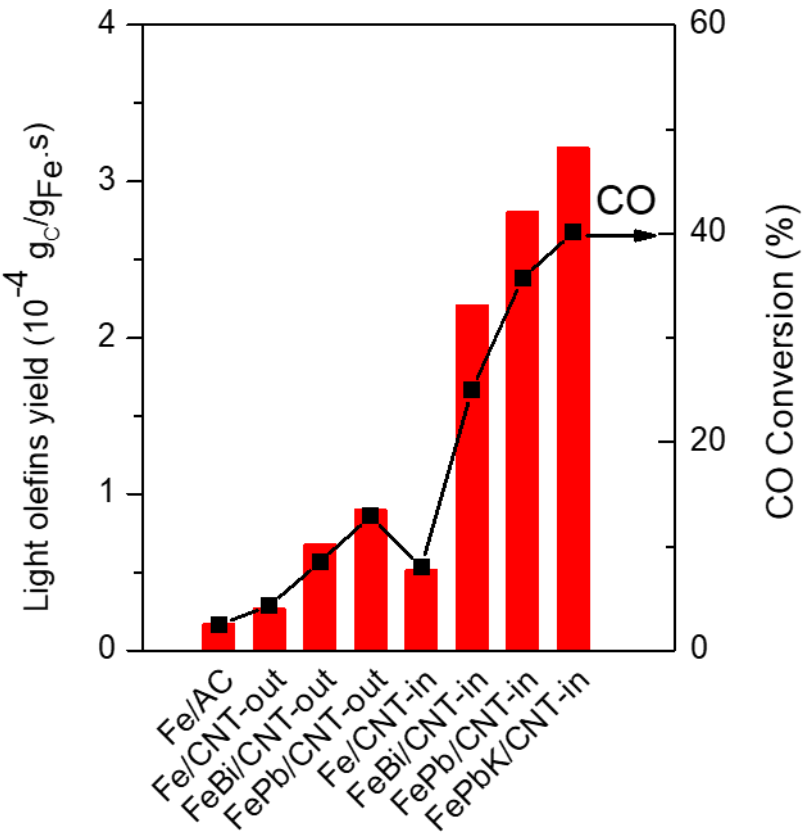

Figure 19. *Light olefins selectivity and CO conversion over the confined and un-confined iron-based catalysts. Reaction conditions: W = 0.1 g, H_2/CO = 1, P = 1 bar, T = 350 °C, GHSV = 3.4 L $h^{-1}g^{-1}$.*

Biomass and coal gasification are usually conducted at near atmospheric pressure, while the FT reaction usually requires higher pressures (10-40 bar). Conducting catalytic reactions at higher pressure requires additional costs, due to gas pressurization. Interestingly and differently to the previously studied iron based FTO catalysts, direct light olefin synthesis from syngas can occur over Bi and Pb-promoted confined catalysts with a high yield even under atmosphere pressure. Table 4.5 and Figure 4.19 display the CO conversion and light olefin yield over confined and non-confined iron-based catalysts under *iso*-GHSV at atmospheric pressure. The non-promoted and non-confined Fe/CNT-out catalysts exhibit very low CO conversion at atmospheric pressure. The light olefin yield increases only 2-3 times after the promotion with Bi and Pb over Fe/CNT-out non-confined catalyst. The reaction rate over the confined Fe/CNT-in catalyst is higher compared with non-confined one. The 4-5.5 times higher

light olefin yields have been observed on the Bi and Pb promotion with the confined Fe/CNT-in catalyst. After adding a small amount of K (1.0 wt. %), the catalytic performance is further improved. The resulting FePbK/CNT-in catalyst exhibits around 18 times higher FTY compared with Fe/CNT-out counterpart with the selectivity toward light olefins higher than ~62 %.

The catalytic results therefore suggest that the nanoconfinement and promotion produce synergetic effects on the catalytic performance of iron catalysts for FT synthesis both at the reaction pressure of 10 bar and atmospheric pressure. The effect of nanoconfinement is relevant to the enhancement of iron dispersion, while the intrinsic activity is only slightly affected. The promotion produces strong effect on the intrinsic activity, while iron dispersion does not change. The nanoconfinement improves the catalytic performance in FT synthesis and the promotion effect is much more pronounced when the iron nanoparticles are located inside the CNT tubes. These confined and promoted catalysts show significant activity even at atmosphere pressure. At 1 bar, the FePb/CNT-in catalyst exhibits the CO conversion 35.9 % and light olefin selectivity of 58.9 %.

4.2.2.3 Stability and sintering

Catalyst deactivation remains one of the main challenges in FT synthesis [46]. The catalyst deactivation in FT reaction is an interplay of several phenomena. Some of these phenomena can be reversible and irreversible. Major deactivation mechanisms of iron catalysts involve metal sintering and carbon deposition [47]. Figure 4.20 shows carbon monoxide conversion as a function of the reaction time on non-confined and confined monometallic and promoted iron catalysts. The catalyst stability is compared at similar carbon monoxide conversion, which was obtained by adjustment of GHSV. The Fe/CNT-out catalyst shows gradual deactivation during the reaction. The promotion of Fe/CNT-out leading to FeBi/CNT-out and FePb/CNT-out results in a slight improvement of the stability. Much more significant improvement in the stability is observed with the Fe/CNT-in confined catalyst. Moreover, when iron and promoted

iron nanoparticles are confined inside the CNT tubes, the resulting catalyst shows no deactivation for more than 100 h (Figure 4.20).

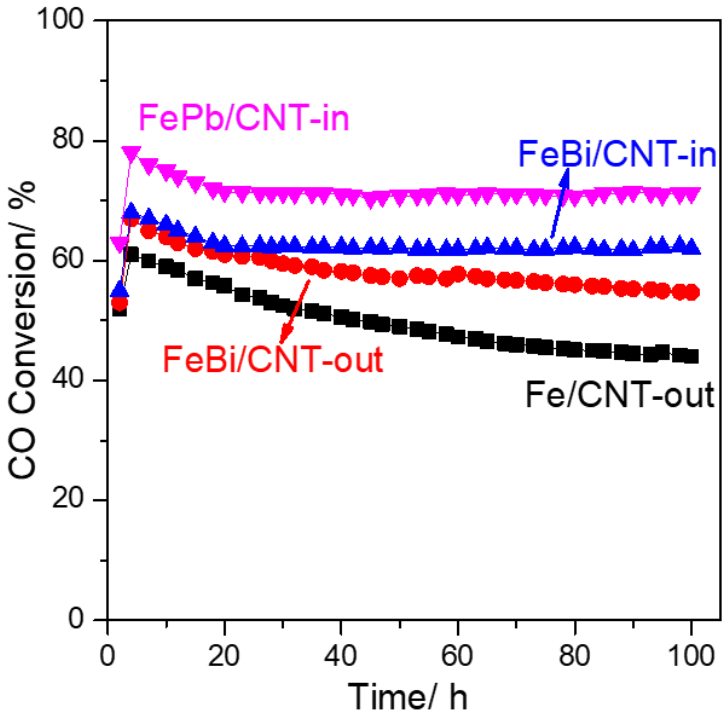

Figure 4.20. *CO conversion as a function of time on stream for CNT confined and un-confined iron-based catalysts. Reaction conditions: W = 0.1 g, H_2/CO = 1, P = 10 bar, T = 350 °C, GHSV = 6.8-20.4 L $h^{-1}g^{-1}$.*

Iron sintering could be one of the reasons of catalyst deactivation. Both the freshly activated and spent catalysts were characterized by TEM. Figure 4.21 shows that the size of confined iron particles remains the same after reaction for 30 h. This indicates that particle sintering is effectively prevented inside CNTs under these reaction conditions. This suggests that nanoconfinement protects iron nanoparticles from sintering. Note that the size of the non-confined nanoparticles in Fe/CNT-out grew to ~15-16 nm after the reaction (Figure 4.21). Even a much stronger sintering was observed over the reference iron catalysts supported by active carbon (Fe/AC). The spent Fe/AC catalysts presents iron nanoparticles of ~24 nm after the catalytic tests (Figure 4.3b) compared to 12.1 nm observed in the freshly activated counterpart. The results indicate that nanoconfinement of CNTs facilitates immobilization of the iron

species and restricts sintering the growth of iron nanoparticles during the reaction. These results are similar to our previous studies of iron catalysts promoted by Bi and Pb and supported over SiO_2 and CNT supports. The CNT nanoconfinement effect for iron particles could restrict sintering.

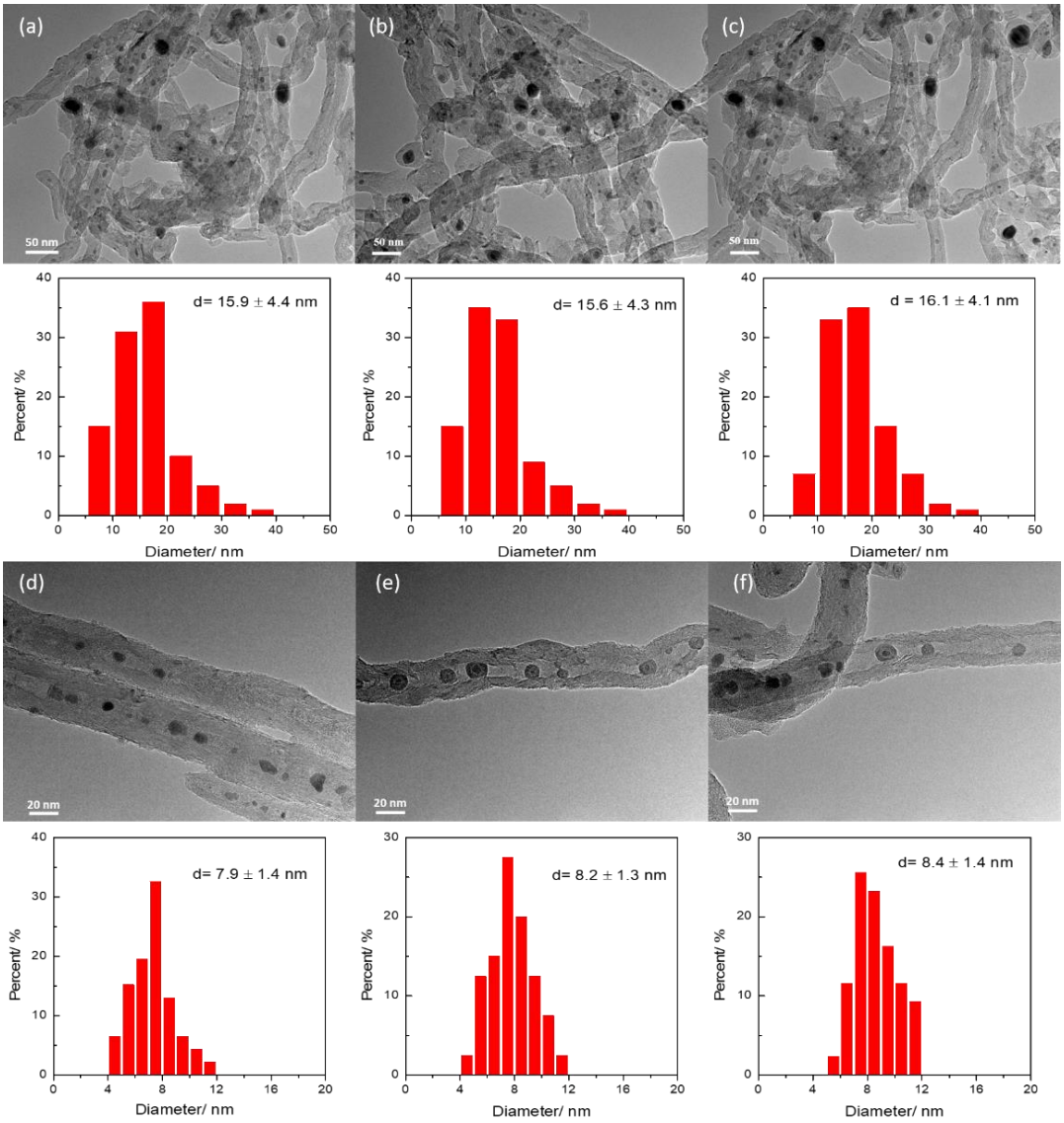

Figure 4.21. *TEM micrographs for spent confined and un-confined Fe catalysts after reaction: (a) Fe/CNT-out-R, (b) Fe/CNT-in-R, (c) FeBi/CNT-out-R, (d) FeBi/CNT-in-R, (e) FePb/CNT-out-R, (e) FePb/CNT-in-R.*

4.3 Conclusion

Nanoconfinement of iron nanoparticles inside CNT and their promotion with Bi and Pb result in synergetic effects on the structure of iron species and their catalytic performance in light olefin synthesis from syngas. A combination of characterization techniques (TEM, XRD, TPR, SSITKA, XPS, *in-situ* XANES and *in-situ* magnetic measurements) was indicative of higher iron dispersion in the confined catalysts, while no effect of the promotion on iron particle size was observed. During catalyst activation in CO, the iron phase transforms from Fe_2O_3 to Fe_3O_4 and then to the Hägg iron carbide (Fe_5C_2). The iron reduction and carbidization proceeds much easier for iron species confined inside CNTs and promoted with Bi and Pb. The initial morphology of iron is pod-like structure and transferred to core-shell structure with Bi and Pb in the shell during activation and reaction. The nanoconfinement assists in controlling the migration of the promoters by restricting the promoters inside the tubes and thus then increase their interaction with iron carbide. The promoting effects and intimate contact of bismuth and lead inside the CNT channels with iron carbides are crucial for obtaining enhanced catalytic performance in high temperature FT synthesis. Both nanoconfinement and promotion with Bi and Pb result in a major increase in FT reaction rates. The increase in FT rate is due to nanoconfinement is principally due to the enhancement of iron dispersion, while the promotion with Bi and Pb produces strong effect on intrinsic activity of iron sites. The promotion effect is stronger in the confined catalysts, which is possible due to the stronger interaction between the promoter and iron carbides inside CNT. The catalysts containing iron carbide nanoparticles confined inside CNT exhibit high catalytic activity even under atmospheric pressure. The light olefin selectivity is also improved by the promotion and nanoconfinement. Nanoconfinement of iron particles in CNTs slows down iron sintering during the reaction and thus improves the catalyst stability.

4.4 Reference

[1] D.B. Bukur, D. Mukesh, S.A. Patel, Promoter effects on precipitated iron catalysts for Fischer-Tropsch synthesis, Industrial & engineering chemistry research, 29 (1990) 194-204.

[2] H. Arakawa, A.T. Bell, Effects of potassium promotion on the activity and selectivity of iron Fischer-Tropsch catalysts, Industrial & Engineering Chemistry Process Design and Development, 22 (1983) 97-103.

[3] H.M.T. Galvis, J.H. Bitter, C.B. Khare, M. Ruitenbeek, A.I. Dugulan, K.P. de Jong, Supported iron nanoparticles as catalysts for sustainable production of lower olefins, Science, 335 (2012) 835-838.

[4] J. Xie, H.M. Torres Galvis, A.C. Koeken, A. Kirilin, A.I. Dugulan, M. Ruitenbeek, K.P. de Jong, Size and promoter effects on stability of carbon-nanofiber-supported iron-based Fischer-Tropsch catalysts, ACS catalysis, 6 (2016) 4017-4024.

[5] B. Gu, V.V. Ordomsky, M. Bahri, O. Ersen, P.A. Chernavskii, D. Filimonov, A.Y. Khodakov, Effects of the promotion with bismuth and lead on direct synthesis of light olefins from syngas over carbon nanotube supported iron catalysts, Applied Catalysis B: Environmental, 234 (2018) 153-166.

[6] V.V. Ordomsky, Y. Luo, B. Gu, A. Carvalho, P.A. Chernavskii, K. Cheng, A.Y. Khodakov, Soldering of Iron Catalysts for Direct Synthesis of Light Olefins from Syngas under Mild Reaction Conditions, ACS Catalysis, 7 (2017) 6445-6452.

[7] Z. Yang, X. Pan, J. Wang, X. Bao, FeN particles confined inside CNT for light olefin synthesis from syngas: Effects of Mn and K additives, Catalysis today, 186 (2012) 121-127.

[8] H. Qin, B. Wang, C. Zhang, B. Zhu, Y. Zhou, Q. Zhou, Lignin based synthesis of graphitic carbon-encapsulated iron nanoparticles as effective catalyst for forming lower olefins via Fischer-Tropsch synthesis, Catalysis Communications, 96 (2017) 28-31.

[9] Z. Sun, B. Sun, M. Qiao, J. Wei, Q. Yue, C. Wang, Y. Deng, S. Kaliaguine, D. Zhao, A general chelate-assisted co-assembly to metallic nanoparticles-incorporated ordered mesoporous carbon catalysts for Fischer-Tropsch synthesis, Journal of the American Chemical Society, 134 (2012) 17653-17660.

[10] G. Yu, B. Sun, Y. Pei, S. Xie, S. Yan, M. Qiao, K. Fan, X. Zhang, B. Zong, Fe_xO_y@ C spheres as an excellent catalyst for Fischer-Tropsch synthesis, Journal of the American Chemical Society, 132 (2009) 935-937.

[11] H. Qin, S. Kang, Y. Wang, H. Liu, Z. Ni, Y. Huang, Y. Li, X. Li, Lignin-Based Fabrication of Co@C Core-Shell Nanoparticles as Efficient Catalyst for Selective Fischer-Tropsch Synthesis of C_{5+} Compounds, ACS Sustainable Chemistry & Engineering, 4 (2016) 1240-1247.

[12] Y. Cao, M. Lu, J. Fang, L. Shi, D. Zhang, Hexagonal boron nitride supported mesoSiO_2-confined Ni catalysts for dry reforming of methane, Chemical communications, 53 (2017) 7549-7552.

[13] X. Yang, W. Wang, L. Wu, X. Li, T. Wang, S. Liao, Effect of confinement of TiO_2 nanotubes

over the Ru nanoparticles on Fischer-Tropsch synthesis, Applied Catalysis A: General, 526 (2016) 45-52.

[14] X. Pan, Z. Fan, W. Chen, Y. Ding, H. Luo, X. Bao, Enhanced ethanol production inside carbon-nanotube reactors containing catalytic particles, Nature materials, 6 (2007) 507-511.

[15] P. Serp, E. Castillejos, Catalysis in Carbon Nanotubes, ChemCatChem, 2 (2010) 41-47.

[16] W. Chen, Z. Fan, X. Pan, X. Bao, Effect of confinement in carbon nanotubes on the activity of Fischer-Tropsch iron catalyst, Journal of the American Chemical Society, 130 (2008) 9414-9419.

[17] W. Chen, X. Pan, X. Bao, Tuning of redox properties of iron and iron oxides via encapsulation within carbon nanotubes, Journal of the American Chemical Society, 129 (2007) 7421-7426.

[18] X. Chen, D. Deng, X. Pan, X. Bao, Iron catalyst encapsulated in carbon nanotubes for CO hydrogenation to light olefins, Chinese Journal of Catalysis, 36 (2015) 1631-1637.

[19] J. Xiao, X. Pan, S. Guo, P. Ren, X. Bao, Toward fundamentals of confined catalysis in carbon nanotubes, Journal of the American Chemical Society, 137 (2014) 477-482.

[20] Z. Yang, S. Guo, X. Pan, J. Wang, X. Bao, FeN nanoparticles confined in carbon nanotubes for CO hydrogenation, Energy & Environmental Science, 4 (2011) 4500-4503.

[21] A.H. Lu, X. Bao, Carbon in the Catalysis Community, ChemCatChem, 7 (2015) 2724-2725.

[22] G. Jacobs, W. Ma, P. Gao, B. Todic, T. Bhatelia, D.B. Bukur, B.H. Davis, The application of synchrotron methods in characterizing iron and cobalt Fischer-Tropsch synthesis catalysts, Catalysis today, 214 (2013) 100-139.

[23] L. Sciortino, A. Alessi, F. Messina, G. Buscarino, F.M. Gelardi, Structure of the FeBTC metal-organic framework: a model based on the local environment study, The Journal of Physical Chemistry C, 119 (2015) 7826-7830.

[24] X. Pan, X. Bao, The effects of confinement inside carbon nanotubes on catalysis, Accounts of chemical research, 44 (2011) 553-562.

[25] C. Wang, X. Pan, X. Bao, Direct production of light olefins from syngas over a carbon nanotube confined iron catalyst, Chinese Science Bulletin, 55 (2010) 1117-1119.

[26] Q. Cheng, Y. Tian, S. Lyu, N. Zhao, K. Ma, T. Ding, Z. Jiang, L. Wang, J. Zhang, L. Zheng, F. Gao, L. Dong, N. Tsubaki, X. Li, Confined small-sized cobalt catalysts stimulate carbon-chain growth reversely by modifying ASF law of Fischer-Tropsch synthesis, Nature Communications, 9 (2018) 3250.

[27] K. Mai, T. Elder, L.H. Groom, J.J. Spivey, Fe-based Fischer Tropsch synthesis of biomass-derived syngas: effect of synthesis method, Catalysis Communications, 65 (2015) 76-80.

[28] V. Subramanian, V.V. Ordomsky, B. Legras, K. Cheng, C. Cordier, P.A. Chernavskii, A.Y. Khodakov, Design of iron catalysts supported on carbon-silica composites with enhanced catalytic performance in high-temperature Fischer-Tropsch synthesis, Catalysis Science & Technology, 6 (2016) 4953-4961.

[29] R.M.M. Abbaslou, A. Tavassoli, J. Soltan, A.K. Dalai, Iron catalysts supported on carbon nanotubes for Fischer-Tropsch synthesis: Effect of catalytic site position, Applied Catalysis A:

General, 367 (2009) 47-52.

[30] T. Li, Y. Yang, C. Zhang, X. An, H. Wan, Z. Tao, H. Xiang, Y. Li, F. Yi, B. Xu, Effect of manganese on an iron-based Fischer-Tropsch synthesis catalyst prepared from ferrous sulfate, Fuel, 86 (2007) 921-928.

[31] P. Chernavskii, V. Kazak, G. Pankina, V. Ordomsky, A. Khodakov, Mechanistic Aspects of the Activation of Silica-Supported Iron Catalysts for Fischer-Tropsch Synthesis in Carbon Monoxide and Syngas, ChemCatChem, 8 (2016) 390-395.

[32] S. Li, G.D. Meitzner, E. Iglesia, Structure and site evolution of iron oxide catalyst precursors during the Fischer-Tropsch synthesis, The Journal of Physical Chemistry B, 105 (2001) 5743-5750.

[33] S. Abelló, D. Montané, Exploring Iron-based Multifunctional Catalysts for Fischer-Tropsch Synthesis: A Review, ChemSusChem, 4 (2011) 1538-1556.

[34] E. de Smit, B.M. Weckhuysen, The renaissance of iron-based Fischer-Tropsch synthesis: on the multifaceted catalyst deactivation behaviour, Chemical Society Reviews, 37 (2008) 2758-2781.

[35] J.B. Butt, Carbide phases on iron-based Fischer-Tropsch synthesis catalysts part I: Characterization studies, Catalysis Letters, 7 (1990) 61-81.

[36] K. Cheng, V. Ordomsky, M. Virginie, B. Legras, P. Chernavskii, V. Kazak, C. Cordier, S. Paul, Y. Wang, A. Khodakov, Support effects in high temperature Fischer-Tropsch synthesis on iron catalysts, Applied Catalysis A: General, 488 (2014) 66-77.

[37] Y. Cheng, J. Lin, T. Wu, H. Wang, S. Xie, Y. Pei, S. Yan, M. Qiao, B. Zong, Mg and K dual-decorated Fe-on-reduced graphene oxide for selective catalyzing CO hydrogenation to light olefins with mitigated CO_2 emission and enhanced activity, Applied Catalysis B: Environmental, 204 (2017) 475-485.

[38] B. An, K. Cheng, C. Wang, Y. Wang, W. Lin, Pyrolysis of Metal-Organic Frameworks to Fe_3O_4@Fe_5C_2 Core-Shell Nanoparticles for Fischer-Tropsch Synthesis, ACS Catalysis, 6 (2016) 3610-3618.

[39] Y. Cheng, J. Lin, K. Xu, H. Wang, X. Yao, Y. Pei, S. Yan, M. Qiao, B. Zong, Fischer-Tropsch synthesis to lower olefins over potassium-promoted reduced graphene oxide supported iron catalysts, ACS catalysis, 6 (2015) 389-399.

[40] V.P. Santos, T.A. Wezendonk, J.J.D. Jaén, A.I. Dugulan, M.A. Nasalevich, H.-U. Islam, A. Chojecki, S. Sartipi, X. Sun, A.A. Hakeem, Metal organic framework-mediated synthesis of highly active and stable Fischer-Tropsch catalysts, Nature communications, 6 (2015) 6451.

[41] H.M. Torres Galvis, J.H. Bitter, T. Davidian, M. Ruitenbeek, A.I. Dugulan, K.P. de Jong, Iron particle size effects for direct production of lower olefins from synthesis gas, Journal of the American Chemical Society, 134 (2012) 16207-16215.

[42] J. Guan, X. Pan, X. Liu, X. Bao, Syngas segregation induced by confinement in carbon nanotubes: a combined first-principles and Monte Carlo study, The Journal of Physical Chemistry C, 113 (2009) 21687-21692.

[43] W. Ngantsoue-Hoc, Y. Zhang, R.J. O'Brien, M. Luo, B.H. Davis, Fischer–Tropsch synthesis:

activity and selectivity for Group I alkali promoted iron-based catalysts, Applied Catalysis A: General, 236 (2002) 77-89.

[44] H. Xiong, M.A. Motchelaho, M. Moyo, L.L. Jewell, N.J. Coville, Effect of Group I alkali metal promoters on Fe/CNT catalysts in Fischer-Tropsch synthesis, Fuel, 150 (2015) 687-696.

[45] K. Cheng, V.V. Ordomsky, B. Legras, M. Virginie, S. Paul, Y. Wang, A.Y. Khodakov, Sodium-promoted iron catalysts prepared on different supports for high temperature Fischer-Tropsch synthesis, Applied Catalysis A: General, 502 (2015) 204-214.

[46] C.H. Bartholomew, Mechanisms of catalyst deactivation, Applied Catalysis A: General, 212 (2001) 17-60.

[47] H.M. Torres Galvis, K.P. de Jong, Catalysts for production of lower olefins from synthesis gas: a review, ACS catalysis, 3 (2013) 2130-2149.

Chapter 5. Size and Promoter Effects on Iron Nanoparticles Confined in Carbon Nanotubes and their Catalytic Performance in Light Olefin Synthesis from Syngas

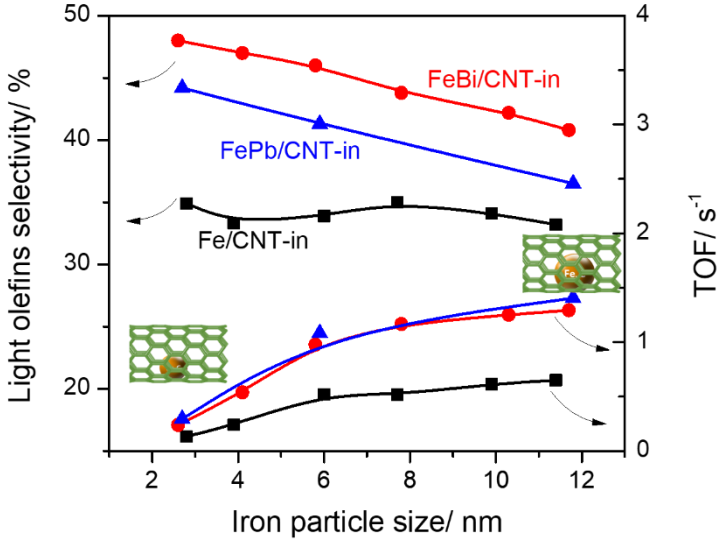

Abstract: Light olefins are important products of high temperature Fischer-Tropsch synthesis over iron catalysts. In this chapter, we found that the catalytic performance of iron catalysts was strongly affected by iron nanoparticle size, their encapsulation inside of carbon nanotubes and promotion with bismuth or lead. The presence of promoters and iron nanoparticle confinement leads to a major increase in the reaction rate. A gradual increase in the TOF numbers with the increase in the iron nanoparticle sizes from 2.5 to 12 nm was observed at both 1 and 10 bar over the carbon nanotubes containing encapsulated monometallic or Bi- or Pb-promoted iron nanoparticles. The size of monometallic iron nanoparticles encapsulated in carbon nanotubes does not show any noticeable effect on the light olefin selectivity, while in the Bi- and Pb-promoted catalysts, the light olefin selectivity was higher over smaller encapsulated iron nanoparticles and decreased with the increase in the nanoparticle size. The stability of iron nanoparticles versus sintering was also improved by the encapsulation.

This chapter is based on the following publication:

Bang Gu, Cheng Zhou, Shun He, Simona Moldovan, Petr A. Chernavskii, Vitaly V. Ordomsky,* and Andrei Y. Khodakov,* *Catalysis Today*, **2019**, (In Press).

5.1 Introduction

FT synthesis is often considered as a structure sensitive reaction and particle size may have noticeable effects both on the activity and selectivity [1-4]. The particle size effects over cobalt [5-8] and ruthenium-based [9-11] catalysts in low temperature FT synthesis have been addressed in numerous publications. The optimum cobalt and ruthenium size were found to be about 6-8 nm. The increase in the size of metal nanoparticles above 8 nm leads to lower overall activity, while the metal particles with the sizes smaller than 6 nm demonstrate both lower intrinsic activity (Turnover Frequency, TOF) and lower selectivity toward the C_{5+} hydrocarbons. The particle size effects over iron-based FT catalysts can be rather complex, because of simultaneous presence of different iron phases and catalyst deactivation.

Previous reports suggest that the selectivities to methane and lighter hydrocarbons increase, when iron nanoparticles in supported catalysts are getting smaller than 6-9 nm [12]. TOF increases with the increase in the particle sizes from 2.4 to 6.2 nm and it remains almost constant up to the particle size of 11.5 nm. The stability of iron particles in silica-supported catalysts was previously studied [13, 14] in the nanoscale range (9-20 nm). On the one hand, smaller iron-carbide nanoparticles were found more difficult to obtain by carbidization of iron oxides and on the other hand, they were less stable than larger particles**.**

The iron particle size effects on the catalytic performance in FT synthesis might be influenced by catalyst promotion and metal-support interactions. In the oxide-supported catalysts, the active metal can react with a support and form barely reducible aluminates or silicates and thus, hinder formation and reduce the stability of active iron carbide phase. The metal support interactions are usually weaker in the carbon-supported catalysts. De Jong [15, 16] *et al* examined the influence of iron carbide particle size in the promoted and unpromoted carbon nanofiber supported iron catalysts on the syngas conversion to light olefins. The TOF numbers of unpromoted catalysts increased 6-8 times with particle size decreasing from 7 to 2 nm, while the selectivity to methane or

light olefins were found independent on the particle size [15]. The iron catalysts promoted with sodium and sulphur showed similar variation of TOF as a function of particle size. The increase in TOF with decrease in iron particle size in the promoted catalysts was principally due to higher yield of methane over the smallest particles. Recently, we have discovered strong promoting effects of Bi and Pb on the catalytic performance of Fe catalysts in FT synthesis [17, 18]. The effects have been attributed to the enhanced C-O dissociation on the surface of iron carbide nanoparticles in the presence of Bi and Pb, which significantly increases catalyst activity and selectivity to light olefins.

A number of previous works suggest important influence of iron nanoparticles confinement in carbon nanotubes (CNT) on the electronic structure, catalytic performance and stability of iron FT catalysts [19-21]. Bao [22] et al found that iron nanoparticles confined in CNT exhibited better reducibility, carbidization and much higher activity in FT synthesis compared to the unconfined counterparts, while the selectivity to light olefins was not much affected by the confinement [23, 24]. Higher reaction rate was principally attributed to higher extent of iron carbidization inside CNTs. The encapsulation of nanoparticles also protects them from sintering [25]. Analysis of the electron distribution in CNT using DFT [26] showed that the curvature of the CNT induced a significant electron disparity. More electrons were distributed on the exterior surface of the CNT. This led to stronger bonding of iron species with the outside CNT surface than those located the inside CNT walls. These electronic effects might result in different catalytic activity of iron inside and outside CNT.

The present work addresses the size effects of iron nanoparticles encapsulated inside of CNT on syngas conversion to light olefins. To the best of our knowledge, there have been no studies about the effect of the size of iron nanoparticles confined inside CNT on their properties and catalytic performance. Both monometallic iron catalysts and catalysts promoted with bismuth and lead have been studied. The syngas conversion to light olefins has been performed at both high and atmospheric pressures at the temperatures typical of high temperature FT synthesis.

5.2 Results and Discussion

5.2.1 Catalyst structure

Tables 5.1 and 5.2 show textural properties and elemental composition of the CNTs supported monometallic and Bi- or Pb-promoted iron nanoparticles exposed to different temperatures. The impregnation of CNTs with iron decreases the surface area, total pore volume and mesopore diameter. Interestingly, the pore volume is decreased after introduction of iron from 0.83 cm^3/g to about 0.50 cm^3/g. This suggests that some iron particles are located inside of the CNT tubes. Localization of iron nanoparticles inside CNT leads to the decrease in the pore volume and partial blocking of the tubes. The presence of the Bi and Pb promoters, in addition to iron, results in only very small effect on the texture of CNT catalysts. Indeed, the BET surface area and pore volume are almost not affected by the presence of the promoters.

Table 5.1. *Characterization of the supports and CNT confined monometallic Fe catalysts.*

Sample	S_{BET}[a] (m^2/g)	V_{tot}[b] (cm^3/g)	D_{meso}[c] (nm)	D_{metal}[d] (nm)	D_{metal}[e] (nm)	Total H_2 consumption[f] (mmol/g)	Fe content[g] (wt%)
CNT-raw	138.2	0.43	14.0				
CNT-HNO_3	230.3	0.83	14.4	-	-	-	-
Fe/CNT-in-300	205.3	0.53	10.9	-	2.8	2.40	10.9
Fe/CNT-in-350	198.7	0.51	10.6	3.8	3.9	-	10.7
Fe/CNT-in-400	192.9	0.52	10.8	6.0	6.0	1.80	10.3
Fe/CNT-in-450	188.3	0.50	11.1	7.8	7.7	-	11.3
Fe/CNT-in-500	193.6	0.51	10.8	11.2	9.9	1.60	11.1
Fe/CNT-in-600	199.9	0.53	11.2	12.7	11.4	1.52	10.7

[a] BET surface area.
[b] Single point desorption total pore volume of pores, P/P_0=0.975.
[c] The pore diameter in the mesoporous region evaluated by the BJH method.
[d] Average particle size of iron oxide by XRD.
[e] Average particle size of iron oxide by TEM.
[f] The total H_2 consumption and iron reducibility degree from TPR analysis.
[g] The Fe content from ICP-OES.

The elemental analysis (Tables 5.1 and 5.2) shows that all monometallic iron catalysts supported by carbon nanotube treated in nitrogen at different temperatures contain around 10 wt. % iron. Iron content in the promoted catalysts was also close to10 wt. %, while the contents of bismuth and lead were respectively ~0.85 wt. % and ~0.90 wt. %.

Table 5.2. *Characterization of CNT with confined iron nanoparticles promoted with Bi or Pb.*

Sample	S_{BET}[a] (m^2/g)	V_{tot}[b] (cm^3/g)	D_{meso}[c] (nm)	D_{metal}[d] (nm)	D_{metal}[e] (nm)	Total H_2 consumPtion[f] (mmol/g)	Fe content[g] (wt%)	Bi or Pb content[g] (wt%)
CNT	230.3	0.83	14.4	-	-	-	-	
FeBi/CNT-in-300	200.3	0.52	11.0	-	2.6	3.0	10.2	0.88
FeBi/CNT-in-350	193.7	0.52	11.2	3.9	4.1	2.83	10.8	0.84
FeBi/CNT-in-400	183.3	0.52	11.3	6.2	5.8	2.53	10.5	0.92
FeBi/CNT-in-450	173.3	0.50	10.4	8.3	7.8	2.51	11.2	0.86
FeBi/CNT-in-500	176.6	0.48	10.8	10.8	10.3	2.40	11.3	0.83
FeBi/CNT-in-600	179.9	0.45	11.2	11.9	11.7	2.12	10.9	0.87
FePb/CNT-in-300	208.2	0.51	10.7	-	2.7	2.70	10.9	0.90
FePb/CNT-in-400	187.8	0.50	10.2	5.3	5.9	2.18	10.6	0.88
FePb/CNT-in-600	180.1	0.48	10.5	11.5	11.8	1.85	11.0	0.87

[a]BET surface area.

[b] Single point desorption total pore volume of pores, P/P_0=0.975.

[c] The pore diameter in the mesoporous region evaluated by the BJH method.

[d] Average particle size of iron oxide by XRD.

[e] Average particle size of iron oxide by TEM.

[f] The total H_2 consumption and iron reducibility degree from TPR analysis.

[g] Fe, Bi, Pb content from ICP-OES.

Figure 5.1a displays XRD profiles of the CNT containing confined monometallic and promoted iron nanoparticles treated in nitrogen at different temperatures. The peaks at 26.3° and 43.8° are attributed to the (002) and (101) reflections of the CNT supports [27]. The diffraction lines at 2θ of 30.2° and 35.6° can be assigned to the hematite phase (Fe_2O_3, JCPDS13-0534), while the diffraction lines at 2θ of 35.8°,43.5° and 53.9° can

be ascribed to the magnetite phase (Fe_3O_4, JCPDS 75-0449). The iron oxide peaks become sharper with higher pre-treatment temperature probably due to increase in the iron oxide particle sizes. The iron crystallite sizes have been evaluated from the Scherrer equation (Table 5.1). The iron crystallite size increases from 2.6-2.8 nm for the iron catalysts treated at 300 °C to 11-12 nm for the catalysts treated in nitrogen at 600 °C. Note that the promotion with Bi and Pb does not noticeably affect the iron oxide particle size (Table 5.2).

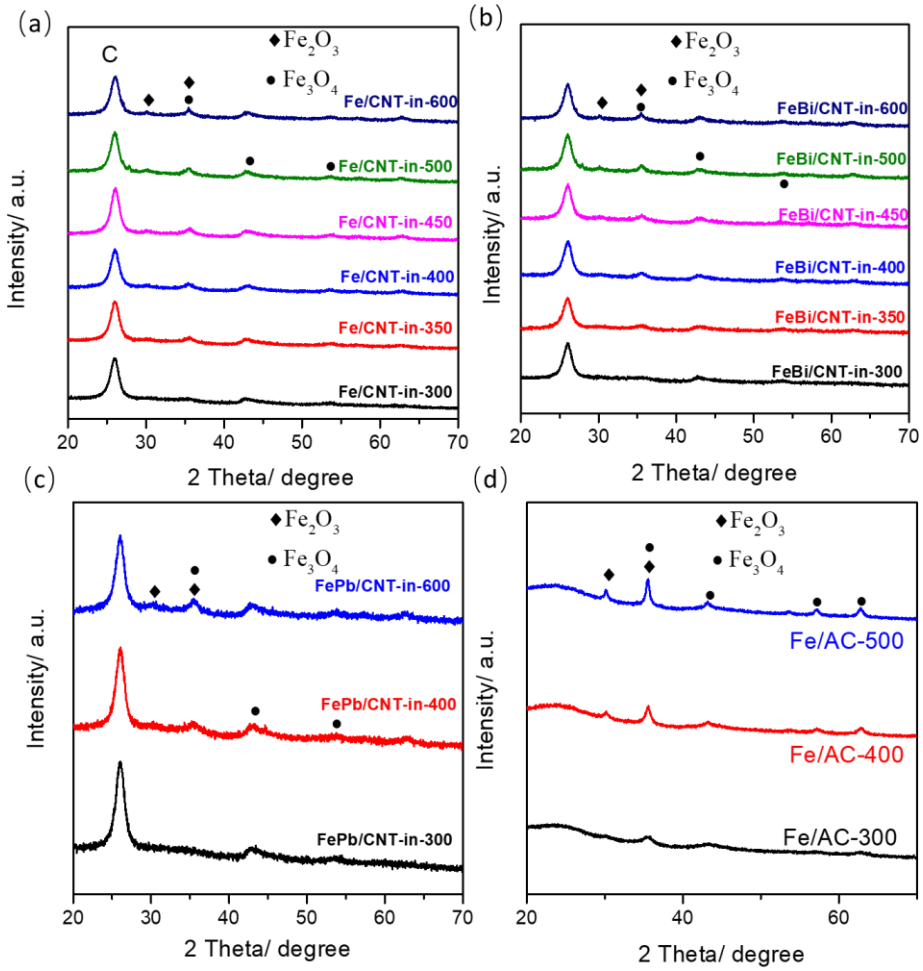

Figure 5.1. *XRD profiles of the supported iron catalysts with different calcination temperature. (a) Fe/CNT-in, (b) FeBi/CNT-in (c) FePb/CNT-in. (d) Fe/AC.*

Our previous studies [17, 18] also showed insignificant effect of the bismuth and lead promotions on iron dispersion and iron oxide nanoparticle sizes in the SiO_2 and CNT supported iron catalysts. The confined iron catalysts contain smaller particles compared with the Fe/AC iron catalysts supported on active carbon **(**Figure 5.1d and Table 5.5).

The difference is more pronounced, when the Fe/AC catalysts were calcined at higher temperatures. It is interesting to note that maximum size of encapsulated metal oxide nanoparticles corresponds to the internal diameter of CNT (14.4 nm). This is consistent with localization of iron oxide nanoparticles inside the CNT and suggests that the growth of iron oxide crystallites inside the CNT could be limited by the CNT diameter.

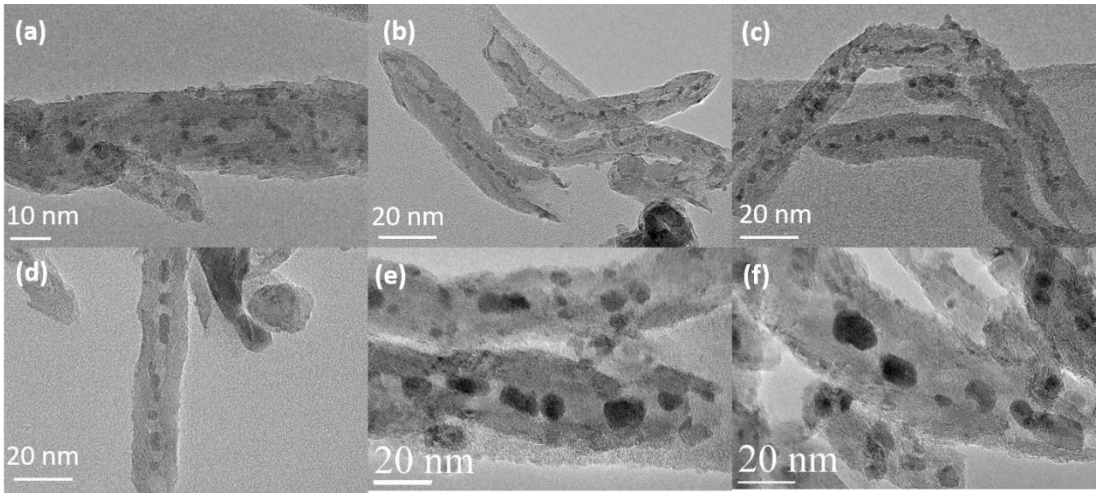

Figure 5.2. *TEM images of the CNT confined iron catalysts under different calcination temperature. (a) Fe/CNT-in-300, (b) Fe/CNT-in-350, (c) Fe/CNT-in-400, (d) Fe/CNT-in-450, (e) Fe/CNT-in-500, (f) Fe/CNT-in-600.*

The TEM images and particle size distribution of the encapsulated monometallic iron catalysts with different calcination temperatures are shown in Figures 5.2 and 5.3**.** It is clear that most of the particles are located inside of the nanotubes. This clearly confirms confinement of iron nanoparticles inside the CNT in the prepared catalysts. The iron oxides particles size increases from 2.8 nm to 11.4 nm with increase in the pre-treatment temperature. The iron oxide nanoparticle size measured by TEM is consistent with XRD results. The TEM images and particle size distribution for the Bi- or Pb-promoted iron catalysts at different calcination temperature are shown in Figures 5.4, 5.5 and 5.6**.** Importantly, in the catalysts, iron oxide nanoparticles are selectively confined inside the CNT. Similar effects of the pre-treatment temperature on the iron oxide particle sizes were observed with and without promoters (Tables 5.1 and 5.2). Thus, the characterisation suggests that the promoter does not affect the size of metal

nanoparticles.

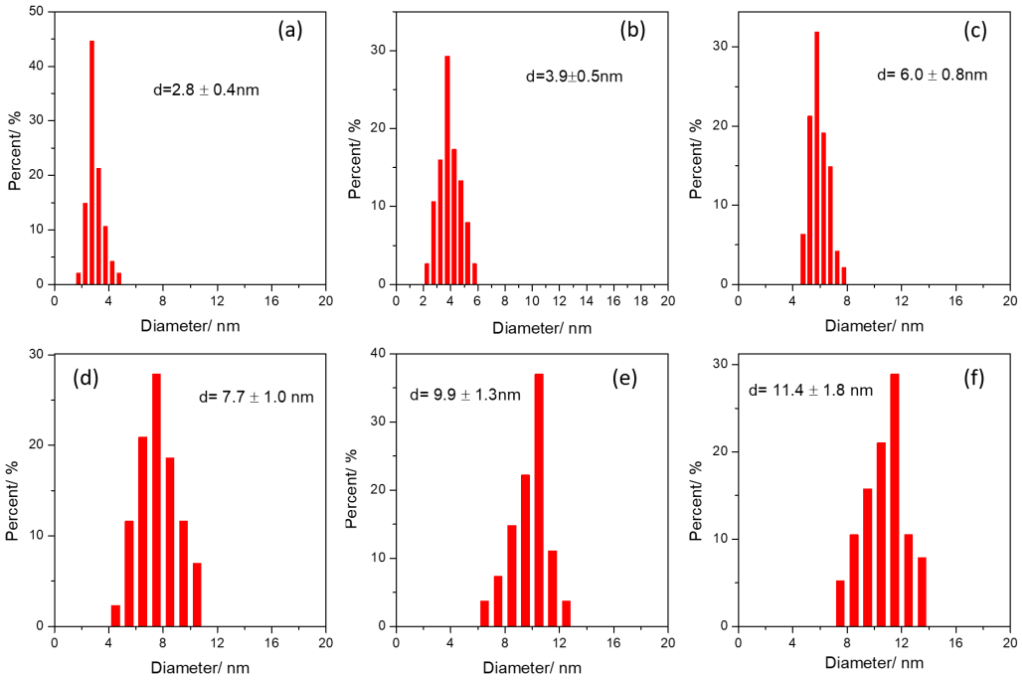

Figure 5.3. *Particle size distribution of the CNT confined iron catalysts under different calcination temperature. (a) Fe/CNT-in-300, (b) Fe/CNT-in-350, (c) Fe/CNT-in-400, (d) Fe/CNT-in-450, (e) Fe/CNT-in-500, (f) Fe/CNT-in-600.*

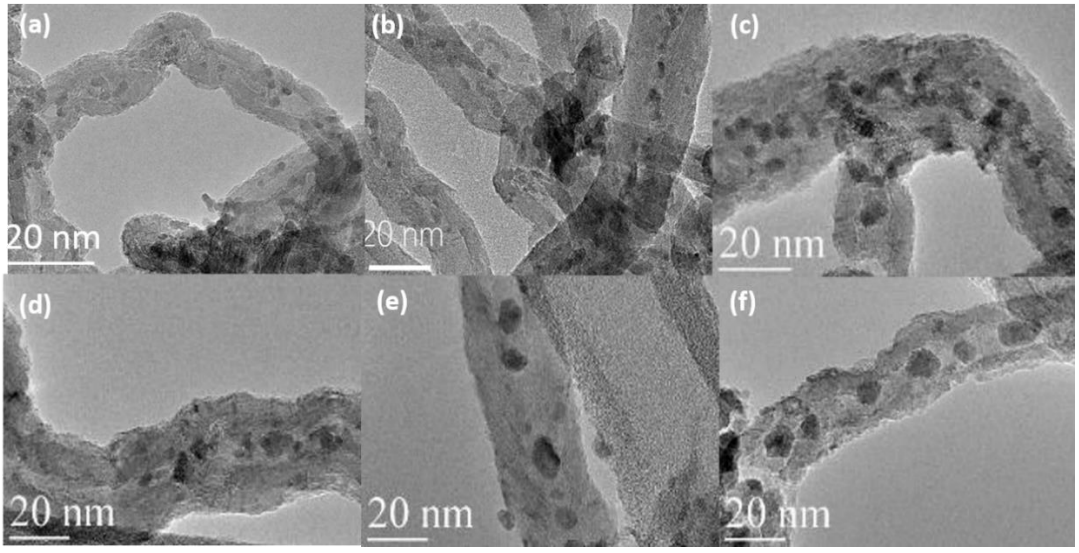

Figure 5.4. *TEM images of the CNT confined iron catalysts promoted with Bi under different calcination temperature. (a) FeBi/CNT-in-300, (b) FeBi/CNT-in-350, (c) FeBi/CNT-in-400, (d) FeBi/CNT-in-450, (e) FeBi/CNT-in-500, (f) FeBi/CNT-in-600.*

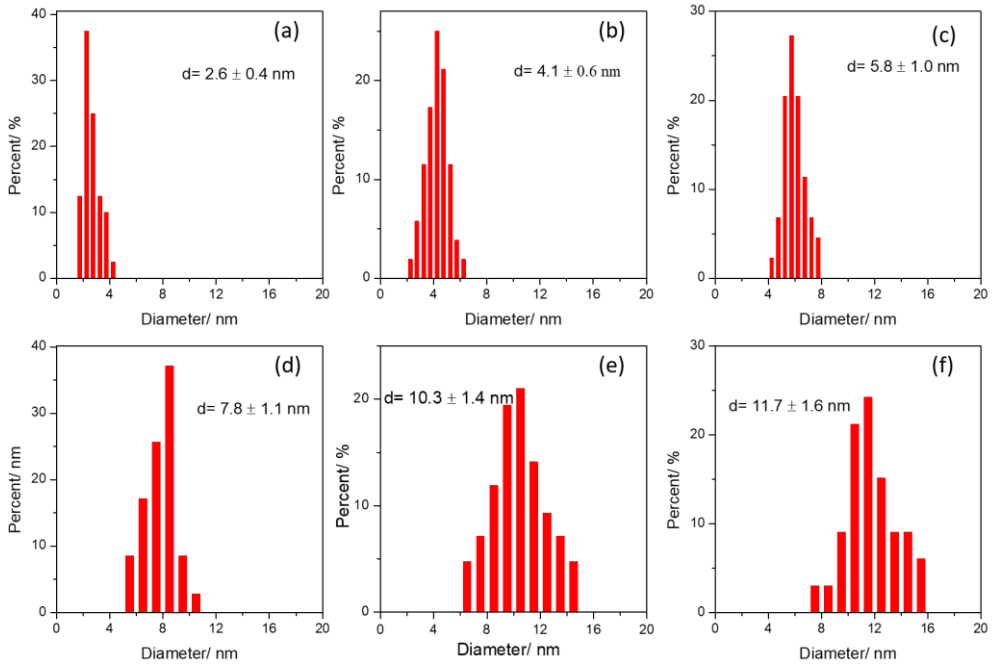

Figure 5.5. *Particle size distribution of the CNT confined iron catalysts promoted with Bi under different calcination temperature. (a)FeBi/CNT-in-300, (b) FeBi/CNT-in-350, (c) FeBi/CNT-in-400, (d) FeBi/CNT-in-450, (e) FeBi/CNT-in-500, (d) FeBi/CNT-in-600.*

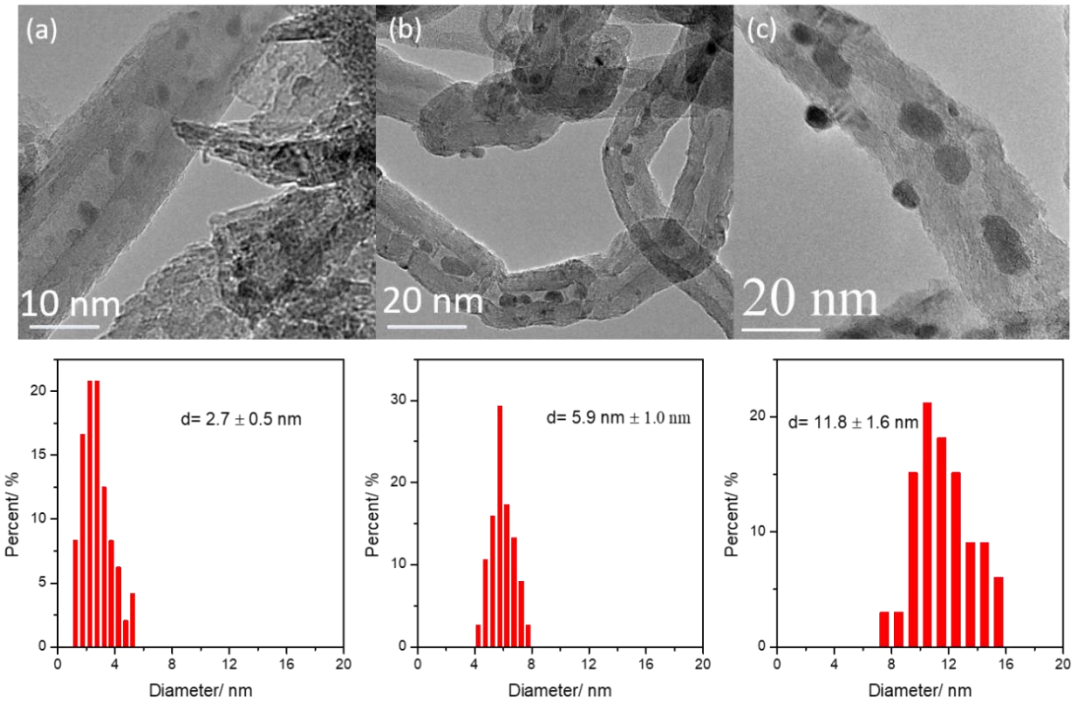

Figure 5.6. *TEM images and particle size distribution of the CNT confined iron catalysts promoted with Pb under different calcination temperature. (a)FePb/CNT-in-300, (b) FePb/CNT-in-400, (c) FePb/CNT-in-600.*

STEM-HAADF and STEM-EDS analysis have been performed in order to further confirm localization of iron and promoters in CNT (Figure 5.7). Bi is a heavier metal compared to iron. In the STEM-HAADF images, the Bi species correspond to brighter spots compared to iron. STEM-EDX indicates that Bi is uniformly distributed on the surface of Fe nanoparticles. These results are similar to our previous data obtained for iron-supported catalysts promoted by Bi and Pb over the SiO_2 and CNT supports. Because of low melting points, metallic bismuth and lead migrate to the iron nanoparticles and form core-shell structures during catalyst activation and reaction. These core-shell structures were identified by the EDS analysis [17, 18].

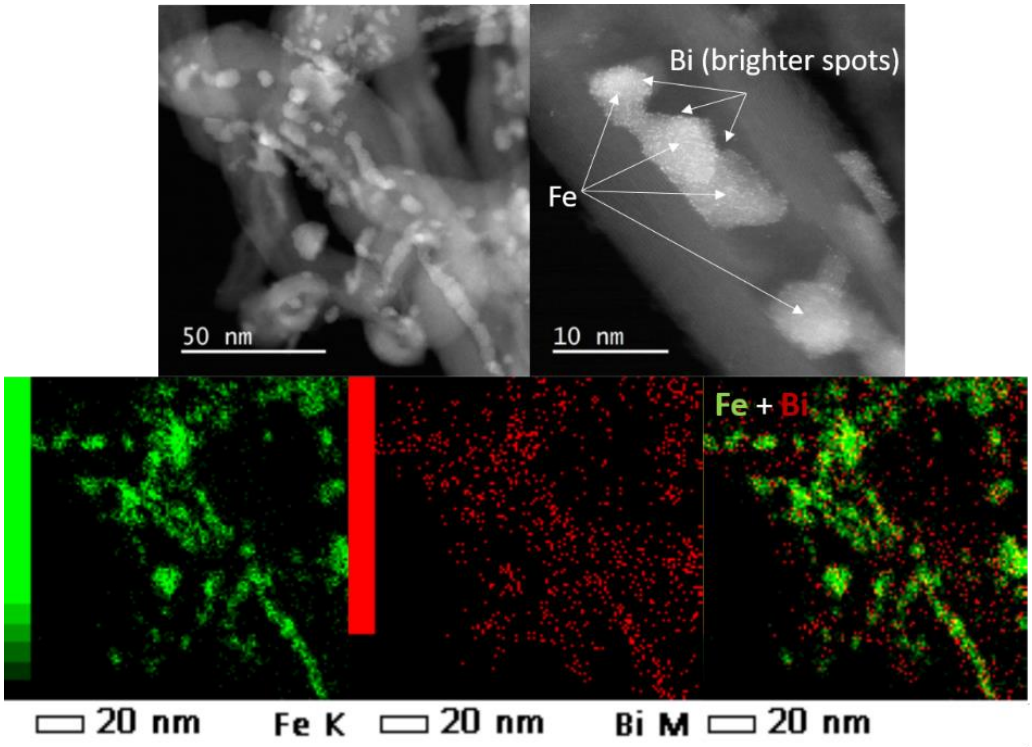

Figure 5.7. *STEM-HAADF and STEM-EDS images for the FeBi/CNT-in-400 catalyst.*

The reducibility of iron oxide nanoparticles encapsulated inside CNT was investigated by H_2-TPR**.** Figure 8a shows the TPR profiles of the monometallic Fe/CNT-in catalysts with encapsulated iron oxide nanoparticles of different sizes. The TPR profiles exhibit three main broad peaks located at around 390, 450 and 650 ºC. According to the literature [21, 28, 29], the first peak can be assigned to the reduction of Fe_2O_3 to Fe_3O_4, the second peak to the reduction of Fe_3O_4 to FeO and the third peak

to the reduction of FeO to metallic Fe. Note that some hydrogen consumption can due to the reductive removal of carboxyl and other oxygen-containing groups from the surface of CNT during the treatment in hydrogen. The small and broad peaks located at 700-800 °C can be caused by gasification of the CNT support [1]. Because of low amounts of bismuth and lead, no TPR peaks could be assigned to the reduction of the promoters**.** The Fe/CNT-out catalyst containing iron nanoparticles outside the CNT channels has been used as a reference (Figure 5.8a). Interestingly, the encapsulated iron catalysts can be reduced at lower temperatures compared with the Fe/CNT-out catalyst. This suggests that the confinement increases the iron reducibility in agreement with the works of Bao' group [22]. Moreover, as the iron particle size inside the CNT channels increases, the intensity of reduction peaks decreases and they slightly shift to lower temperatures. Similar effect also has been discovered by Park [12] over alumina supported iron catalysts with different crystal sizes. This effect might be explained by easier reducibility of larger iron oxide nanoparticles. Easier reducibility of larger metal oxide nanoparticles compared to smaller counterparts has been previously observed in numerous publications [13, 30, 31].

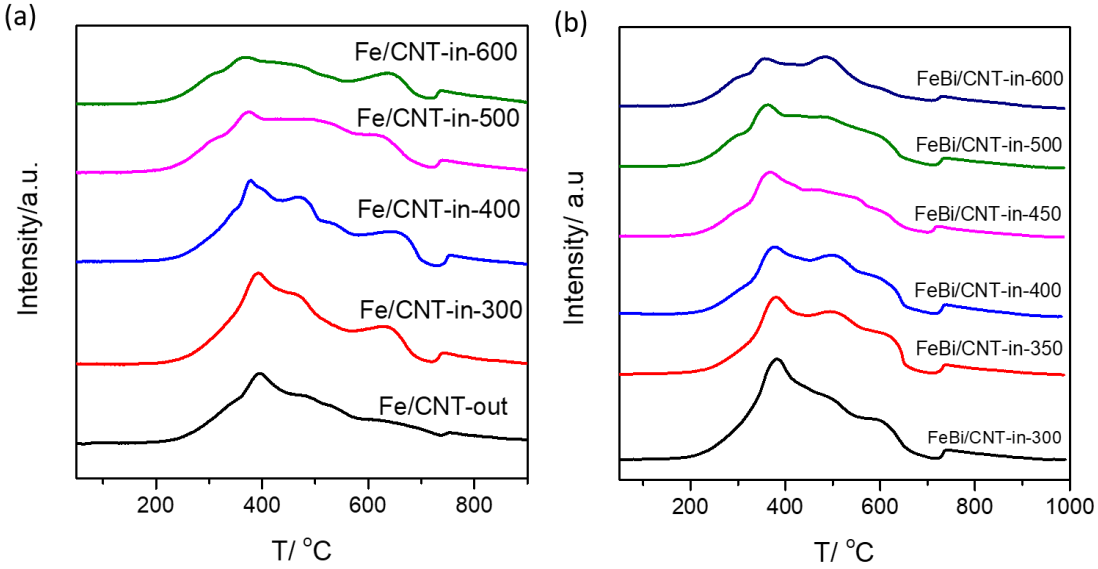

Figure 5.8. *H_2-TPR profiles of the CNT confined iron catalysts under different calcination temperature. (a) Fe/CNT-in, (b) FeBi/CNT-in.*

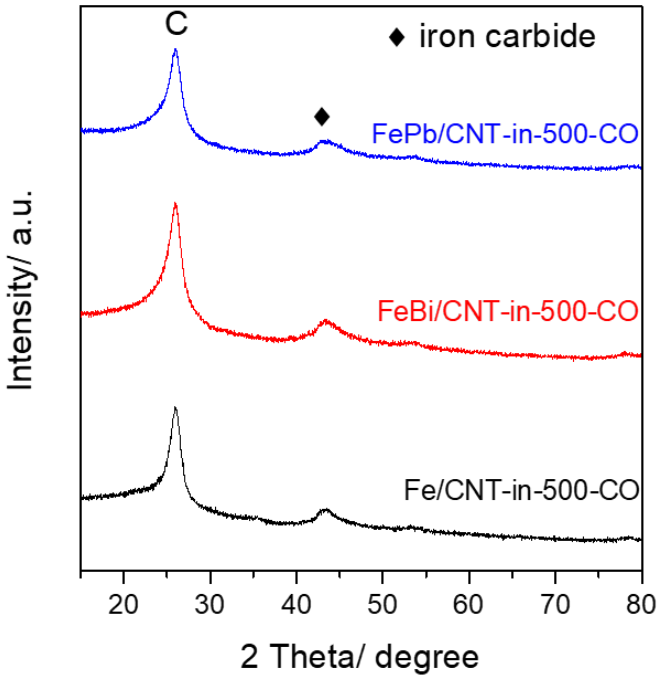

Figure 5.9. *XRD profiles of the activated iron-based confined catalysts after treatment with CO at 350°C for 10h.*

Introduction of the Bi and Pb promoters to the iron catalysts does not change significantly the relative position of the TPR peaks but shifts their maximums by approximately 10 ºC to lower temperatures (Figure 5.8b, Table 5.2). This indicates that promotion of the CNT containing confined iron nanoparticles enhances iron reducibility. Similar effects were also observed recently for the silica and CNT supported FeBi and FePb catalysts [17, 18]. Note that previously prepared promoted iron catalysts supported over CNT contained iron nanoparticles only outside the CNT [18]. Thus, Bi and Pb also promote iron reducibility by increasing total hydrogen consumption and decreasing the reduction temperature in both confined and non-confined systems.

Iron carbide has been considered active phase for iron-based Fischer-Tropsch catalysts. Iron carbide can be formed during activation in the presence of CO prior to the reaction. The XRD for the used catalysts shows a broad peak, which corresponds to the mixture of different iron carbide phase (χ-Fe_5C_2, ε-$Fe_{2.2}C$, Fe_3C, or Fe_7C_3, Figure 5.9). Similar results were obtained for the Fe/CNT and FeBi/CNT catalysts [18]. In order to identify iron carbide phase, the *in-situ* magnetic measurements [32, 33] were conducted in the flow of CO or syngas at different temperatures (Figure 5.10). The two

examined Fe/CNT-in and FeBi/CNT-in catalysts present a similar shape of thermomagnetic curves with the Curie temperature of ~ 250 ºC. According to our previous report [18], the main iron carbide phase has been identified as χ-Fe_5C_2 in the catalysts exposed to the flow of CO or syngas. Interestingly, the iron carbide concentration was higher in the Bi promoted iron catalyst.

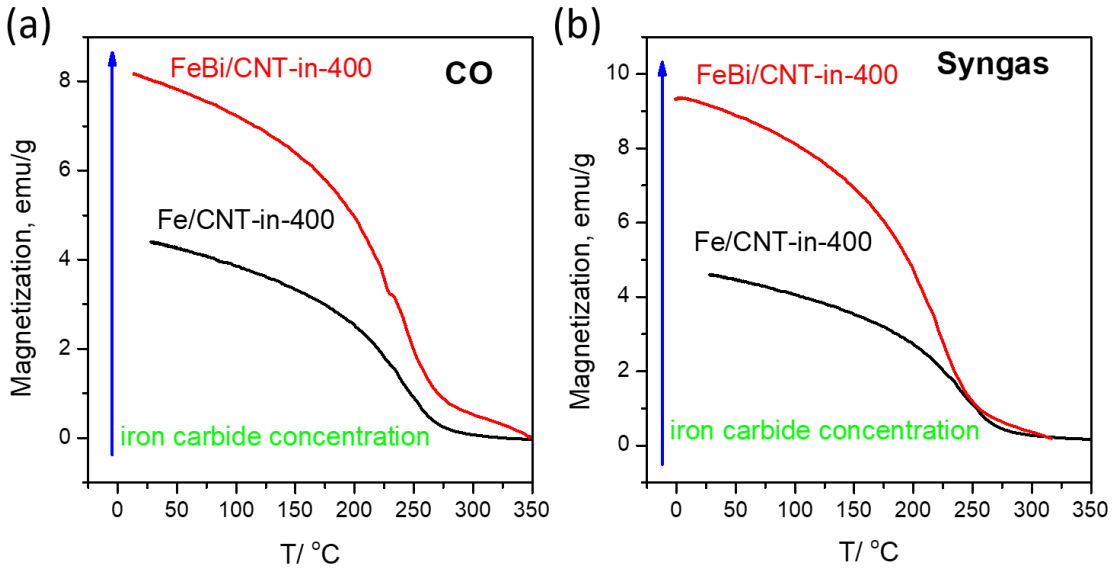

Figure 5.10. *In-situ magnetization characterization: (a) during cooling down after CO treatment at 350 ºC, (b) during cooling down after syngas treatment at 350 ºC.*

5.2.2 Catalytic results

The catalytic data are shown in Tables 5.3 and 5.4 and in Figures 5.11-17. High temperature FT synthesis yields methane, C_2-C_4 hydrocarbons, C_{5+} hydrocarbons, CO_2 and water. The CNT with encapsulated monometallic and Bi- or Pb-promoted iron nanoparticles with different sizes have been tested in a fix-bed reactor both at high (10 bar) and atmospheric pressure at T = 350 ºC and H_2/CO = 1/1. For comparison, Fe/CNT-out and Fe/AC have been also tested under the same conditions (Table 5.3). The activity of Fe/CNT-out is 1.5 times higher than for the Fe/AC catalyst. Note however that the confined catalysts present 2-4 times higher reaction rate compared with the Fe/AC catalyst.

Table 5.3. *Catalytic performance of CNT with encapsulated iron nanoparticles with different sizes in FT synthesis (350 °C, H_2/CO = 1/1, GHSV = 17 L/g.h (10bar) or 3.4 L/g.h (1bar), TOS = 10 h)*

Catalysts	P (bar)	FTY 10^{-4} $mol_{CO}g_{F}^{-1}s^{-1}$	TOF (s^{-1})	CO conv. (%)	CO_2 sel. (%)	Hydrocarbon selectivity (%)				C_2-$C_4^=$/ C_2-C_4^o
						CH_4	C_2-$C_4^=$	C_2-C_4^0	C_{5+}	
Fe/AC	10	0.77	0.244	7.4	28.7	36.2	27.3	22.9	13.6	1.19
Fe/CNT-out	10	1.25	0.288	12.0	29.8	33.6	32.5	19.8	14.1	1.64
Fe/CNT-in-300	10	1.90	0.132	18.3	30.0	29.2	38.2	16.5	16.1	2.32
	1	0.09	0.006	4.3	14.0	33.4	42.0	12.3	12.3	3.41
Fe/CNT-in-350	10	2.50	0.242	24.2	32.0	28.9	37.3	15.5	18.3	2.41
	1	0.12	0.012	5.6	20.0	32.5	41.6	12.1	13.8	3.44
Fe/CNT-in-400	10	3.50	0.521	33.7	40.0	28.5	35.9	15.0	19.9	2.39
	1	0.18	0.027	8.6	27.0	32.1	41.2	11.9	14.8	3.46
Fe/CNT-in-450	10	2.70	0.516	26.0	36.0	28.6	35.7	15.7	20.0	2.27
	1	0.11	0.021	5.4	18.0	31.9	40.9	11.7	15.5	3.50
Fe/CNT-in-500	10	2.80	0.614	27.0	35.0	28.4	36.1	16.0	19.5	2.26
	1	0.11	0.027	5.3	16.0	32.2	41.1	11.8	14.9	3.48
Fe/CNT-in-600	10	2.70	0.651	26.3	33.0	28.1	36.2	16.3	19.4	2.22
	1	0.11	0.031	5.2	15.0	31.5	40.1	11.6	16.8	3.46

Table 5.4. *Catalytic performance of CNT with encapsulated iron nanoparticles with different particle size promoted with Bi and Pb in FT synthesis (350 °C, H_2/CO = 1/1, GHSV = 17 L/g.h (10bar) or 3.4 L/g.h (1bar), TOS = 10 h)*

Catalysts	P (bar)	FTY 10^{-4} $mol_{CO}g_{Fe}^{-1}s^{-1}$	TOF (s^{-1})	CO conv. (%)	CO_2 sel. (%)	Hydrocarbon selectivity (%)				C_2-$C_4^=$/ C_2-C_4^o
						CH_4	C_2-$C_4^=$	C_2-C_4^0	C_5^+	
FeBi/CNT-in-300	10	3.7	0.239	35.7	40.1	26.4	49.0	15.1	9.5	3.25
	1	0.21	0.014	10.3	14.0	28.3	64.0	6.0	1.7	10.70
FeBi/CNT-in-350	10	4.8	0.488	46.2	42.9	25.9	47.0	17.0	10.	2.76
	1	0.37	0.038	17.6	20.0	27.6	63.2	6.5	2.7	9.72
FeBi/CNT-in-400	10	6.1	0.878	58.7	46.0	25.5	45.0	17.0	12.	2.65
	1	0.52	0.075	25.1	31.0	27.3	62.6	6.7	3.4	9.34
FeBi/CNT-in-450	10	5.0	0.968	48.0	43.3	25.3	43.8	18.7	12.	2.34
	1	0.43	0.083	20.6	18.0	26.8	62.0	6.9	4.3	8.99
FeBi/CNT-in-500	10	4.9	1.252	47.0	41.3	24.6	42.2	20.7	12.	2.04
	1	0.38	0.097	18.3	16.0	26.2	61.1	7.5	5.2	8.15
FeBi/CNT-in-600	10	4.8	1.394	46.3	41.0	24.1	40.8	22.8	12.	1.79
	1	0.36	0.104	17.2	15.0	25.4	60.1	7.9	6.6	7.61
FePb/CNT-in-300	10	4.4	0.295	42.7	40.1	25.0	44.2	19.1	11.	2.31
	1	0.38	0.025	18.3	20.2	25.8	62.0	6.0	6.2	10.30
FePb/CNT-in-400	10	7.4	1.083	70.7	46.0	23.4	39.9	20.7	16.	1.93
	1	0.74	0.108	35.7	36.0	25.0	59.1	8.3	7.6	7.12
FePb/CNT-in-600	10	4.9	1.406	49.3	41.0	20.1	36.5	23.5	19.	1.55
	1	0.42	0.123	20.2	26.0	22.1	55.5	10.7	11.	5.19

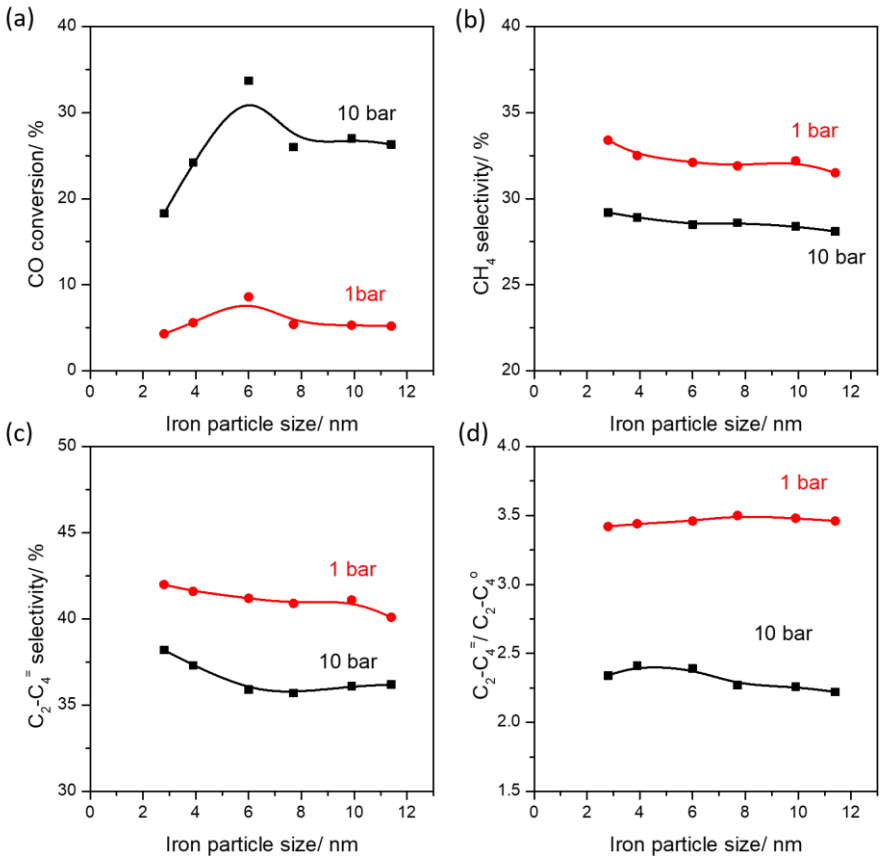

Figure 5.11. *CO conversion and products selectivity versus iron particle size over unpromoted iron catalysts. The reaction condition: 350 °C, H_2/CO = 1/1, GHSV = 17 L/g.h, P = 1 or 10 bar, TOS = 10 h.*

The selectivity to light olefins and C_{5+} hydrocarbons follows the sequence: Fe/AC < Fe/CNT-out < Fe/CNT-in, whereas the methane selectivity shows the opposite trend. These results are consistent with earlier data of Bao's group [22]. The effect of confinement on the chain growth probability is relatively small, while the ratio of olefins to paraffins increases in the confined catalysts. Stronger interaction of CO with the CNT internal surface [34, 35] can lead to lower H_2/CO ratio inside the CNT and thus decreases the secondary olefin hydrogenation. Figure 11 displays CO conversion and products selectivities for the CNT containing encapsulated iron monometallic nanoparticles as functions of iron particle sizes. At high pressure and at GHSV = 17 L/g.h, carbon monoxide conversion over monometallic iron catalysts increases from 18 to 34 % with the increase in the encapsulated iron particle sizes from 2.8 to 6 nm. Interestingly, further increase in the iron nanoparticle sizes leads to the decrease in the

CO conversion. Note that the FT reaction rates were much lower at atmospheric pressure compared to the tests conducted at 10 bar. The selectivities to methane and light olefins over the iron unpromoted nanoparticles at the 10 bar test were about 28 % and 37 %, respectively. Interestingly, these two values do not change much with increasing iron particles size.

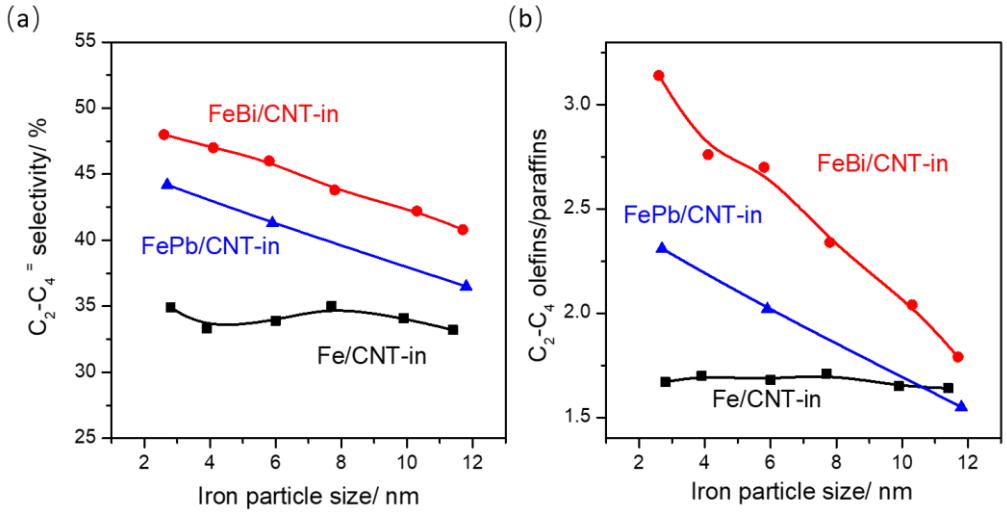

Figure 5.12. *C_2-C_4 olefin selectivity and olefin to paraffin ratio as function of the size of iron nanoparticles confined in CNT at CO conversion of 40-50 %. The reaction condition: 350 °C, H_2/CO = 1/1, GHSV = 10.2-23.8 L/g.h, P = 10 bar, TOS = 10 h.*

In order to compare the reaction selectivity, the carbon monoxide conversion was adjusted to the 40-50 % level by varying GHSV. Relevant selectivity data are presented in Figure 5.12**.** The increase in the size of iron nanoparticles encapsulated in CNT does not significantly affect the olefin selectivity and olefin to paraffin ratio over the unpromoted iron catalysts. The selectivity to the C_{5+} hydrocarbons increases from 16.1 to 19.9 % with the iron particles size increase from 2.8 nm to 6.0 nm and then stabilises. Further particle size increase from 6.0 nm to 11.4 nm does not affect the reaction selectivity [12]. For comparison, iron catalysts supported over active carbon with different particles size (Fe/AC) has been tested in FT synthesis (Table 5.5). Similar trend has been found as for the Fe/CNT-in-T catalysts. Thus, we found that over the unpromoted, confined or unconfined iron catalysts, particle size does not noticeable affect the light olefin selectivity. These results are consistent with the data of de Jong

[15] who also observed similar selectivity to methane and light olefins is over the iron particles of different sizes in FT reaction over unpromoted iron catalysts.

Table 5.5. *Catalytic performance of active carbon supported iron nanoparticles with different calcination temperature in FT synthesis (350 °C, H_2/CO = 1/1, GHSV = 17 L/g.h (10bar), TOS = 10 h)*

Catalysts	D_{metal}[a] (nm)	FTY 10^{-4} $mol_{CO}g_{Fe}^{-1}s^{-1}$	TOF (s^{-1})	CO conv. (%)	CO_2 select. (%)	Hydrocarbon selectivity (%)				C_2-$C_4^=$/ C_2-C_4^o
						CH_4	C_2-$C_4^=$	C_2-C_4^0	C_{5+}	
Fe/AC-300	8.8	0.96	0.162	9.2	29.4	36.9	27.0	23.7	12.4	1.14
Fe/AC-400	15.9	0.77	0.244	7.4	28.7	36.2	27.3	22.9	13.6	1.19
Fe/AC-500	21.8	0.63	0.266	6.1	22.5	35.4	28.0	22.6	14.0	1.24

[a]average particle size of iron oxide by XRD

Different to the unpromoted iron catalysts, the size of Bi-promoted and encapsulated iron particles has strong effects both on the activity and selectivity (Figures 5.12 and 5.13). The presence of the promoters significantly increases the FT reaction rate. The FeBi/CNT-in catalyst shows more than 2 times higher FTY in comparison with the Fe/CNT-in catalyst at the pressure of 10 bar (Figures 5.14 - 16)**.** The reaction selectivity shifts to the C_2-C_4 light hydrocarbons compared to the monometallic Fe/CNT-in catalyst. The methane selectivity decreases from ~29 % to ~ 25 % and C_{5+} decreases from ~ 20 % to ~12 %. In addition, the selectivity of light olefins increases from ~ 35 % to ~ 45 %. The selectivity to CO_2 also increases over the FeBi/CNT-in catalysts compared with the monometallic Fe/CNT-in counterparts. The effect can be due to easing CO dissociation on iron carbide via oxygen removal from iron carbide by scavenging with the promoters [18]. The catalytic activity in the presence of the promoters increases with increase in iron nanoparticle size until 6 nm and then decreases at the larger iron nanoparticle sizes. More importantly, this promotion effect is also significant even under atmospheric pressure with the 2-3 times increase in the FTY in comparison with the non-promoted catalysts. Compared with the Bi promoted

iron catalysts, the FePb/CNT-in catalysts present even much more significant increase in FTY (~2.5 times higher than Fe/CNT-in). Different to CNT containing monometallic iron nanoparticles, the C_2-C_4 olefins selectivity and olefin to paraffin ratio decrease with increase in the iron particle size both at 10 bar and under atmospheric pressure (Table 5.4, Figures 5.13 and 5.14). Higher, but slightly different, light olefins selectivity over the promoted iron catalysts with different particle size might be ascribed to different coverages of the iron carbide surface with the promoters. de Jong [15] also observed this effect over Na and S promoted iron catalysts with different iron carbide particle size.

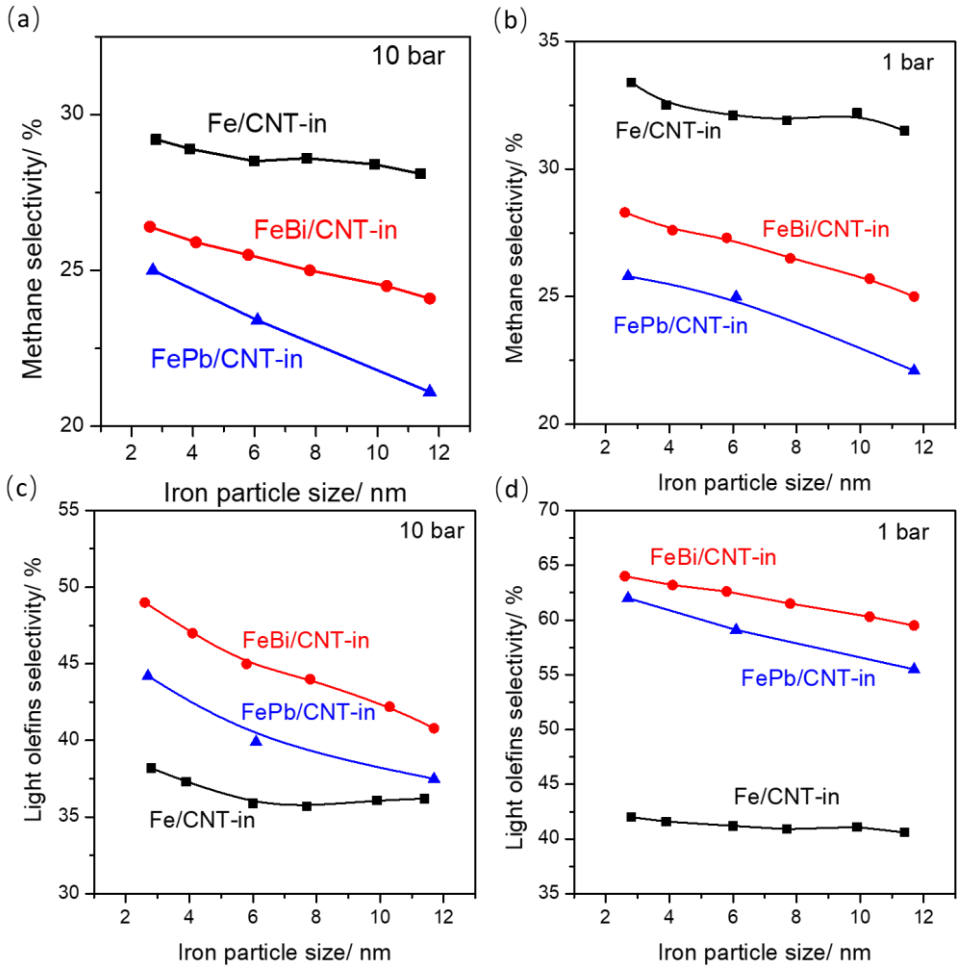

Figure 5.13. *Iron particle size effect on the selectivity of methane and light olefins over Bi or Pb promoted and unpromoted iron catalysts. (350 °C, H_2/CO = 1/1, GHSV = 17 L/g.h (10bar) or 3.4 L/g.h (1bar), TOS = 10 h).*

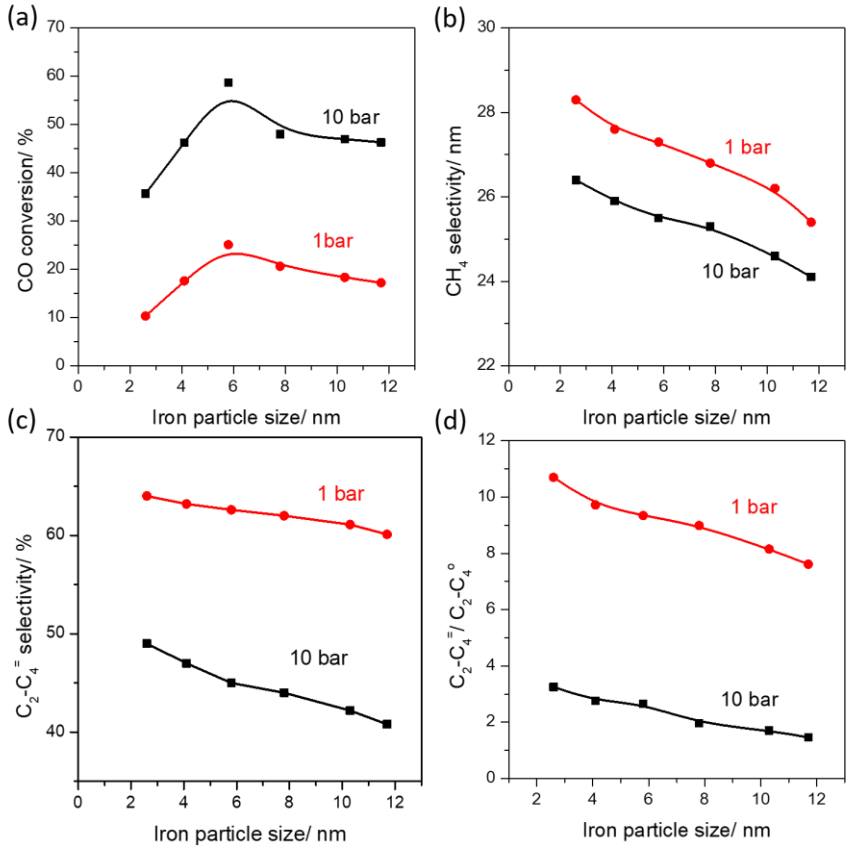

Figure 5.14. *CO conversion and product selectivity versus iron particle size over Bi promoted iron catalysts. (350 °C, H_2/CO = 1/1, GHSV = 17 L/g.h (10bar) or 3.4 L/g.h (1bar), TOS = 10 h).*

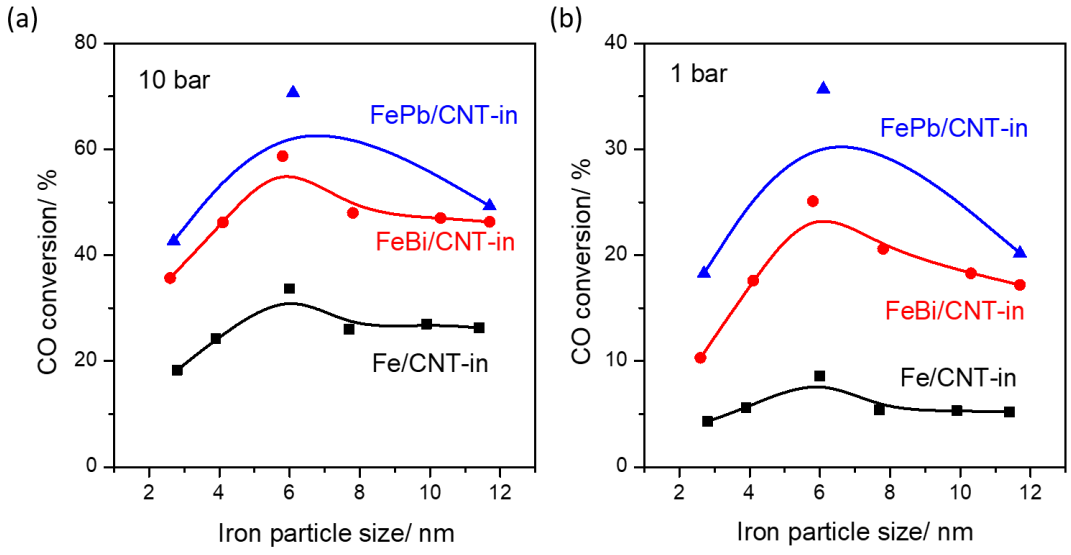

Figure 5.15. *Iron particle size effect on the CO conversion over Bi or Pb promoted and unpromoted iron catalysts (350 °C, H_2/CO = 1/1, GHSV = 17 L/g.h (10bar) or 3.4 L/g.h (1bar), TOS = 10 h).*

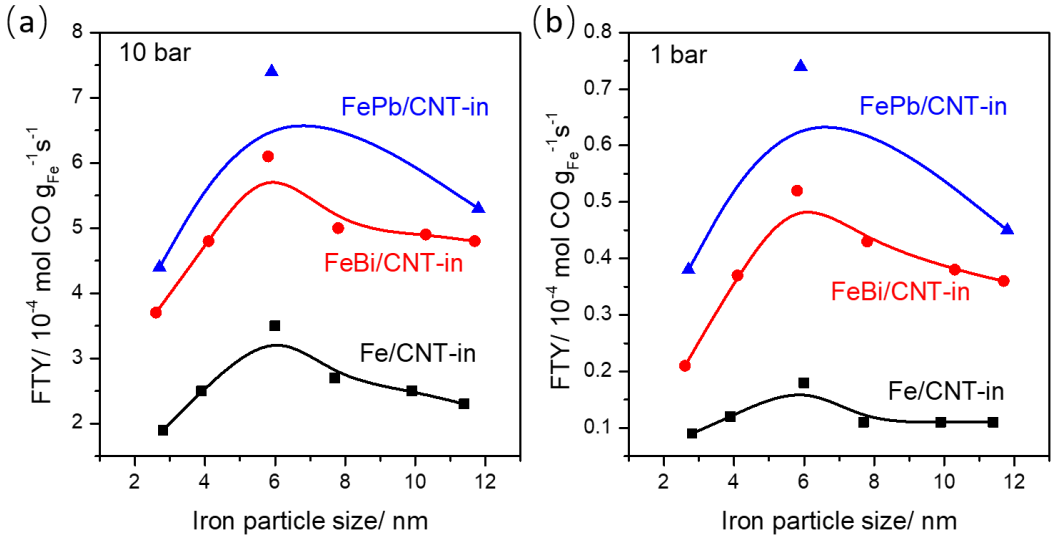

Figure 5.16. *Iron particle size effect on the FTY (350 °C, H_2/CO = 1/1, GHSV = 17 L/g.h (10bar) or 3.4 L/g.h (1bar), TOS = 10h).*

More detailed information about the intrinsic activity of CNT containing encapsulated monometallic iron nanoparticles and those promoted with Bi and Pb was obtained from the TOF values. The TOF values assuming the presence of the Fe_5C_2 under the reaction conditions are presented in Tables 5.3 and 5.4. TOFs are plotted as a function of iron particle size for CNT containing encapsulated monometallic and promoted iron nanoparticles measured at the 10 bar and atmospheric pressure (Figure 5.17). As expected, higher TOF were obtained at higher reaction pressure. The TOF numbers for unpromoted catalysts at both high and low pressure reaction conditions increase rapidly with increase in the particle sizes up to 6 nm and stabilise for larger metal nanoparticles. These results are consistent with those for cobalt and ruthenium catalysts for which TOF increases with the particle size up to 6-8 and stabilize at larger sizes [8, 11]. Park [12] also found the similar results over iron catalysts with varying particle size from 2 nm to 12 nm in FTS. It is noteworthy that the Bi and Pb promoted iron catalysts present ~3 times (10 bar) and ~ 5 times (1 bar) higher TOF values compared with monometallic iron catalysts.

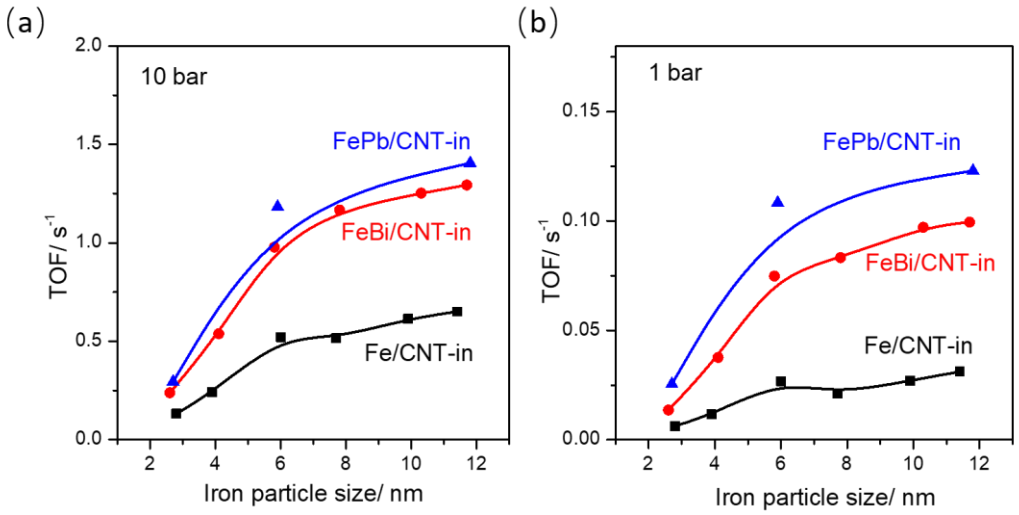

Figure 5.17. *Iron particle size effect on the TOF (350 °C, H_2/CO = 1/1, GHSV = 17 L/g.h (10bar) or 3.4 L/g.h (1bar), TOS = 10 h).*

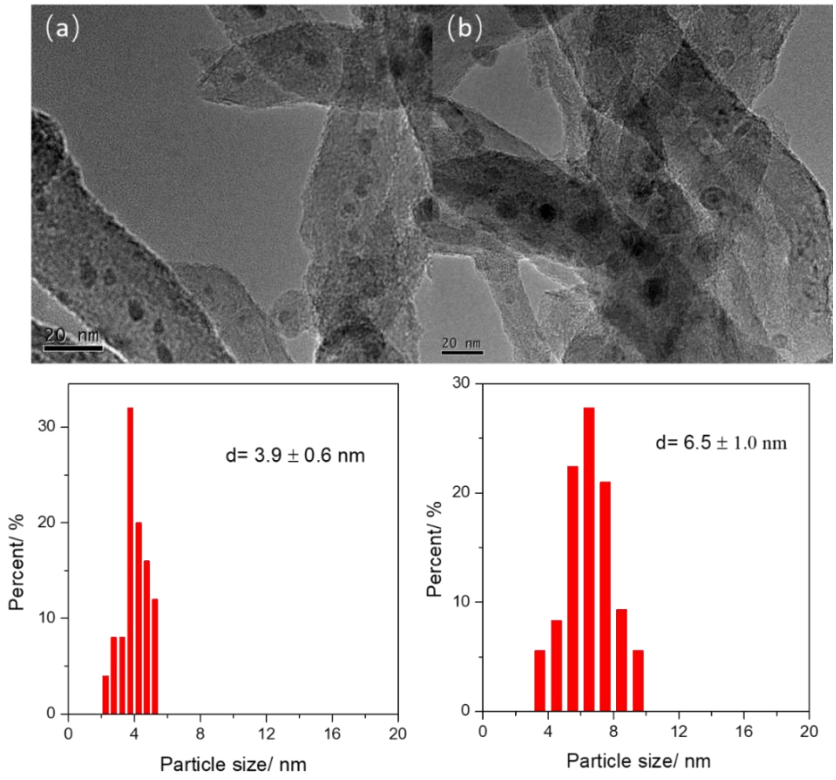

Figure 5.18. *TEM images and particle size distribution of the spent catalysts. (a)FeBi/CNT-in-300, (b) FeBi/CNT-in-400. (350 °C, H_2/CO = 1/1, GHSV = 17 L/g.h (10bar), TOS = 10 h).*

Apart from the enhancement of FT reaction rate, confinement of iron nanoparticles in CNT also improves the catalyst stability. Figure 5.18 shows micrographs of two spent Bi-promoted iron catalysts and calculated respective particle size distribution. The

average particle size of spent FeBi/CNT-in-300 is 3.9 nm, while for the FeBi/CNT-in-400 the average size after reaction is 6.5 nm. Both the FeBi/CNT-in-300 and FeBi/CNT-in-400 catalysts show very slight sintering compared with the fresh catalysts. We can conclude that confinement is also an efficient way to improve the stability of small iron carbide nanoparticles.

5.3. Conclusion

Encapsulation inside carbon nanotubes affects the properties of iron nanoparticles, their catalytic performance and stability in high temperature FT synthesis. The temperature of catalyst thermal treatment has a strong effect on the size of iron nanoparticles encapsulated inside CNT. Larger iron nanoparticles were obtained after treatment at higher temperature and they exhibit better reducibility. The promoters (Bi and Pb) are located in the surface of iron with close contact and the iron sintering degree is restricted by confinement in CNT.

The presence of promoters strongly influences on the catalytic performance of iron carbide nanoparticles. The specific reaction rates (TOF) were 3-5 times higher over the Bi- and Pb-promoted catalysts compared to the unpromoted counterparts. In the unpromoted iron catalysts with confined iron nanoparticles, the TOF increases with the increase in the iron nanoparticle size from 2.5 nm to 6-8 nm and then remains stable with further increase in the iron particle size, while the product selectivity is not affected by the nanoparticle size variation.

In the Bi and Pb promoted iron catalysts, the size of encapsulated iron nanoparticles affects both the activity and selectivity. The activity shows similar trend with the unpromoted iron catalysts, while the selectivity to light olefins decreases with the increase in the iron particle size. These findings shed further light on the fundamental effects of confinement on catalysis, and provide more insights into the particle size effects in iron-based FT catalysts.

5.4. Reference

[1] J. Lu, L. Yang, B. Xu, Q. Wu, D. Zhang, S. Yuan, Y. Zhai, X. Wang, Y. Fan, Z. Hu, Promotion Effects of Nitrogen Doping into Carbon Nanotubes on Supported Iron Fischer-Tropsch Catalysts for Lower Olefins, ACS Catalysis, 4 (2014) 613-621.
[2] A. Nakhaei Pour, M.R. Housaindokht, M. Irani, S.M. Kamali Shahri, Size-dependent studies of Fischer-Tropsch synthesis on iron based catalyst: New kinetic model, Fuel, 116 (2014) 787-793.
[3] Z.-j. Wang, S. Skiles, F. Yang, Z. Yan, D.W. Goodman, Particle size effects in Fischer-Tropsch synthesis by cobalt, Catalysis Today, 181 (2012) 75-81.
[4] V.K. Jones, L.R. Neubauer, C.H. Bartholomew, Effects of crystallite size and support on the carbon monoxide hydrogenation activity/selectivity properties of iron/carbon, The Journal of Physical Chemistry, 90 (1986) 4832-4839.
[5] J. Den Breejen, P. Radstake, G. Bezemer, J. Bitter, V. Frøseth, A. Holmen, K.d. Jong, On the origin of the cobalt particle size effects in Fischer-Tropsch catalysis, Journal of the American Chemical Society, 131 (2009) 7197-7203.
[6] J.-Y. Park, Y.-J. Lee, P.R. Karandikar, K.-W. Jun, K.-S. Ha, H.-G. Park, Fischer-Tropsch catalysts deposited with size-controlled Co_3O_4 nanocrystals: Effect of Co particle size on catalytic activity and stability, Applied Catalysis A: General, 411-412 (2012) 15-23.
[7] G. Prieto, A. Martínez, P. Concepción, R. Moreno-Tost, Cobalt particle size effects in Fischer-Tropsch synthesis: structural and in situ spectroscopic characterisation on reverse micelle-synthesised Co/ITQ-2 model catalysts, Journal of Catalysis, 266 (2009) 129-144.
[8] G.L. Bezemer, J.H. Bitter, H.P. Kuipers, H. Oosterbeek, J.E. Holewijn, X. Xu, F. Kapteijn, A.J. van Dillen, K.P. de Jong, Cobalt particle size effects in the Fischer-Tropsch reaction studied with carbon nanofiber supported catalysts, Journal of the American Chemical Society, 128 (2006) 3956-3964.
[9] J.M.G. Carballo, J. Yang, A. Holmen, S. García-Rodríguez, S. Rojas, M. Ojeda, J.L.G. Fierro, Catalytic effects of ruthenium particle size on the Fischer-Tropsch synthesis, Journal of catalysis, 284 (2011) 102-108.
[10] J.L. Eslava, X. Sun, J. Gascon, F. Kapteijn, I. Rodríguez-Ramos, Ruthenium particle size and cesium promotion effects in Fischer-Tropsch synthesis over high-surface-area graphite supported catalysts, Catalysis Science & Technology, 7 (2017) 1235-1244.
[11] J. Kang, S. Zhang, Q. Zhang, Y. Wang, Ruthenium nanoparticles supported on carbon nanotubes as efficient catalysts for selective conversion of synthesis gas to diesel fuel, Angewandte Chemie International Edition, 48 (2009) 2565-2568.
[12] J.-Y. Park, Y.-J. Lee, P.K. Khanna, K.-W. Jun, J.W. Bae, Y.H. Kim, Alumina-supported iron oxide nanoparticles as Fischer-Tropsch catalysts: Effect of particle size of iron oxide, Journal of Molecular Catalysis A: Chemical, 323 (2010) 84-90.
[13] K. Cheng, M. Virginie, V.V. Ordomsky, C. Cordier, P.A. Chernavskii, M.I. Ivantsov, S. Paul, Y. Wang, A.Y. Khodakov, Pore size effects in high-temperature Fischer-Tropsch synthesis over supported iron catalysts, Journal of catalysis, 328 (2015) 139-150.
[14] P.A. Chernavskii, V.I. Zaikovskii, G.V. Pankina, A.Y. Khodakov, Dimensional effects in the carbidization of supported iron nanoparticles, ChemCatChem, 5 (2013) 1758-1761.
[15] H.M. Torres Galvis, J.H. Bitter, T. Davidian, M. Ruitenbeek, A.I. Dugulan, K.P. de Jong, Iron

particle size effects for direct production of lower olefins from synthesis gas, Journal of the American Chemical Society, 134 (2012) 16207-16215.
[16] J. Xie, H.M. Torres Galvis, A.C. Koeken, A. Kirilin, A.I. Dugulan, M. Ruitenbeek, K.P. de Jong, Size and promoter effects on stability of carbon-nanofiber-supported iron-based Fischer-Tropsch catalysts, ACS catalysis, 6 (2016) 4017-4024.
[17] V.V. Ordomsky, Y. Luo, B. Gu, A. Carvalho, P.A. Chernavskii, K. Cheng, A.Y. Khodakov, Soldering of Iron Catalysts for Direct Synthesis of Light Olefins from Syngas under Mild Reaction Conditions, ACS Catalysis, 7 (2017) 6445-6452.
[18] B. Gu, V.V. Ordomsky, M. Bahri, O. Ersen, P.A. Chernavskii, D. Filimonov, A.Y. Khodakov, Effects of the promotion with bismuth and lead on direct synthesis of light olefins from syngas over carbon nanotube supported iron catalysts, Applied Catalysis B: Environmental, 234 (2018) 153-166.
[19] W. Chen, Z. Fan, L. Gu, X. Bao, C. Wang, Enhanced capacitance of manganese oxide via confinement inside carbon nanotubes, Chemical communications, 46 (2010) 3905-3907.
[20] P. Serp, E. Castillejos, Catalysis in Carbon Nanotubes, ChemCatChem, 2 (2010) 41-47.
[21] G. Yu, B. Sun, Y. Pei, S. Xie, S. Yan, M. Qiao, K. Fan, X. Zhang, B. Zong, Fe_xO_y@ C spheres as an excellent catalyst for Fischer-Tropsch synthesis, Journal of the American Chemical Society, 132 (2009) 935-937.
[22] W. Chen, Z. Fan, X. Pan, X. Bao, Effect of confinement in carbon nanotubes on the activity of Fischer-Tropsch iron catalyst, Journal of the American Chemical Society, 130 (2008) 9414-9419.
[23] C. Wang, X. Pan, X. Bao, Direct production of light olefins from syngas over a carbon nanotube confined iron catalyst, Chinese Science Bulletin, 55 (2010) 1117-1119.
[24] Z. Yang, X. Pan, J. Wang, X. Bao, FeN particles confined inside CNT for light olefin synthesis from syngas: Effects of Mn and K additives, Catalysis today, 186 (2012) 121-127.
[25] H. Tian, X. Li, L. Zeng, J. Gong, Recent advances on the design of group VIII base-metal catalysts with encapsulated structures, ACS Catalysis, 5 (2015) 4959-4977.
[26] L. Yu, W.-X. Li, X. Pan, X. Bao, In-and out-dependent interactions of iron with carbon nanotubes, The Journal of Physical Chemistry C, 116 (2012) 16461-16466.
[27] R.M.M. Abbaslou, J. Soltan, A.K. Dalai, Effects of nanotubes pore size on the catalytic performances of iron catalysts supported on carbon nanotubes for Fischer-Tropsch synthesis, Applied Catalysis A: General, 379 (2010) 129-134.
[28] K. Mai, T. Elder, L.H. Groom, J.J. Spivey, Fe-based Fischer Tropsch synthesis of biomass-derived syngas: effect of synthesis method, Catalysis Communications, 65 (2015) 76-80.
[29] V. Subramanian, V.V. Ordomsky, B. Legras, K. Cheng, C. Cordier, P.A. Chernavskii, A.Y. Khodakov, Design of iron catalysts supported on carbon-silica composites with enhanced catalytic performance in high-temperature Fischer-Tropsch synthesis, Catalysis Science & Technology, 6 (2016) 4953-4961.
[30] R.M.M. Abbaslou, A. Tavassoli, J. Soltan, A.K. Dalai, Iron catalysts supported on carbon nanotubes for Fischer-Tropsch synthesis: Effect of catalytic site position, Applied Catalysis A: General, 367 (2009) 47-52.
[31] Z. Yu, D. Chen, B. Tøtdal, A. Holmen, Effect of catalyst preparation on the carbon nanotube growth rate, Catalysis today, 100 (2005) 261-267.
[32] P.A. Chernavskii, A.Y. Khodakov, G.V. Pankina, J.-S. Girardon, E. Quinet, In situ characterization of the genesis of cobalt metal particles in silica-supported Fischer-Tropsch catalysts using Foner magnetic method, Applied Catalysis A: General, 306 (2006) 108-119.

[33] P. Chernavskii, J.-A. Dalmon, N. Perov, A. Khodakov, Magnetic characterization of fischer-tropsch catalysts, Oil & Gas Science and Technology-Revue de l'IFP, 64 (2009) 25-48.
[34] X. Pan, X. Bao, The effects of confinement inside carbon nanotubes on catalysis, Accounts of chemical research, 44 (2011) 553-562.
[35] J. Guan, X. Pan, X. Liu, X. Bao, Syngas segregation induced by confinement in carbon nanotubes: a combined first-principles and Monte Carlo study, The Journal of Physical Chemistry C, 113 (2009) 21687-21692.

Chapter 6. Selectivity shift from paraffins to α-olefins in low temperature Fischer-Tropsch synthesis in the presence of carboxylic acids

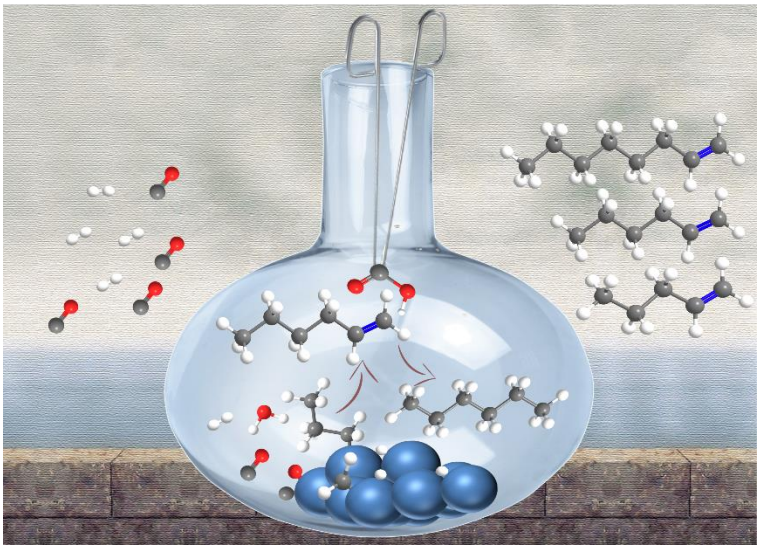

Abstract: A shift of selectivity to long chain α-olefins has been observed during Fischer-Tropsch synthesis over Co catalysts in the presence of carboxylic acids. The total selectivity 39 % to α-olefins was obtained in the presence of acids. The effect has been ascribed to intermediate formation of esters which hinder secondary olefin hydrogenation.

This chapter is based on the following publication:

Bang Gu, Andrei Y. Khodakov* and Vitaly V. Ordomsky*, *ChemComm* 54 (**2018**) 2345-2348.

6.1. Introduction

Higher linear α-olefins are valuable products and intermediates, which are used in a large number of commercial products like polymers, surfactants and additives. For example, C_5-C_8 are used as co-monomers in polyethylene products, C_{10}-C_{14} are used for the synthesis of surfactants like LABS (linear alkyl benzene sulfonate) for aqueous detergent formulations; C_{16}-C_{18} find their primary application as the hydrophobes in oil-soluble surfactants and as lubricating fluids; C_{20}-C_{30} are used for the synthesis of polymers [1]. At the present, almost all processes for production of linear α-olefins are based on oligomerization of ethylene or propylene [2]. The mostly employed Ziegler process uses triethyl aluminum for the synthesis of linear olefins with a broad Schulz-Flory distribution. These processes require expensive complexes as catalysts.

Syngas is a mixture of hydrogen and carbon monoxide. It can be produced from fossil and renewable resources like methane by steam reforming or partial oxidation or from coal or biomass by gasification. Fischer-Tropsch (FT) synthesis is surface polymerization of CH_x monomers formed by hydrogenation of CO over metallic catalysts with formation of a broad range of hydrocarbons according to Anderson-Schulz-Flory (ASF) distribution [3]. Termination of hydrocarbon chains on the surface of metal catalyst might involve β-hydrogen abstraction leading to α-olefins or hydrogenation of surface hydrocarbon fragments to form linear paraffins. The primary α-olefins, however, participate in fast secondary hydrogenation to paraffins. This effect is more pronounced with the increase in the chain length due to a longer residence time of heavier α-olefins over metal surface.

The synthesis of α-olefins by FT synthesis is a very desirable and sustainable process. Nowadays, a great deal of research activities are devoted to the direct synthesis of light olefins (C_2-C_4) from syngas in high temperature FT synthesis [4]. The selectivity of about 60 % which is close to that predicted by ASF distribution has been reached over

promoted Fe based catalysts [5, 6]. The promoters like sodium, sulfur, lead and bismuth seem to restrict chain growth and suppress hydrogenation activity of the catalysts. Zn- and Na-modulated Fe catalysts demonstrated high selectivity toward alkenes in C_{5+} hydrocarbons due to change of electronic structure and suppression of hydrogenation activity of Fe [7]. At the moment the highest selectivity to light olefins from syngas has been attained by combination of the catalyst for methanol synthesis and MTO reaction [8].

Low temperature FT synthesis over Ru and Co based catalysts leads mainly to the synthesis of paraffins. Recently cobalt carbide nanoprisms catalysts have been reported to convert syngas with high selectivity to light olefins accompanied by low amount of methane and hydrocarbons as the main side product [9]. However, usually hydrogenation activity of the metals is very high and promoters cannot suppress it without a major decline in the reaction rate.

Another strategy for low temperature FT synthesis of olefins available from the literature is based on application of supercritical conditions in FT synthesis. The content of α-olefins in supercritical conditions during FTS has been found to be higher in comparison with the conventional FT synthesis [10-12]. Enhanced diffusion and desorption of α-olefins in supercritical conditions leads to their lower secondary hydrogenation to paraffins. However, this route requires high excess of solvents and high pressure in the reactor, which is hard to implement in the industry.

Our approach for the synthesis of linear α-olefins addresses application of carboxylic acids for stabilization of olefins formed during low temperature FT process over Co based catalysts. We found that the presence of carboxylic acids shifts the selectivity patterns from paraffins to olefins by intermediate stabilization of olefins in the form of esters (Figure 6.1).

The effect of co-feeding with labelled acetic acid has been earlier studied by Davis et al. [13] but only over Fe catalyst in batch reactor at 270 ºC during FT synthesis. The authors observed formation of ethane by hydrogenation of acetic

acid and increase in the olefin to paraffin ratio with additional formation of different oxygenates such as glycol and ether. To the best of our knowledge, there is no information about effect of addition of carboxylic acids on the reaction selectivity during low temperature FT synthesis over Co based catalysts in fixed bed reactor.

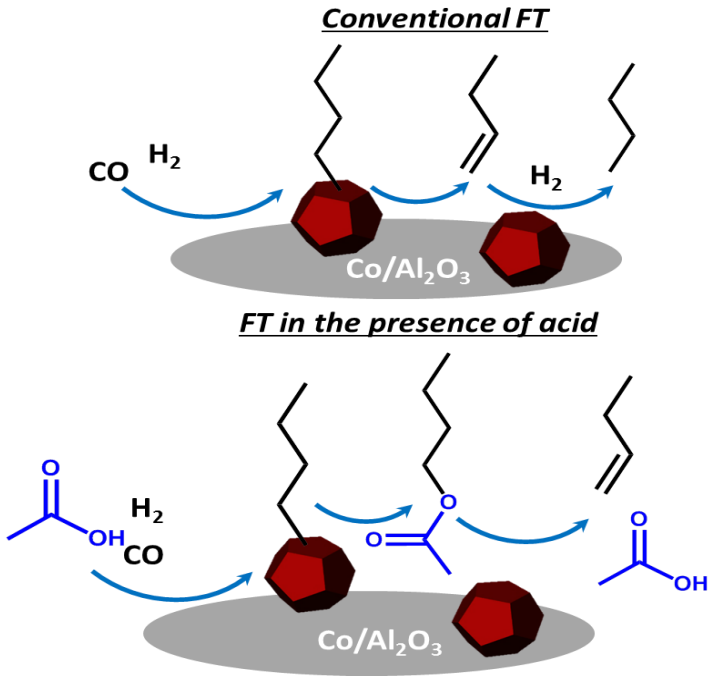

Figure 6.1. *Scheme of FT synthesis without and in the presence of carboxylic acids*

6.2 Results and Discussion.

The catalytic activities and selectivities in FT synthesis before acid addition at different gas space velocities are shown in Table 6.1. Methane, light olefins, light paraffins, C_5+ hydrocarbons were the main products of FT synthesis on cobalt catalysts under the reaction conditions. Without acid addition, the selectivity to methane decreases from 10 to 5 % with the increase in the conversion of CO from 24 to 82 %. The lower methane selectivity at higher CO conversion can be due to the suppression of methanation activity in a large amount of water produced by the FT reaction [14].

Table 5.1. *Results of catalytic tests without and in the presence of carboxylic acids (T = 220 ºC, p = 20 bar, H_2/CO = 2, GHSV = 13-54 L/g_{cat}·h)*

Flow, mmol/h·g		Acid transformation		CO transformation											
		Conv.,	Sele.	Conv.,	Selectivity, Cat. %										
CO	Acid	%	to alcohol, %	%	CH_4	C_2-C_4			C_5-C_{12}			C_{13}-C_{25}			C_{25+}
						olef.	par.	*ratio*	olef.	par.	*ratio*	olef.	par	*ratio*	
no acid addition															
50	-	-	-	82	5	3	2	*1.5*	5	12	*0.4*	-	38	*0*	35
100	-	-	-	49	6	4	2	*2*	7	14	*0.5*	-	35	*0*	32
200	-	-	-	24	10	5	2	*2.5*	12	13	*0.9*	-	32	*0*	26
Acetic acid															
50	12	14	86	32	6	5	3	*1.6*	17	13	*1.3*	9	15	*0.6*	32
100	25	11	90	22	5	5	3	*1.6*	18	14	*1.3*	12	15	*0.8*	28
100	12	5	95	25	6	5	3	*1.6*	15	11	*1.4*	7	21	*0.4*	32
100	-*	-	-	18	8	5	3	*1.6*	14	11	*1.3*	-	35	-	24
Butyric acid															
50	12	5	79	27	6	5	3	*1.6*	14	11	*1.3*	8	14	*0.6*	39
100	25	3	80	16	7	5	3	*1.6*	16	11	*1.5*	9	12	*0.8*	37

* - addition of acid has been switched off

The selectivities to the C_2-C_4 and C_5-C_{12} paraffins are about 2 % and 12 %, respectively, at all ranges of conversions over Co/Al_2O_3 (Table 6.1). At the same time, the selectivity to olefins decreases with the increase in the conversion of CO. For example, the total selectivity to the C_2-C_{12} olefins is 17 % at the 24 % CO conversion and only 8 % at the 82 % CO conversion. This effect has been explained by secondary hydrogenation of olefins [15] at high conversion levels. The main products of low temperature FT synthesis over Co catalysts are long chain paraffins (C_{13+}). Their selectivity is about 80 %. Figure 6.2a shows the distributions of selectivities to olefins and paraffins over Co/Al_2O_3 as a function of the chain length before the addition of acid. The fraction of olefins decreases dramatically with the increase in the chain length. The residence time for long chain olefins on the catalyst surface is longer compared to the short chain counterparts [16]. This leads to their almost complete hydrogenation to paraffins.

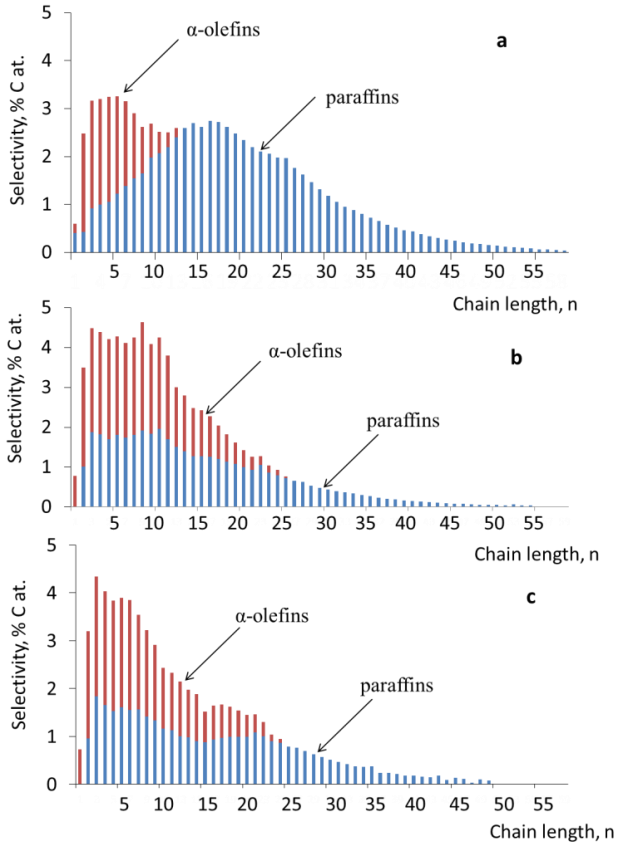

Figure 6.2. *Olefins and paraffins selectivities as functions of the chain length over Co/Al_2O_3 without addition of acid (a), with addition of acetic acid (b) and with addition of butyric acid (c). Conditions: T=220 ºC, p=20 bar, H_2/CO =2, conversion of CO about 20 %.*

Acetic acid co-feeding with the molar ratio acetic acid to CO 0.25 mol/mol leads to significant changes in the activity and selectivity of the catalyst. Conversion of CO decreases almost twice in the presence of acetic acid at the initial reaction time with stabilization afterwards (Figure 6.3). Interestingly, a halt in the acid addition does not lead to recovery of the Co catalyst activity. Earlier studies indicated partial acid decomposition on cobalt catalysts under the conditions of FT synthesis leading to carbon deposition [17]. Analysis of the spent catalysts after the reaction by IR spectroscopy and XRD analysis shows the presence of Co acetates [18] (Figures 6.4 and 6.5). TG analysis (Figure 6. 6) shows that decomposition of acetate species happens in the range 220-270 °C which means that catalyst might be regenerated continuously during reaction.

Use of Ru as active metal could be another option to avoid deactivation of the catalyst.

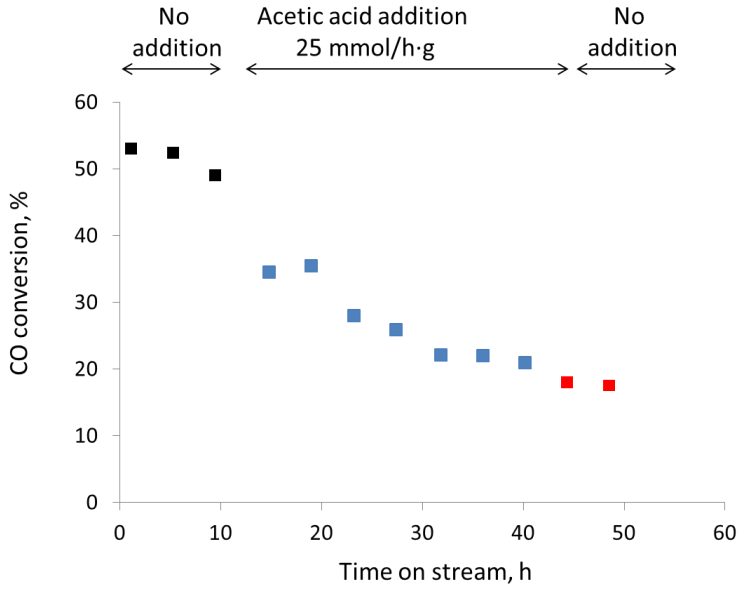

Figure 6.3. *Effect of acetic acid addition on the CO conversion as a function of time. Reaction conditions: p = 20 bar, H_2/CO = 2, GHSV = 6.7 $Lg^{-1}h^{-1}$.*

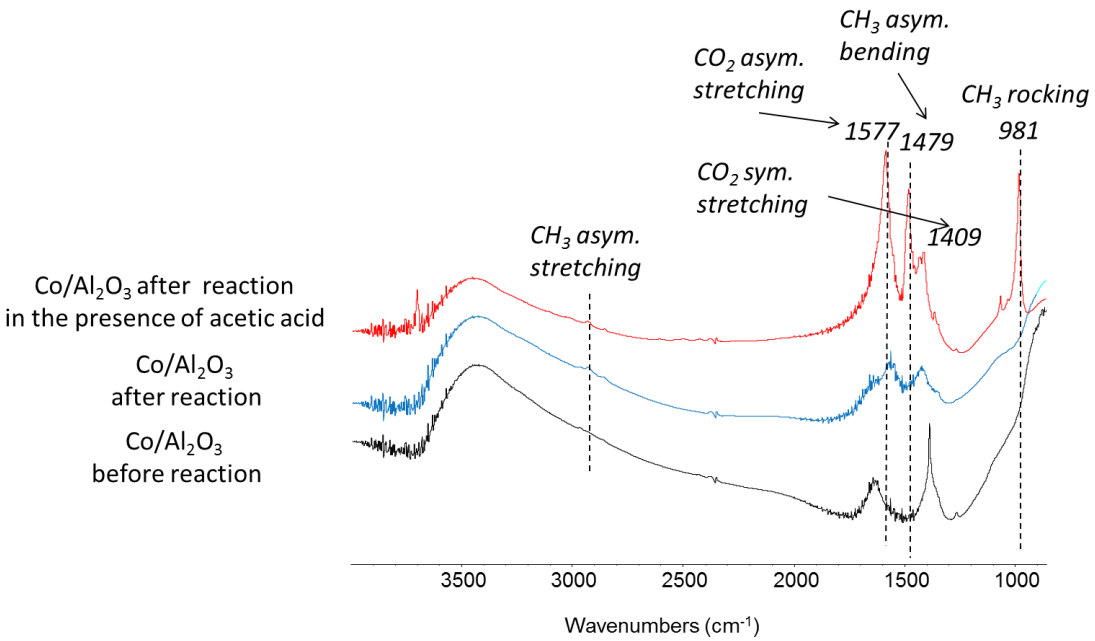

Figure 6.4. *FTIR spectra of the catalyst before and after FT synthesis in the presence of acetic acid.*

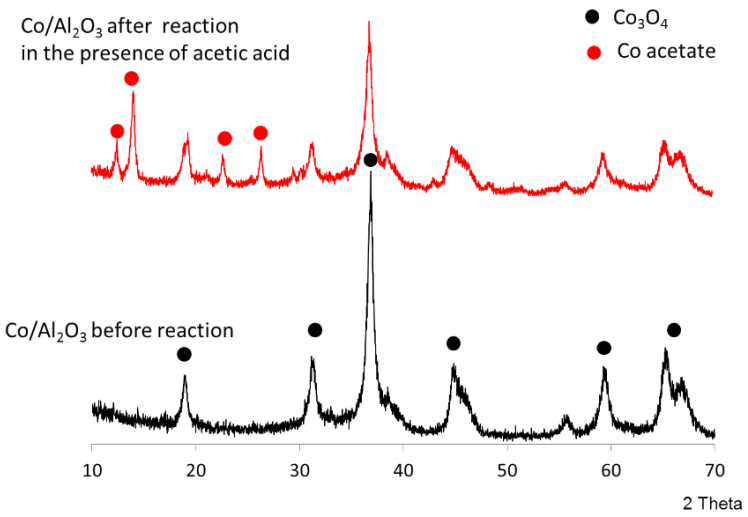

Figure 6.5. *XRD of the catalyst before and after FT synthesis in the presence of acetic acid.*

The formation of cobalt acetates suggests an additional mechanism of catalyst deactivation, which is relevant to cobalt oxidation. Note however that even after extended exposure to acetic acid, the catalyst still maintains noticeable activity. Cobalt deactivation is therefore is only partial. Addition of butyric acid has similar effect on the catalytic performance.

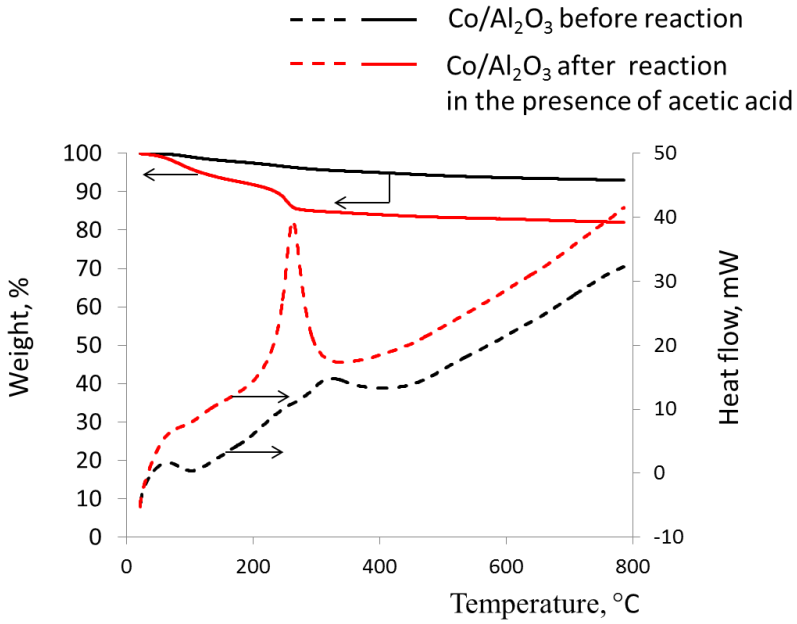

Figure 6.6. *TG analysis of the catalyst before and after FT synthesis in the presence of acetic acid.*

Table 6.2. *Results of hydrogenation of acetic acid over Co/Al_2O_3 catalyst (T=220 ºC, p=20 bar)*

Flow, mmol/h·g		Conversion of acetic acid, %	Selectivity, %			
			Ethanol	Hydrocarbons		
H_2	Acid			C_2	C_4	C_6
200	25	27	83	6	3	2

The transformation of acetic and butyric acids over Co catalyst could involve their hydrogenation and incorporation in the FT reaction products. Davis [13] et al. observed significant incorporation of labelled acetic acid in the hydrocarbons during FT synthesis in CSTR reactor over Fe based catalysts at 270 °C. The observed phenomenon has been explained by participation of acetic acid in chain initiation. Analysis of hydrogenation of acetic acid without CO addition shows that the main products of the reaction are ethanol and ethane with traces of the C_4 and C_6 hydrocarbons most probably because of condensation reactions (Table 6.2). In the presence of syngas, conversion of acetic acid is significantly lower due to its competitive adsorption with CO on the metal surface (Table 6.1). It is interesting to note that decrease of the flow of acetic acid to CO from 0.25 to 0.12 leads to decrease of the transformation of acetic acid which is most probably result of hindering of active sites by CO. The main products of the transformation of acids are alcohols. In order to identify reaction path for the formation of hydrocarbons and incorporation of acetic acid in the reaction products, FT synthesis has been performed in the presence of labeled acetic acid ($^{13}CH_3$-COOH). Analysis of the products of the reaction does not show visible presence of ^{13}C in the hydrocarbons. Only ethanol and ethane containing ^{13}C were produced from the labelled acetic acid. This suggests that no incorporation of acetic acid occurs under the conditions of low temperature FT synthesis on cobalt catalyst

The methane selectivity is lower over Co catalyst in the presence of acetic acid and butyric acid at the same conversions in comparison with the catalysis before acid addition (Table 6.1). The selectivity to methane remained the same after switching off addition of acid (Table 6.1). It indicates that during co-feeding with acetic acid, a part of cobalt metal sites active in methanation are deactivated. This would result in a lower methane selectivity.

Importantly, addition of acetic acid leads to a significant increase in the selectivity to olefins (Table 6.1, Figure 6.2). While the olefin fraction is still decreasing with increase in the chain length, the olefins only with the length larger than 25 carbon atoms disappear in the products. Addition of butyric acid gives comparable effect, however, the selectivity to olefins is lower. The effect decreases with increase of the ratio of CO to acid (Table 6.1).

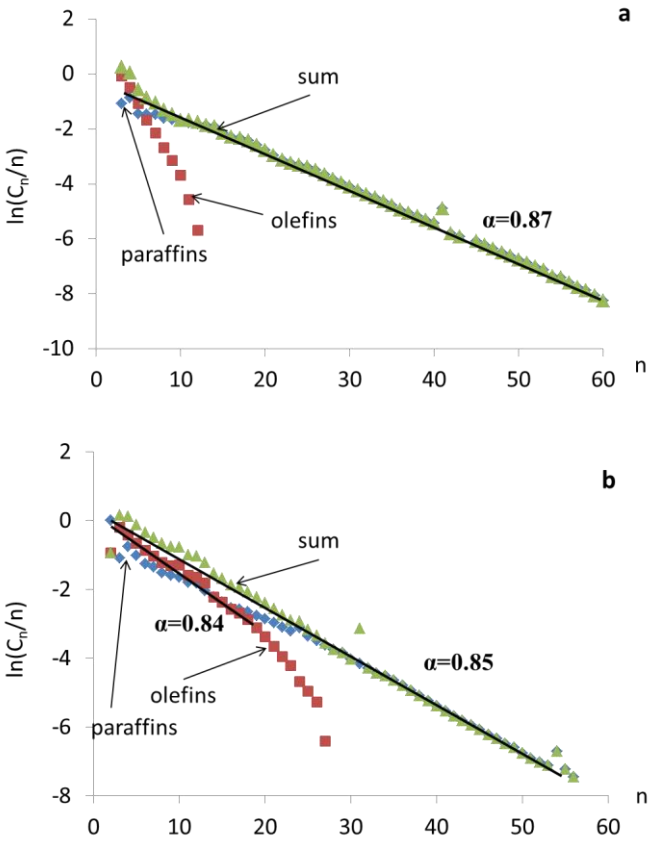

Figure 6.7. *ASF distribution of paraffins, olefins and total without (a) and with addition of acetic acid (b)*

One of the possible explanations could be modification of the catalyst, for example, due to the deactivation of the most active hydrogenation sites by formation of acetate species. In order to verify this assumption, the product distribution has been studied after switching off acetic acid addition (Table 6.1). The results show that the selectivity pattern returns to that which was observed before addition of acid. Thus, irreversible modification of the catalyst cannot explain formation of α-olefins. Another possible explanation could be in stabilization of olefins by interaction with carboxylic acid.

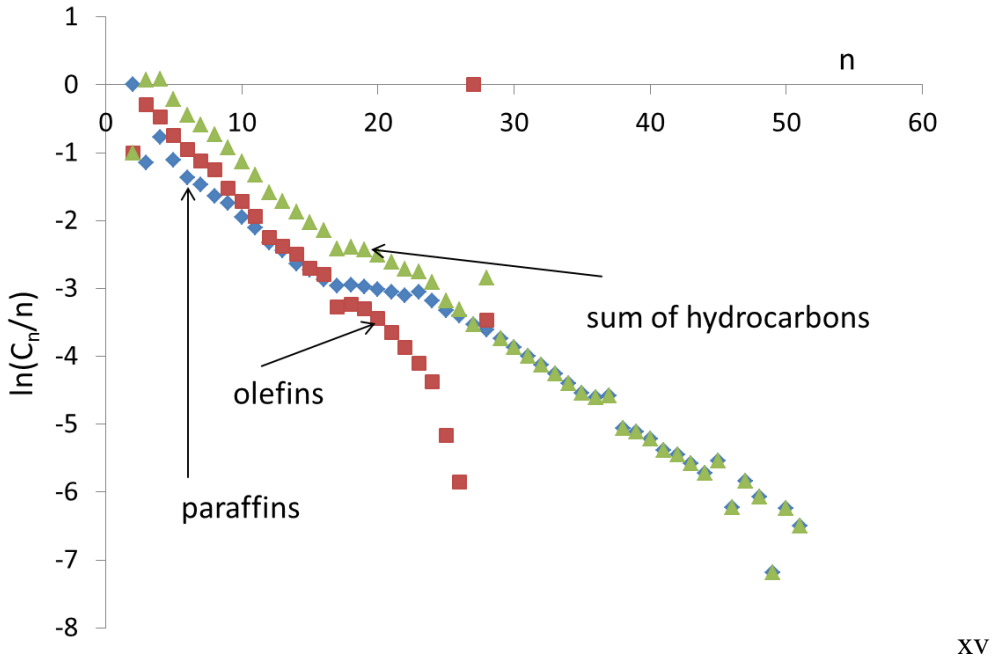

Figure 6.8. *ASF distribution for olefins, paraffins and sum of hydrocarbons for FT synthesis with addition of butyric acids*

Deep analysis of hydrocarbons distribution has been performed to clarify these phenomena. The hydrocarbon chain length distribution follows Anderson-Schulz-Flory (ASF) statistics in FT synthesis. Linearization of distribution for olefins, paraffins and total hydrocarbons according to the ASF model for catalysis without and in the presence of acids is presented in Figures 6.7 and 6.8. It can be clearly seen that olefins and paraffins in the presence of acid have similar linear distributions with chain growth probabilities (α) 0.84 and 0.85, respectively. At higher chain length, olefins disappear and the linear distribution

of paraffins changes a slope to lower α. The distribution of sum of hydrocarbons is totally linear for the whole range of hydrocarbons. FT synthesis without addition of acid leads to the distribution of hydrocarbons with α equal to 0.87. These results indicate that co-feeding with carboxylic acids results in parallel synthesis of paraffins and olefins with similar chain growth probabilities.

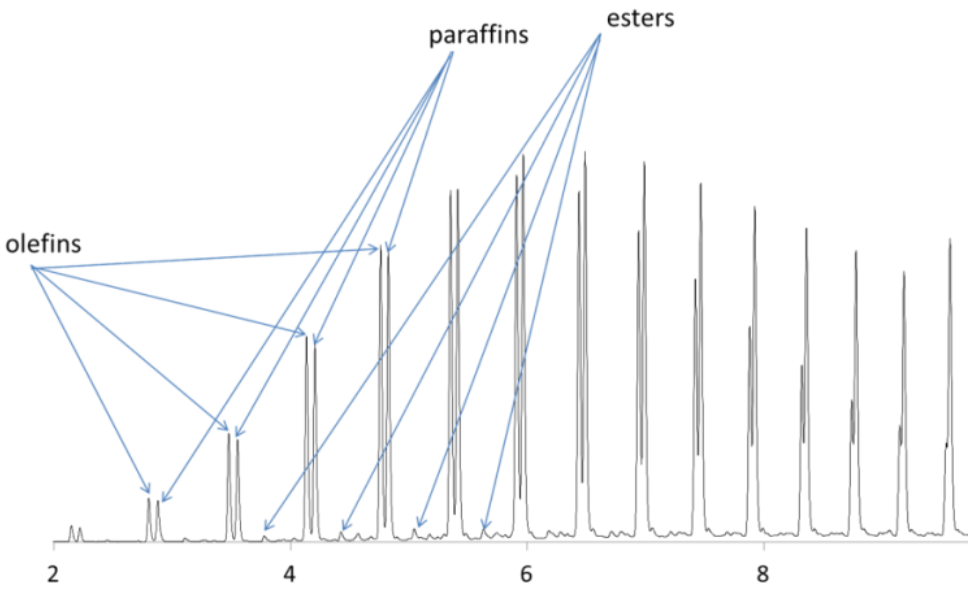

Figure 6.9. *Chromatogram of SimDist analysis with identification of the peaks by GC-MS analysis*

The unique character of carboxylic acids in stabilization of olefins during FT synthesis might be explained by interaction of olefins with acids with formation of intermediate products (Figure 6.1). Analysis of the products by GC-MS technique revealed the presence of small peaks of esters besides those of olefins and paraffins in the reaction products, which have the distribution similar to those of olefins (Figure 6.9). The possible explanation of the effect of acid could be intermediate formation of esters from olefins and acids leading to stabilization of olefins from subsequent hydrogenation (Figure 6.1). In order to support this assumption, we have performed hydrogenation of 1-octene and octyl acetate at the conditions of FT synthesis. The conversion of 1-octene to octane in this case was 51 % (Figure 6.10). Octyl acetate decomposes to octene and acetic acid at

the FT reaction conditions. Octene might be hydrogenated further to octane. However, the analysis of the products has shown that conversion of octene to octane is only 25 %. This means that the presence of acetic acid significantly suppresses hydrogenation of olefins. Note that formation and decomposition of ester takes place continuously during reaction leading to protection of olefins from deep hydrogenation. Acetic acid is more volatile than butyric acid which leads to more efficient interaction with olefins and higher selectivity.

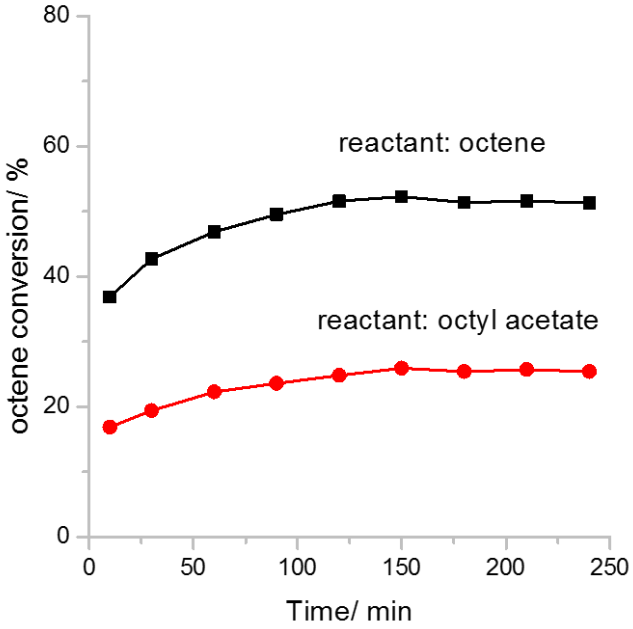

Figure 6.10. *Time on stream for octene and octyl acetate hydrogenation under FT condition. Reaction condition: catalyst 20 mg, H_2 6 ml/min, CO 2 ml/min, P = 20 bar, T = 220 ^oC, octene or octyl acetate rate: 5 mmol/h.*

6.3 Conclusion

To conclude, co-feeding with carboxylic acids leads to a shift of selectivity from paraffins to α-olefins in low temperature FT synthesis on cobalt catalysts. The total selectivity of 39 % to α-olefins has been attained in the presence of acetic acid. The effect has been assigned to stabilization of olefins with intermediate formation of esters with their subsequent decomposition.

6.4 Reference

[1] B. Jager, Developments in Fischer-Tropsch technology, in, Elsevier Science Publishers, Amsterdam (Netherlands), Netherlands, 1998.

[2] J. Skupinska, Oligomerization of α-olefins to higher oligomers, Chemical Reviews, 91 (1991) 613-648.

[3] A.Y. Khodakov, W. Chu, P. Fongarland, Advances in the development of novel cobalt Fischer-Tropsch catalysts for synthesis of long-chain hydrocarbons and clean fuels, Chemical Reviews, 107 (2007) 1692-1744.

[4] H.M. Torres Galvis, K.P. de Jong, Catalysts for production of lower olefins from synthesis gas: a review, ACS catalysis, 3 (2013) 2130-2149.

[5] H.M.T. Galvis, J.H. Bitter, C.B. Khare, M. Ruitenbeek, A.I. Dugulan, K.P. de Jong, Supported iron nanoparticles as catalysts for sustainable production of lower olefins, Science, 335 (2012) 835-838.

[6] V.V. Ordomsky, Y. Luo, B. Gu, A. Carvalho, P.A. Chernavskii, K. Cheng, A.Y. Khodakov, Soldering of Iron Catalysts for Direct Synthesis of Light Olefins from Syngas under Mild Reaction Conditions, ACS Catalysis, 7 (2017) 6445-6452.

[7] P. Zhai, C. Xu, R. Gao, X. Liu, M. Li, W. Li, X. Fu, C. Jia, J. Xie, M. Zhao, Highly Tunable Selectivity for Syngas-Derived Alkenes over Zinc and Sodium-Modulated Fe5C2 Catalyst, Angewandte Chemie International Edition, 55 (2016) 9902-9907.

[8] K. Cheng, B. Gu, X. Liu, J. Kang, Q. Zhang, Y. Wang, Direct and Highly Selective Conversion of Synthesis Gas into Lower Olefins: Design of a Bifunctional Catalyst Combining Methanol Synthesis and Carbon-Carbon Coupling, Angewandte Chemie, 128 (2016) 4803-4806.

[9] L. Zhong, F. Yu, Y. An, Y. Zhao, Y. Sun, Z. Li, T. Lin, Y. Lin, X. Qi, Y. Dai, Cobalt carbide nanoprisms for direct production of lower olefins from syngas, Nature, 538 (2016) 84-87.

[10] L. Fan, K. Fujimoto, Fischer-Tropsch synthesis in supercritical fluid: characteristics and application, Applied Catalysis A: General, 186 (1999) 343-354.

[11] K. Yokota, Y. Hanakata, K. Fujimoto, Supercritical phase Fischer-Tropsch synthesis, Chemical Engineering Science, 45 (1990) 2743-2749.

[12] W. Linghu, X. Liu, X. Li, K. Fujimoto, Selective synthesis of higher linear α-olefins over cobalt Fischer-Tropsch catalyst, Catalysis letters, 108 (2006) 11-13.

[13] A. Sarkar, R.A. Keogh, S. Bao, B.H. Davis, Fischer-Tropsch Synthesis: Reaction Pathways for 14 C-Labeled Acetic Acid, Catalysis Letters, 120 (2008) 25-33.

[14] W. Ma, G. Jacobs, T.K. Das, C.M. Masuku, J. Kang, V.R.R. Pendyala, B.H. Davis, J.L.S. Klettlinger, C.H. Yen, Fischer-Tropsch Synthesis: Kinetics and Water Effect on Methane Formation over 25%Co/γ-Al_2O_3 Catalyst, Industrial & Engineering Chemistry Research, 53 (2014) 2157-2166.

[15] N.O. Elbashir, C.B. Roberts, Enhanced Incorporation of α-Olefins in the Fischer-Tropsch Synthesis Chain-Growth Process over an Alumina-Supported Cobalt Catalyst in Near-Critical and

Supercritical Hexane Media, Industrial & Engineering Chemistry Research, 44 (2005) 505-521.
[16] E. Iglesia, S.L. Soled, R.A. Fiato, G.H. Via, Bimetallic Synergy in Cobalt Ruthenium Fischer-Tropsch Synthesis Catalysts, Journal of Catalysis, 143 (1993) 345-368.
[17] D. Kistamurthy, A.M. Saib, D.J. Moodley, H. Preston, I.M. Ciobîcă, W.J. van Rensburg, J.W. Niemantsverdriet, C.J. Weststrate, The role of carboxylic acid in cobalt Fischer-Tropsch synthesis catalyst deactivation, Catalysis Today, 275 (2016) 127-134.
[18] Z. Nickolov, G. Georgiev, D. Stoilova, I. Ivanov, Raman and IR study of cobalt acetate dihydrate, Journal of molecular structure, 354 (1995) 119-125.

Chapter 7. Self-regeneration of Cobalt and Nickel Catalysts Promoted with Bismuth and Non-deactivating Performance in Carbon Monoxide Hydrogenation

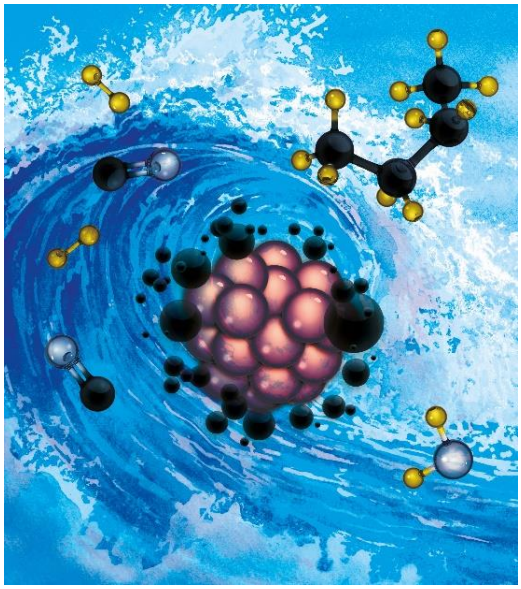

Abstract: Carbon monoxide hydrogenation over Co and Ni catalysts has provided important opportunities to store energy and to manufacture alternative renewable transportation fuels. Catalyst deactivation is one of the most serious issues restricting application of this reaction. Hereby, we propose a simple and efficient way to enhance the stability of supported cobalt and nickel catalysts via their promotion with bismuth. In the promoted catalysts, bismuth is localized at the interface between metal nanoparticles and support covering the Co surface. Bismuth oxidation-reduction cycling during carbon monoxide hydrogenation results in the removal of deposed carbon and catalyst self-regeneration. Formation of the bismuth layer in the surface of cobalt nanoparticles protects them against sintering.

This chapter is based on the following publication:

Bang Gu, Mounib Bahri, Ovidiu Ersen, Andrei Y. Khodakov*, Vitaly V. Ordomsky*, *ACS Catalysis* 9 (**2019**) 991-1000.

7.1. Introduction

Syngas is an important intermediate and can be produced from methane steam reforming or partial oxidation, coal and biomass gasification. Syngas conversion into hydrocarbons and oxygenates by Fischer-Tropsch (FT) synthesis or into substitute natural gas (SNG) via the methanation reaction [1, 2] are major industrial processes. Indeed, carbon monoxide methanation reaction was first discovered by Sabatier and Senderens in 1902 [3]. FT synthesis, which produces liquid hydrocarbons from syngas, was developed in 1920ies by Franz Fischer and Hans Tropsch [4, 5]. These processes have been currently receiving growing interest for synthesis of renewable fuels. The thermo-chemical conversion of renewable feedstocks (e.g. biomass, plastic and organic waste) into SNG and hydrocarbons is also an opportunity to minimize anthropogenic greenhouse gas emissions.

Low temperature FT synthesis on cobalt catalysts, which occurs at 220-240°C, 20 bar and H_2/CO molar ratio of 2, is very attractive for synthesis of middle distillates and wax, because of high cobalt intrinsic activity, high conversion per single pass and better catalyst stability than with iron catalysts [6]. In the syngas conversion to methane, nickel catalysts are often used due to their relatively high activity and low cost. The methanation often runs with a stoichiometric H_2/CO feed ratio of a 3.0 and at high temperatures (300-600 °C) [7].

Catalyst deactivation remains one of the main challenges of these processes. Catalyst deactivation results in lower process efficiency, periodic regenerations, high energy consumption and catalyst loss [8-10]. Catalyst deactivation for syngas conversion is a complex phenomenon and may be an interplay of several phenomena. Major deactivation mechanisms of cobalt and nickel catalysts involve metal sintering and carbon deposition [8-10]. Metal sintering seems to principally occur during the initial reaction period, while carbon deposition proceeds at longer time-on-stream and leads to the accumulation of refractory carbon species on the catalyst surface.

Cobalt sintering at both nano- and microscopic scales during FT synthesis has been reported using transmission [9], scanning electron microscopies (TEM, SEM) [11] and operando X-ray diffraction (XRD) [12]. Moodley [13] and Peña [14, 15] have recently investigated carbon deposition, resulting in formation of different carbon species on alumina supported cobalt catalysts. Bartholomew et al. [16, 17] studied the effect of temperature, chemical and physical properties of alumina and water on the activity loss of nickel catalysts due to sintering. Shen et al. [18] also investigated sintering due to nickel carbonyl formation. Recently, deactivation of nickel catalysts due to nickel sintering, carbon deposition and poisoning was studied using steady-state isotopic transient kinetic analysis (SSITKA) and operando Fourier-transform infrared (FTIR) spectroscopy [19, 20].

Several strategies have been used to increase the stability of the supported metal catalysts. Carbon deposition can be reduced by promotion with noble metals. Iglesia et al. [21] showed that promotion with ruthenium inhibited the deactivation of cobalt catalysts by increasing the rate of removal of carbon and oxygen species during reaction and regeneration. The presence of Pd has been also shown to increase stability of small size nanoparticles and decrease of polymeric carbon formation by hindering C-C coupling [22].

Other strategies have focused on reducing sintering of metal nanoparticles. Using graphene as a support has been shown to suppress sintering of metal nanoparticles [23]. Metal-organic framework (MOF) decomposition has been used for preparation of highly dispersed Fe carbide nanoparticles encapsulated in carbon shells [24]. Sintering was also remarkably slow-down in silica-shell cobalt and ruthenium nanoreactors [25]. The main drawbacks of previous methodologies to stabilize the catalytic performance in carbon monoxide hydrogenation are use of precious metals, expensive supports and complex catalyst preparation procedures.

Recently, we have uncovered a strong promoting effect of soldering metals such as Bi and Pb on the performance and stability of Fe catalysts in high temperature FT synthesis [26, 27]. The observed phenomena have been attributed to the decoration of

Fe carbide nanoparticles with the promoting elements, which have low melting point and remain highly mobile under the reaction conditions. The promoters seem to facilitate CO dissociation by scavenging O atoms from iron carbide. It can be suggested that these promoters may influence the performance of other metal catalysts.

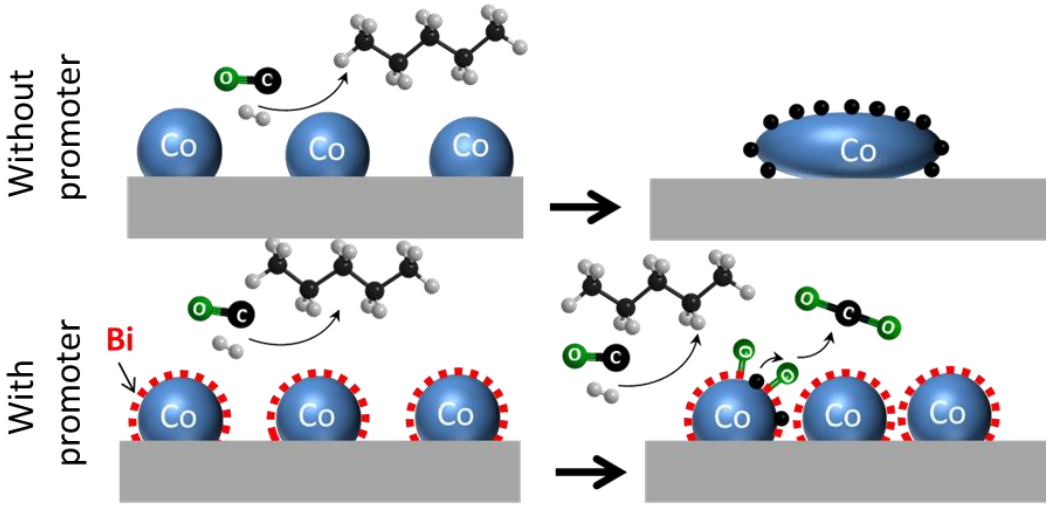

Figure 7.1. *Effect of the Bi promotion on stability of the supported cobalt catalysts. In the non-promoted catalysts, deactivation proceeds via carbon deposition and cobalt sintering. The presence of bismuth at the interface with the support slows down cobalt sintering and facilitate removal of carbon species with CO_2 formation.*

This chapter addresses the effects of the promotion with Bi on the performance of supported Co and Ni catalysts for FT synthesis and methanation. Surprisingly, we have uncovered that the Bi-promotion even at low content remarkably increases the stability of both cobalt and nickel catalysts in comparison with the non-promoted counterparts. The presence of the promoter at the interface of cobalt and nickel nanoparticles and support seems to slow down both carbon deposition and metal sintering (Figure 7.1).

7.2. Results and Discussion

7.2.1. Catalyst characterization

Nitrogen adsorption and BET analysis show similar surface area and pore sizes in the catalysts without Bi and promoted with different Bi contents (Table 7.1). Figure 7.2 displays XRD patterns of the cobalt and nickel catalysts, which indicate the presence

of cobalt and nickel oxides. The XRD peak broadening is indicative of Co_3O_4 and NiO nanoparticles with the sizes of around 10 nm in all promoted and non-promoted catalysts (Table 7.1).

Table 7.1. *Physical properties of supports and supported Co and Ni catalysts.*

Sample	S_{BET}[a] (m^2/g)	V_{tot}[b] (cm^3/g)	D_{meso}[c] (nm)	D_{metal}[d] (nm)	Total H_2 consumption[e] (mmol/g)	EOR (%)[f]	Co or Ni content[g] (wt%)	Bi content[g] (wt%)	CO adsorption (%)[h]
SiO_2	301.7	1.37	16.0	-	-	-	-	-	-
Co/SiO_2	225.6	1.05	16.5	10.2	2.55	59	13.8	-	6.5
$Co0.1Bi/SiO_2$	220.2	1.08	15.9	11.1	-	71	12.9	0.07	1.8
$Co0.2Bi/SiO_2$	217.8	1.10	16.0	10.5	2.86	-	13.2	0.15	-
$Co1.0Bi/SiO_2$	213.2	1.11	16.8	10.0	3.04	74	13.0	0.75	0.4
Ni/SiO_2	256.7	1.05	14.8	13.3	2.73	-	14.3	-	-
$Ni0.03Bi/SiO_2$	258.1	1.06	14.6	13.5	2.86	-	13.9	0.03	-
$Ni0.1Bi/SiO_2$	256.1	1.09	15.0	12.5	2.96	-	14.0	0.078	-
$Ni0.2Bi/SiO_2$	255.6	1.03	14.6	12.8	3.03	-	13.7	0.16	-

[a] BET surface area.

[b] Single point desorption total pore volume of pores, P/P_0=0.975.

[c] The pore diameter in the mesoporous region evaluated by the BJH method.

[d] Average particle size of cobalt or nickel oxide by XRD.

[e] The total H_2 consumption from TPR analysis.

[f] The reduction degree of Co catalysts (EOR) was measured by O_2 pulse oxidation method.

[f] The Co, Ni and Bi content from ICP-OES.

[h] CO adsorption amount from CO chemisorption measurements.

Figures 7.3 and 7.4 show STEM-EDX images and corresponding EDX mapping of the non-promoted and promoted Co/SiO_2 catalyst after calcination. The calcined non-promoted catalyst demonstrates 50 nm aggregates constituted by Co oxide nanoparticles of 5-10 nm. The particle sizes were calculated from particle size distribution (Figure 7.5). The size of individual cobalt nanoparticles is consistent with the cobalt oxide crystallite sizes calculated from XRD peak broadening (Figure 7.2, Table 7.1).

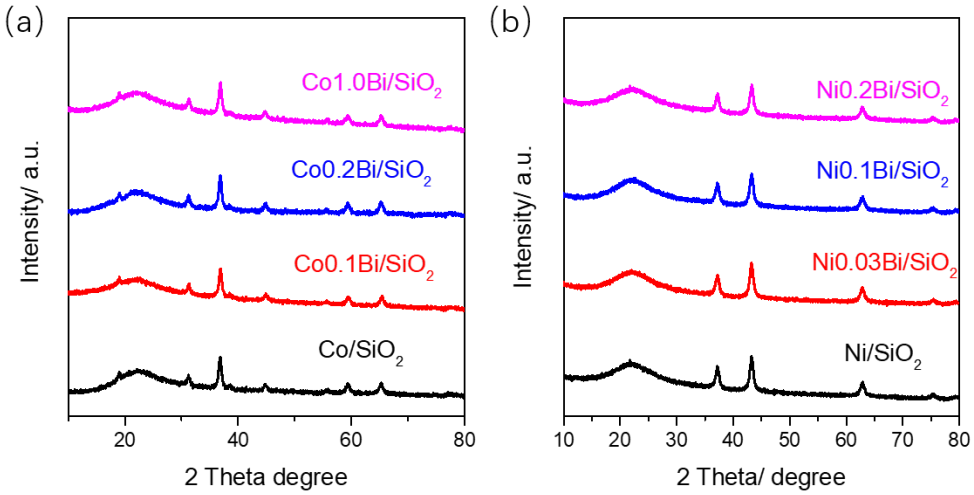

Figure 7.2. *XRD profiles of the calcined catalysts: (a) CoxBi/SiO2 (b) NixBi/SiO2.*

The presence of Bi in Co0.1Bi/SiO_2 after calcination does not change the distribution of Co oxide nanoparticles in comparison with the non-promoted catalyst (Figures 7.3 and 7.4). Note that according to STEM-EDX images, Bi is located closely to Co nanoparticles in the calcined catalyst. This suggests high mobility, strong affinity of Bi to Co and partial coating of cobalt with bismuth.

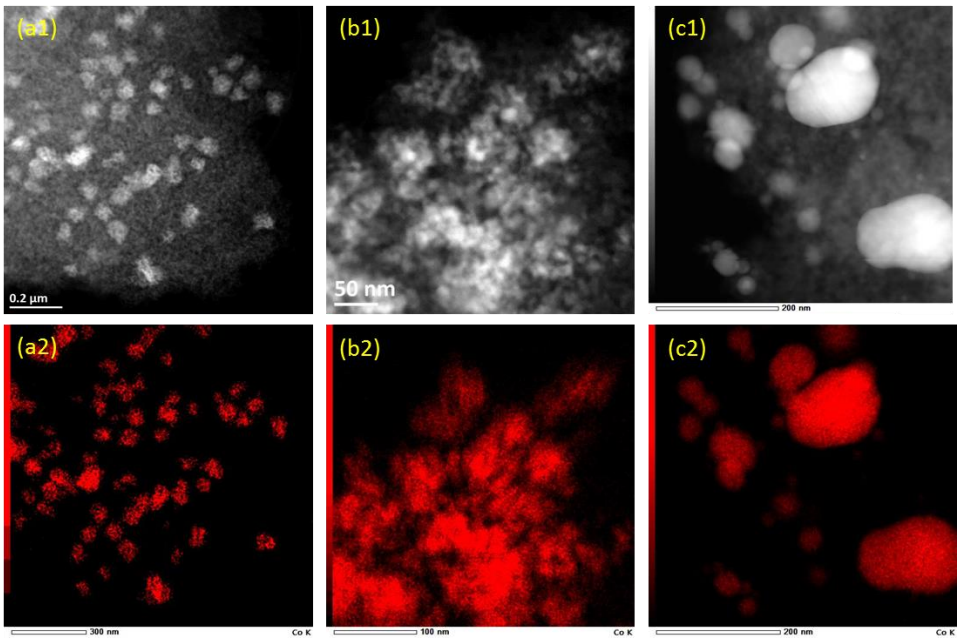

Figure 7.3. *STEM-HAADF images and corresponding Co elemental maps (in red, below) obtained by EDX on some typical Co/SiO2 catalytic grains after calcination (a1, a2), reduction (b1, b2) and catalytic reaction (c1, c2).*

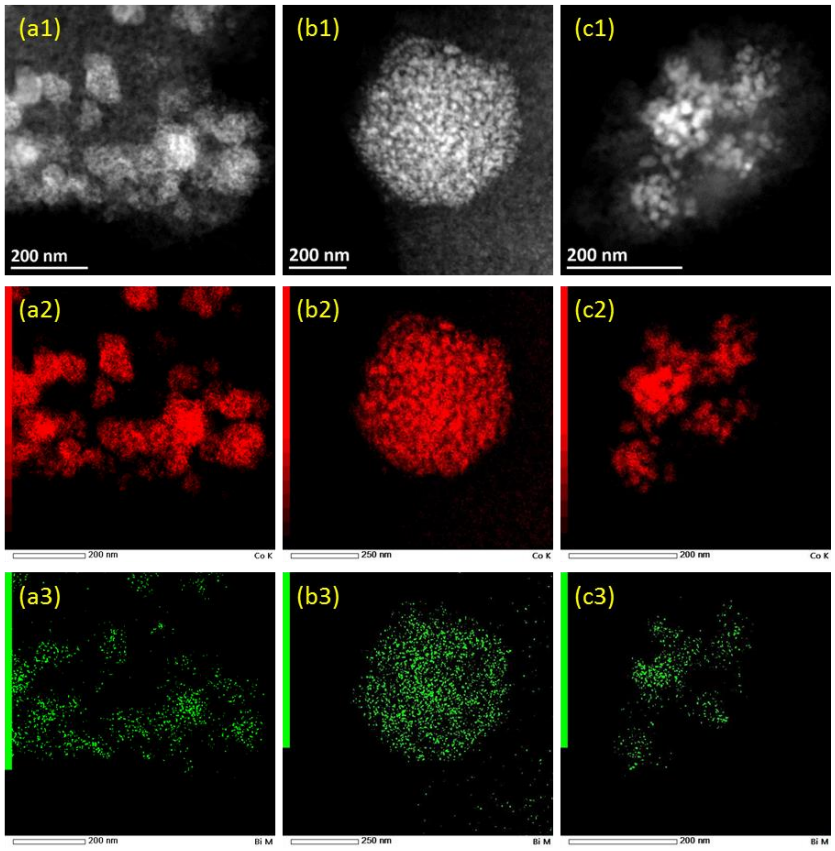

Figure 7.4. *STEM-HAADF images and corresponding Co (in red) and Bi (in green) elemental maps obtained by EDX on some typical Co0.2Bi/SiO₂ catalytic grains after calcination (a1, a2, a3), reduction (b1, b2, b3) and catalytic reaction (c1, c2, c3).*

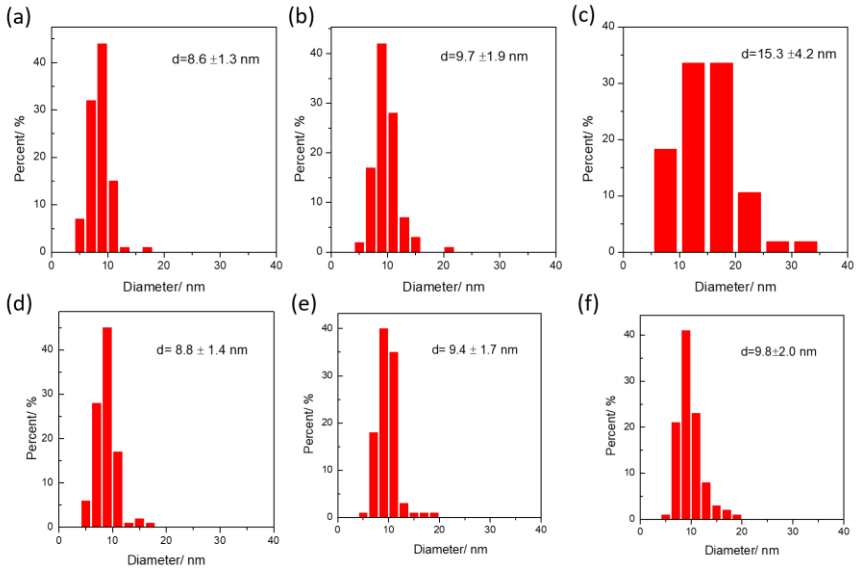

Figure 7.5. *Particle size distribution of Co/SiO₂ and Co0.2Bi/SiO₂ catalyst after calcination (a) (d), reduction (b) (e) and FT catalytic test(c) (f).*

The promoter amount in the catalysts (<1.0 wt.%) was too low to detect the relevant bismuth phases by XRD. The reducibility of Co and Ni before and after addition of Bi was studied by TPR (Figure 7.6). The TPR profiles of Co catalysts exhibit hydrogen consummation peaks between 250 and 500 °C, which corresponds to the two-step reduction of Co_3O_4 to metallic cobalt with intermediate formation of CoO [28]. The nickel catalysts exhibit several TPR peaks between 300 and 600 °C. Integration of the TPR data suggests slightly easier reducibility of both cobalt and nickel in the Bi-promoted catalysts compared to the non-promoted counterparts (Table 7.1). The extent of oxygen reduction (EOR) measured by oxygen titration at 400 ºC correlates with TPR results (Table 7.1) and suggests easier Co reduction in the presence of Bi promoter.

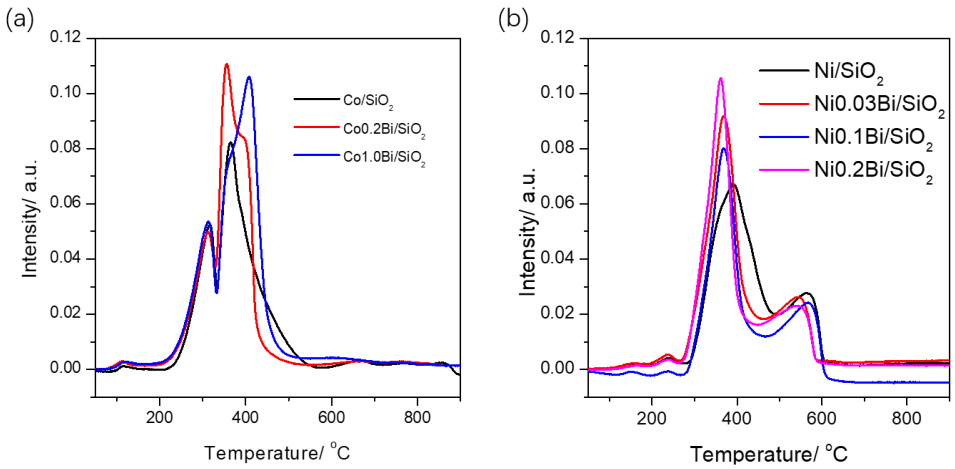

Figure 7.6. *H_2-TPR profiles of the calcined catalysts: (a) CoxBi/SiO_2 (b) NixBi/SiO_2.*

Analysis of the metal dispersion by CO adsorption of reduced catalysts shows relatively low dispersion of 6 % over non-promoted Co/SiO_2 catalyst (Table 7.1), which corresponds to earlier results [29]. Increase in the Bi content leads to gradual decrease in the CO adsorption (Table 7.1), which could be explained by partial coating cobalt nanoparticles with Bi species uncovered by STEM-EDX.

7.2.2. Catalytic performance

FT synthesis over cobalt catalysts leads to syngas conversion to methane, light and heavier hydrocarbons and water. Small amounts of carbon dioxide were also produced. The tests were conducted at higher reaction temperature (250 °C) than usually used for

low temperature FT synthesis in order to accelerate catalyst deactivation. Note that Bi/SiO_2 has no activity in CO hydrogenation (Table 7.2). Carbon monoxide conversion at iso-GHSV as a function of time on stream over Co/SiO_2 catalyst is presented in Figure 7.7 a. Carbon monoxide conversion initially increases. The carbon monoxide conversion gradually decreases during 110 h on Co/SiO_2 from 60 to 44 %. Interestingly, the promotion with 0.1 wt. % and 0.2 wt. % of Bi does not lead to any significant changes of initial CO conversion, while a much more stable catalytic performance was observed. Indeed, carbon monoxide conversion remains unchanged for more than 100 h over $Co0.1Bi/SiO_2$ and $Co0.2Bi/SiO_2$. Higher Bi content (1.0 wt. %) results however, in a drop of the catalytic activity. In addition, $Co1.0Bi/SiO_2$ exhibits noticeable deactivation (Figure 7.7a).

Table 7.2. *Catalytic performance in FT synthesis over Co catalysts (20 bar, H_2/CO = 2, T = 250 ºC, 110 h) and methanation over Ni catalysts (1 bar, H_2/CO = 3, T = 300 ºC, 60 h).*

Catalyst sample	GHV, L/h·g	X_{CO}, %	S_{CO2}, %	S_{CH4}, %	S_{C2-C4}, %	S_{C5+}, %
Co/SiO_2	3.6	44	0.5	6.8	5.7	87.5
$Co0.1Bi/SiO_2$	3.6	55	3.6	7.6	7	85.4
$Co0.2Bi/SiO_2$	3.6	54	2.8	7.8	6.9	85.3
$Co1Bi/SiO_2$	3.6	29	1.5	9.8	8.7	81.5
Bi/SiO_2	3.6	0	-	-	-	-
Ni/SiO_2	18	26	1.0	97.2	2.8	-
Ni0.03Bi/SiO	18	31	1.9	97.5	2.5	-
$Ni0.1Bi/SiO_2$	9	30	2.2	97.4	2.6	
$Ni0.2Bi/SiO_2$	6.8	27	1.6	97.3	2.7	-

Interestingly, hydrocarbons selectivities at comparable carbon monoxide conversions were not much affected by promotion with Bi (Table 7.2). The CO_2 selectivity increases from the almost zero CO_2 selectivity over the non-promoted cobalt catalyst to 3.6 % and 2.8 % in $Co0.1Bi/SiO_2$ and $Co0.2Bi/SiO_2$ at the CO conversion of 54-55 %. Thus, low bismuth content has a strong positive effect on the catalyst

stability of silica supported cobalt catalysts, while a high loading of the promoter is detrimental on the overall catalytic performance.

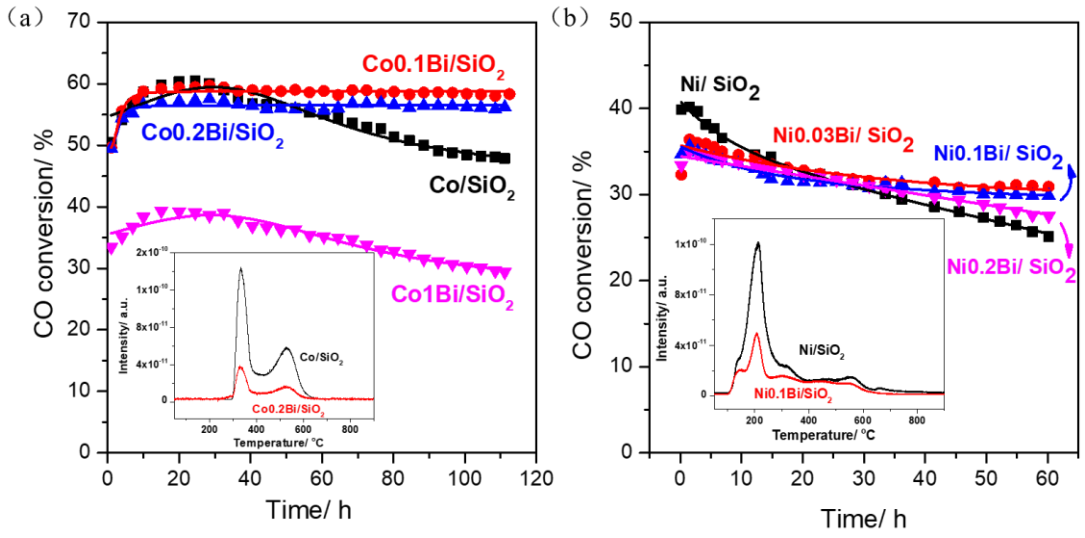

Figure 7.7. *Stability of Co catalysts during FT synthesis (T = 250 °C, H_2/CO = 2, 20 bar, 3.6 L/g·h) and Ni catalysts during methanation (T = 300 °C, H_2/CO = 3, 1 bar, 6-18 L/g·h) with TPH-MS analysis of carbon deposition after reaction.*

Similarly, the stability enhancement in CO hydrogenation to methane was also observed for the Bi-promoted Ni catalysts (Figure 7.7b). Promotion with Bi has only a slight influence on the catalyst activity. At the same GHSV, Ni0.03Bi/SiO_2 showed almost the same initial CO conversion as the non-promoted catalyst. The non-promoted nickel catalyst exhibited a noticeable deactivation; the CO conversion gradually decreased from 40 to 25 % during the 60 h of reaction. The presence of small Bi amounts (0.03 wt. %) leads to a significant enhancement of catalyst stability. The conversion remains quasi stable over Ni0.03Bi/SiO_2. Higher Bi content (0.1 wt. %) leads to lower catalytic activity (Figure 7.7b). Note however that the Ni0.1Bi/SiO_2 catalyst also showed higher stability at comparable conversion than the non-promoted catalyst. Similar to Co counterparts, further increase in the Bi content (up to 0.2 wt. %) results in a less active nickel catalyst, which also showed a visible deactivation with time on stream. The selectivity to methane was close to 97 % for all nickel catalysts with about 3 % selectivity to light hydrocarbons. Some CO_2 production with the

selectivity of 1.0 % was observed on Ni/SiO_2, where CO_2 seems to come from the water gas shift (WGS) reaction. In the presence of small amount of Bi, the selectivity to CO_2 increases almost twice. The effect is similar to the Co catalysts (Table 7.2).

7.2.3. Coke deposition

Carbon deposition is considered as one of the reasons of catalyst deactivation in CO hydrogenation [10, 13-15]. Carbon deposition can produce several negative effects on the catalytic performance of supported metal catalysts: [9, 14, 15, 17] pore blocking and introducing diffusion limitations, poisoning and electronic effects on the intrinsic metal site activity, restructuring and fracturing of metal nanoparticles and support.

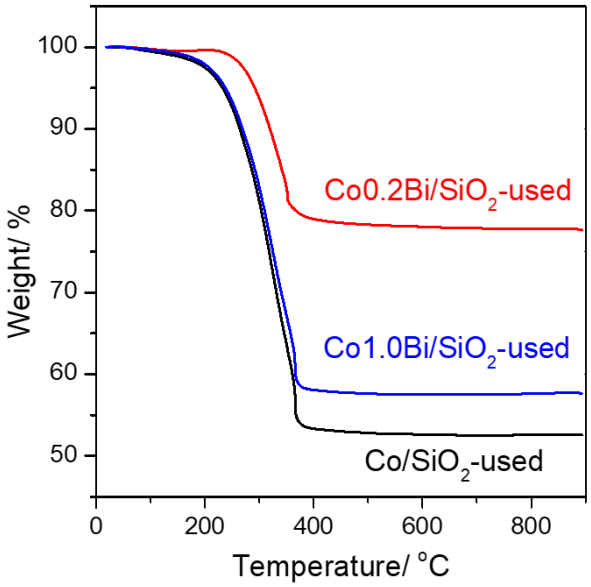

Figure 7.8. *Thermogravimetric analysis (TG) measurements of the used cobalt catalysts.*

TPH-MS and TGA have been used for identification of carbon species present after catalytic tests in the cobalt catalysts (Figure 7.7a, insert, Figure 7.8). The hydrogenation of deposed carbon species in pure hydrogen over Co/SiO_2 proceeds in the temperature range from 400 to 600 °C with the amount of released CH_4 corresponding to the deposed carbon amount almost equal to 16.3 wt. % of the catalyst weight. The TPH-MS profiles exhibit the presence of several peaks, which can be attributed to different carbon species. The peak around 300 °C was assigned to the hydrogenation and

desorption of strongly adsorbed heavy hydrocarbons, while high temperature TPH peaks correspond to hydrogenation of more refractory carbon species [9, 14, 15]. Surprisingly, the cobalt catalyst containing 0.2 wt. % of Bi shows only traces of deposed carbon (2.4 wt. %). This suggests that carbon deposition was drastically reduced in the Bi-promoted catalyst. TGA was consistent with TPH data; it also shows less significant weight loss in the spent Bi-promoted catalysts, which can be relevant to lower carbon deposition (Figure 7.8). Similar situation was observed with the Ni catalysts. The presence of 0.1 wt.% of Bi resulted in the major decrease in the carbon content in the spent nickel catalysts measured by TPH-MS (Figure 7.7b, insert) from 9.5 to 3.3 wt. %.

Table 7.3. *Catalytic performance in WGS reaction over Bi/SiO_2 catalysts (1 bar, N_2 30ml/min, CO 5 ml/min, H_2O 0.5ml/h, T = 250 or 350 ºC, 10 h)*

Catalysts	T/ ºC	CO conv. %	Selectivity/ %	
			CH_4	CO_2
Bi/SiO_2	250	0	-	-
	350	0	-	-

Then, we examined in a greater detail the reasons of lower carbon deposition over the Bi-promoted cobalt and nickel catalysts. Note that lower carbon deposition over the promoted Ni and Co catalysts coincides with higher selectivity to CO_2. The Bi/SiO_2 catalyst did not show any activity in WGS even at higher reaction temperature (Table 7.3). This, it is not likely that the produced CO_2 is due to WGS enhanced in the presence of bismuth. We suggest that higher catalyst stability and observed simultaneously higher CO_2 selectivity over the Bi-promoted can be explained by the continuous carbon removal from the catalysts under the reaction conditions yielding CO_2.

In order to check the hypothesis about possible conversion of deposed carbon into CO_2 under the FT reaction conditions, we performed additional experiments. Carbon species were intentionally deposed on Co catalysts by impregnation with fructose in order to reach 10 wt. % in the final catalyst, followed by treatment in hydrogen at

400 °C. As expected, the non-promoted Co/SiO_2 catalyst carbonized with fructose showed a twice-lower activity in comparison with the parent catalyst (Figure 7.9a). In addition, a noticeable catalyst deactivation was observed after the start of reaction. The CO conversion dropped from 37 to 24 % after 100 h on stream.

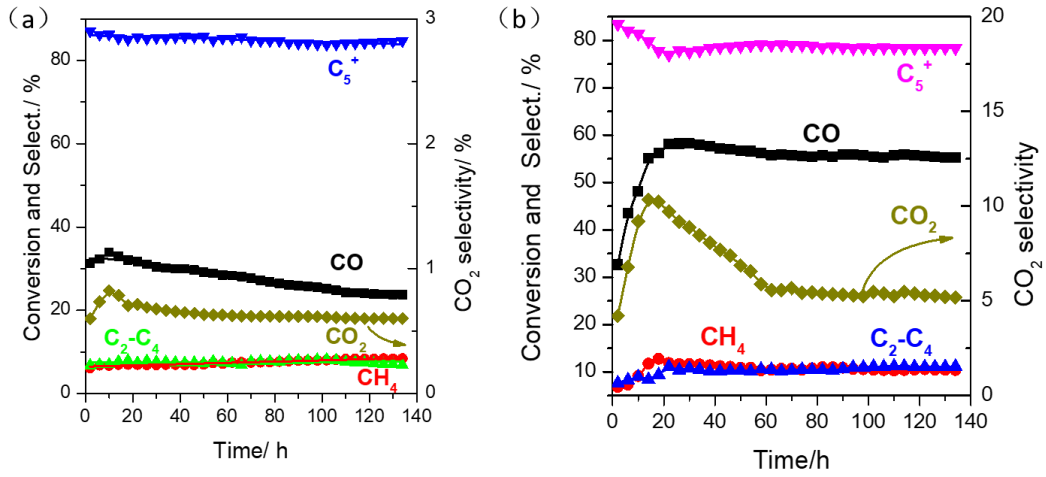

Figure 7.9. *Stability of the catalysts during FT synthesis after carbon deposition on Co/SiO_2 (a) and $Co0.2Bi/SiO_2$ (b) and (T = 250 °C, H_2/CO = 2, 20 bar, 3.6 L/g·h)*

The results were rather different for the carbonized Bi-promoted catalyst. The promoted $Co0.2Bi/SiO_2$ catalyst impregnated with fructose also exhibited lower activity at the beginning of the catalytic test (Figure 7.9b). Remarkably, in comparison with the non-promoted catalyst, the CO conversion over carbonized $Co0.2Bi/SiO_2$ increases with time on stream reaching the CO conversion level, which was observed over the same Bi-promoted catalyst without carbonization. Note that the recovery of the catalytic activity over $Co0.2Bi/SiO_2$ coincided with an important release of CO_2 during the first 60 h of reaction. After the recovery of the catalytic performance, the CO_2 production decreased to lower level observed on this catalyst without fructose pretreatment. Thus, the conducted experiment confirms a relationship between the carbon removal and CO_2 production over the Bi-promoted catalysts.

The deposed carbon to be converted into CO_2 should react with oxygen species. There are two molecules, which might provide oxygen for carbon oxidation during CO hydrogenation: water and CO. In order to evaluate the effect of water, we pretreated the

Bi-promoted catalyst carbonized with fructose in the flow of hydrogen and H_2O. The H_2 and H_2O concentrations in the feed corresponded to the amounts typically present in the CO hydrogenation. No CO_2 release was detected during this experiment. No recovery of the catalytic activity was either observed when the catalyst treated for 3 h in H_2/H_2O was again exposed to syngas. This suggests that the exposure of the spent cobalt catalyst to water under the reaction conditions is not sufficient to remove the deposed carbon species. Indeed, oxidation of carbon by water is not thermodynamically favorable:

$$C_{coke} + 2H_2O = CO_2 + 2H_2,\ \Delta G = 40.4\ KJ/mol\ (523\ K)$$

Carbon monoxide dissociation over cobalt catalysts results in surface carbon and oxygen species. Thus, another possibility for catalyst self-regeneration could come from oxidation of the refractory carbon deposits by oxygen species generated during dissociation of CO. Simultaneously, carbon species produced from CO dissociation can be hydrogenated to hydrocarbons. Note that a combination of CO hydrogenation and carbon oxidation is required to make the process thermodynamically favorable and to remove the deposed carbon:

$$C_{coke} + 2CO + 4H_2 = CO_2 + 2CH_4,\ \Delta G = -142.0\ KJ/mol\ (523\ K)$$

This also explains CO_2 production during CO hydrogenation, which accompanies removal of deposed carbon.

Our recent works [26, 27]revealed a strong effect of the Bi and Pb promoters on the catalytic performance of Fe catalysts in high temperature FT synthesis. The observed major enhancement of the reaction rate was explained by oxygen scavenging during CO dissociation by Bi and Pb leading with the promoter oxidation. The oxidized Bi and Pb species are then reduced by CO to the metal state with release of CO_2.

It can be suggested that in the cobalt and nickel catalysts, bismuth can also change its oxidation state during CO hydrogenation. In order to verify this suggestion, we performed XPS analysis of the $Co0.1Bi/SiO_2$ catalyst after its activation and exposure to the reaction conditions. After these pretreatments, the catalyst was transferred from the XPS pretreatment to the analysis chamber without any exposure to air. The in-situ

XPS shows (Figure 7.10) that the Bi in the fresh catalysts is present as oxide phase and is reduced to the metallic state after catalyst activation in hydrogen. Under the reaction conditions, Bi is present in the cobalt catalyst in both metallic and oxidized states [26, 27]. Similar to iron catalysts, bismuth oxidation may involve scavenging of oxygen generated during CO dissociation over cobalt nanoparticles. Deposed carbon can then be oxidized by bismuth oxide species with production of carbon dioxide and reduction of bismuth to metal. The in-situ XPS shows that Bi in the fresh catalysts is present as oxide phase, after reduction the Bi is in the metallic phase. The metallic Bi oxidizes after syngas treatment. The sample was transferred from the reaction to the analysis chamber of XPS without any exposure to air.

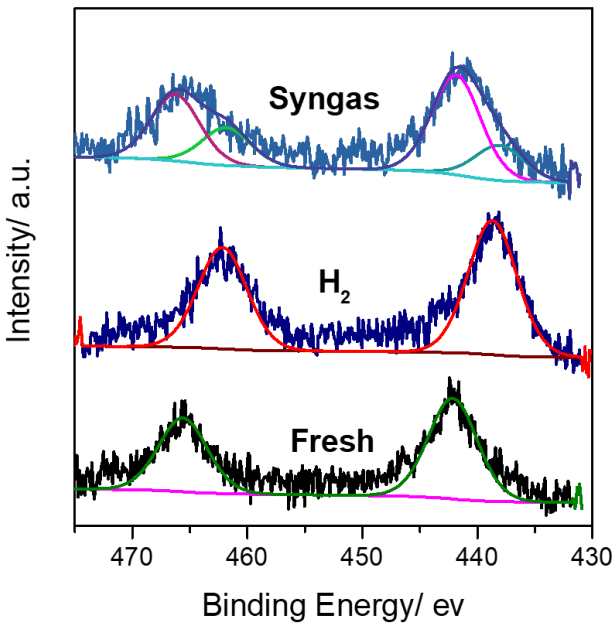

Figure 7.10. *High-resolution Bi 4d XPS spectra of Co0.2Bi/SiO₂ catalyst after calcination, reduction and FT catalytic test.*

XPS analysis of Co and Ni in the samples with and without promoter after exposure to hydrogen and syngas the XPS pretreatment chamber and transfer to the measurement chamber without exposure to air shows besides metallic Co and Ni also the presence of Co_3O_4 with CoO and Ni_2O_3 with NiO, respectively. The contribution of oxide species increases for both catalysts after exposure to syngas. This could be explained by partial surface oxidation of metal during reaction [30]. The main difference between promoted

and non-promoted catalysts is higher contribution of metallic species in promoted catalyst which corresponds to the higher extent of reduction (Figure 7.11).

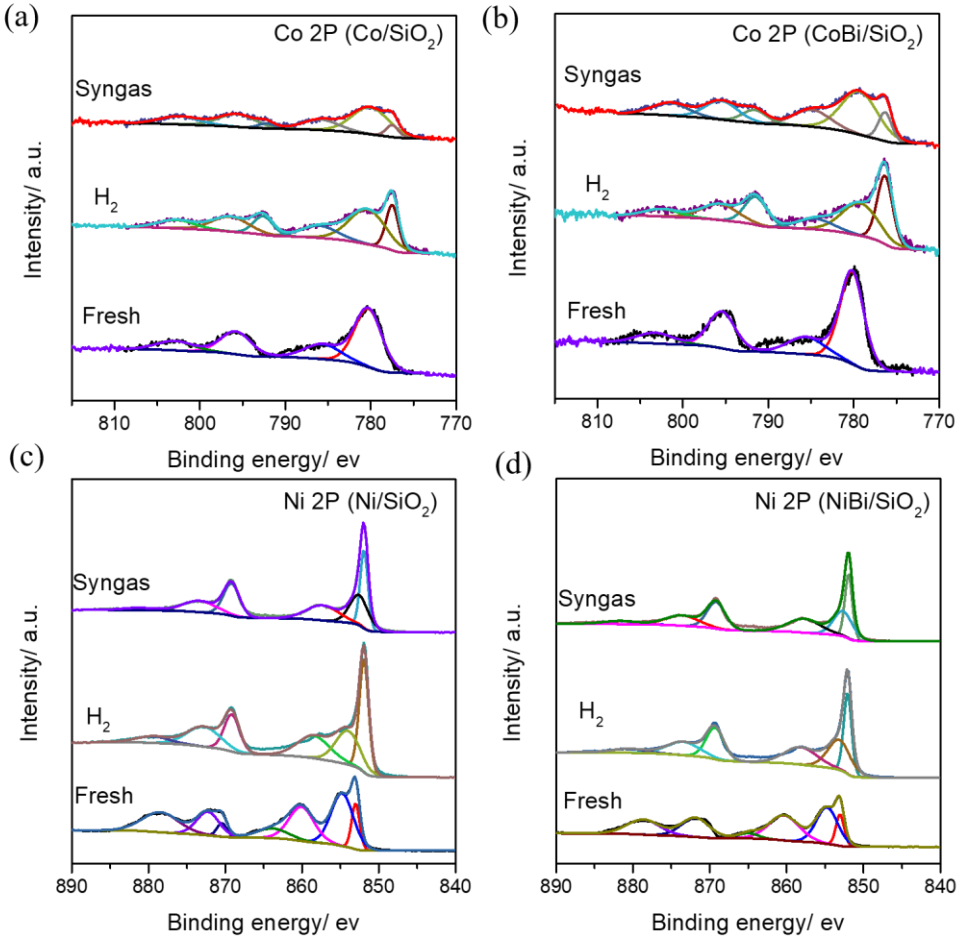

Figure 7.11. *High-resolution Co 2P and Ni 2P XPS spectra of CO/ SiO_2, CoBi/SiO_2, Ni/ SiO_2 and Ni/ SiO_2 catalyst after calcination, reduction and FT catalytic test.*

To confirm the possible reduction of bismuth oxide by deposed carbon, the Bi/SiO_2 with 15 wt. % of Bi impregnated with fructose was heated at 250 °C in nitrogen (P = 20 bar) for 36 h. The measured XRD profiles (Figure 7.12) showed reduction of bismuth oxide after its exposure to deposed carbon species. Analysis of gas phase demonstrated CO_2 formation, which is probably due to oxidation of carbon species by bismuth oxide (Figure 7.13). Carbon removal and self-regeneration of cobalt and nickel catalyst during FT synthesis can be then explained by coupling of oxidation of deposed carbon by bismuth species with carbon monoxide hydrogenation.

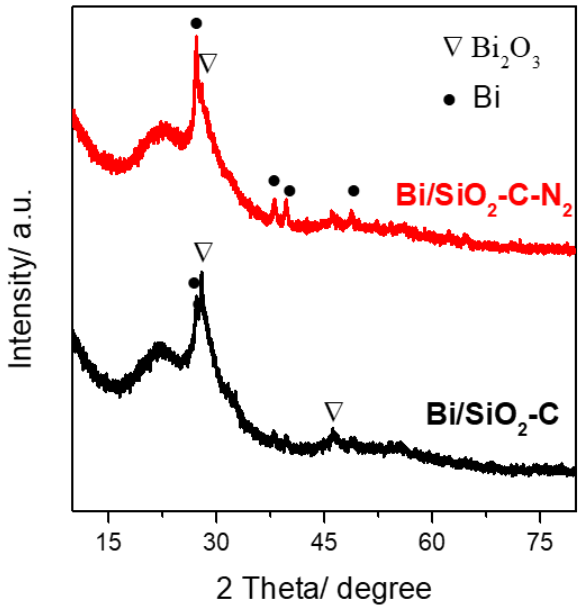

Figure 7.12. *XRD profiles of the fresh pre-carbon deposited Bi/SiO₂ catalysts and after high pressure N₂ treatment (N₂ 20 bar, T = 250 °C, 36 h)*

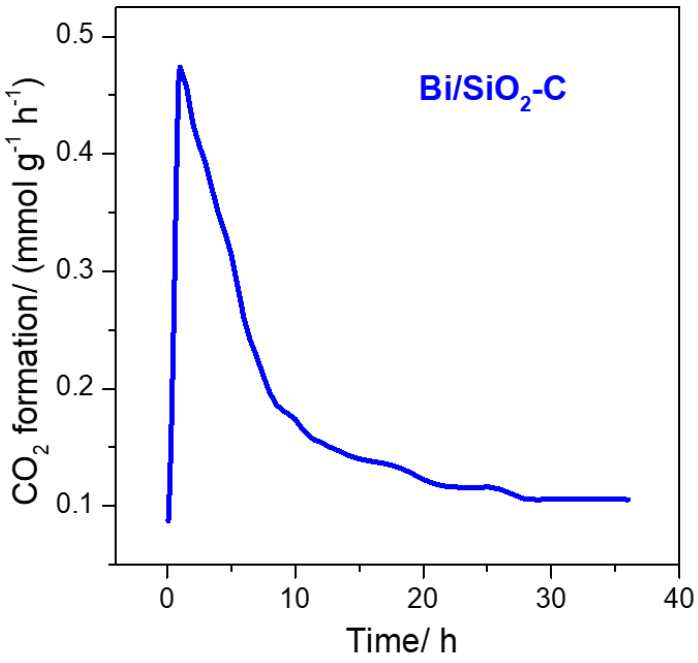

Figure 7.13. *CO₂ formation rate over pre-carbon deposited Bi/SiO₂ catalysts in high pressure N₂ treatment (N₂ 20 bar, T = 250 °C, 36 h)*

7.2.4. Sintering

Metal sintering is also known as an important reason of catalyst deactivation [9-11, 17] in carbon monoxide hydrogenation (Figure 7.1). Previous works [12, 31] show that the rate of FT synthesis depend on the size of individual cobalt nanoparticles rather than on larger nanoparticle agglomerates. After FT synthesis over the non-promoted catalyst, TEM images are indicative of noticeable cobalt sintering with significant increase in the sizes of Co nanoparticles (Figures 7.3 and 7.5).

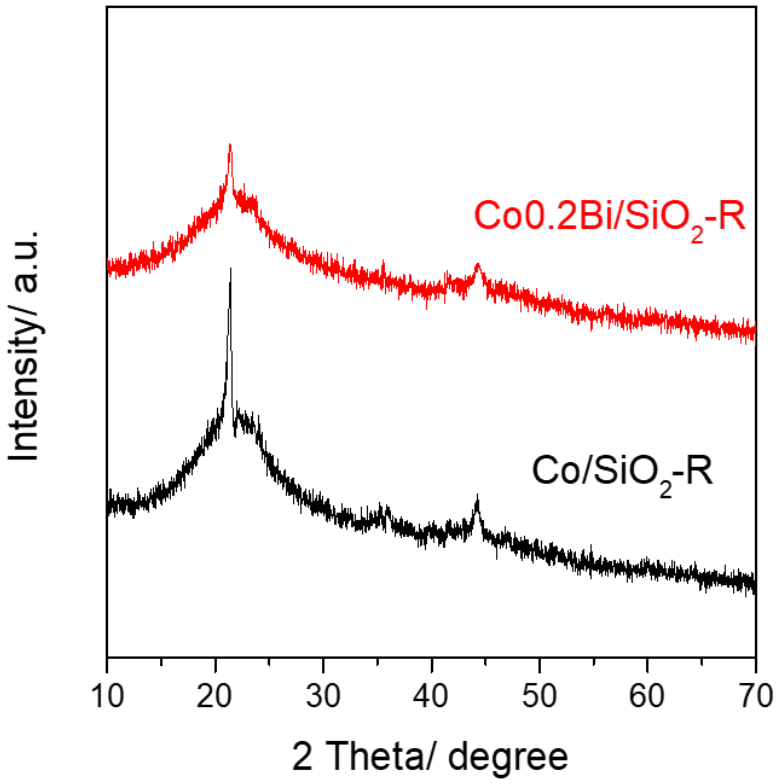

Figure 7.14. *XRD profiles of the used Co/SiO₂ and Co0.2Bi/SiO₂ catalysts (20 bar, T=250 °C, 110 h)*

This observation is consistent with XRD patterns measured for the spent non-promoted Co/SiO₂ catalyst (Figure 7.14). The Scherrer equation suggests an increase in the metallic cobalt nanoparticle size to 15 nm. Different to the non-promoted counterparts, no cobalt sintering was detected in the spent Bi promoted cobalt catalysts according to TEM and XRD analysis (Figures 7.4, 7.5 and 7.14). EDX analysis is indicative of bismuth localization at the interface between cobalt and support (Figure

7.15). The cobalt-bismuth systems are characterized by phase separation in the solid and liquid state [32]. Thus, the eutectic composition of Bi-Co contains 97 % of Bi at 260 ºC. This suggests that at the reaction conditions Bi will be pushed out to the surface of Co nanoparticles. It explains presence of Bi on the surface of Co nanoparticles (Figures 7.4 and 7.15). Thus, it is expected that under the reaction conditions Bi should have very high mobility [26, 27]. Coating of Co nanoparticles by Bi film should decrease the surface energy of unsaturated Co atoms and slow down the sintering process. Thus, promotion of cobalt and nickel catalyst slows down both carbon deposition and metal sintering and results in more stable catalytic performance.

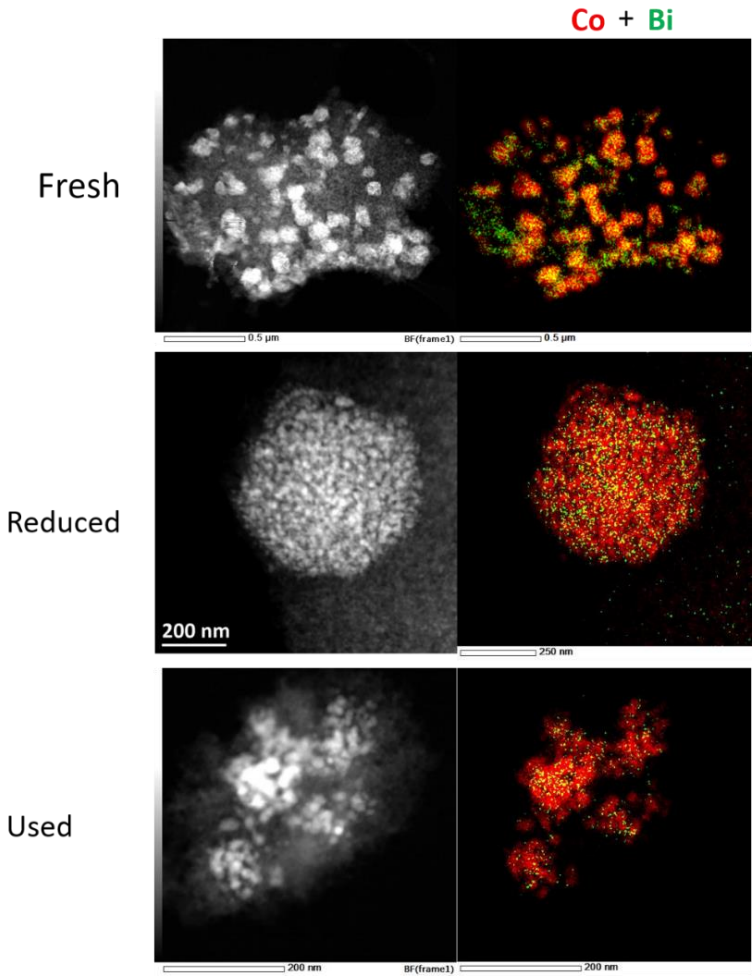

Figure 7.15. *STEM-HAADF images and corresponding Co (in red) and Bi (in green) elemental maps (in red, below) obtained by EDX on some typical CoBi/SiO_2 catalytic grains after calcination, reduction, and catalytic reaction.*

7.3. Conclusion

We uncovered a strong effect of the promotion with bismuth on the stability of cobalt and nickel catalysts for carbon monoxide hydrogenation (Figure 7.1). At low content of promoters, bismuth does not affect the catalytic performance of FT synthesis and methanation. Bismuth reduces both carbon deposition and metal sintering. Coupling of carbon oxidation with CO hydrogenation over the Bi-promoted catalysts reduces carbon deposition and results in the continuous catalyst self-regeneration under FT reaction conditions. Decoration of metal nanoparticles with Bi, which is highly mobile under the reaction conditions, protects them from sintering.

7.4. Reference

[1] V. Ponec, Some Aspects of the Mechanism of Methanation and Fischer-Tropsch Synthesis, Catalysis Reviews, 18 (1978) 151-171.

[2] S. Rönsch, J. Schneider, S. Matthischke, M. Schlüter, M. Götz, J. Lefebvre, P. Prabhakaran, S. Bajohr, Review on methanation-From fundamentals to current projects, Fuel, 166 (2016) 276-296.

[3] P. Sabatier, J. Senderens, New methane synthesis, Compte Rendu Acad. Sci. Paris, 134 (1902) 514-516.

[4] B.H. Davis, M.L. Occelli, Advances in Fischer-Tropsch synthesis, catalysts, and catalysis, CRC press, 2009.

[5] A.Y. Khodakov, W. Chu, P. Fongarland, Advances in the development of novel cobalt Fischer-Tropsch catalysts for synthesis of long-chain hydrocarbons and clean fuels, Chemical Reviews, 107 (2007) 1692-1744.

[6] F. Diehl, A.Y. Khodakov, Promotion of cobalt Fischer-Tropsch catalysts with noble metals: a review, Oil & Gas Science and Technology-Revue de l'IFP, 64 (2009) 11-24.

[7] D. Hu, J. Gao, Y. Ping, L. Jia, P. Gunawan, Z. Zhong, G. Xu, F. Gu, F. Su, Enhanced investigation of CO methanation over Ni/Al_2O_3 catalysts for synthetic natural gas production, Industrial & Engineering Chemistry Research, 51 (2012) 4875-4886.

[8] G. Jacobs, P.M. Patterson, Y. Zhang, T. Das, J. Li, B.H. Davis, Fischer-Tropsch synthesis: deactivation of noble metal-promoted Co/Al_2O_3 catalysts, Applied Catalysis A: General, 233 (2002) 215-226.

[9] A.M. Saib, D.J. Moodley, I.M. Ciobîcă, M.M. Hauman, B.H. Sigwebela, C.J. Weststrate, J.W. Niemantsverdriet, J. van de Loosdrecht, Fundamental understanding of deactivation and regeneration of cobalt Fischer-Tropsch synthesis catalysts, Catalysis Today, 154 (2010) 271-282.

[10] N.E. Tsakoumis, M. Rønning, Ø. Borg, E. Rytter, A. Holmen, Deactivation of cobalt based Fischer-Tropsch catalysts: A review, Catalysis Today, 154 (2010) 162-182.

[11] D. Peña, A. Griboval-Constant, F. Diehl, V. Lecocq, A.Y. Khodakov, Agglomeration at the Micrometer Length Scale of Cobalt Nanoparticles in Alumina-Supported Fischer-Tropsch Catalysts in a Slurry Reactor, ChemCatChem, 5 (2013) 728-731.

[12] H. Karaca, O.V. Safonova, S. Chambrey, P. Fongarland, P. Roussel, A. Griboval-Constant, M. Lacroix, A.Y. Khodakov, Structure and catalytic performance of Pt-promoted alumina-supported cobalt catalysts under realistic conditions of Fischer-Tropsch synthesis, Journal of catalysis, 277 (2011) 14-26.

[13] D.J. Moodley, J. van de Loosdrecht, A.M. Saib, M.J. Overett, A.K. Datye, J.W. Niemantsverdriet, Carbon deposition as a deactivation mechanism of cobalt-based Fischer-Tropsch synthesis catalysts under realistic conditions, Applied Catalysis A: General, 354 (2009) 102-110.

[14] D. Peña, A. Cognigni, T. Neumayer, W. van Beek, D.S. Jones, M. Quijada, M. Rønning, Identification of carbon species on iron-based catalysts during Fischer-Tropsch synthesis, Applied

Catalysis A: General, 554 (2018) 10-23.

[15] D. Peña, A. Griboval-Constant, C. Lancelot, M. Quijada, N. Visez, O. Stéphan, V. Lecocq, F. Diehl, A. Khodakov, Molecular structure and localization of carbon species in alumina supported cobalt Fischer-Tropsch catalysts in a slurry reactor, Catalysis Today, 228 (2014) 65-76.

[16] C. Bartholomew, R. Pannell, R. Fowler, Sintering of alumina-supported nickel and nickel bimetallic methanation catalysts in H_2H_2O atmospheres, Journal of Catalysis, 79 (1983) 34-46.

[17] C.H. Bartholomew, Mechanisms of catalyst deactivation, Applied Catalysis A: General, 212 (2001) 17-60.

[18] W. Shen, J. Dumesic, C. Hill Jr, Criteria for stable Ni particle size under methanation reaction conditions: Nickel transport and particle size growth via nickel carbonyl, Journal of Catalysis, 68 (1981) 152-165.

[19] D. Lorito, H. Li, A. Travert, F. Maugé, F.C. Meunier, Y. Schuurman, C. Mirodatos, Understanding deactivation processes during bio-syngas methanation: DRIFTS and SSITKA experiments and kinetic modeling over Ni/ Al_2O_3 catalysts, Catalysis Today, 299 (2018) 172-182.

[20] B. Legras, V.V. Ordomsky, C. Dujardin, M. Virginie, A.Y. Khodakov, Impact and detailed action of sulfur in syngas on methane synthesis on Ni/γ-Al_2O_3 catalyst, ACS Catalysis, 4 (2014) 2785-2791.

[21] A. Belambe, R. Oukaci, J. Goodwin Jr, Effect of Pretreatment on the Activity of a Ru-Promoted Co/ Al_2O_3 Fischer-Tropsch Catalyst, Journal of Catalysis, 166 (1997) 8-15.

[22] G. Jacobs, W. Ma, B.H. Davis, Influence of reduction promoters on stability of cobalt/g-alumina Fischer-Tropsch synthesis catalysts, Catalysts, 4 (2014) 49-76.

[23] Y. Cheng, J. Lin, K. Xu, H. Wang, X. Yao, Y. Pei, S. Yan, M. Qiao, B. Zong, Fischer-Tropsch synthesis to lower olefins over potassium-promoted reduced graphene oxide supported iron catalysts, ACS catalysis, 6 (2015) 389-399.

[24] T.A. Wezendonk, Q.S. Warringa, V.P. Santos, A. Chojecki, M. Ruitenbeek, G. Meima, M. Makkee, F. Kapteijn, J. Gascon, Structural and elemental influence from various MOFs on the performance of Fe@ C catalysts for Fischer-Tropsch synthesis, Faraday discussions, 197 (2017) 225-242.

[25] V. Subramanian, K. Cheng, C. Lancelot, S. Heyte, S. Paul, S. Moldovan, O. Ersen, M. Marinova, V.V. Ordomsky, A.Y. Khodakov, Nanoreactors: An efficient tool to control the chain-length distribution in Fischer-Tropsch synthesis, ACS Catalysis, 6 (2016) 1785-1792.

[26] B. Gu, V.V. Ordomsky, M. Bahri, O. Ersen, P.A. Chernavskii, D. Filimonov, A.Y. Khodakov, Effects of the promotion with bismuth and lead on direct synthesis of light olefins from syngas over carbon nanotube supported iron catalysts, Applied Catalysis B: Environmental, 234 (2018) 153-166.

[27] V.V. Ordomsky, Y. Luo, B. Gu, A. Carvalho, P.A. Chernavskii, K. Cheng, A.Y. Khodakov, Soldering of iron catalysts for direct synthesis of light olefins from syngas under mild reaction conditions, ACS Catalysis, 7 (2017) 6445-6452.

[28] A.Y. Khodakov, A. Griboval-Constant, R. Bechara, F. Villain, Pore-size control of cobalt

dispersion and reducibility in mesoporous silicas, The Journal of Physical Chemistry B, 105 (2001) 9805-9811.

[29] K. Cheng, V. Subramanian, A. Carvalho, V.V. Ordomsky, Y. Wang, A.Y. Khodakov, The role of carbon pre-coating for the synthesis of highly efficient cobalt catalysts for Fischer-Tropsch synthesis, Journal of Catalysis, 337 (2016) 260-271.

[30] C. Lancelot, V.V. Ordomsky, O. Stéphan, M. Sadeqzadeh, H.l. Karaca, M. Lacroix, D. Curulla-Ferré, F. Luck, P. Fongarland, A. Griboval-Constant, Direct Evidence of Surface Oxidation of Cobalt Nanoparticles in Alumina-Supported Catalysts for Fischer-Tropsch Synthesis, ACS Catalysis, 4 (2014) 4510-4515.

[31] P. Munnik, P.E. de Jongh, K.P. de Jong, Control and impact of the nanoscale distribution of supported cobalt particles used in Fischer-Tropsch catalysis, Journal of the American Chemical Society, 136 (2014) 7333-7340.

[32] S. Tencé, O. Janson, C. Krellner, H. Rosner, U. Schwarz, Y. Grin, F. Steglich, $CoBi_3$-the first binary compound of cobalt with bismuth: high-pressure synthesis and superconductivity, Journal of Physics: Condensed Matter, 26 (2014) 395701.

Chapter 8. General Conclusion and Perspectives

8.1 General Conclusion

Fischer-Tropsch synthesis is one of the key reactions in the utilization of non-petroleum carbon resources, such as coal, biomass, natural gas. for the sustainable production of clean fuels, light olefins, long chain α olefins and other valuable chemicals from syngas. Selectivity control and catalyst stability are among the most important challenges in FTS. Recently, many efforts have been made to develop novel FT catalysts with high selectivity and stability. Understanding of key factors determining the activity, selectivity and stability is crucial for the rational design of efficient FT catalysts. The main research content of this thesis is to explore several strategies for the design of highly selective and stable metal catalysts and process of carbon monoxide hydrogenation. The main conclusions are as follows:

8.1.1 Syngas direct conversion to olefins over iron and cobalt catalysts

New efficient Bi- and Pb- promoted iron catalysts supported by carbon nanotubes for syngas directly to light olefins have been developed. The promoted iron catalysts present higher FT reaction rate and higher selectivity to the C_2-C_4 olefins (55 %-65 %) and can operate even under atmospheric pressure. A combination of characterization techniques reveals remarkable migration of the promoting elements, which occurs during the catalyst activation. After the activation, the iron carbide nanoparticles are decorated with the promoting elements. The lower melting points and high mobility of these two metal promoters during the catalyst activation are crucial for the intimate contact between Fe and promoters. The promoting effects of bismuth and lead result in a better reducibility and easier carbidization of iron nanoparticles. Carbon monoxide dissociation on the promoted catalysts seems to be facilitated by oxygen scavenging from iron carbide to the promoters. The presence of the promoters slows down secondary hydrogenation of olefins and decreases the chain growth probability and

selectivity to the C_{5+} hydrocarbons.

Low temperature FT synthesis over Co based catalysts leads to mainly to the paraffins. Our approach for the synthesis of long-chain linear α-olefins addresses application of carboxylic acids for stabilization of olefins formed during the low temperature FT process over Co based catalysts. The total selectivity of 39 % to α-olefins has been attained in the presence of acetic acid. The effect has been assigned to stabilization of olefins with intermediate formation of esters and their subsequent decomposition.

8.1.2 Synergy of nanoconfinement and promotion for iron catalysts in FTO

Nanoconfinement of iron nanoparticles inside CNT and their promotion with Bi and Pb result in synergetic effects on the structure of iron species and their catalytic performance in Fischer-Tropsch to olefins (FTO). Higher iron dispersion has been obtained in the confined catalysts, while no effect of the promotion on iron particle size was observed. The iron reduction and carbidization proceeds much easier for iron species confined inside CNT and promoted with Bi and Pb. The initial morphology of iron is pod-like structure and transferred to core-shell structure with Bi and Pb in the shell during activation and reaction. The nanoconfinement assists in controlling the migration of the promoters by restricting the promoters inside the tubes and thus then increase their interaction with iron carbide. The promoting effects and intimate contact of bismuth and lead inside the CNT channels with iron carbides are crucial for obtaining enhanced catalytic performance in high temperature FT synthesis. Both nanoconfinement and promotion with Bi and Pb result in a major increase in FT reaction rates. The increase in FT rate because of nanoconfinement is principally due to the enhancement of iron dispersion, while the promotion with Bi and Pb produces strong effect on intrinsic activity of iron sites. The promotion effect is stronger in the confined catalysts, which is possible due to the stronger interaction between the promoter and iron carbides inside CNT. The catalysts containing iron carbide nanoparticles confined inside CNT exhibit high catalytic activity even under

atmospheric pressure. The light olefin selectivity is also improved by the promotion and nanoconfinement. Nanoconfinement of iron particles in CNT slows down iron sintering during the reaction and thus improves the catalyst stability.

FT synthesis is often considered as a structure sensitive reaction and particle size may have noticeable effects on catalytic performance. Apart from the confinement effect, we address the size effects of iron nanoparticles encapsulated inside of CNT on syngas conversion to light olefins. In the unpromoted iron catalysts with confined iron nanoparticles, the TOF increases with the increase in the iron nanoparticle size from 2.5 nm to 6-8 nm and then remains stable with further increase in the iron particle size, while the product selectivity is not affected by the nanoparticle size variation. However, in the Bi and Pb promoted iron catalysts, the size of encapsulated iron nanoparticles affects both the activity and selectivity. The activity shows similar trend with the unpromoted iron catalysts, while the selectivity to light olefins decreases with the increase in the iron particle size. These findings shed further light on the fundamental effects of confinement on catalysis, and provide more insights into the particle size effects in iron-based FT catalysts.

8.1.3 Design of high stable cobalt and nickel catalysts

Carbon monoxide hydrogenation over Co and Ni catalysts has provided important opportunities to store energy and to manufacture alternative renewable transportation fuels. Catalyst deactivation is one of the most serious issues restricting application of this reaction. Hereby, we propose a simple and efficient way for better stability and in-situ self-regeneration of supported cobalt and nickel catalysts under the reaction conditions via their promotion with bismuth.

Promotion with small amount (0.1 wt.% and 0.2 wt.%) of Bi does not lead to any significant changes of initial CO conversion, while a much more stable catalytic performance was observed. Similarly, the stability enhancement in CO hydrogenation to methane was also observed for the Bi-promoted Ni catalysts. Interestingly,

hydrocarbon selectivities at comparable carbon monoxide conversions were not much affected by the promotion with Bi.

A combination of characterization techniques (TPH-MS, TEM-EDX, XPS, XRD) reveals that this remarkable stability could be caused by slowing down carbon deposition and catalyst sintering. In the promoted catalysts, bismuth is localized at the interface between metal nanoparticles and support covering the Co surface. Bismuth oxidation-reduction cycling during carbon monoxide hydrogenation results in the removal of deposed carbon and continuous catalyst self-regeneration. Formation of the thin bismuth layer in the surface of cobalt nanoparticles protects them against sintering.

8.2 Perspectives

8.2.1 Increase in the olefin selectivity over iron and cobalt catalysts

The growing interest of different countries to secure their supply of olefins will continue to drive research and development of catalysts and process for the production of these important commodity chemicals from non-oil-based feedstocks. Syngas direct conversion to olefins offers feedstock flexibility. One of the obstacles for commercialization of FTO process is to balance the activity and selectivity of olefins. Iron catalysts are widely used for the generation of light olefins because of inexpensive and highly selective towards light olefins. However, it is difficult to obtain high CO conversion with high light olefins selectivity. The active species, catalysts support and promoters have strong impact on catalytic performance of FT synthesis. Thus, it is necessary to rational design of efficient FTO catalysts by control the relationship of active species, catalysts support and promoters. Another challenge is the high activity of WGS reaction and methane selectivity over Fe catalysts.

The catalytic performance in light olefins synthesis from syngas can be further improved by selective control of active phases (Fe, $Fe_{2.2}$ C, Fe_3C, Fe_5C_2, Fe_3C_7) in the working catalysts by using efficient promoters. The goal is to identify iron carbide most selective to light olefins by using other elements (Sb, Sn, etc.) with lower melting point

or by dual promotion with Bi and Pb.

There has been a great interest in the society to utilization of CO_2. The iron catalysts promoted with soldering metals developed in this thesis can be efficient in the CO_2 hydrogenation. The potential of these catalysts should be evaluated in the olefin synthesis from CO_2.

This thesis showed an opportunity to produce long chain α-olefins in low-temperature FT synthesis by cofeeding with acids. In future works, the α-olefin selectivity in low temperature FT synthesis combined with co-feeding with acids can improved by optimizing cobalt catalysts via variation of cobalt particle size, support and use of catalyst promoters.

8.2.1 Design high stable metal catalysts in CO hydrogenation

Apart from the selectivity limitation in CO hydrogenation, catalysts deactivation especially in high conversion is also one reason which restricts the wide application. In this thesis, we have been successful in improving the stability of cobalt and nickel catalysts by their promotion with soldering metals. This approach can be extended to other catalytic reactions (methanol to olefins, CO or CO_2 conversion to dimethyl ether, organic molecules transformation, et al.).

Deeper information is also required about the deactivation phenomena occurring during Fischer-Tropsch synthesis. Development of a reproducible, better defined, model metal system and utilization of *in-situ* and *operando* characterization tools should provide in the future better understanding deactivation mechanisms in the CO hydrogenation catalysts.

Author Introduction

Bang Gu was born in May 1990 in Henan province, China. He obtained his bachelor's degree in materials chemistry from South-Central university of Nationalities in 2009. After that, he continued his studies in physical chemistry at Xiamen University under the guidance of Prof. Ye Wang. His research during Master focus on designing high selective catalysts in syngas to light olefins: from traditional iron-based catalysts to bifunctional oxides-zeolite catalysts. In 2016, he was sponsored by China Scholarship Council for his PhD programs at Unité de catalyse et de chime du solide (UCCS), Université de Lille, France. His PhD thesis was supervised by Dr. Andrei Khodakov. His research, described in this thesis, focuses on designing efficient metal catalysts with high selectivity and stability in CO hydrogenation.

List of Published Papers

(1) **B. Gu**, C. Zhou, S. He, S. Moldovan, P. A. Chernavskii, V. V. Ordomsky*, A. Y. Khodakov*. Size and Promoter Effects on Iron Nanoparticles Confined in Carbon Nanotubes and their Catalytic Performance in Light Olefin Synthesis from Syngas. *Catalysis Today*, **2019** (In Press).

(2) **B. Gu**, S. He, D. V. Peron, D. R. Strossi Pedrolo, S. Moldovan, M. C. Ribeiro, B. Lobato, P. A. Chernavskii, V. V. Ordomsky* A. Y. Khodakov*. Synergy of Nanoconfinement and Promotion in the Design of Efficient Supported Iron Catalysts for Direct Olefin Synthesis from Syngas. *Journal of Catalysis*, **2019**, 376, 1-16.

(3) **B. Gu**, M. Bahri, O. Ersen, A. Khodakov*, V. V. Ordomsky*. Self-regeneration of cobalt and nickel catalysts promoted with bismuth for non-deactivating performance in carbon monoxide hydrogenation. *ACS Catalysis*, **2019**, 9(2), 991-1000.

(4) **B. Gu**, A. Y. Khodakov and V. V. Ordomsky*. Selectivity shift from paraffins to α-olefins in low temperature Fischer-Tropsch synthesis in the presence of carboxylic acids. *Chemical Communications*, **2018**, 54, 2345-2348.

(5) **B. Gu**, Vitaly V. Ordomsky*, M. Bahri, O. Ersen, P. A.Chernavskii, D. Filimonov, A. Y. Khodakov*. Effects of the promotion with bismuth and lead on direct synthesis of light olefins from syngas over carbon nanotube supported iron catalysts. *Applied Catalysis B: Environmental*, **2018**, 234 (15), 153-166.

(6) **B. Gu**, S. He, W. Zhou, J. Kang, K. Cheng*, Q. Zhang, Y. Wang*. Polyaniline-supported iron catalyst for selective synthesis of lower olefins from syngas. *Journal of Energy Chemistry*, **2017**, 26, 608-615.

(7) V.V. Ordomsky, Y. Luo, **B. Gu**, A. Carvalho, P.A. Chernavskii, K. Cheng, A. Y. Khodakov*. Soldering of iron catalysts for direct synthesis of light olefins from syngas under mild reaction condition. *ACS Catalysis*, **2017**, 7, 6445-6452.

(8) K. Cheng^{+}, **B. Gu**$^{+}$, X. Liu^{+}, J. Kang, Q. Zhang*, Y. Wang*. Direct and highly selective conversion of synthesis gas into lower olefins: design of a bifunctional catalyst combining methanol synthesis and carbon-carbon coupling. *Angewandte Chemie International Edition*, **2016**, 128(15), 4803-4806. (**Very Important Paper and Press Release, +equal contribution**)

(9) X. Peng+, K. Cheng+, J. Kang+, **B. Gu**, X. Yu, Q. Zhang, Y. Wang. Impact of hydrogenolysis on the selectivity of the Fischer-Tropsch synthesis: disel fuel production over mesoporous zeolite-Y-supported cobalt nanoparticles. *Angewandte Chemie International Edition*, **2015**, 15, 4553-4556. (**Very Important Paper**)

Conference

(1) **B. Gu**, V. V. Ordomsky, M. Bahri, O. Ersen, P. A. Chernavskii, A. Y. Khodakov*. Soldering of iron and cobalt catalysts in Fischer-Tropsch synthesis, *12th Natural Gas Conversion Symposium*, San Antonio, **2019**, Oral presentation.

(2) **B. Gu**, V. V. Ordomsky, A. Y. Khodakov*, Confinement of iron and promoters in carbon nanotubes for direct selective synthesis of lower olefins from syngas over Bi and Pb promoted iron catalysts, *8th International Symposium on Carbon for Catalysis: CarboCat-VIII*, Porto, **2018**, student short oral and poster presentation (**Best Poster Prize**)

(3) **B. Gu**, V. V. Ordomsky, M. Bahri, O. Ersen, P. A. Chernavskii, A. Y. Khodakov*.

Migration of the promoters and direct synthesis of lower olefins from syngas over iron catalysts supported on carbon nanotubes, *GECAT*, TREGUNC, **2018**, poster presentation. (**Best Poster Prize**)

Acknowledgement

I am gratefully thankful to my supervisors, Dr. Andrei Y. Khodakov. He is such a gentleman and his encouragement, guidance and support enabled me to finish my PhD thesis. I am also grateful to Dr. Vitaly V. Ordomsky for the kind suggestion and guidance.

Many thanks to Olivier Gardoll, Laurence Burylo, Pardis Simon and Martine Frère for help with TPR, XRD and XPS measurements. Thanks to Dr. Mauro C. Ribeiro and Dr. Bruno Lobato for the help with synchrotron based XPS and EXAFS in Campinas. Thanks to Mauro C. Ribeiro and Bruno Lobato for the kind help of the synchrotron experiments in Campinas.

I would also like to thank the jury members of my thesis, Dr. Cuong Pham-Huu and Prof. Joris Thybaut for the reading and the examination of this manuscript.

I am so appreciating to meet you all my dear group membership: Dr. Mirella Virginie, Dr. Nuno Batalha, Dr. Yanping Chen, Dr. Guanfeng Liang, Dr. Shaohua Xie, Dr. Sara Navarro-jaen, Dr. Tong Li, Xiang Yu, Feng Niu, Dan Wu, Deizi V. Peron, Ana Sofia Borrego, Aleksandra Peregudova, Camila Flores, Renata De Carvalho Teles Bertotto, Iñigo Perez, Débora Strossi, Melissa de la Rocha, Alan Josue Barrios Medina.

I would like to thank my friends in France: Dr. Zhiping Ye, Dr. Hao Hu, Dr. Binyu Yang, Dr. Shuo Chen, Dr. Zhang Jian, Dr. Wang Yue, Dr. Yuchen Xie, Dr. Xiaofeng Yi, Dr. Yaqian Wei, Dr. Xuemei Liu, Dr. Jin Sha, Dr. Yin Xu, Dr. Peixin Li, Dichao Shi, Jingpeng Zhao, Jianxiong Wu, Li Zhang, Hua Liu, Xiu Liu, Yuanshuang Zheng, Yash, Francesco, Sarah, Tanushree, Anouchka, Camila, Bertrand, Parnian, Guillaume, Herman, Maya, Aleksandra, Shreya, Grece, Noura, Juliana, Shilpa and all the PhD students in UCCS, for their support and help during my PhD studies.

I am grateful to the China Scholarship Council (CSC) for the financial support of my PhD project.

Finally, I would like to thank my family for their endless care and understanding in my study and life. I overcame many difficulties because of you and love you forever! I wish my family and all the friends a healthy and happy life.